Two-dimensional quantum field theory in and out of equilibrium

PhD Dissertation

Kristóf Hódsági

Supervisor: Dr. Márton Kormos
senior research fellow
BME Institute of Physics
Department of Theoretical Physics

MŰEGYETEM 1782

Budapest University of Technology and Economics
2022.

“Beauty is in the eye of the beholder”

“A szépség a tekintetben rejlik.”

Acknowledgements

This is the time and place for me to express my gratitude towards the numerous people—even if the actual chance of them reading this is quite modest—who contributed to the process in which this thesis was created. First and foremost, sincere thanks to Márton Kormos, for your careful supervision, the many discussions, lot of inspiring ideas, and a seemingly inexhaustible patience towards my often unorganised reasoning. And, not the least, for your careful reading of this lengthy manuscript.

I am indebted to Gábor Takács as well: thank you for guiding my interest towards quantum field theory in the first place, for the stimulating discussions be it in a classroom or a canteen, and for your unflagging enthusiasm towards physics.

Many thanks to Dávid (X. Horváth), I am grateful that we had the opportunity to collaborate and discuss various topics both related and unrelated to physics. Thank you Máté (Lencsés) for your most careful reading of the manuscript, for the plotting ideas that made the lengthy writing process enjoyable at times, and I am grateful for the shared office. I retain fond memories of all the people from my previous office, the "DocRoom", with special thanks to Bende and Zoli for a camaraderie of almost nine years now. Due thanks to András, for alleviating me of my teaching duties in the last moment, so that I would stand a chance to write up this work in time.

I am grateful to all my friends, who renewed my sometimes fading motivation with questions (or the absence of them) regarding my PhD, and for the conversations and various shared experiences. It is wisest not to list names here, but I hope that my gratitude compensates for whatever omission I would make.

It is right and just to finish with saying thanks for all the support I received from my family, especially around the time of the first quarantine. A complete list, thankfully, would also not fit, but I take the space to say one last thanks: köszönöm a hátteret Édesapa és Édesanya!

Contents

Chapter 1

Introduction

With over 120 years having passed since it was born [1], quantum theory now enjoys a lifespan longer than that granted to the doyens of humankind. Even at such a venerable age, the field retains much of its youthful appeal, marked by an intriguing variety of traits. These characteristics—a counterintuitive conceptual basis necessitating a scientific metanoia, various imposing mathematical problems inviting great computational effort, and an abundant promise in terms of possible technical applications—have captivated generations of physicists.

Indisputably, the most renowned scientific conquests within quantum theory are due to the description of the dynamics in terms of quantum fields in the context of quantum field theory (QFT) [2]. Originally, QFT was developed to study the field of atomic and subatomic physics, opening up a revolutionary perspective on the microscopic structure of matter. The unrelenting struggle to unveil the most fundamental aspects of the physical world resulted in one of the most successful scientific theories, the standard model of particle physics, housing the plethora of particles discovered in the last century. Propelled by its success, quantum field theory soon emerged as a lingua franca of modern theoretical physics, capturing collective traits of systems that have essentially quantum degrees of freedom.

In particular, QFT has a long history of modelling quantum many-body dynamics in the field of condensed matter physics. Analogously to classical models of statistical physics, quantum many-body systems exhibit second order phase transitions, characterised by the divergence of the correlation length. In the description of critical phenomena, the microscopic length scale can be neglected, and the long-wavelength modes of the lattice models are subject to a field theoretical description [3]. The validity of QFT reflects the universal behaviour near the quantum critical point.

The study of quantum phase transitions is one of the most important contemporaneous applications of quantum field theory models. The curiosity of quantum critical points lies in the fact that they occur in the ground state of the quantum many-body Hamiltonian H. In other words, unlike classical ordering, quantum

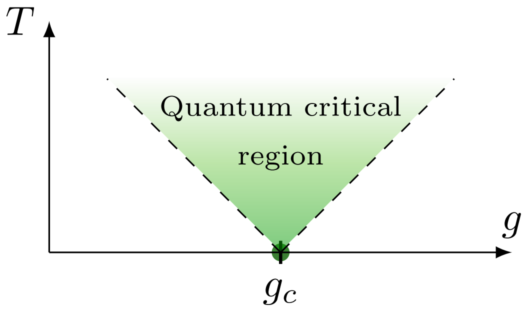

Figure 1.1: Illustration of the quantum critical region near a quantum phase transition. The quantum critical point is located at $g = g_c$ and $T = 0$, but universal dynamics is expected in a broader region extending to nonzero temperatures. Based on a similar illustration in Ref. [4].

phase transitions are zero temperature phenomena, happening at a critical value g_c of some coupling parameter g of the Hamiltonian. Nevertheless, the fingerprints of universal behaviour captured by field theory are present for low finite temperatures as well, outlining a quantum critical region [4], illustrated in Fig. 1.1. By probing this region, quantum critical systems can be investigated experimentally.

A serious bottleneck in the observation of the quantum phases of matter is the delicate nature of quantum correlations, which are easily subdued by thermal fluctuations, long hindering the exploration of the quantum world outside particle colliders. This motivates the focus on low-dimensional models, where quantum fluctuations are enhanced. Coincidentally, for systems with a single spatial dimension, it is possible to obtain exact solutions for the dynamics under appropriate circumstances. These circumstances are the conditions for quantum integrability, a powerful tool in the exact description of strongly interacting quantum models. Quantum integrable models both on the lattice and in field theory have provided theoretical physics with numerous illuminating results for almost a century now [5]. The exact solutions reveal that exotic configurations of the elementary degrees of freedom form a variety of particle-like collective excitations in one-dimensional quantum systems.

The recent decades have witnessed several experimental breakthroughs leading to the realisation of well-known low-dimensional theoretical models, instigating a renewed interest in them. Precise experiments can now be performed on metallic alloys with a chain-like crystalline structure on the one hand [4], and on gases of ultracold atoms in optical traps, with manipulable dimensionality and effective interactions on the other [6]. In particular, the cold atom experiments offer an optimal setting to study isolated quantum systems, both in and out of equilibrium. The latter aspect attracts a particularly heightened attention from theorists, as non-equilibrium settings touch upon the very foundations of statistical physics by explicitly probing the thermalisation of closed quantum systems.

The immense theoretical study triggered by modern experiments led to the clarification of the fundamental concepts of statistical physics, especially in relation to integrable systems [7]. The concurrent experimental and theoretical works have produced a new paradigm, the quantum quench [8], to study non-equilibrium behaviour. Quenching corresponds to the simple and experimentally viable protocol of implementing a sudden change in the coupling parameters of the quantum Hamiltonian. The study of the subsequent time evolution is at the forefront of the research in the field of quantum dynamics out of equilibrium. A parallel approach is the slow change, or ramp, of parameters near critical points, with the aim of unveiling universal features in the dynamics [9].

In this thesis, I attempt to contribute to this line of work by advancing the theoretical modelling of low-dimensional quantum systems both in and out of equilibrium. As a preface, in Chapter 2 I overview the established results and previous findings concerning the out-of-equilibrium behaviour of closed quantum systems, and introduce the methodology of this thesis together with the theoretical background and the experimental context of my work.

Chapters 3-7 discuss my main scientific results. The topic of Chapter 3 is the exact calculation of matrix elements in the E_8 integrable field theory, which is obtained as the scaling limit of the critical Ising model under a longitudinal magnetic field. The results, obtained through the solution of the form factor bootstrap, find an immediate experimental application in the observation of the exotic E_8 particle spectrum in the quasi-1D anti-ferromagnetic $BaCo_2V_2O_8$ material.

In Chap. 4 I discuss the time evolution following a quantum quench in the E_8 model, where significant features of the post-quench dynamics are extracted by comparing numerical and analytical results. Chap. 5 develops a perturbative expansion to characterise the excitation content of the initial state following a global quench in a quantum field theory model. The formulae are evaluated for quenches in the E_8 model, analogously to the previous chapter.

Chapter 6 presents an improvement to the numerical modelling method employed to solve the post-quench dynamics earlier. The numerical approach is applicable in perturbed conformal field theory models, where the algorithmic development allows for a more economic handling of the Hilbert space, while making the method more available to a wider community of researchers.

Chap. 7 investigates the effects of ramps within the parameter space of the Ising field theory. This specific non-equilibrium protocol is known to bring about a universal dynamical behaviour, the Kibble–Zurek scaling, in near-critical models. My work expounds on the validity of this scaling in an interacting field theory, using various observables to carry out a thorough theoretical examination. Finally, in Chap. 8 I summarise my findings in the form of thesis statements.

Supplements, where required, are provided in the appendices in the form of detailed calculations. Appendices A-C contain the extended calculations related to the form factor bootstrap, the perturbative overlaps, and the ramp dynamics, respectively. App. D discusses the systematic improvement of data obtained from the numerical modelling method used throughout the thesis.

Chapter 2

Low-dimensional quantum many-body dynamics

In this chapter we outline the context of the novel results presented in this thesis, focusing on the general traits of quantum many-body systems in one temporal and one spatial dimensions. Firstly, we overview the theoretical basis provided by prior research regarding the non-equilibrium dynamics of closed quantum systems in general. Secondly, we introduce the methodology of the subsequent chapters by defining the specific quantum field theory we are going to use to model the low-dimensional quantum dynamics, together with a highly efficient numerical method. Finally, we briefly introduce the contemporary experimental techniques, through which the discussed theoretical concepts take root within the observable reality.

2.1 Fundamental non-equilibrium concepts

Even from a mere theoretical point of view, the study of closed quantum systems out of equilibrium is a vast subject with many branches. In this section we identify two important strands that are fundamental to this field, and elaborate on them in order to sketch the context of the new results in this thesis. These two topics are the late-time dynamics, going under the name of equilibration; and a paradigmatic protocol to realise and test non-equilibrium behaviour, the quantum quench. Both aspects are illuminated by results coming from quantum integrability, a field which quickly became an essential guide to contextualise and explain non-equilibrium phenomena. In the following, we maintain a specific focus on integrable models which play a central role in all subsequent chapters.

2.1.1 Late-time dynamics: thermalisation

The first question we expound on regarding the non-equilibrium quantum many-body dynamics addresses the generic features of the late-time behaviour.

The intuition coming from classical statistical mechanics is clear: generic classical systems eventually approach a thermal equilibrium due to ergodicity, leading to the equivalence of statistical and time averages. For quantum systems, thermal states are described by the density operator corresponding to the Gibbs ensemble (GE):

$$\rho_{\mathrm{GE}} = \frac{1}{Z}\mathrm{e}^{-\beta H} = \frac{1}{Z}\sum_{n}\mathrm{e}^{-\beta E_n}\left|n\right\rangle\left\langle n\right| \,, \tag{2.1}$$

which is a mixed state of the eigenstates $|n\rangle$ of the Hamiltonian H. The mixed nature of the Gibbs state poses a conundrum for the thermalisation of closed quantum systems, since under unitary time evolution an initial pure state remains pure:

$$\rho(t) = \left|\Psi(t)\right\rangle\left\langle\Psi(t)\right| = \sum_{m,n} c_n c_m^* \mathrm{e}^{-i(E_n - E_m)t}\left|n\right\rangle\left\langle m\right| \,. \tag{2.2}$$

In other words, thermalisation cannot occur at the level of the density operator corresponding to the full system.

The first step towards the resolution of this challenge is to consider that experimental probes of the thermalisation do not have access to the density matrix itself, but to (a set of) observables $\mathcal{O}_n$, so the physically meaningful formulation of thermal equilibration is a statement on the observables:

$$\mathrm{Tr}(\rho(t)\mathcal{O}_n) \to \mathrm{Tr}(\rho_{\mathrm{GE}}\mathcal{O}_n) \,. \tag{2.3}$$

Here the limit involves time-averaging over long times and then taking the thermodynamic limit of infinite system size. Applying these limits to the density operator $\rho(t)$ itself yields the diagonal ensemble:

$$\lim_{T\to\infty}\frac{1}{T}\int_0^T \mathrm{d}t\rho(t) = \rho_{\mathrm{DE}} = \sum_n \left|c_n\right|^2\left|n\right\rangle\left\langle n\right| \,, \tag{2.4}$$

where we assumed that the Hamiltonian H does not have an extensive set of degeneracies, so only the diagonal contributions survive in the thermodynamic limit, from where the equality follows. Then, to answer how (or whether) closed quantum systems reach thermal equilibrium, one has to show that for the physically relevant observables the diagonal ensemble average is equivalent to the predictions of the Gibbs ensemble.

To resolve this question, Deutsch [10] and Srednicki [11] proposed the eigenstate thermalisation hypothesis (ETH), which can be summarised in the assumption that in the thermodynamic limit the matrix elements of observables in the eigenbasis of H exhibit a smooth dependence on the eigenstate energy E_n: [12]

$$\left\langle m\right|\mathcal{O}\left|n\right\rangle = f_{\mathcal{O}}\left(E_n\right)\delta_{mn} + \mathrm{e}^{-S\left(\frac{E_n+E_m}{2}\right)/2} g_{\mathcal{O}}\left(\frac{E_n+E_m}{2}, E_n - E_m\right) R_{mn} \,, \tag{2.5}$$

where $f_{\mathcal{O}}\left(E\right)$ is a smooth function which coincides with the microcanonical ensemble value, S is the entropy and R_{mn} are random variables with zero mean.

On this basis, thermalisation (2.3) follows for all observables that satisfy the ETH, assuming that the initial state have a narrow energy distribution in the thermodynamic limit [13]. There is strong numerical evidence for the ETH in the case of few-body operators [12], and more recent numerical and analytical arguments for the validity of ETH of any observable confined to a subsystem not larger than 1/2 of the system size (which is infinite in the thermodynamic limit!) [14]. Roughly speaking, the generic understanding is that ETH is behind the thermalisation of closed quantum systems in the sense that it holds for all physically relevant and experimentally accessible quantities.

This reasoning explains the thermalisation of generic quantum systems, with results completely analogous to the classical statistical mechanics, as the equilibrium state is given by a Gibbs ensemble. The analogy extends further, covering the case of further conserved quantities. The late-time equilibrium state in this case is given by a generalisation of Eq. (2.1), taking into account all the charges Q_i:

$$\rho_{\mathrm{GGE}} = \frac{1}{Z} \sum_i \mathrm{e}^{-\beta_i Q_i} \,, \tag{2.6}$$

where the β_i parameters can be calculated from the expectation value of the charges in the initial state, by virtue of the conservation laws. The acronym GGE stands for the generalised Gibbs ensemble, a name coined in the context of integrable models [15], where an extensive set of charges is conserved by the dynamics.

Integrable models are peculiar in the sense that they provide a way to create “nonthermal” states (i.e., GGE and not GE states), however, they also often require a fine-tuning of parameters: in realistic systems, at least a small integrability breaking is always present. Nevertheless, the integrable steady state (2.6) has profound consequences on the thermalisation of closed quantum systems through the process called prethermalisation. Prethermalisation amounts to a separation of timescales: close to integrable systems first approach the GGE value, and thermalise to the Gibbs ensemble much later. As it realises long-living quantum correlations, prethermalisation is heavily studied both experimentally [16–18] and theoretically [19–23].

2.1.2 A paradigmatic protocol: the quantum quench

Above we identified important general aspects of out-of-equilibrium quantum dynamics. The concepts we encountered are touching upon the foundations of statistical mechanics at the level of quantum theory, and it is desirable to have a computationally and experimentally viable method to study them in detail—i.e. a way to realise quantum systems with a finite energy density. A particularly simple approach, called the quantum quench protocol, is to perform an abrupt change in the parameters of the quantum Hamiltonian.

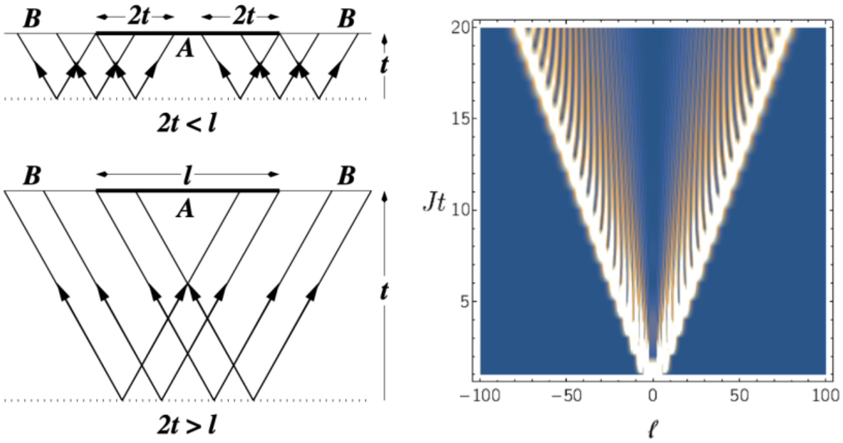

Figure 2.1: The quasi-particle picture of post-quench dynamics. Left (figure from Ref. [26]): the spreading of entanglement in a bipartite system. Subsystem A gets entangled with the environment through the quasiparticles entering it, which predicts $S_A(t)$ to grow linearly in time and then saturate to a finite value. Right (figure from Ref. [27]): connected part of the density-density correlator in a free fermionic lattice model after a global quantum quench. The nonzero part is localised within the lightcone.

The quantum quench was introduced already in the 70's [24], but it stepped into the spotlight with the advent of experimentally realisable quantum Hamiltonians in the new millennium. The first analytical solutions were worked out in critical models around 15 years ago [8, 25], and with subsequent works the quantum quench quickly evolved to be a paradigm in the study of non-equilibrium quantum systems. In general, quenching means time evolution with some Hamiltonian H such that the initial state $|\Psi_0\rangle$ is not an eigenstate of H. Although the quench problem is in general a very broad topic, here we restrict our attention to global quantum quenches which form the basis of Chaps. 4-5, to formulate the protocol.

Global quenches correspond to a sudden change of parameters (say, at $t = 0$) such that both the $t < 0$ and the $t > 0$ Hamiltonians (H_0 and H, respectively) have translational invariance. The preparation of the initial state is performed by the pre-quench Hamiltonian, such that $|\Psi_0\rangle$ is usually the ground state of H_0. While the late-time behaviour is well understood (see above), general features appearing on shorter timescales are much harder to identify, even though a myriad of studies discussed the post-quench dynamics in various models. It is in integrable theories that a more precise understanding can be achieved on an analytical basis, for a volume of reviews see Ref. [7]. Perhaps the most successful picture describing the short-time post-quench dynamics in this context is the spreading of correlation and entanglement due to quasi-particle pairs.

In the quasi-particle pair picture, illustrated in Fig. 2.1, the finite particle density in the post-quench state is attributed to particles created in pairs with zero overall momentum, travelling in opposite directions. Crucially, there is a maximal velocity that the particles can assume, playing the role of the speed of light in the post-quench dynamics. As a consequence, correlations are nonzero in the system only within a lightcone projected by the maximal quasi-particle velocity, and the growth rate of the entanglement entropy $S_A(t) = -\operatorname{Tr}\{\rho_A(t) \ln \rho_A(t)\}$ corresponding to a subsystem A is also limited. The latter quantity can be expressed in a particularly concise form using the quasi-particle picture [26]:

$$S_A(t) \propto 2t \int_{2|v|t<\ell} \mathrm{d}p v_p f(p) + \ell \int_{2|v|t>\ell} \mathrm{d}p f(p)\,, \tag{2.7}$$

where ℓ is the length of the subsystem A, v_p is the velocity of a particle with momentum p and $f(p)$ depends on the probability of creating such a particle pair. The first term corresponds to a linear growth in time, eventually saturating to the value given by the second term. This quantitative behaviour can be shown to hold in generic integrable models [28]. There are some notable exceptions, caused by nontrivial interactions between the components of the particle pair (see the confinement of mesons later on [29]), but the quasi-particle picture remains an important ingredient in the understanding of quench dynamics, especially in light of the difficulties in identifying further general traits.

To understand the complexities of modelling the post-quench time evolution, let us calculate the dynamical expectation value of an observable $\mathcal{O}$. It can be expressed on the basis of the post-quench Hamiltonian as

$$\langle \mathcal{O}(t) \rangle = \sum_{k,l} \langle \Psi_0 | \phi_k \rangle \langle \phi_k | \mathcal{O} | \phi_l \rangle \langle \phi_l | \Psi_0 \rangle \, e^{-i(E_l - E_k)t} \tag{2.8}$$

with $|\phi_k\rangle$ denoting the eigenstates of the post-quench Hamiltonian H with eigenvalues E_k. The long time average of the observable is given by the diagonal ensemble average (cf. Eq. (2.4))

$$\overline{\langle \mathcal{O}(t) \rangle} = \langle \mathcal{O} \rangle_{\mathrm{DE}} = \sum_k |\langle \Psi_0 | \phi_k \rangle|^2 \langle \phi_k | \mathcal{O} | \phi_k \rangle \ . \tag{2.9}$$

To evaluate these expressions, first we need to have access to the $\mathcal{O}_{kl} = \langle \phi_k | \mathcal{O} | \phi_l \rangle$ matrix elements of the observable, and the energy levels E_k—these are equilibrium ingredients, available in free theories, and, to some extent, in integrable models. (See Chap. 3 for an elaboration in integrable field theories.) Second, the dynamical ingredients are the overlap functions

$$g_k = \langle \Psi_0 | \phi_k \rangle \ , \tag{2.10}$$

expressing the initial state in the basis of the post-quench Hamiltonian. And finally, to solve the dynamics, we have to be able to perform the (double) summation in Eqs. (2.8-2.9). This is in general a problem of formidable difficulty, since there is an extensive set of eigenstates inserted. Here we comment on two methods that perform the summation.

The first method is called the quench action (QA) approach [30–32]. The QA employs ideas from the thermodynamical Bethe Ansatz (TBA), arguing that in the thermodynamic limit the summation over the states can be performed, to identify the sole contribution coming from states with their energy density given by the initial state. This selects a single term (a representative state) from one of the summations, while from the second sum only states with non-extensive energy difference contribute. The second approach will be introduced in more detail in Chap. 4, here we merely remark that it is a linked cluster expansion utilising the properties of matrix elements in integrable models [33, 34]. This is an approximate expansion with the post-quench energy density as a small parameter, and the resummation of the expansion contains hints of the late-time dynamics and the precursors of thermalisation.

There are two common factors in these approaches. First, both utilise the constraints coming from integrability to identify the set of basis states and perform the summations analytically. Second, for the concrete evaluation of the results, the overlap functions has to be obtained from an independent calculation, motivating a quest for the post-quench overlaps related to integrable models. These considerations set the stage for Chap. 4, which discusses a numerical solution of a specific quench problem in comparison with the analytic approaches; and especially for Chap. 5, where a perturbative calculation for field theory post-quench overlaps is presented. Now we turn to the introduction of the model, where these studies are carried out.

2.2 Model and methods

Various choices are available for the theoretical study of the universal non-equilibrium dynamics of closed quantum systems. As discussed above, utilising the tools of quantum integrability sheds light on different complex dynamical questions from the details of thermalisation to the spread of correlations following a quantum quench. A substantial part of this thesis is devoted to the investigation of short-time dynamics out of equilibrium, where integrable models are expected to provide further insight. Moreover, it is desirable to complement the analytical studies with an efficient numerical modelling method, which holds the promise to transcend the boundaries of analytical calculations.

In this section we outline the closer context of the subsequent chapters. Firstly, we introduce the field theory model most heavily studied below: the paradigmatic Ising field theory (IFT), which admits a simple formulation and is a repository of various experimentally relevant and theoretically intriguing non-equilibrium phenomena. Charting the parameter space of the IFT we comment on the variety of analytical tools applicable to characterise the model both in and out of equilibrium. Secondly, we discuss the basics of Hamiltonian truncation, an approach to study field theories numerically. More precisely, we are going to focus on the truncated conformal space approach (TCSA), a method working in quantum field theories defined as perturbations of some conformal field theory. In particular, the TCSA is applicable in the context of the Ising field theory, where it is able to supplement and surpass the analytical calculations.

2.2.1 The Ising field theory

The IFT is defined as the scaling limit of the critical transverse field Ising chain. The Hamiltonian of the latter reads

$$H_{\mathrm{TFIC}} = -J\left(\sum_i \sigma_i^x\sigma_{i+1}^x + h_x\sum_i \sigma_i^x + h_z\sum_i \sigma_i^z\right) , \tag{2.11}$$

where σ_i^α with $\alpha = x, y, z$ are the Pauli matrices at site i, the strength of the ferromagnetic coupling J sets the energy scale, and h_xJ and h_zJ are the longitudinal and transverse magnetic fields, respectively. We set periodic boundary conditions, $\sigma_{L+1}^\alpha = \sigma_1^\alpha$. The model is fully solvable in the absence of the longitudinal field, $h_x = 0$, when it can be mapped to free Majorana fermions via the nonlocal Jordan–Wigner transformation [35, 36]. The Hilbert space is composed of two sectors based on the conserved parity of the fermion number. The fermionic Hamiltonian will be local provided we impose anti-periodic boundary conditions for the fermionic operators in the even Neveu–Schwarz (NS) sector and periodic boundary conditions in the odd Ramond (R) sector [3].

The transverse field Ising model is a paradigm of quantum phase transitions: in infinite volume, for $h_z < 1$ the ground state manifold is doubly degenerate, spontaneous symmetry breaking selects the states $(|0\rangle_{\mathrm{NS}} \pm |0\rangle_{\mathrm{R}})/\sqrt{2}$ with finite magnetisation $\langle\sigma\rangle = \pm(1-h_z^2)^{1/8}$ (here $|0\rangle_{\mathrm{NS/R}}$ are the ground states in the two sectors). In finite volume, there is an energy split between the states $|0\rangle_{\mathrm{NS}}$ and $|0\rangle_{\mathrm{R}}$, which is exponentially small in the volume, and the ground state is $|0\rangle_{\mathrm{NS}}$. In the paramagnetic phase for $h_z > 1$, the ground state is always $|0\rangle_{\mathrm{NS}}$ and the magnetisation vanishes. The quantum critical point (QCP) separating the ordered and disordered phases is located at $h_z = 1$, which can also be seen from the behaviour of the gap, $\Delta = 2J|1-h_z|$, vanishing at the QCP. In the ferromagnetic phase, the massive fermionic excitations can be thought of as domain walls separating domains of opposite magnetisations, and with periodic boundary conditions their number is always even.[1] In the paramagnetic phase the excitations are essentially spin flips in the z direction.

The low energy effective theory describing the model near the critical point is the Ising field theory, obtained in the scaling limit $J \to \infty$, $a \to 0$, $h_z \to 1$ such that speed of light $c_\ell = 2Ja$ and the gap $\Delta = 2J|1-h_z|$ are fixed (a is the lattice spacing) [37]. The critical point corresponds to the theory of a free massless Majorana fermion, which is also one of the simplest conformal field theories (CFT). The two relevant operators at the quantum critical point are

---

[1] This is true even in the Ramond sector, as $|0\rangle_{\mathrm{R}}$ contains a zero-momentum particle.

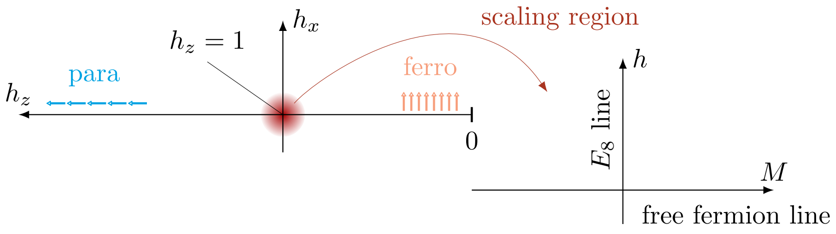

Figure 2.2: The parameter space of the transverse field Ising model (2.11). The critical point at $h_z = 1$ separates the paramagnetic and ferromagnetic phases. Low-energy modes of the critical region are captured by the Ising field theory (2.12), where the two axes in the parameter plane correspond to two integrable field theories.

the magnetisation σ (scaling dimension 1/8) and the so-called 'energy density' ϵ (scaling dimension 1), corresponding to the longitudinal and transverse magnetic fields in the scaling limit. The Hamiltonian of the resulting field theory in finite volume R is given by

$$H_{\text{IFT}} = H_{\text{FF}} + \frac{M}{2\pi}\int_0^R \epsilon(x)\mathrm{d}x + h\int_0^R \sigma(x)\mathrm{d}x\,. \tag{2.12}$$

Here H_{FF} is the Hamiltonian of the free massless Majorana fermion, a minimal CFT with central charge $c = 1/2$. The precise relations between the lattice and continuum versions of the longitudinal magnetic field and the magnetisation operator are

$$\sigma(x = ja) = \bar{s}J^{1/8}\sigma_j^x\,, \tag{2.13}$$

$$h = 2\bar{s}^{-1}J^{15/8}h_x\,, \tag{2.14}$$

with $\bar{s} = 2^{1/12}\mathrm{e}^{-1/8}\mathcal{A}^{3/2}$ where $\mathcal{A} = 1.2824271291\ldots$ is Glaisher's constant.

For $h = 0$ the Hamiltonian describes the dynamics of a free Majorana fermion field with mass $|M|$ (we set the speed of light to one, $c_\ell = 1$). We will refer to this choice of parameters in the $M - h$ parameter plane of the theory (2.12) as the "free fermion line" (see Fig. 2.2). The QCP at $M = 0$ separates the paramagnetic phase $M < 0$ from the ferromagnetic phase $M > 0$, and the coupling is proportional to the mass gap.[2]

Interestingly, there is another set of parameters that corresponds to an integrable field theory: $M = 0$ with h finite.[3] The spectrum of this theory can be

---

[2] The quantum phase transition is analogous to the temperature-induced phase transition of the classical two-dimensional Ising model by virtue of the quantum-classical correspondence, which relates a classical model to a quantum theory living in a lower dimension. Consequently, adding the ϵ field to the critical model is sometimes referred to as a "thermal perturbation", since M plays the role of the distance from the critical temperature.

[3] The lattice model is not integrable for $h_z = 1$ and $h_x \neq 0$, this is a feature of the field theory in the scaling limit.

described in terms of eight stable particles, the mass ratios and scattering matrices of which can be written in terms of the representations of the exceptional E_8 Lie group. From now on, we are going to refer to this specific set of parameters as the "E_8 integrable line" (see Fig. 2.2). The lightest particle with mass m_1 sets the energy scale which is connected to the coupling h as [38]

$$m_1 = (4.40490857\dots)|h|^{8/15}\,. \tag{2.15}$$

The masses of the remaining particle species are expressed in terms of m_1 as [39]

$$\begin{aligned}
m_2 &= 2m_1 \cos\frac{\pi}{5} = (1.618033989...)m_1\,,\\
m_3 &= 2m_1 \cos\frac{\pi}{30} = (1.989043791...)m_1\,,\\
m_4 &= 2m_2 \cos\frac{7\pi}{30} = (2.404867172...)m_1\,,\\
m_5 &= 2m_2 \cos\frac{2\pi}{15} = (2.956295201...)m_1\,,\\
m_6 &= 2m_2 \cos\frac{\pi}{30} = (3.218340459...)m_1\,,\\
m_7 &= 4m_2 \cos\frac{\pi}{5}\cos\frac{7\pi}{30} = (3.891156823...)m_1\,,\\
m_8 &= 4m_2 \cos\frac{\pi}{5}\cos\frac{2\pi}{15} = (4.783386117...)m_1\,,
\end{aligned} \tag{2.16}$$

featuring the golden ratio in m_2/m_1. The energy spectrum also contains moving particle states, which are built up as combinations of particles with finite momenta from the same or different species. Note that only three of the one-particle masses are below the two-particle threshold $2m_1$, the other five are stable only under the aegis of integrability.

The equilibrium properties of the Ising field theory are well understood apart from the two integrable directions as well (see Fig. 2.3). For later convenience, let us introduce the dimensionless quantity η to parameterise the position in the $M - h$ parameter plane:

$$\eta = \frac{M}{|h|^{8/15}}\,. \tag{2.17}$$

For $|\eta| \ll 1$ the particle spectrum is insensitive of the sign of η, and it can be described using the tools of form factor perturbation theory developed in Ref. [41]. Due to integrability breaking, only 3 stable particles remain, the other five obtain a finite life-time and decay [42, 43].

For larger values of η, however, the physics is markedly different depending on the sign of the coupling. In the ferromagnetic regime there appear mesons[4] whose

---

[4] The terminology comes from the analogy with quark confinement in the strong interaction. The domain walls of the lattice model with $h = 0$ are confined by the longitudinal field, as the energy cost increases with the distance between two neighbouring domain walls that have a domain of the wrong magnetisation between them, effectively confining the domain walls.

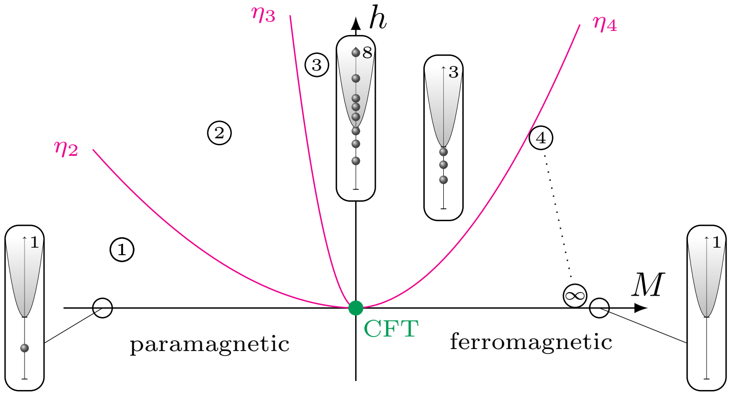

Figure 2.3: The parameter space of the Ising field theory with the spectral content related to the position on the $M-h$ plane. The circled numbers denote the number of stable particles in each case, magenta lines illustrate the decay threshold of the various particle states. Schematic representations of the particle spectra are added in four special settings, where balls denote stable single-particle states, and the shaded region depicts the two-particle continuum. The increasing number of mesons towards the ferromagnetic phase eventually form the two-particle continuum on the $h = 0$ axis in the McCoy-Wu scenario. The figure is inspired by a similar illustration in Ref. [40].

number increases with the magnitude of M. When approaching the thermal axis ($\eta = \infty$), the related poles in the scattering matrix fuse together to form a branch cut corresponding to a continuum of two-kink states under the so-called McCoy–Wu scenario [44]. The meson spectrum appearing close to the $h = 0$ axis is well-understood [45–47].

In the paramagnetic regime, with increasing magnitude of η the number of stable particles is first reduced to two and then to one. The threshold values for the decays of the third and second particles are $\eta_3 = -0.138$ and $\eta_2 = -2.08$, respectively [48].

Preceding the works presented in this thesis, a few studies already discussed the non-equilibrium dynamics of the Ising field theory [29, 33, 49]. These explorations mainly focused on quantum quenches in the vicinity of the thermal axis $h = 0$, the most notable results being the interesting time evolution originating from the confinement of kink states [29]. The message of these early works is that the universal features of the non-equilibrium dynamics can be identified against the background of the well understood equilibrium context of the IFT. This message serves as a direct inspiration to this thesis, which is to a great extent devoted to the investigation of non-equilibrium behaviour of quantum field theories, with a specific focus on the Ising field theory.

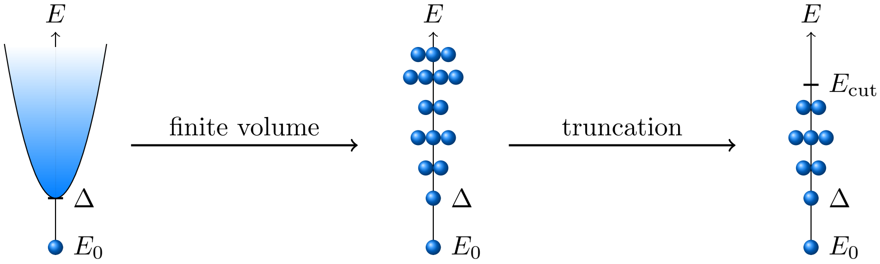

Figure 2.4: Schematic depiction of the process of Hamiltonian truncation. In finite volume the continuous energy spectrum is discretised to an infinite set of separate energy levels, which in turn can be truncated to yield a finite Hilbert space. The figure is inspired by a similar illustration in Ref. [53].

2.2.2 The truncated conformal space approach

The above depiction of the IFT parameter space suggests a variety of approaches to model the dynamics of the theory. We already commented on the analytical tools available, from the exact treatment of the integrable lines to form factor perturbation theory in the vicinity of the axes. A common denominator of these methods is that the application to non-equilibrium protocols is incomparably more complex than the equilibrium calculations in the ground state, similarly to the case of dynamical correlators at finite temperatures [50–52]. Consequently, it is desirable to utilise the available information in a more computationally efficient way, which at the same time maintains an edge over simple perturbative calculations. By and large, this is the motivation at the basis of truncated space approaches (abbr. TSA, see [53] for a review).

The TSA is a nonperturbative numerical method, which operates on the Hilbert space of an exactly solvable Hamiltonian H_0, composed of discrete energy levels in finite volume. The Hilbert space is truncated such that only a finite set of eigenstates $\{|n\rangle\}$ with $E_n < E_{\text{cut}}$ is kept, as illustrated in Fig. 2.4. In turn, the properties of a more generic Hamiltonian $H = H_0 + V$ can be calculated on the truncated basis assuming that the matrix elements V_{mn} are known. The results retain an error coming from the truncation, but the errors can be diminished by increasing the cutoff parameter E_{cut}.

In the context of the IFT, the two simplest choices for H_0 are the massive free fermion model [54], and the conformal theory [55, 56], respectively. Truncating the free fermionic basis is expected to work best in the vicinity of the thermal axis with $h = 0$, and it was indeed successfully applied to quantum quenches in this region in Ref. [49]. In this thesis, we opt for the other choice, the truncated conformal space approach (TCSA), which is applicable in other perturbed CFTs as well. A detailed introduction to this algorithm is postponed to Chap. 6, which presents a recent development to the method. Here we just briefly elaborate on the basic idea, set up some notation, and comment on the systematic procedure of treating the truncation errors.

The TCSA was developed by Yurov and Zamolodchikov in Ref. [55], and applied in the IFT already in Ref. [56] with a resounding success, adequately describing the bottom of the energy spectrum using a modest 18-dimensional truncated Hilbert space. A significant development of the TCSA was the explicit application of the conformal Ward identities [57] to calculate the finite volume matrix elements of the perturbing operator exactly, after mapping the space-time cylinder to the conformal plane.

Utilising these results, we can express the matrix elements of the Hamiltonian (2.12) on the truncated basis. It is convenient to set up the numerics such that all quantities are measured in the appropriate powers of the mass gap Δ. Depending on the specific physical problem, the mass unit is either $\Delta = m_1$, the mass of the lightest particle in the E_8 model; or $\Delta = m$, the mass of the elementary excitation on the free fermion line. With this notation, the Hamiltonian matrix H can be expressed in a dimensionless form for numerical calculations:

$$H/\Delta = \frac{2\pi}{r}\left(L_0 + \bar{L}_0 - c/12 + \tilde{\kappa}_1 \frac{r^{2-\Delta_\epsilon}}{(2\pi)^{1-\Delta_\epsilon}} M_\epsilon + \tilde{\kappa}_2 \frac{r^{2-\Delta_\sigma}}{(2\pi)^{1-\Delta_\sigma}} M_\sigma\right) , \tag{2.18}$$

where $r = \Delta R$ is the dimensionless volume parameter, $M_{\epsilon,\sigma}$ are the matrices of the operators ϵ, σ having scaling dimensions $\Delta_\epsilon = 1$ and $\Delta_\sigma = 1/8$. Here $\tilde{\kappa}_{1,2}$ are the dimensionless coupling constants that characterise the strength of the perturbation.

The conformal Hamiltonian consists of three terms: $c = 1/2$ is the central charge, while L_0 and $\bar{L}_0$ are the generators of the conformal scaling transformations. States in the conformal Hilbert space are characterised by their L_0 and $\bar{L}_0$ eigenvalues, which can be labelled by the integers $n, \bar{n}$. The sum $N = n + \bar{n}$ is called the descendent level of the conformal state. The truncation scheme operates by introducing a maximal descendent level N_{cut}, which is related to the conformal cutoff energy as[5]

$$N_{\text{cut}} = \frac{R}{2\pi} E_{\text{cut}} \, . \tag{2.19}$$

The cutoff parameters used in this work and the corresponding dimensions of the truncated basis are listed in App. D.

Achieving higher and higher cutoffs is computationally demanding, so it is essential to have a model for the cutoff-dependence. The strength of TCSA (in contrast with some other truncated Hamiltonian approaches) lies in its systematic treatment of truncation errors. The contribution of high energy states can be taken into account through a renormalisation group (RG) approach [58–63]. The RG analysis introduces running couplings into the model, governed by a power-law function of the energy cutoff. Most of the works in this thesis concern the E_8 model, where the running of the couplings converges to the infinite-cutoff

---

[5] This relation between the two cutoffs holds only if there is no operator with $\Delta > 1$, which is the case for the applications of the TCSA in this work.

value so rapidly that including them does not make any difference to the dynamics. Consequently, we take a simpler approach to cure the truncation errors, following Refs. [59, 64].

This approach focuses on the cutoff-dependence of the distinct observables instead of the coupling parameters. By a reasoning analogous to the RG arguments, it can be shown that the results for some arbitrary quantity[6] at infinite cutoff are related to TCSA data as

$$\langle \phi \rangle = \langle \phi \rangle_{\mathrm{TCSA}} + A N_{\mathrm{cut}}^{-\alpha_\phi} + B N_{\mathrm{cut}}^{-\beta_\phi} + \dots \,, \tag{2.20}$$

where the $\alpha_\phi < \beta_\phi$ exponents are positive numbers which depend on the scaling dimension of the perturbation, the operator related to the quantity ϕ under consideration, and those appearing in their operator product expansion. Ellipses denote further subleading corrections that decay faster as $N_{\mathrm{cut}} \to \infty$. This expression then can be used to extract the infinite-cutoff value from a set of data points obtained using different N_{cut} cutoff parameters via extrapolation. Unless commented otherwise, all TCSA data presented below are extrapolated using this formula, with the appropriate exponents in the different cases. The exponents with some examples of the extrapolation procedure are gathered in Appendix D.

2.3 Experimental context

As a conclusion to this introductory chapter, let us briefly overview the experiments which provide a background to the subsequent theoretical calculations. As already discussed, all of the theoretical work presented in this thesis focuses on the properties of quantum field theory models which capture universal behaviour in the quantum critical region. Experimentally, this region can be attained both in and out of equilibrium. The non-equilibrium dynamics can be realised in cold atomic gases, triggering considerable theoretical efforts to explain the observations. Moreover, the signatures of quantum criticality are present in the equilibrium properties of low-dimensional systems as well (cf. Fig. 1.1). For this reason, quasi-1D materials are increasingly studied in connection with the well-known theoretical models of quantum many-body systems. In particular, specific spin chains at low temperatures host the exotic E_8 physics of the previous section, thus creating an immediate link between our calculations and real-life materials. Below we list a few interesting experimental results complementing the theoretical focus of this thesis.[7]

---

[6] More precisely, the calculation of Ref. [59] applies to the equilibrium one-point function of some operator $\mathcal{O}$. We apply the same formula to time-dependent one-point functions in non-equilibrium settings, and also for state overlaps, which are related to the identity operator from this point of view. The most remote application is for the cumulants of a full counting statistics, where the precision of the extrapolation justifies the approach.

[7] Naturally, the two selected branches do not cover all relevant experimental aspects. A notable omission is the system of trapped ions, which can act as quantum simulators of spin-1/2 systems. Let us mention two works related to this thesis, Refs. [65, 66].

Cold atoms out of equilibrium

The renewed interest in the behaviour of quantum many-body systems in low dimensions largely stems from the plentiful possibilities offered by cold atomic gases to realise them experimentally. Fuelled by the initial quest for the observation of Bose–Einstein condensates, cold atoms emerged as a cornerstone of studying low-dimensional physics in the past decades [6, 9]. Cold atomic gases provide an excellent realisation of closed quantum systems, since they can be well separated from the environment, and their dimensionality can be manipulated by applying optical lattices to create quasi-1D cigar-shaped clouds. Moreover, by manipulating the frequencies of the optical traps, effective couplings can be induced between the atoms, opening the possibility to engineer quantum Hamiltonians with tunable parameters.

One of the most famous experiments with one-dimensional Bose gases is the celebrated quantum Newton's cradle [16]. The initialisation amounted to preparing two clouds of ^{87}Rb atoms confined to a tube with an increasing potential energy towards the end of the tube. Astonishingly, the initial motion induced by the potential gradient continued after several collisions, resulting in a periodic motion akin to the classical Newton's cradle. The apparent lack of thermalisation, which instigated substantial work along the lines of Sec. 2.1.1, is due to the nearly integrable dynamics of the clouds.

The ^{87}Rb atoms are central to the ongoing experimental effort in the field of non-equilibrium quantum dynamics. They can be used to realise the antiferromagnetic version of the transverse field Ising chain in tilted optical lattices (2.11) [67, 68], and study the role of entanglement spreading and the process of thermalisation [69, 70]. At the same time, the phase dynamics of coupled Bose gases provides insight into prethermalisation [17, 71, 72], and is argued to realise a famous integrable model, the quantum sine-Gordon theory, along with other quantum many-body problems [73].

To reiterate the point made earlier, cold atomic gases not only emulate well-known models of quantum many-body theory, but they coincidentally provide a realisation of out-of-equilibrium dynamics. Apart from the quantum quenches introduced in Sec. 2.1.2, other non-equilibrium protocols are possible, such as the slow change (or ramping) of coupling parameters, which is the setting of Chap. 7. For reviews on this topic, see Refs. [9, 74].

Spin chains and the transverse field Ising model

A separate path to attain the quantum critical region depicted in the first chapter is via quasi-1D spin chains, where the effective degrees of freedom are described by a one-dimensional quantum Hamiltonian. Here we focus our attention to the realisation of the transverse field Ising model (2.11), and especially on the appearance of the exotic E_8 spectrum.

The first observation of the E_8 model was done over a decade ago in the ferromagnetic $\mathrm{CoNb_2O_6}$ material [75]. The effective spin degrees of freedom originate from the spin of the Co^{2+} ions which are arranged into quasi-1D chains within the crystalline structure. At low temperatures, the chains are ferromagnetically ordered, and applying a large enough external transverse magnetic field to a large $\mathrm{CoNb_2O_6}$ single crystal the authors of Ref. [75] managed to realise the (near) critical TFIM. Criticality is broken by the weak interaction between the chains, which acts as a longitudinal magnetic field in the one-dimensional systems, in other words, they are governed by the E_8 Hamiltonian. Indeed, neutron scattering spectroscopy revealed two prominent peaks, whose energies were related via the golden ratio. Peaks corresponding to the higher particles were hidden in the two-particle continuum.

The observed fingerprint of the E_8 symmetry group elevates the model beyond a mathematical curiosity, and instigates an ongoing experimental effort to corroborate the initial findings. Another particularly promising quasi-1D material along this line is the $\mathrm{BaCo_2V_2O_8}$ crystal [76], where the interaction between the Co^{2+} spins is anti-ferromagnetic. Applying a strong transverse field induces an effective staggered transverse field felt by the individual spins, so the chains exhibit an AFM-PM transition that belongs to the Ising universality class. Coincidentally, the coupling between the chains can be taken into account as a staggered longitudinal field, thus realising the anti-ferromagnetic counterpart of the earlier experiment. Performing a similar neutron scattering probe, Ref. [77] demonstrated strong evidence for the presence of seven of the single-particle states at the theoretically predicted masses (2.16), and tentatively pinpointed the eighth particle.[8]

The identification of the universal features within the experimental data requires a careful theoretical analysis. The neutron scattering experiment probes the dynamical properties of the model via the dynamical structure functions (DSF) $D^{\alpha\beta}(\omega, \mathbf{Q})$:

$$D^{\alpha\beta}(\omega, \mathbf{Q}) = \int \mathrm{d}t \sum_{\mathbf{r}} \mathrm{e}^{i(\omega t - \mathbf{Q}\mathbf{r})} \left\langle S^{\alpha}(t, \mathbf{r}) S^{\beta}(0,0) \right\rangle \, , \tag{2.21}$$

where $\alpha, \beta = x, y, z$, so the DSF are the spin-spin correlators in Fourier space. The correlation functions of the E_8 model can be calculated exactly in the knowledge of the matrix elements of its operators: σ and ϵ. This experimental application sets the stage for the next chapter, which details the quest after these matrix elements.

---

[8] We remark that contemporaneously a more precise optical measurement increased the number of observed E_8 particles in the ferromagnetic $\mathrm{CoNb_2O_6}$ chain as well [78].

Chapter 3

Form factor bootstrap in the Ising field theory

Modelling a quantum many-body system oftentimes results in a computational problem of irresolvable complexity. Although one has to resort to numerical approximations in generic cases, integrable models are a beacon of hope that exact analytic solutions do not always elude discovery [5]. A particularly fruitful approach in the context of integrable quantum field theories is the bootstrap program, a method that translates the numerous constraints arising from integrability to a set of consistency relations between the specific functions under consideration. In this chapter we introduce the form factor bootstrap, where the functions subject to the consistency constraints are the matrix elements of local operators. We will show how from the resulting generic equations the matrix elements of specific local operators can be obtained on the basis of asymptotic scattering states, i.e. how one can solve the form factor bootstrap.

Following the general formulation of the form factor bootstrap we present its solution in the field theory describing the critical Ising model in a magnetic field, also known as the E_8 field theory. As discussed above, this model is of experimental relevance, apart from being a theoretical curiosity. The calculation of new exact form factors in the E_8 model, which is the first important original result presented in this thesis, touches both the theoretical and the experimental aspects.

3.1 General form factor properties

3.1.1 Asymptotic states and the S-matrix

Obtaining the solution of an interacting quantum field theory is a notoriously complex problem, which admits several different formulations. One approach is to describe the interactions by scatterings: events which are preceded and followed by a state where particles are essentially free [2]. This statement about the state content is asymptotic in the sense that the state before the scattering (the 'in-state') and the one after the scattering (the 'out-state') are assumed to be a valid description of the physical system in the infinite past and future, in other words, at asymptotically distant time instances. The operator that relates these asymptotic states to each other is called the scattering matrix or the S-matrix. Formally, we can express the S-matrix as

$$S_{\text{out,in}} = \langle \text{out} | \, S \, | \text{in} \rangle \ . \tag{3.1}$$

Considering a matrix element of this general S-matrix between an in-state with n particles and an out-state with m particles we get

$$|A_{a_1} A_{a_2} ... A_{a_m}\rangle = S^{b_1, b_2, ... b_n}_{a_1, a_2, ..., a_m} \, |A_{b_1} A_{b_2} ... A_{b_n}\rangle \ , \tag{3.2}$$

where a_j and b_k index the possibly different types of particles, i.e. they label the particle species. The standard way of calculating the matrix elements of the scattering matrix is to separate the kinematics invoking relativistic invariance and treat the dynamics perturbatively in the interaction strength employing the technique of Feynman diagrams [2].

The repertoire of integrable field theories offers an alternative route, where the S-matrix can be computed exactly. Integrable field theories are defined on a two-dimensional Minkowski spacetime, where the two-momentum of on-shell particles can be parameterised by a single variable, the relativistic rapidity ϑ:

$$(p^0, p^1) = (m \cosh \vartheta, m \sinh \vartheta) \, , \tag{3.3}$$

where p^0 and p^1 are respectively the energy and momentum of a particle with mass m. The asymptotic states thus take the form

$$|A_{a_1}(\vartheta_1) A_{a_2}(\vartheta_2) ... A_{a_m}(\vartheta_m)\rangle \tag{3.4}$$

with a specific ordering of the rapidities: they are decreasing

$$\vartheta_1 \geq \vartheta_2 \geq \dots \geq \vartheta_m \tag{3.5}$$

for an in-state and increasing for an out-state. The ordering expresses that since all motion is constrained to a line, the leftmost particle must possess the largest velocity for the scattering event to take place, as it has to pass all the others. Consequently, the order is reversed after the scattering. On the basis of the asymptotic states (3.4) the S-matrix takes the form

$$S^{b_1, b_2, ... b_n}_{a_1, a_2, ..., a_m}(\vartheta_1^{\text{out}}, \vartheta_2^{\text{out}}, \dots, \vartheta_m^{\text{out}}; \vartheta_1^{\text{in}}, \vartheta_2^{\text{in}}, \dots, \vartheta_n^{\text{in}}) \, . \tag{3.6}$$

In an integrable field theory there is an extensive set of local conserved charges, and as a consequence, the scattering is purely elastic and completely factorised. Pure elasticity means that all momenta are conserved separately—as a corollary, particle creation or annihilation is not permitted—while complete factorisation means that the S-matrix of an $n \to n$ process is the product of all possible $2 \to 2$ processes.[1] Therefore, we can write Eq. (3.6) as

$$S^{b_1,b_2,\dots b_n}_{a_1,a_2,\dots,a_n}(\vartheta_1,\vartheta_2,\dots,\vartheta_n) = \prod_{i<j} S^{\beta_i\beta_j}_{\alpha_i\alpha_j}(\vartheta_i-\vartheta_j)\,, \tag{3.7}$$

where the dependence of the two-particle S-matrix on the rapidity difference reflects Lorentz invariance. The α_i, β_i particle indices respectively contain the in and out sets $\{a_j\}, \{b_j\}$ with the addition of all intermediate particle states. In general, the scattering is not diagonal in the particle species space, that is, $\alpha_i \neq \beta_i$ and $\alpha_j \neq \beta_j$. However, in the following we are going to focus on diagonal scattering models, where the equality holds and the two-body S-matrix is labelled by only two particle indices. The factorised S-matrix satisfies a set of consistency equations, which can be used to identify the particle spectrum of the theory, and write down the two-particle scattering matrices exactly, yielding the solution of the so-called S-matrix bootstrap [39, 81–83]. For a pedagogical introduction to the S-matrix bootstrap the reader is referred to Ref. [79]. In what follows, we assume that the $S_{ij}(\vartheta)$ are known exactly, and use them as an input to the form factor bootstrap.

3.1.2 Form factor definition and axioms

Given the above formalism, it is natural to express the matrix elements of local operators in an integrable field theory on the basis of asymptotic states. The elementary matrix elements are called form factors and they are defined to be

$$F^{\mathcal{O}}_{a_1,a_2,\dots,a_n}(\vartheta_1,\vartheta_2,\dots,\vartheta_n) \equiv \langle 0|\,\mathcal{O}(0,0)\,|\vartheta_1,\vartheta_2,\dots,\vartheta_n\rangle_{a_1,a_2,\dots,a_n}\,, \tag{3.8}$$

where $\langle 0|$ is the vacuum state of the theory. Matrix elements with particles in the left-hand-side state are obtained by crossing their momenta, which amounts to a $\vartheta \to i\pi - \vartheta$ transformation in terms of the rapidity:

$$\begin{aligned}&\langle \vartheta'_1,\vartheta'_2,\dots,\vartheta'_m|\,\mathcal{O}(0,0)\,|\vartheta_1,\vartheta_2,\dots,\vartheta_n\rangle = \\ &F^{\mathcal{O}}(i\pi-\vartheta'_1, i\pi-\vartheta'_2,\dots, i\pi-\vartheta'_m,\vartheta_1,\vartheta_2,\dots,\vartheta_n)\,,\end{aligned} \tag{3.9}$$

where we suppressed the particle species index for brevity. The form factors satisfy a set of equations called the form factor axioms:

1. *Lorentz invariance*

$$F^{\mathcal{O}}_n(\vartheta_1+\lambda,\dots\vartheta_n+\lambda) = e^{s_{\mathcal{O}}\lambda}F^{\mathcal{O}}_n(\vartheta_1,\dots\vartheta_n)\,, \tag{3.10}$$

---

[1] Interestingly, the property of factorised scattering does not require the vast amount of local conserved charges, two extra is enough besides momentum conservation [79]. On the other hand, the coexistence of interactions and complete factorisation is special to two space-time dimensions: the same reasoning renders all theories with factorised scattering trivial in $d > 2$. See the famous Coleman–Mandula theorem for $d = 4$ [80].

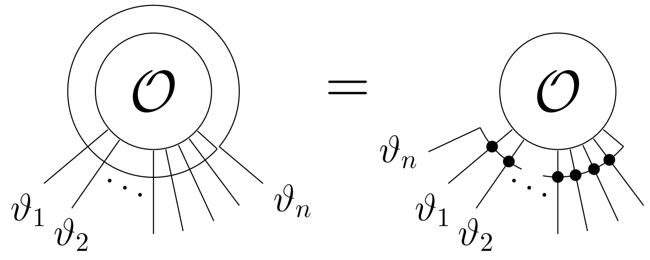

Figure 3.1: Graphical depiction of the cyclic property of form factors. The black dots at the intersections represent an S-matrix factor.

where $s_{\mathcal{O}}$ is the Lorentz spin of the local field $\mathcal{O}$, which is zero for Lorentz scalars considered later on. A consequence of the above equation is that the form factors of scalar operators only depend on the rapidity differences.

2. *Exchange property*

$$F_n^{\mathcal{O}}(\vartheta_1, \dots \vartheta_j, \vartheta_{j+1}, \dots \vartheta_n) = \\ = S(\vartheta_j - \vartheta_{j+1}) F_n^{\mathcal{O}}(\vartheta_1, \dots \vartheta_{j+1}, \vartheta_j, \dots \vartheta_n)\,. \tag{3.11}$$

3. *Cyclic property*

$$F_n^{\mathcal{O}}(\vartheta_1, \dots, \vartheta_{n-1}, \vartheta_n + 2\pi i) = F_n^{\mathcal{O}}(\vartheta_n, \vartheta_1, \dots \vartheta_{n-1})\,. \tag{3.12}$$

4. *Kinematical singularities*

$$-i \lim_{\tilde{\vartheta} \to \vartheta} (\tilde{\vartheta} - \vartheta) F_{n+2}^{\mathcal{O}}(\tilde{\vartheta} + i\pi, \vartheta, \vartheta_1, \vartheta_2, \dots \vartheta_n) = \\ = \left(1 - \prod_{i=1}^{n} S(\vartheta - \vartheta_i)\right) F_n^{\mathcal{O}}(\vartheta_1, \vartheta_2, \dots \vartheta_n)\,. \tag{3.13}$$

5. *Bound state singularities*

$$-i \lim_{\vartheta_{ab} \to iu_{ab}^c} (\vartheta_{ab} - iu_{ab}^c) F_{n+2}^{\mathcal{O}}(\vartheta_a, \vartheta_b, \vartheta_1, \vartheta_2, \dots \vartheta_n) = \\ = \Gamma_{ab}^c F_{n+1}^{\mathcal{O}}(\vartheta_c, \vartheta_1, \vartheta_2, \dots \vartheta_n)\,, \tag{3.14}$$

with $\vartheta_{ab} = \vartheta_a - \vartheta_b$ and $\vartheta_c = \vartheta_a - i(\pi - u_{bc}^a) = \vartheta_b + i(\pi - u_{ac}^b)$, where u_{ab}^c is the position of the bound state pole corresponding to the occurrence of particle A_c in the scattering of A_a and A_b:

$$S_{ab}(\vartheta \sim iu_{ab}^c) \sim \frac{i(\Gamma_{ab}^c)^2}{\vartheta - iu_{ab}^c}\,. \tag{3.15}$$

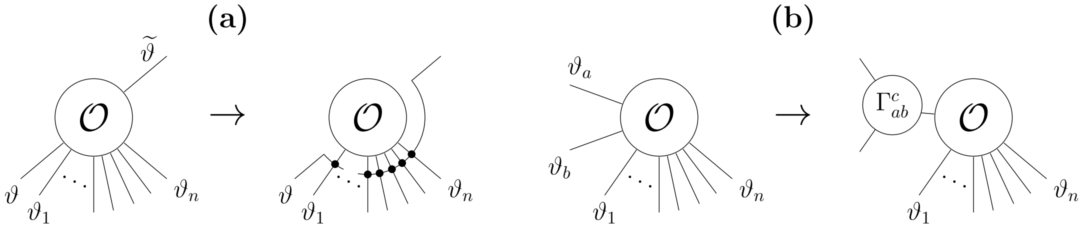

Figure 3.2: Graphical illustration of the form factor axioms in Eqs. (3.13, 3.14). The black dots represent the S-matrix, while Γ^c_{ab} is the residue of the pole in the scattering matrix related to an $A_aA_b \to A_c$ fusion.

In most of the above equations again the species indices are suppressed for simplicity.

The first two equations are straight consequences of the form factor definition and the Lorentz transformation property of the operator $\mathcal{O}$. The cyclic property is illustrated in Fig. 3.1. The figure on the right-hand side of the equation depicts the sequential "disentangling" needed to bring the rapidity arguments of $F_n^{\mathcal{O}}(\vartheta_n, \vartheta_1, \dots \vartheta_{n-1})$ on the right-hand side of Equation (3.12) to canonical order, where each exchange brings in an S-matrix factor. The second and third equations together are usually called Watson's equations [84].

The fourth equation signals the presence of a kinematical pole in the form factor: when two particles from the same species with the same rapidities are present in both asymptotic states, they form a disconnected piece and give rise to a simple pole. The last equation is linked to the bound state poles in the S-matrix: they correspond to two particles having such rapidity difference so that they can be fused to form a third particle as a bound state. The kinematical and bound state poles are depicted in Fig. 3.2.

3.1.3 The form factor bootstrap

The form factor axioms serve as a basis for the form factor bootstrap program, the quest to obtain exact analytical expressions for the matrix elements of local operators in integrable field theories. In the following we outline the general procedure of solving the form factor bootstrap, for further details the reader is referred to the review [85].

The starting point is the general solution of Watson's equations, which is of the form [3, 86–88]

$$F_n^{\mathcal{O}}(\vartheta_1, \vartheta_2, \dots \vartheta_n) = K_n^{\mathcal{O}}(\vartheta_1, \vartheta_2, \dots \vartheta_n) \prod_{i<j} F^{\min}(\vartheta_{ij}) \,, \tag{3.16}$$

where we introduced the shorthand notation $\vartheta_{ij} = \vartheta_i - \vartheta_j$. The minimal two-particle form factors $F^{\min}(\vartheta)$ encode the nontrivial exchange properties appearing in Watson's equations and can be expressed in a closed form [3, 88]. The prefactor

$K_n^{\mathcal{O}}(\vartheta_1, \vartheta_2, \ldots \vartheta_n)$ is a completely symmetric and $2\pi i$-periodic function of its variables that contains the physical poles prescribed by Eqs. (3.13, 3.14). Its pole structure is independent of the operator under consideration, hence it can be further decomposed to

$$K_n^{\mathcal{O}}(x_1, x_2, \ldots x_n) = \frac{Q_n^{\mathcal{O}}(x_1, x_2, \ldots, x_n)}{D_n(x_1, x_2, \ldots, x_n)}\,, \tag{3.17}$$

where the information about the kinematical and bound state poles is encoded in D_n, and the operator-dependence is only present in the $Q_n^{\mathcal{O}}$ function. We also introduced a new variable $x_i \equiv \exp(\vartheta_i)$ for later convenience. Importantly, $K_n^{\mathcal{O}}$ is a rational function of the variables x_i, hence D_n and $Q_n^{\mathcal{O}}$ are expressed as polynomials x_i. This property simplifies the Ansatz that can be used to find the $Q_n^{\mathcal{O}}$ functions to a great extent.

To summarise the first part of the form factor bootstrap, the n-particle form factor can be decomposed into three functions, two of which can be written in closed form knowing the particle content of the asymptotic state and the S-matrix. After that, all that remains is to find the $Q_n^{\mathcal{O}}$ function. Note that the kinematical and bound state pole equations relate form factors with different particle number, hence they impose a recurrence relation on the Q_n polynomials. Eventually, the solution of the form factor bootstrap boils down to solving this recurrence after pinning down its starting elements from separate considerations. We remark that the situation is slightly more complex when we restore the particle species index, but the principle is the same. We will encounter a detailed example of the case of multiple particle species in the next section.

3.2 Solution of the form factor bootstrap in the E_8 model

In the previous section we have introduced the form factor bootstrap program, from the foundations of the problem to the method of solving it. Here we discuss its solution in a specific integrable field theory, the E_8 model, with the aim of presenting the original results related to the first thesis statement.

3.2.1 Definition of the model

The E_8 model is obtained by setting $M = 0$ in the the Ising field theory Hamiltonian (2.12):

$$H = H_{\mathrm{CFT},\, c=1/2} + h \int \sigma(x) \mathrm{d}x\,, \tag{3.18}$$

which corresponds to an integrable field theory. The mass gap (2.15) and the particle spectrum (2.16) of the model were stated already in Sec. 2.2.1. In addition, the S-matrix of the theory can be calculated exactly using the S-matrix bootstrap [39, 83, 89]. As an example, let us present the fundamental two-particle scattering matrix describing the scattering process $A_1A_1 \to A_1A_1$:

$$S_{11}(\vartheta) = (20)_\vartheta\,(12)_\vartheta\,(2)_\vartheta\ , \qquad (k)_\vartheta = \frac{\sinh\vartheta + i\sin\pi k/30}{\sinh\vartheta - i\sin\pi k/30}\,. \tag{3.19}$$

For completeness, we include the full S-matrix in Appendix A. Knowing the exact two-particle S-matrix $S_{ab}(\vartheta)$, the minimal form factors $F_{ab}^{\mathrm{min}}(\vartheta)$ can be expressed in closed form, they are also reported in App. A.

With all these ingredients at hand, the task is to find the $Q^{\mathcal{O}}$ functions introduced in Eq. (3.17). Two comments are in order: first, we have to identify for what set of operators $\mathcal{O}$ the bootstrap is to be solved, and second, we have to find a way to construct solutions for the 8 particle species present in the E_8 model. The answer to the first question is that in a perturbed CFT the operator content is completely determined by the primary fields [90]. We recall that the scaling limit of the transverse field Ising model has two nontrivial primary operators: the longitudinal magnetisation σ introduced above, and the transverse magnetisation field ϵ. The solution of the form factor bootstrap in the E_8 model amounts to finding the matrix elements of these two operators.

As for the question of multiple particle species, there is no conceptual difficulty involved in the construction of form factors containing particles of different types. Due to the closure of the S-matrix bootstrap, any single-particle state in the theory can be obtained as the bound state of two particles. This suggests a “principled” approach outlined in Ref. [89], i.e. to calculate first those form factors that contain only the lightest A_1 particles. All other form factors containing the higher ones can be obtained by the subsequent application of the bound state equation (3.14). This is the approach that we pursue here, thus we discuss it in detail in the following.[2]

3.2.2 General solution

Let us denote the n-particle form factor of the A_1 particles as F_n. We look for F_n in the form of the following Ansatz satisfying the first three axioms:

$$F_n^{\mathcal{O}}(\vartheta_1, \vartheta_2, \ldots \vartheta_n) = H_n^{\mathcal{O}} \frac{\Lambda_n^{\mathcal{O}}(x_1, \ldots, x_n)}{(x_1 \ldots x_n)^n} \prod_{i<j}^{n} \frac{F_{11}^{\mathrm{min}}(\vartheta_i - \vartheta_j)}{D_{11}(\vartheta_i - \vartheta_j)(x_i + x_j)}\,, \tag{3.20}$$

---

[2] We remark that the full S-matrix (see Table A.1) contains further (higher order) poles apart from those appearing in Eqs. (3.13, 3.14). These require the different form factors to satisfy extra consistency relations, providing a somewhat orthogonal approach in the solution of the E_8 form factor bootstrap. This approach is particularly powerful in the determination of two- and three-particle form factors [42, 89]. On the other hand, it becomes more complicated when calculating many-particle form factors, which is the main reason why we take the other path.

where we recall that $x_j \equiv e^{\vartheta_j}$. H_n is a constant factor, and $\Lambda_n^{\mathcal{O}}$ is a symmetric polynomial. The D_{11} factors defined through

$$D_{11}(\vartheta) = P_{2/3}(\vartheta)P_{2/5}(\vartheta)P_{1/15}(\vartheta)\,, \qquad P_\gamma(\vartheta) = \frac{\cos(\pi\gamma) - \cosh(\vartheta)}{2\cos^2\left(\frac{\pi\gamma}{2}\right)} \tag{3.21}$$

encode the positions of the bound state poles, while kinematic poles are included in $(x_i + x_j)$ factors. The minimal form factor $F_{11}^{\min}$ is a function with no poles for $\operatorname{Im}\vartheta \in [0, \pi]$, its explicit form is stated in App. A.1.

Using this Ansatz, the kinematical and bound state equations can be brought to the form of recurrence relations for the polynomials $\Lambda_n^{\mathcal{O}}$, which can be solved inductively in particle number n. For the E_8 model, solutions of these equations were previously constructed in [89, 91] and later in [42]; the latter article is accompanied with an explicit set of form factors at [92]. The available functions have been used in a number of works [93, 94], providing strong evidence that they are correct.

However, for the purposes of our work in Ref. [95], and later on in Refs. [77, 96], further form factors were needed with respect to those available in the above sources. Unfortunately, the bound state recursive equation appearing in [89] has some misprints, which required the rederivation of the bound state recursion [95]. The detailed calculation is in App. A.2, and we leap to the end result here:

$$\begin{aligned}\frac{\Lambda_{n+2}(xe^{i\pi/3}, xe^{-i\pi/3}, x_1, \ldots, x_n)}{x^4\prod_{j=1}^n (x - e^{-11i\pi/15}x_j)(x - e^{11i\pi/15}x_j)(x + x_j)} &= \\ = (-1)^n \Lambda_{n+1}(x, x_1, \ldots, x_n)&\end{aligned} \tag{3.22}$$

with

$$\begin{aligned}\frac{H_{n+2}}{H_{n+1}} = &\frac{\Gamma_{11}^1 \sin\left(\frac{2\pi}{15}\right)\sin\left(\frac{11\pi}{30}\right)\sin\left(\frac{8\pi}{15}\right)\sin\left(\frac{3\pi}{10}\right)}{2\cos^2(\pi/3)\cos^2(\pi/5)\cos^2(\pi/30)G_{11}(2\pi i/3)} \times \\ &\times \left[\frac{\sin^2(11\pi/30)\gamma}{4\cos^2(\pi/3)\cos^2(\pi/5)\cos^2(\pi/30)}\right]^n ,\end{aligned} \tag{3.23}$$

where γ and $G_{11}(2\pi i/3)$ are constants defined in the appendix. Once the recurrence of the H_n constants are fixed, a similar equation can be derived from the kinematic singularity equation (3.13). The final expression is [89]

$$(-1)^n \Lambda_{n+2}(-x, x, x_1, \ldots, x_n) = \mathcal{A}_n U(x, x_1, \ldots, x_n)\Lambda_n(x_1, \ldots, x_n) \tag{3.24}$$

with

$$\begin{aligned}U(x, x_1, \ldots, x_n) = \frac{1}{2}x^5 &\sum_{k_1, k_2, \ldots, k_6 = 0}^{n} (-1)^{k_1+k_3+k_5} x^{6n-(k_1+\cdots+k_6)} \\ \sin&\left(\frac{\pi}{15}(10(k_1 - k_2) + 6(k_3 - k_4) + (k_5 - k_6))\right)\omega_{k_1}\ldots\omega_{k_6}\,,\end{aligned} \tag{3.25}$$

and

$$\mathcal{A}_n = \frac{4\gamma \sin^2\left(\frac{11\pi}{30}\right)\left(\cos\left(\frac{\pi}{3}\right)\cos\left(\frac{\pi}{5}\right)\cos\left(\frac{\pi}{30}\right)\right)^2\left(G_{11}\left(\frac{2\pi i}{3}\right)\right)^2}{\left(\Gamma_{11}^1 \sin\left(\frac{2\pi}{15}\right)\sin\left(\frac{11\pi}{30}\right)\sin\left(\frac{8\pi}{15}\right)\sin\left(\frac{3\pi}{10}\right)\right)^2} \times \\ \times \left(\frac{\sin\left(\frac{2\pi}{3}\right)\sin\left(\frac{2\pi}{5}\right)\sin\left(\frac{\pi}{15}\right)}{8\sin^4\left(\frac{11\pi}{30}\right)G_{11}(0)\gamma^2}\right)^n . \tag{3.26}$$

Note that we suppressed the operator subscript $\mathcal{O}$ for H_n and Λ_n above. This reflects the fact that the recurrence relations themselves are independent of the operator: their solution yields the form factor of a general operator $\mathcal{O}$, a linear combination of the two primary fields:

$$\mathcal{O} = \alpha\sigma + \beta\varepsilon\,. \tag{3.27}$$

Consequently, further input is needed to tell the operators apart. This ambiguity is not resolved by fixing different initial conditions for the different operators, the ambiguity is present at each level n [3]. In the following we discuss the separate solutions for the σ and ϵ fields, respectively.

3.2.3 Solution for the σ field

We begin with the solution for the σ operator, as it is both conceptually and practically simpler. The simplification stems from the proportionality of the perturbing field and the trace of the stress-energy tensor in a perturbed CFT, a direct consequence of the c-theorem [97, 98]. In the E_8 model we have

$$\Theta(x) = 4\pi h\,(1-\Delta_\sigma)\,\sigma(x)\,, \tag{3.28}$$

where $\Theta(x)$ is the trace of the stress-energy tensor and $\Delta_\sigma = 1/16$ is the conformal weight of the magnetisation field.

First, this proportionality fixes the constant H_2^σ, as the diagonal matrix element of the stress-energy tensor is known from the thermodynamical Bethe Ansatz [38, 89]

$$F_{11}^{\Theta}(i\pi) = \langle A_1|\Theta|A_1\rangle = 2\pi m_1^2\,, \tag{3.29}$$

which in turn can be used to fix H_1^σ by the application of the bound state equation. To completely pin down the initial conditions of the recurrence, one extra constraint is required provided by the common bound states of the A_1A_1 and A_1A_2 pairs [89].

Second, properties of the stress-energy tensor form factor distinguish the σ solution and select the corresponding solution from the general solution of the form factor recursion at each step. As discussed earlier, the Λ_n functions are completely symmetric polynomials, hence they can be expressed in terms of the ω_n elementary symmetric polynomials generated by

$$\prod_{k=1}^{n}(x+x_k) = \sum_{j=0}^{n} x^{n-j}\omega_j(x_1,\ldots,x_n)\,. \tag{3.30}$$

In other words, Λ_n is the linear combination of products of the ω polynomials. The solution of the recurrence relations (3.22,3.24) then amounts to finding the coefficients in this linear combination. On the one hand, the number of the coefficients is restricted, since the total polynomial degree is fixed by Lorentz invariance, and the partial degrees are bounded by the asymptotic behaviour of the form factors [42]. On the other hand, the conservation of the stress-energy tensor means that the form factors of Θ must be proportional to the product P^+P^- [89], with

$$P^{\pm} = \sum_{j=1}^{n} p_j^{\pm} \,, \qquad\qquad p^{\pm} = p^0 \pm p^1 = \pm e^{\pm\vartheta} \,, \tag{3.31}$$

where n is the number of particles in the form factor. Using $x = e^{\vartheta}$ it is not hard to see that $P^+P^- = \omega_{n-1}\omega_1/\omega_n$. Therefore, only the coefficients corresponding to a term with at least one $\omega_{n-1}\omega_1$ product are nonzero. At each level n, this reduces the number of unknowns sufficiently to obtain the solution directly.

The final step is to fuse the one-particle states to form higher-lying particles as a bound state, with a suitable generalisation of the Ansatz in Eq. (3.20) to multiple particle species. Although each fusion involves a calculation comparable in complexity to the bound state recurrence relation, the computation process can eventually be automated using a software capable of symbolic processing such as e.g. `Wolfram Mathematica` [99]. An example calculation is presented in Appendix A.3. A useful shortcut in the line of fusions is provided by including bound state singularities involving particles also from the species A_2 and A_3. Using this approach we constructed several new exact form factors for σ in Ref. [95]; it is an extension of the results available earlier [92].

3.2.4 Solution for the ϵ field

The case of the ϵ field demands a slightly different approach, as the ambiguity of Eq. (3.27) is not resolved by any conservation laws. However, it can be resolved by applying a nonlinear condition which is provided by the clustering property of form factors [100]:

$$\begin{aligned}\lim_{\Lambda\to\infty} F^{\phi}_{r+l}(\vartheta_1+\Lambda,\vartheta_2+\Lambda,...,\vartheta_r+\Lambda,\vartheta_{r+1},...,\vartheta_{r+l}) = \\ \frac{1}{\langle\phi\rangle} F^{\phi}_{r}(\vartheta_1,\vartheta_2,...,\vartheta_r) F^{\phi}_{l}(\vartheta_1,\vartheta_2,...,\vartheta_l) \,.\end{aligned} \tag{3.32}$$

This property was used in Ref. [91] to set the initial condition for the recurrence for the ϵ field. Furthermore, the same constraint can be utilised at each level to identify the ϵ operator in terms of already available form factors from the lower levels.

To this end, one has to calculate the asymptotic behaviour of the minimal form factors and the bound state pole factor D_{11}. They read:

$$\lim_{\vartheta\to\infty} G_\lambda(\vartheta) = -\imath c_\lambda \exp(\vartheta/2) \tag{3.33}$$

where the functions G_λ defined in Eq. (A.4) are the building blocks of the minimal form factors. The c_λ are real constants that can be obtained from the numerical evaluation of the defining expression for G_λ, yielding

$$\lim_{\vartheta\to\infty} F_{11}^{\min}(\vartheta) = -\frac{1}{2} c_{1/15} c_{2/5} c_{2/3} \exp(2\vartheta) \tag{3.34}$$

for the asymptotic behaviour of the minimal form factor. In the case of the bound state pole factor we have

$$\lim_{\vartheta\to\infty} D_{11}(\vartheta) = -\frac{1}{8}\frac{1}{2\cos^2(\pi/30)2\cos^2(\pi/5)2\cos^2(\pi/3)} \exp(3\vartheta)\,. \tag{3.35}$$

The asymptotes of the two functions can be combined to impose the constraint coming from the clustering property on the symmetric polynomials, in the simplest case "clustering" only a single rapidity (i.e. $r = 1$ and $l = n - 1$ in the notation of Eq. (3.32)). Applying this prescription, exact form factors of the ϵ field can be obtained analogously to the σ operator.

The newly derived form factors were used to calculate the dynamical structure function (2.21) in Ref. [77], to be tested against an experimental probe of the E_8 spectrum in the quasi-1D material $BaCo_2V_2O_8$. More precisely, the quantity calculated therein is the DSF at zero transfer-momentum, which can be expressed from Eq. 2.21 by inserting a complete set of asymptotic states:

$$\begin{aligned} D^{\alpha\alpha}(\omega,0) = \sum_{n=0}^{\infty} \sum_{\{a_1,\dots,a_n\}} \frac{1}{N} \left(\prod_{j=1}^{n} \int \frac{\mathrm{d}\vartheta_j}{2\pi} \right) \left| F^{\alpha}_{a_1,a_2,\dots,a_n}(\vartheta_1,\vartheta_2,\dots,\vartheta_n) \right|^2 \times \\ \times\, 2\pi\delta(E-\omega) 2\pi\delta(P)\,, \end{aligned} \tag{3.36}$$

where the form factor is $F^\alpha = F^\epsilon(F^\sigma)$ for $\alpha = x(z)$ the transverse (longitudinal) component of the spin. N is a combinatorial factor to calculate the contributions containing identical particles properly, and $E(P)$ are the energy (momentum) of the inserted multi-particle state.

The goal of the experiment was to identify the full particle spectrum up to the eighth particle, which is merely below $5m_1$. Consequently, the function in Eq. (3.36) was calculated up to $\omega_{\max} = 5m_1$, truncating the infinite sum over the inserted states. The newly acquired form factors completed the list of terms in this truncated sum to give a full theoretical prediction in the measured energy interval. The analytically calculated DSF matched the neutron scattering image, corroborating the claim that the $BaCo_2V_2O_8$ chain under strong magnetic field realises the E_8 model, and simultaneously serving as a relevant application of the form factors. Later, in Ref. [96] the theoretical background of the form factor calculations was presented in detail.

3.3 Summary

In this chapter we discussed the solution of the form factor bootstrap in the E_8 model. We introduced the general problem of finding the matrix elements of local operators in an integrable field theory. We identified the set of equations the form factors satisfy and outlined the method of solving them in general in the context of the form factor bootstrap.

In a specific model, the E_8 integrable field theory, we presented our results: the calculation of new form factors, which required a careful reconstruction of the recurrence relations satisfied by the matrix elements. The general solution is exemplified by the two unique solutions for the two relevant operators in the theory: the longitudinal and transverse magnetisation fields. As a net result, we extended the list of previously available form factors in the E_8 field theory. The results were published in three articles:

1. Initially in Ref. [95], with the derivation of the recurrence relations and the solution for the σ operator. The form factors were used as an ingredient of a form factor perturbation theory calculation to model the post-quench overlaps in the E_8 theory. For a detailed presentation of this application, the reader is referred to Chapter 5.

2. As an input to the dynamical structure function that was compared against a neutron scattering experiment in the $BaCo_2V_2O_8$ material in Ref. [77]. This application required the solution for the ϵ operator by exploiting the clustering property.

3. The development regarding the ϵ solution together with a synopsis of the E_8 form factor bootstrap were included in Ref. [96].

Chapter 4

Post-quench time evolution in the Ising field theory

In the previous chapter we presented the calculation of matrix elements in the E_8 model and introduced a formalism to obtain equilibrium properties of integrable field theories. In the following we shift our attention to the behaviour of physical systems out of equilibrium.

The broad and vivid field of out-of-equilibrium quantum many-body dynamics was already introduced in Chapter 2. In particular, the quantum quench protocol was proposed as a paradigmatic setting to study non-equilibrium properties in closed quantum systems. Here we report on a numerical simulation of the time evolution following a quantum quench in the Ising field theory. Evaluating the numerical results in comparison with analytical approximations to the post-quench time evolution in field theory, we expand upon the second thesis statement in this chapter.

4.1 Quenches in quantum field theory

Quantum field theories provide an effective description of quantum systems near their quantum critical point and capture universal behavior [4]. It is natural to ask whether universality extends to non-equilibrium systems. The first works that introduced the quench protocol into quantum field theories argued that the answer is positive [8, 25]. Their assumption was that the Hamiltonian governing the dynamics after the quench is conformally invariant, corresponding to a system in its critical point. Under this assumption, universal dynamical correlation functions can be exactly calculated from the formalism of conformal field theory.

The reasoning can be generalised to small quenches in the vicinity of the critical point, opening the possibility to capture universal out-of-equilibrium physics even if the system is not exactly in the critical point. Universality in these cases is described by quantum field theories with less symmetries than their conformal counterparts. As a consequence, the exact solution of a field theory quench is generally not possible to obtain: it is only available in non-interacting cases [101–107]. There are various approximate solutions available under special settings, such as a semi-classical approach for small quenches [108–110], or a mean-field approximation for bosonic field theories [111–113].

Integrable field theories are another example where analytical approaches are fruitful in solving the post-quench dynamics, even if not to the same extent as in describing equilibrium physics. Constraints from integrability are most powerful in characterising the infinite-time steady state [114–116] and in the expression of the post-quench initial state [117–120]. The complete solution of the time evolution is an arduous task even with the arsenal of integrable field theories at hand. However, using the exactly known form factors and assuming a not too large quench, even the dynamical correlations can be approximated through form factor series, exemplified by the calculations for one-point functions in Refs. [33, 34, 40, 121–123].

Faced with the slow progress of analytical results, accurate numerical modelling of out-of-equilibrium dynamics becomes paramount. The Truncated Space Approach (TSA) numerical method introduced in Chapter 2 has a long-standing history of describing field theories in equilibrium, its applications including calculating the spectrum of perturbed minimal conformal field theories [54–56, 124], the sine–Gordon model [125], Landau–Ginzburg models [62, 63, 126, 127], and Wess–Zumino models [128–130]. As discussed earlier, the essence of the method is the exact calculation of the matrix elements of the finite volume Hamiltonian in the conformal or free basis, followed by the exact diagonalisation of the finite Hamiltonian matrix obtained by cutting off the spectrum at some energy value.

TSA was used in combination with other numerical methods in Refs. [131, 132], and first in Ref. [49] on its own to model non-equilibrium time evolution following a quantum quench. Notably, it was applied with success to calculate dynamical multi-point correlations in the sine–Gordon model [133]. Our work in Ref. [94] was an early adopter of the application of TSA to field theory quenches, followed by others later on [134–137]. The numerical results are highly accurate and their comparison to the analytical form factor calculations provides a satisfying description of the post-quench time evolution, while outlining the timescale of validity for the analytic approaches.

To this end, in the next section we present the results of quenches in and near Zamolodchikov's E_8 integrable field theory [39], the same model that was considered in the previous chapter. We recall that this massive field theory emerges as the scaling limit of the quantum Ising spin chain in a small longitudinal magnetic field when the transverse field is tuned to the quantum critical point. This system has been realised experimentally in $\mathrm{CoNb_2O_6}$ [75], and recently in $\mathrm{BaCo_2V_2O_6}$ [77]. The quenches we study here correspond to sudden changes of the transverse and longitudinal magnetic field in the spin chain.

We investigate the time evolution of various observables in quenches to both integrable and non-integrable Hamiltonians. We compare our numerical results with two different analytic descriptions. Both of them are form factor expansions but they differ in important aspects. The approach developed in Refs. [40, 121] is a perturbative one that exploits the integrability of the *pre-quench* system but does not require integrability of the post-quench Hamiltonian. The approach developed by Refs. [33, 34, 122] relies on the integrability of the *post-quench* system and makes certain assumptions about the initial state. This approach is expected to be valid for small quenches but it is not perturbative in the same sense as the pre-quench expansion. Both methods can be applied to small quenches between integrable systems, e.g. to a parameter quench in an integrable model, which allows for a comparison of the two methods using the numerical TSA results. In the following we present the results of the comparison in the E_8 model and discuss the characteristic features of quenches in this field theory.

4.2 Modelling the time evolution in E_8 field theory quenches

4.2.1 Quench protocols

To formulate the quenches in the E_8 model we consider the Hamiltonian defined in Eq. (2.12). We recall that the different values of the h and M parameters define different quantum field theories, which can be visualised in a two-dimensional $M-h$ parameter plane. The axis $h=0$ yields a field theory of free massive Majorana fermions, while setting $M=0$ results in the E_8 integrable model. The quantum field theory with both parameters being nonzero is not integrable.

The quenches we consider here are in the close vicinity of the E_8 axis with $M=0$ and are described by the following action:

$$\mathcal{A}=\mathcal{A}_{CFT,\,c=1/2}-h_{\mathrm{i}}\int\sigma(x)\mathrm{d}^2x+\lambda\int\Theta(t)\Psi(x)\mathrm{d}^2x\,, \tag{4.1}$$

where $\Psi(x)$ is the quenching operator, with either $\Psi(x)=\sigma(x)$ or $\Psi(x)=\epsilon(x)$, and $\Theta(t)$ is the step function, such that the quench takes place at $t=0$. This prescription corresponds to a global quench, where the initial state is the ground state of the $t<0$ theory.

There are two types of quench protocols corresponding to the two possible choices for the quenching field. The first type (Type I) is realised through choosing the σ direction, which means that both the $t<0$ (pre-quench) theory and the (post-quench) model with $t>=0$ is integrable. The second type (Type II) follows from setting $\Psi(x)=\epsilon(x)$, and consequently the post-quench model is non-integrable. We illustrate the two quench protocols on the $M-h$ parameter plane in Fig. 4.1.

We choose a dimensionless parameter to characterise the magnitude of the quench in both cases. For Type I quenches, denoting the pre-quench value of the

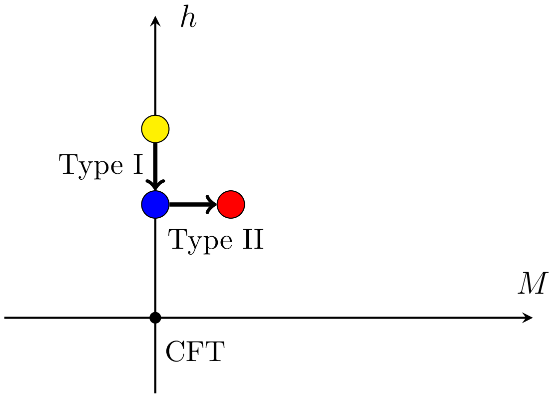

Figure 4.1: Illustration of quenches considered in this chapter in the $M - h$ parameter space. The lower (blue) dot on the axis represents the post-quench Hamiltonian for Type I quenches, and the pre-quench Hamiltonian for Type II quenches, which were performed in both (negative and positive M) directions.

coupling h_{i} and the post-quench parameter h_{f} we introduce the dimensionless combination ξ through

$$\xi \equiv \frac{\lambda}{h_{\mathrm{f}}} = \frac{h_{\mathrm{i}} - h_{\mathrm{f}}}{h_{\mathrm{f}}} \,. \tag{4.2}$$

Note that the choice of h_{f} simply sets the energy scale of the post-quench system through Eq. (2.15). We choose it such that the mass gap m_1 of the post-quench Hamiltonian is set to unity, $m_1 = 1$.

The magnitude of Type II quenches is measured by the dimensionless combination η of M and h, defined in Eq. (2.17). In this case the post-quench model is non-integrable, hence the choice of h_{i} sets the energy scale of the pre-quench theory. We choose it such that the mass gap $m_1^{(0)}$ of the pre-quench Hamiltonian is set to unity, $m_1^{(0)} = 1$, where we introduced the notation superscript (0) to differentiate between quantities on the pre- and post-quench bases.

Having set the energy scales for both types of quenches we measure each physical quantity in appropriate powers of the mass gap (m_1 or $m_1^{(0)}$, depending on the quench protocol considered): e.g. energy differences are measured in mass gap units, while time and distance with the inverse of the energy scale set by the mass gap.

4.2.2 Modelling methods

As alluded to in Sec. 4.1, we have three ways to describe the time evolution following a global quench in the E_8 field theory. The first one is a numerical method based on Hamiltonian truncation, the latter two are analytical approaches: a perturbative expansion in the λ parameter of Eq. (4.1) (later on referred to as ‘perturbative quench expansion’) and a linked cluster expansion on the post-quench basis (‘post-quench expansion approach’ from now on) assuming a specific form of the post-quench initial state with a sufficiently small energy density. Before proceeding to the presentation of the post-quench dynamics, we introduce these three methods in a bit more detail. We focus on the evaluation of dynamical one-point functions, as both analytical approaches are worked out on this example.

The numerical method is the conformal Hamiltonian truncation introduced in Sec. 2.2.2. The numerical treatment of the quench problem proceeds via an initial determination of the ground state $|0\rangle$ of the pre-quench Hamiltonian (with $\lambda = 0$), and then solving the Schrödinger equation involving the post-quench Hamiltonian with $|0\rangle$ as an initial condition. For the TCSA computations periodic boundary conditions are used. As the time-evolved state is explicitly constructed, virtually any physical quantity related to the quench can be calculated this way, the only limitation being the errors arising from the truncation of the Hamiltonian to a finite dimension. To alleviate the limitations, we perform extrapolation in cutoff using Eq. (2.20). The finite volume parameter induces an upper time limit, until when the numerical results provide an accurate depiction of the dynamics. We return to this question in Sec. 4.3.1.

The first analytical approach we consider is the perturbative quench expansion [40, 121]. Its basic assumption is that the quench starts from an integrable Hamiltonian H_0, which is changed during the quench by the addition of an extra local interaction to

$$H = H_0 + \lambda \int dx \Psi(x) \,, \tag{4.3}$$

where λ is small enough to justify the application of perturbation theory. To first order in λ and including only one-particle contributions, the perturbative prediction for the post-quench time evolution of a local operator Φ is [40]

$$\langle \Phi(t) \rangle = \langle 0|\Phi|0\rangle + \lambda \sum_{j=1}^{8} \frac{2}{\left(m_j^{(0)}\right)^2} F_j^{(0)\Psi *} F_j^{(0)\Phi} \cos\left(m_j^{(0)} t\right) + \cdots + C_\Phi \,, \tag{4.4}$$

where $|0\rangle$ is the pre-quench vacuum, $m_j^{(0)}$ are pre-quench one-particle masses and C_Φ is included to satisfy the initial condition that the $\langle \Phi(t) \rangle$ function is continuous at $t = 0$. The amplitudes $F_j^{(0)\Phi}$ are the one-particle form factors of the Φ operator defined by Eq. (3.8), with an additional particle species index j. Note that all quantities are taken at their pre-quench values reflecting that this approach only assumes integrability of the pre-quench Hamiltonian.

The ellipsis denotes the contribution of higher particle states; their omission corresponds to a low-energy approximation valid for long enough times $t \gtrsim 1/m_1^{(0)}$. Validity of perturbation theory for the time evolution operator also places a theoretical upper time limit for the validity of this expression in terms of the quench amplitude

$$t^* \sim \lambda^{-1/(2-\Delta_\Psi)} \,, \tag{4.5}$$

where Δ_Ψ is the scaling dimension of the quenching Ψ operator.

The second method, introduced for quenches in the free massive Majorana field theory [33] and developed further in Refs. [34, 122, 123], builds upon the premise that the post-quench system is integrable. It can be considered as a systematic expansion in the post-quench particle density as a small parameter, which means that it is limited to small enough quenches, which are, however, not necessarily perturbative in the Hamiltonian sense used above. Consequently, it has no upper time limit, while due to being a low-energy expansion it has a lower time limit in terms of the post-quench mass m_1. Adapting the results of [122] to the case of the E_8 model, the following time evolution is obtained for operator Φ to leading order:

$$\begin{aligned}\langle\Phi(t)\rangle = \langle\Omega|\Phi|\Omega\rangle + \sum_{j=1}^{8}\frac{|g_j|^2}{4}\mathrm{Re}[F^{\Phi}_{jj}(i\pi,0)] + \sum_{j=1}^{8}\mathrm{Re}[g_j F^{\Phi}_{j} e^{-im_j t}] \\ + \sum_{k\neq j}\mathrm{Re}\left[\frac{g_k^* g_j}{2}F^{\Phi}_{kj}(i\pi,0)e^{-i(m_j-m_k)t}\right] + \dots\,,\end{aligned} \tag{4.6}$$

where $|\Omega\rangle$ is the post-quench vacuum state,

$$\frac{g_j}{2} = \langle\Psi(0)|A_j(0)\rangle \tag{4.7}$$

is the overlap of the initial state $|\Psi(0)\rangle$ with a zero-momentum post-quench one-particle state of species j, and the F^{Φ} form factors are matrix elements on the post-quench basis.

Once again, the ellipsis indicates the contribution involving higher many-particle states. In Refs. [33, 34, 122, 123] the first few of them were evaluated, and they were found to contain secular terms proportional to powers of t. Their resummation may lead to the appearance of frequency shifts and decay factors through functions $\sim e^{iat}$ and $\sim e^{-bt}$ respectively. Both effects are consequences of the finite post-quench particle densities. We neglected these terms in our considerations for two reasons. First, the TCSA data for the relevant quenches show no signs of damping or substantial frequency shifts on the time-scales of our simulations (see below). Second, their computation requires the knowledge of two-particle overlap functions, and their numerical determination requires considerable effort, see Chapter 5.

We note that unlike the perturbative approach, the second method does not construct the initial state but needs the one-particle overlaps g_j as inputs. We determined them by explicitly constructing the corresponding states in TCSA and computing their scalar products with the initial state. Apart from this numerical input, the evaluation of Eqs. (4.4,4.6) is a mere substitution exploiting the exact relations for the particle masses and the form factors. For the latter we use the ones available at Ref. [92].[1]

---

[1] The only caveat is that we normalise our operators according to their short-distance op-

With the three approaches at hand, we turn to the presentation of the results. We treat the two types of quenches separately. For Type I quenches that connect two points on the integrable E_8 axis, all three approaches introduced in the previous section can be used to describe the post-quench time evolution. In contrast, Type II quenches do not allow for the application of the post-quench expansion as the resulting model is not integrable.

For each type, we consider three dynamical quantities: the Loschmidt echo, and the one-point functions of the σ and ϵ fields. The Loschmidt echo can be used to test the validity of TCSA data, outlining the limitations to the applicability of the approach in light of truncation errors and finite volume effects. The dynamical one-point functions then serve as a benchmark for the analytical approaches in comparison with our numerical method. The time evolution is also analysed through the lens of Fourier transformation in the spirit of the "quench spectroscopy" idea put forward in Ref. [40].

4.3 Results of quenches preserving integrability

4.3.1 Loschmidt echo

The Loschmidt echo characterises the return of a dynamical system to its initial state [139]. For quantum systems, it is defined through the squared overlap

$$\mathcal{L}(t) = |\left\langle\psi(t)|0\right\rangle|^2 \propto e^{-r\ell(t)} \tag{4.11}$$

between the pre-quench ground state $\langle 0|$ and the time-evolved state $|\psi(t)\rangle = \exp(-iHt)\,|0\rangle$. The Loschmidt echo is an important dynamical quantity: its non-analytic behaviour is the signature of a dynamical phase transition [140], and, more relevantly to our case, it serves as an indicator of finite-size effects in the post-quench dynamics. The latter property is due to the revival phenomenon: the kinematics of quasi-particles is constrained to a ring of circumference R, which eventually leads to the reappearance of the initial state. The corresponding timescale can be extremely large, but partial revivals are predicted by the

---

erator product expansion:

$$\langle\Phi(x)\Phi(0)\rangle = \frac{1}{|x|^{4h_\Phi}} + \dots\,. \tag{4.8}$$

This differs from the normalisation of the form factors at [92], hence they must be rescaled using the exact vacuum expectation values

$$F^{\Phi} = F^{\Phi}_{\langle\Phi\rangle=1}\,\langle\Phi\rangle\,. \tag{4.9}$$

The exact expectation values of the σ and ϵ fields were obtained in Ref. [138]:

$$\langle\sigma\rangle = (-1.06144\dots)\,m_1^{1/8}\,,\quad \langle\epsilon\rangle = (0.454752\dots)\,m_1\,. \tag{4.10}$$

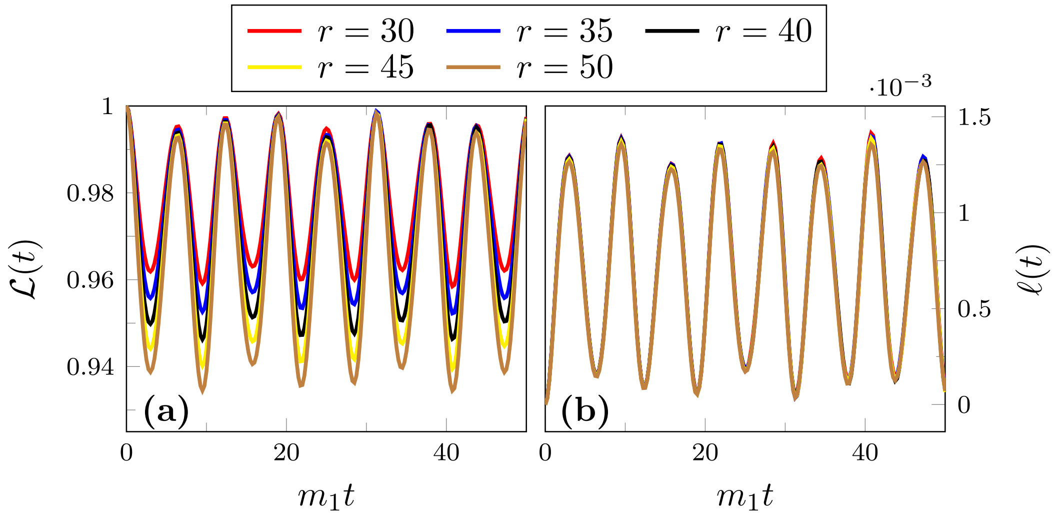

Figure 4.2: (a) Loschmidt echo $\mathcal{L}(t)$ and (b) Loschmidt rate function $\ell(t)$ after a quench of size $\xi = (h_\mathrm{i} - h_\mathrm{f})/h_\mathrm{f} = 0.5$ at five different volumes in the range $r = 30 \dots 50$. Volume dependence is almost completely absent for the rate function $\ell(t)$. Time and volume is measured in units of the inverse mass m_1^{-1} of the lightest particle, $r = m_1 R$.

quasi-particle picture after some time that is of the order of the volume of the system. The appearance of revivals in the Loschmidt echo indicates the time instance until finite volume numerical modelling captures the universal behaviour in the thermodynamic limit. Due to translational invariance, the Loschmidt echo depends exponentially on the volume parameterised by $r = m_1 R$, and $\ell(t)$ is the so-called rate function which displays no significant volume dependence until the revivals appear.

To establish the usage of TCSA in modelling the post-quench time evolution, we show in Fig. 4.2 the Loschmidt echo extracted from the numerical simulation for a quench of size $\xi = 0.5$ corresponding to the relation $h_\mathrm{i} = 1.5 h_\mathrm{f}$. To eliminate volume dependence we also plot the Loschmidt rate function $\ell(t)$, cf. (4.11). The data display neither partial nor full revivals. Revivals would occur at times depending on the volume, which would manifest in the curves in Fig. 4.2b at different volumes ceasing to overlap. The almost perfect overlap of the curves also shows that other possible finite size effects are negligible, too. Note that the oscillations in the Loschmidt echo exhibit no damping which means that the system does not equilibrate on the time scales considered here. As $\xi = 0.5$ is the magnitude of the largest quench we consider along the E_8 axis, the behaviour of the corresponding Loschmidt echo suggests that TCSA is an adequate approach to model the time evolution in this parameter range.

4.3.2 σ operator

We begin the presentation of dynamical one-point functions with the σ operator. As it corresponds to the continuum limit of the spin chain magnetisation, the σ field is of the greatest physical significance. We now discuss how to apply Eqs. (4.4) and (4.6) to the time evolution of the magnetisation.

The perturbative prediction Eq. (4.4) yields

$$\langle\sigma(t)\rangle = \langle 0|\sigma|0\rangle + \lambda\sum_{j=1}^{8}\frac{2}{\left(m_j^{(0)}\right)^2}\left|F_j^{(0)\sigma}\right|^2\cos\left(m_j^{(0)}t\right) + \dots + C_\sigma\,. \tag{4.12}$$

The constant C_σ is given in Ref. [40] as an infinite form factor series. A self-consistent choice in the spirit of the derivation of this constant is to truncate its series at the one-particle term, this guarantees the continuity of $\langle\sigma(t)\rangle$ at $t=0$ at this order of the form factor expansion. However, for the quench under consideration the form factor series can be summed up with the result

$$C_\sigma = \frac{1}{15}\frac{h_\mathrm{f}-h_\mathrm{i}}{h_\mathrm{i}}\langle 0|\sigma|0\rangle\ . \tag{4.13}$$

Eq. (4.13) should give a more accurate prediction for the baseline of the oscillations so we use this expression for C_σ in Fig. 4.3a.

For the post-quench method we obtain from Eq. (4.6)

$$\begin{aligned}\langle\sigma(t)\rangle = \langle\Omega|\sigma|\Omega\rangle + \sum_{j=1}^{8}\frac{|g_j|^2}{4}\mathrm{Re}[F_{jj}^\sigma(i\pi,0)] + \sum_{j=1}^{8}\mathrm{Re}[g_j F_j^\sigma e^{-im_jt}]\\ + \sum_{k\neq j}\mathrm{Re}\left[\frac{g_k^* g_j}{2}F_{kj}^\sigma(i\pi,0)e^{-i(m_j-m_k)t}\right] + \dots\,.\end{aligned} \tag{4.14}$$

The comparison between the TCSA simulations and the analytic expansions for small quenches is shown in Figs. 4.3-4.5. As a foreword, let us comment on the precision of the numerical results. The errors from truncation can be systematically minimised through a cutoff extrapolation scheme (cf. Eq. (2.20) and Appendix D), leaving only the residual error of the extrapolation fit. In all cases presented in this section, the error is restricted to a shift in the time-independent baseline of oscillations, and the time-dependent uncertainty is comparable to the linewidth of Fig 4.3. Since the baseline is adjusted for comparison (see below), we decided to omit error bars in our plots. The volume dependence is similarly absent: the difference between curves measured at $r = 30$ and $r = 50$ is practically invisible. As a result, our simulation results can be interpreted as being identical to the physical ones for infinite volume and cutoff for the time windows shown.

We start our systematic analysis with very small quenches and move towards larger quenches afterwards. Fig. 4.3a shows the time evolution of the σ operator

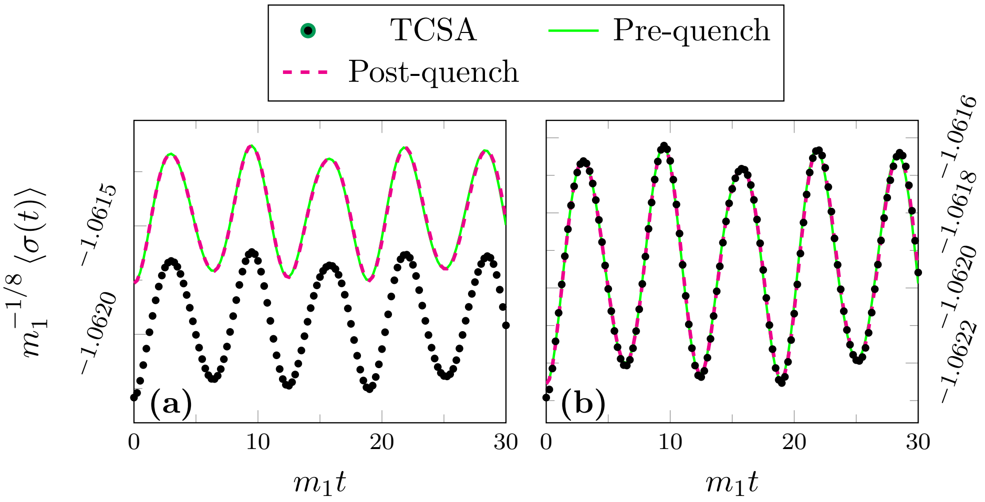

Figure 4.3: Time evolution of the σ operator after a small quench of size $\xi = (h_\text{i} - h_\text{f})/h_\text{f} = 0.005$. Comparison of the TCSA data (black dots) with the perturbative quench expansion result (4.12) (green line) and the prediction of the post-quench expansion (4.14) (magenta dashed line). In panel (b) both theoretical results are shifted to the diagonal ensemble value obtained from TCSA. TCSA data are for volume $r = 40$ and are extrapolated in the truncation level. Time is measured in units of the inverse mass m_1^{-1} of the lightest particle. Expectation values are measured in units of $m_1^{1/8}$.

after a quench of size $\xi = 0.005$. The two analytic approaches give identical results which however differ from the TCSA data. The deviation is well within the error bar of the TCSA method (note the scale on the y-axis!). In Fig. 4.3b we shifted the curves on top of each other to show that for such a small quench there is perfect agreement between the two analytic approaches and, up to a minuscule constant, with the numerical data.

Before proceeding to larger quenches, let us comment on the baseline of oscillations. The TCSA data oscillates around the (truncated) diagonal ensemble value, cf. Eq. (2.9). However, the analytical expressions are worked out only to leading order, hence their time-independent parts are a leading order approximation of the diagonal ensemble expectation value. It is clear that for the post-quench approach a complete resummation of time-independent terms would resolve the mismatch, while for the perturbative expansion higher order terms in λ would correct the result. As the diagonal average can be easily computed in the TCSA framework, in the following figures we present the results with a slight modification. The modification amounts to shifting the constant terms in the analytical predictions to match the numerical diagonal ensemble, i.e. setting a common baseline for the three approaches.

Working in this convention, let us now consider larger quenches of magnitudes $\xi = 0.05$ and $\xi = 0.5$. They are plotted in Fig. 4.4 which shows that while the

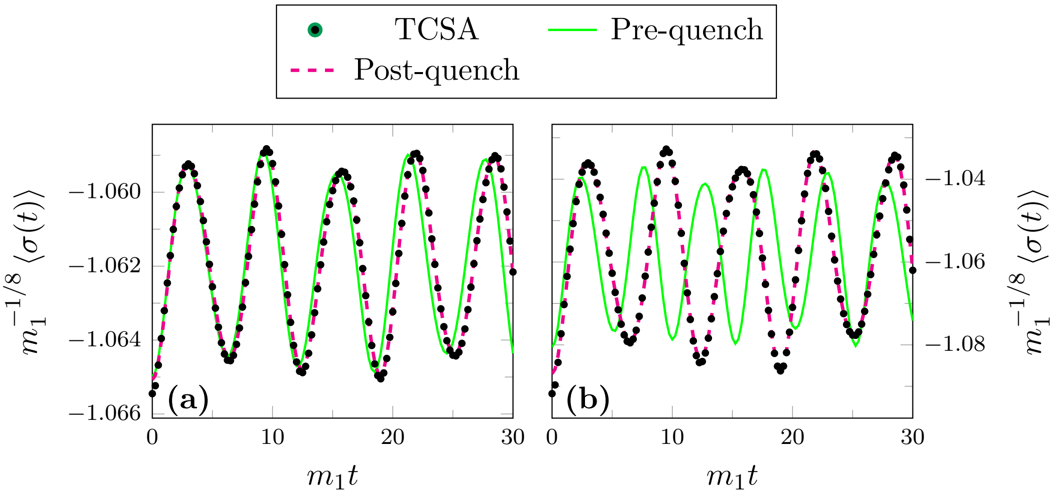

Figure 4.4: Time evolution of the σ operator after larger quenches of size (a) $\xi = 0.05$ and (b) $\xi = 0.5$. TCSA data are for volume $r = 40$ and are extrapolated in the truncation level. Notations and units are as in Fig. 4.3.

post-quench expansion supplemented by the numerical overlaps can be brought to perfect agreement with the TCSA data by a constant shift, the first order perturbative quench expansion shows a frequency mismatch. As the omitted higher form factors in the series are expected to modify the short time behaviour and vanish for large time, the discrepancy indicates that larger quenches are beyond the domain of validity of first order perturbation theory.

We recall that the post-quench approach is not fully analytic as it needs the g_j overlaps as inputs. As the amplitudes of the oscillations in Fig. 4.4a set by these overlaps are close in the different approaches, the better agreement between numerics and the post-quench approach does not come from a more precise knowledge of the overlaps but from the fact that the post-quench expansion predicts oscillations with frequencies set by the post-quench particle masses, while the perturbative expansion uses the pre-quench frequencies in the time evolution.

However, let us note that the mismatch between the perturbative approach and TCSA data appears roughly at the predicted time range of validity of the former. For the $\xi = 0.05$ quench the upper time limit predicted by Eq. (4.5) is $t^* = |h_\mathrm{i} - h_\mathrm{f}|^{-8/15}$ which in terms of our dimensionless time used in the plots is $m_1 t^* \approx 4.4\xi^{-8/15}$. For $\xi = 0.05$ we get $t^* \approx 20$, whose order of magnitude agrees with the range of good agreement seen in Fig. 4.4a.

For the much larger quench with $\xi = 0.5$ shown in Fig. 4.4b there is a starker contrast between the two analytical approaches. The post-quench expansion matches excellently with the TCSA data, which implies that this quench is still in the low density regime. As for the pre-quench approach, apart from the frequency mismatch the amplitudes exhibit a similar disagreement with the TCSA data. This shows that this quench is well beyond the perturbative regime.

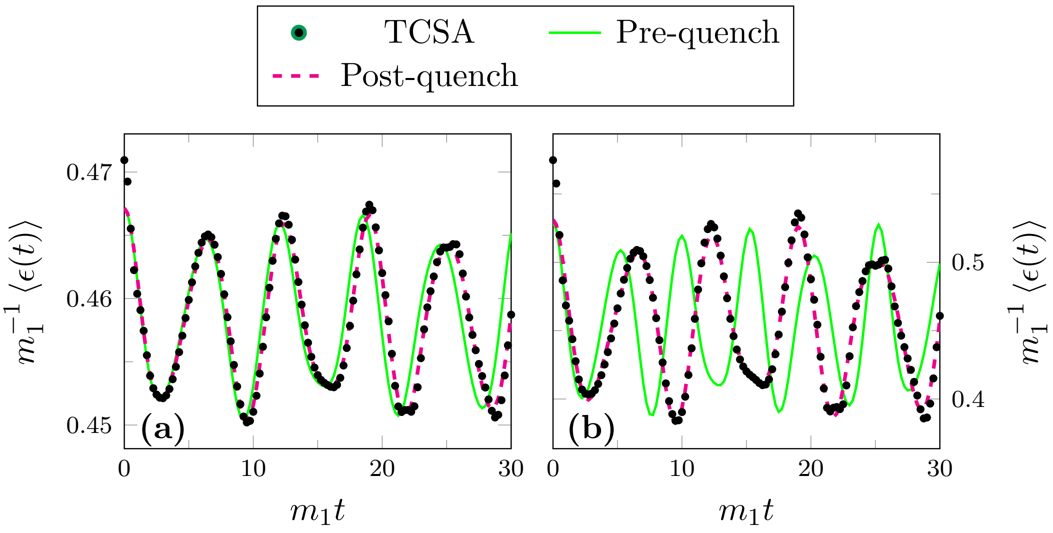

Figure 4.5: Time evolution of the ϵ operator after a quench of size (a) $\xi = 0.05$ and (b) $\xi = 0.5$ TCSA data are for volume $r = 40$ and are extrapolated in the truncation level. Notations and units are as in Fig. 4.3. Expectation values are measured in units of m_1.

4.3.3 ϵ operator

The scaling Ising field theory has another relevant operator, the field ϵ with scaling dimension $\Delta_\epsilon = 1$, which corresponds to the transverse magnetisation in the spin chain.

The comparison of the two approaches with the TCSA results is shown in Fig. 4.5. Similarly to the case of the σ operator, for a $\xi = 0.05$ quench the perturbative prediction agrees well with the numerical result up to $m_1 t \approx 10$ after which the frequency mismatch causes deviations. The quench of size $\xi = 0.5$ is outside of the perturbative domain, but the post-quench expansion shows a convincing agreement with the TCSA data.

4.3.4 Fourier spectra of the post-quench time evolution

In the previous subsections we observed that the post-quench time evolution for intermediate times is dominated by single-particle oscillations. We pointed out that the main difference between the two approaches is that the perturbative expansion predicts the frequency of the oscillations incorrectly. This observation is reinforced by the analysis of the Fourier spectra to which we turn now.

We calculate the Fourier spectra of the three dynamical quantities presented above from the TCSA data. The Fourier spectra in Fig. 4.6 attest that single-particle oscillations dominate the time evolution. This observation supports the idea of quench spectroscopy [40], which proposes to identify the particle spectrum of a model by monitoring the time evolution following a quantum quench. We

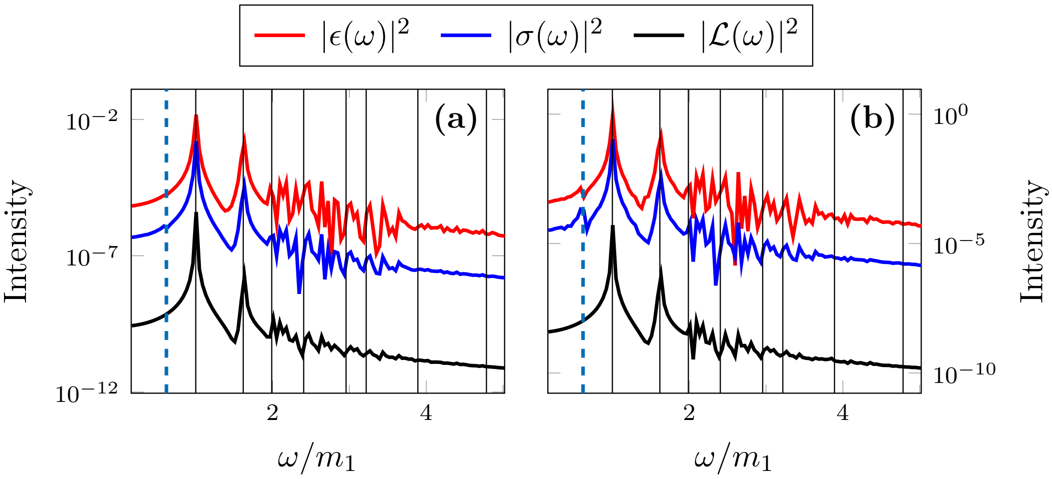

Figure 4.6: Fourier spectra of the time evolved operators and the Loschmidt echo for quenches of size (a) $\xi = 0.05$ and (b) $\xi = 0.5$ in volume $r = 50$. Continuous gridlines are at single particle masses of the E_8 spectrum, and the blue (leftmost) dashed line is located at the difference of the first two masses. The frequency ω is measured in units of the mass of the lightest particle m_1, operator expectation values are measured in units of appropriate powers of m_1.

note however, that although the E_8 spectrum consists of eight particles, only the first three of those can be seen clearly in the spectra. The rest are above the two-particle threshold and are hard to distinguish against the background of many-particle states.

Interestingly, there is an additional peak left of the tallest one corresponding to the lightest particle, most visible in Fig. 4.6b. Its position is at $m_2 - m_1$, where it is predicted to be by the post-quench expansion (4.6). Its smallness together with the absence of further difference frequency peaks is explained by the following consideration. The overlap factors g_j are of order ξ, so while the amplitudes of the frequencies m_j are of order ξ, those of $m_j - m_k$ are of order ξ^2, leading to a suppression of difference frequencies.

We remark that within the available frequency resolution we cannot observe the frequency shifts originating from the finite post-quench particle density (cf. the discussion in Subsection 4.2.2). Also note that the prominence of peaks depends on the observable, which can be understood from Eq. (2.8): in addition to the overlap factors, their height also depends on the operator matrix element (form factor) associated to the given observable.

The erratic behaviour, consisting of a jagged landscape of multiple Fourier peaks right above the two-particle threshold $\omega = 2$ is due to two effects. First, there are five stable one-particle states in the E_8 spectrum above the two-particle threshold that correspond to localised peaks; the E_8 masses are indicated by the continuous (black) vertical lines in Fig. 4.6. Second, the spectrum of multi-particle levels in a finite volume is also discrete, corresponding to isolated peaks in the spectrum, which acquire a non-zero width in the finite density post-quench environment. The spacing between these levels decreases with increasing ω, therefore the Fourier spectrum eventually becomes smooth for larger ω, which is confirmed by the data displayed in Fig. 4.6.

4.4 Integrability breaking quenches

Let us now turn to Type II quenches that break integrability. Non-integrable systems, in contrast to integrable ones, are generally thought to thermalise in the sense of locally equilibrating to a thermal Gibbs ensemble. It is an interesting question which features of the time evolution observed for the integrable case are robust under integrability breaking. A related and interesting question is whether there is any sign of relaxation, i.e. damping of the oscillations, which was notably absent for integrable quenches, at least for the time scales accessible for the TCSA simulation.

Non-integrable quenches in the vicinity of the axis $h = 0$ were already studied in Ref. [49]; these correspond to a small breaking of integrability of the free massive Majorana theory. Here we look at the opposite limit keeping h finite and fixed, and quenching by switching on a nonzero value of M, which corresponds to breaking integrability of the E_8 theory. This can be done in two ways: either towards the ferromagnetic or the paramagnetic phase, depending on whether the sign of M is positive/negative, respectively. These quenches can be described in terms of the dimensionless parameter η (cf. Eq.(2.17)). Note that since the post-quench theory is non-integrable, the post-quench series (4.6) cannot be applied and the only analytical prediction comes from the pre-quench perturbative expansion (4.4).

The equilibrium properties of the post-quench theory are well understood in both regimes, see Sec. 2.2.1, and especially Fig. 2.3 therein. Here we only recall that for small M there is no strong dependence on the sign, but as the quench magnitude increases, the two directions become markedly different. Most notably, in the ferromagnetic regime the number of stable particles increases, while in the paramagnetic regime, the number of stable single-particle excitations is first reduced to two and then to one. The threshold values for the decays of the third and second particles are $\eta_3 = -0.138$ and $\eta_2 = -2.08$, respectively [48].

4.4.1 Small quenches

We start with very small quenches in both directions, choosing $|\eta| = 0.0044$ to be safely in the perturbative regime, so that we can compare the TCSA results with the prediction of the perturbative quench expansion. In this case Eq. (4.4)

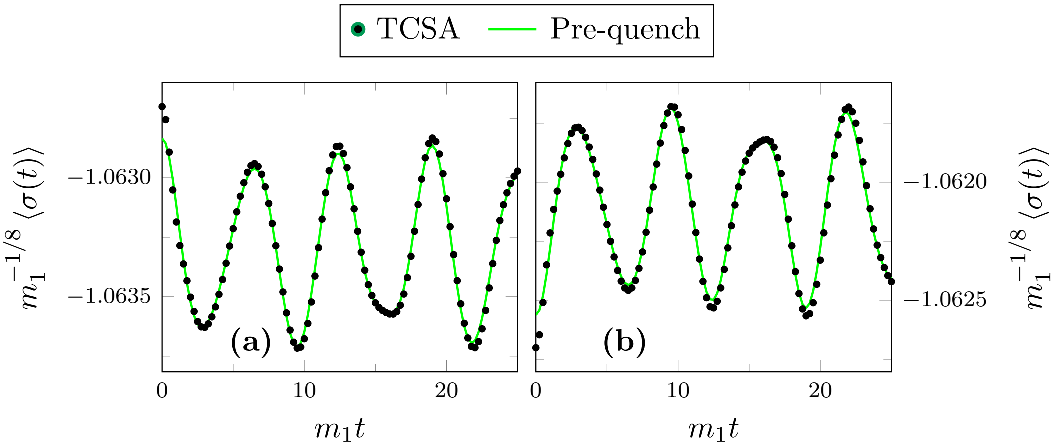

Figure 4.7: Plot of $\langle\sigma(t)\rangle$ after quenches of size $|\eta| = 0.0044$ in the (a) paramagnetic and (b) ferromagnetic direction. The black dots are the TCSA results, the prediction of the perturbative quench expansion is shown in green lines. TCSA data are for volume $r = 50$ and are extrapolated in the truncation level. Time is measured in units of the pre-quench mass of the lightest particle $m_1^{(0)}$. Note that this unit coincides with m_1 of Sec. 4.3.

predicts the following evolution for the magnetisation:

$$\langle\sigma(t)\rangle = \langle 0|\sigma|0\rangle + \lambda \sum_{i=1}^{8} \frac{2}{\left(m_i^{(0)}\right)^2} F_i^{(0)\epsilon *} F_i^{(0)\sigma} \cos\left(m_i^{(0)} t\right) + \cdots + \tilde{C}_\sigma \,, \tag{4.15}$$

where

$$\lambda = -\frac{M}{2\pi} = -\frac{\eta |h|^{8/15}}{2\pi} \,. \tag{4.16}$$

Analogously to the previous section, instead of the perturbative prediction for $\tilde{C}_\sigma$ we use the numerically evaluated diagonal ensemble value.

Note that the prediction is symmetric in the two directions apart from a relative sign in the oscillations, despite the fact that the physics essentially differs in the ferromagnetic/paramagnetic domains. This is a feature of first order perturbation theory. The numerical simulation is consistent with this behaviour demonstrating that quenches of this size are truly in the perturbative domain: as Fig. 4.7 shows, there is excellent agreement between the two approaches apart from a very short initial transient. Note that there is no sign of damping of one-particle oscillations at the time scale of the simulation. Our results show that for very small quenches away from the E_8 axis the perturbative expansion gives a very good approximation in a reasonably wide time window.

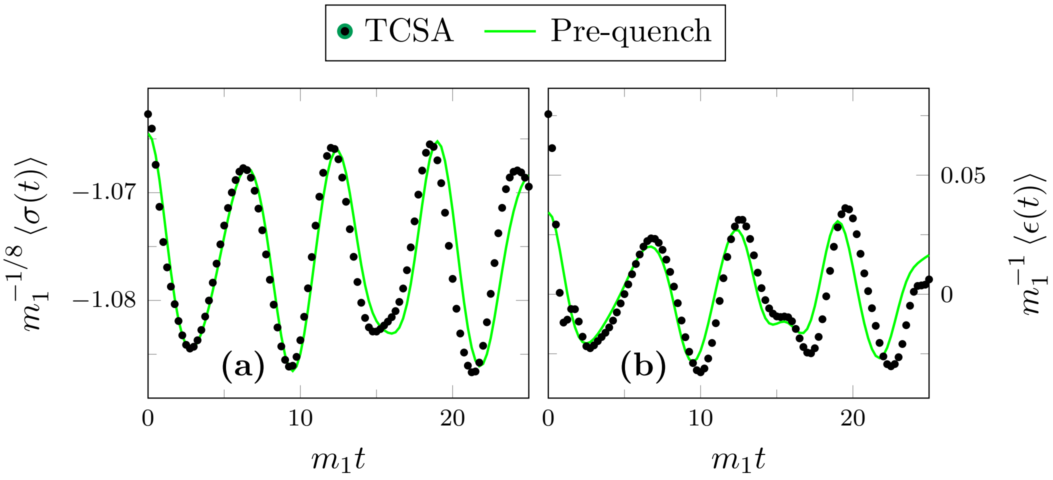

Figure 4.8: Time evolution of the (a) σ operator after a quench of size $\eta = 0.125$, and (b) the ϵ operator after a quench with $\eta = -0.125$. TCSA data are for volume $r = 50$ and are extrapolated in the truncation level. Notations and units are as in Fig. 4.7.

4.4.2 Midsize quenches

Let us proceed with quenches of moderate size $|\eta| = 0.125$ in both directions. As we increase the quench parameter, the different physics of the two directions is expected to manifest itself in the post-quench dynamics. It is also an interesting question whether the perturbative approach continues to provide reliable predictions.

We present two examples of dynamical one-point functions in Fig. 4.8: $\langle\sigma(t)\rangle$ after a ferromagnetic quench, and $\langle\epsilon(t)\rangle$ following a paramagnetic quench.[2] The agreement with the first order perturbative expansion involving the pre-quench frequencies is now less satisfactory, because the difference between the pre- and post-quench frequencies becomes visible. Apart from this, there is a difference in the amplitudes as well.

For these quenches the time scale (4.5) is $m_1^{(0)}t^* = m_1^{(0)}/|\lambda| \approx 4.4 \cdot 2\pi/|\eta|$ which for $\eta = 0.125$ gives $m_1^{(0)}t^* \approx 220$. In contrast to this, deviations from the numerical data are clearly visible at times that are at least an order of magnitude smaller than t^*. Including more terms in the form factor series would lead to a better agreement but mainly for short times at the order of $m_1^{(0)}t \sim 1$. The crux of the mismatch is that first-order perturbation theory is insufficient to

---

[2] Let us remark that for non-integrable quenches the evaluation of $\langle\epsilon(t)\rangle$ involves a subtlety. Due to the presence of the Hamiltonian perturbation ϵ the expectation value $\langle\epsilon(t)\rangle$ diverges logarithmically with the cutoff [49] and it needs to be regularised. The divergent term is proportional to the identity operator, so it merely causes a time-independent constant shift that changes logarithmically with cutoff, which is easy to compensate during the cutoff extrapolation (for details cf. Appendix D).

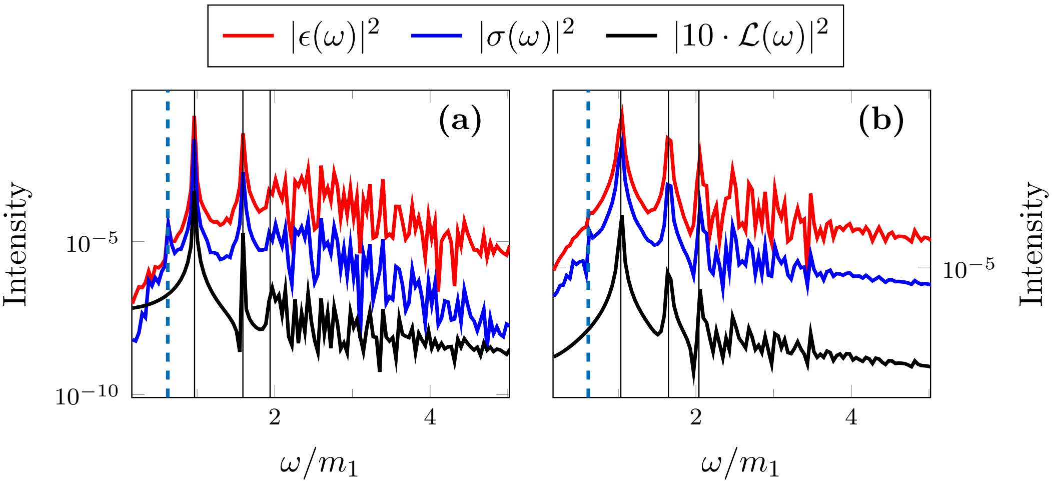

Figure 4.9: Fourier spectra of various quantities after a quench of size (a) $\eta = -0.125$ and (b) $\eta = 0.125$ in volume $r = 50$. The Fourier amplitude of the Loschmidt echo is magnified for convenience. Continuous gridlines refer to the three stable particle masses given in Eq. (4.18). Frequency is measured in units of $m_1^{(0)}$.

capture a shift in oscillation frequencies. To elucidate this point, let us consider the following Taylor expansion:

$$\cos[(\omega_0 + \lambda\omega_1)t] = \cos(t\omega_0) - \lambda t\omega_1 \sin(t\omega_0) + O\left(\lambda^2\right) . \tag{4.17}$$

Note the appearance of a secular term proportional to t in leading order, which is absent from the perturbative expansion (4.4).

In the vicinity of the E_8 axis, form factor perturbation theory (FFPT) predicts the following corrections to the masses of the three stable particles up to leading order:

$$m_j \simeq m_j^{(0)} + M \frac{F_{jj}^{\epsilon(0)}(i\pi, 0)}{m_j} , \qquad j = 1, \ldots, 8 , \tag{4.18}$$

where $m_j^{(0)}$ is the mass of the jth particle ($j = 1, 2, 3$) in the E_8 model. The gridlines in Fig. 4.9 are positioned at the leading order perturbative predictions. The corrections are in the order of the frequency resolution in the figure, and the observed shifts are consistent with the FFPT predictions. Also note the appearance of Fourier peaks corresponding to mass differences; the expected position of the dominant one is indicated by the leftmost vertical blue line. The second difference between the two directions is that, at this value of the coupling in the paramagnetic direction, the third particle is still stable but it is very close to the threshold of instability, which is indeed reflected in the Fourier spectra displayed in Fig. 4.9a. The absence of a prominent peak at the third particle mass is in stark contrast with Fig. 4.9b.

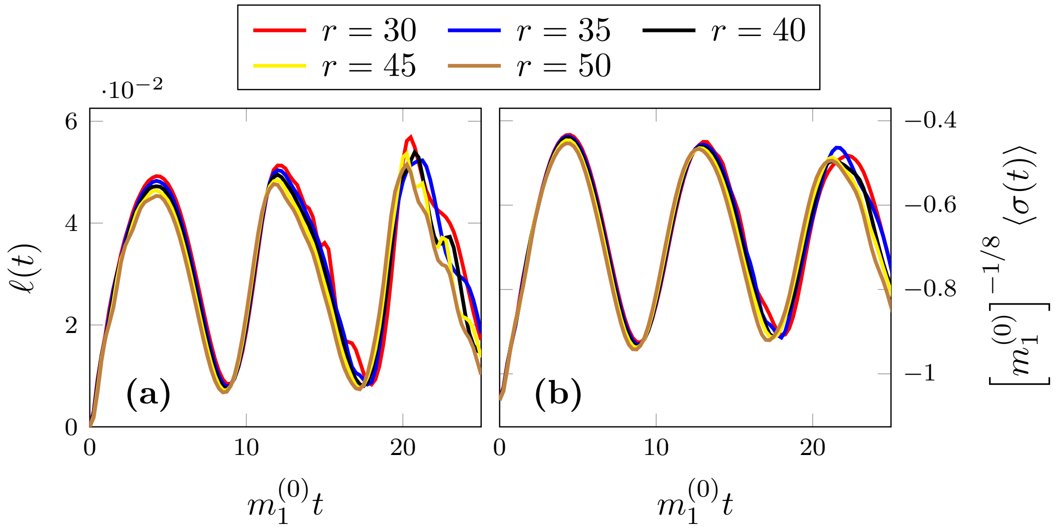

Figure 4.10: Time evolution of the (a) Loschmidt rate function and the (b) σ operator after a quench of size $\eta = -1.38$ in different volumes. Time is measured in units of the inverse mass of the lightest particle $\left(m_1^{(0)}\right)^{-1}$, operator expectation values are measured in units of appropriate powers of $m_1^{(0)}$.

4.4.3 Large quenches

The third class of integrability breaking quenches presented here is at $|\eta| = 1.38$. At this value of the η parameter the equilibrium physics is markedly different, most notably due to decay of the third massive particle in the paramagnetic direction. For this reason, we treat the two directions separately.

Paramagnetic direction

The $\eta = -1.38$ quench is where we get the first observation of damping which appears both in the oscillations of the Loschmidt echo and the expectation value of the magnetisation σ. For this quench cutoff errors in TCSA are much larger, but extrapolation in the cutoff is still reliable. On the other hand, the numerical results now also display a visible volume dependence as shown in Fig. 4.10, in particular, the Loschmidt echo becomes quite noisy for times $t > R/2$. For a quench this large, perturbative approaches for both the time evolution and the mass shifts are unreliable, and so we have no analytic predictions to compare with our simulation results.

Despite these limitations, we can still draw some robust conclusions. The damping is clearly visible in the time evolution of the magnetisation, and is also manifested in the broadening of the quasi-particle peaks in the Fourier spectra in Fig. 4.11 compared to those in Fig. 4.9a. The observation of the Fourier spectra also reveals the decay of the third particle: the corresponding peak is not

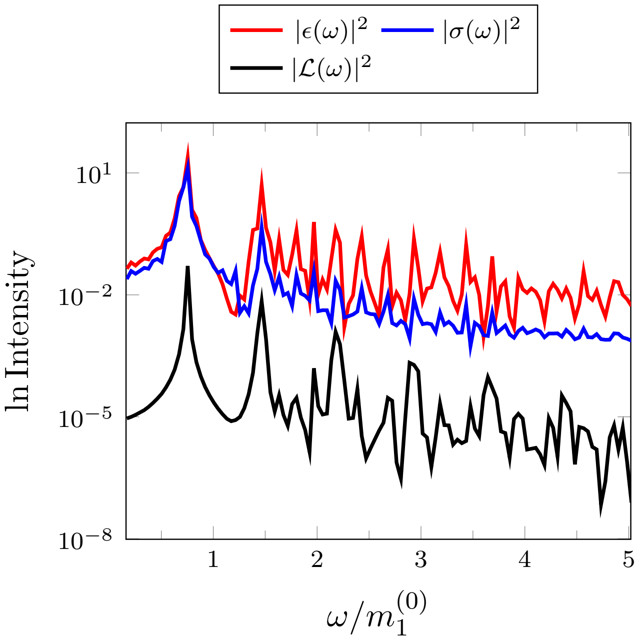

Figure 4.11: Fourier spectra of the time evolution after a quench of size $\eta = -1.38$ in volume $r = 45$. Units are as in Fig. 4.9.

present. Although in a different regime of the Ising field theory the decay rate was accurately extracted from the TSA data [49], in the present case it is unfortunately not possible to reliably estimate the relaxation time due to the limited time window in which the TCSA is valid.

For even larger quenches, necessary to access the domain in which there is only a single quasi-particle, the TCSA is not convergent enough to extract any useful information and so we do not consider them here.

Ferromagnetic quenches

Consistently with the different equilibrium physics, the non-equilibrium dynamics shows a marked qualitative difference in the ferromagnetic direction, compare Fig. 4.12 with Fig. 4.10. There is no observable damping, however, the magnetisation shows the strong presence of a mass difference frequency.

The Fourier spectra in Fig. 4.13 display a nice regular sequence of meson excitations, which is a signal of confinement [29, 49]. The meson masses in the Ising field theory are well described by analytic methods [45–47]. However, instead of using these predictions we determined the meson masses from the TCSA spectrum of the post-quench Hamiltonian in the same volume ($r = 50$) in which the time evolution was considered, which also accounts for finite size mass corrections. As shown in Ref. [64], the TCSA meson masses agree with theoretical predictions to a high precision, so displaying the analytic results would not amount to any visible change in Fig. 4.13. Even so, the peaks in the Fourier

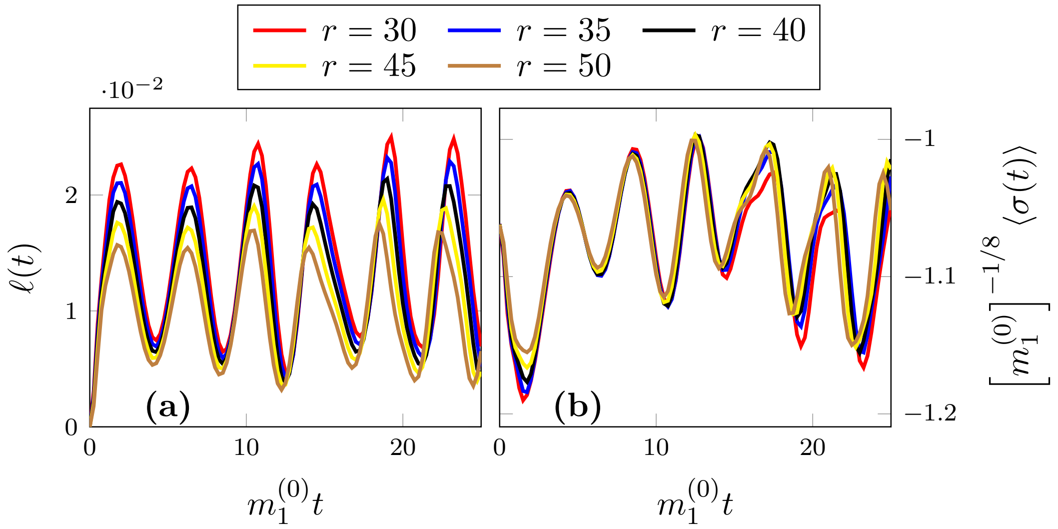

Figure 4.12: (a) Loschmidt rate function $\ell(t)$ and (b) magnetisation $\langle\sigma(t)\rangle$ after a quench of size $\eta = 1.38$ in various volumes. No damping can be observed in contrast to the paramagnetic quenches. Time is measured in units of the inverse mass of the lightest particle $\left(m_1^{(0)}\right)^{-1}$, operator expectation values are measured in units of appropriate powers of $m_1^{(0)}$.

spectra do not coincide exactly with the masses, which indicates corrections due to the effect of the finite post-quench particle density.

4.5 Summary

In this chapter we expanded on the second thesis statement based on the work in Ref. [94]. We started with the description of the quench paradigm in quantum field theories and discussed a specific QFT quench in detail. The work we presented treats quenches starting from the E_8 axis of the Ising field theory. This line in the two-dimensional parameter space corresponds to an integrable field theory, which leads to two distinctive quench types: first those that conserve the integrable dynamics upon quenching, i.e. that have an integrable post-quench dynamics, and second, quenches pointing to the non-integrable domain. We addressed both type of quenches using the non-perturbative TCSA method.

For the first quench type, there are two analytical expansions to compare with the numerical results. We found that, for small enough quenches, both predict the dynamics correctly. As the dimensionless quench parameter is increased, the pre-quench perturbative method becomes less reliable in a way that is consistent with its limitations coming from being a first-order expansion. On the other hand, the post-quench approach continues to perform excellently in comparison with the numerics for all quench magnitudes considered above.

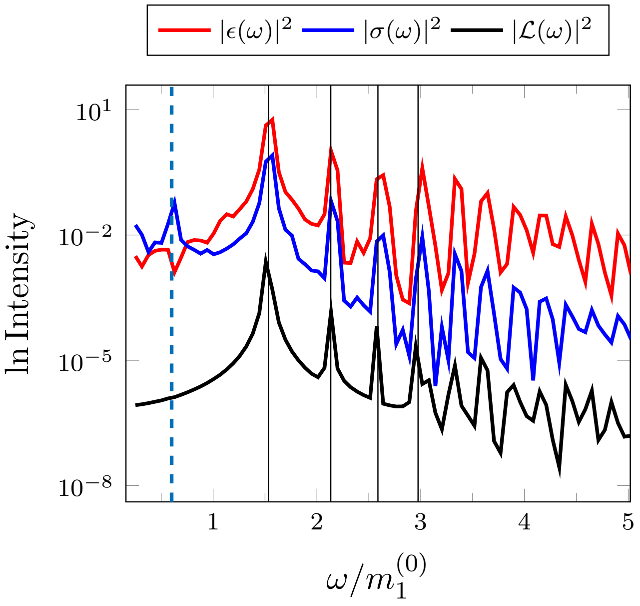

Figure 4.13: Fourier spectra for a quench of size $\eta = 1.38$ in volume $r = 50$. Meson masses are seen to get slightly shifted for more massive mesons due to the finite particle density. Units are as in Fig. 4.9.

We showed that the dynamical one-point functions exhibit single-particle oscillations, which showed no signs of damping up to the timescale available to TCSA. The Fourier analysis revealed that the frequencies of the oscillations are determined by the particle spectrum of the post-quench theory. This observation explains the success of the post-quench expansion and is consistent with the suggestion of using quench protocols to identify the particle content via quench spectroscopy.

For the second type of quenches only the pre-quench expansion makes predictions for the dynamical operator expectation values. While agreement with the numerical data is found for very small integrability breaking quenches, first order perturbation theory breaks down for larger quenches at times an order of magnitude smaller than its estimated time range of validity. We argued that the source of mismatch is inherent in the first order perturbative approximation as a leading order calculation cannot reveal the frequency shifts coming from two sources: the change of the energy spectrum and the presence of finite energy density in the system via the quench protocol.

In contrast to the limitations of available analytic approaches, the application of TCSA allows for a more far-reaching exploration of the non-integrable regime. This probe revealed the non-equilibrium signatures of the different equilibrium physics on the two sides of the axis: the paramagnetic and ferromagnetic directions, respectively. In particular, the analysis of the Fourier spectra showed the absence of the third massive particle beyond its predicted decay threshold towards the paramagnetic direction. The largest quenches in the paramagnetic direction also exhibited a damping phenomenon in the time evolution of the magnetisation operator. In the other direction, the Fourier analysis of post-quench dynamics indicated the presence of mesonic excitations in the spectrum, characteristic features of the confinement phenomenon of the ferromagnetic region.

Chapter 5

Post-quench overlaps in quantum field theory

The previous chapter presented an extensive analysis of post-quench time evolution, exposing several important traits of quantum field theory quenches, most notably, the important role played by single-particle oscillations. In this chapter we work out a different aspect of the quench protocol in quantum field theory: the overlap functions characterising the initial state.

The overlaps are defined as the scalar product of the initial state with the post-quench eigenstates. As discussed in Chap. 2, they are an important input for many analytical approaches to the post-quench dynamics, including the Quench Action approach [30–32] and form factor expansions [33, 34]. In free theories, overlaps can be directly obtained through a Bogoliubov transformation, but they are also known for a number of quenches in interacting Bose gases and integrable spin chains [141–153], including results in the context of the AdS/CFT correspondence [154–157].

In contrast, for the generic QFT quench setting discussed in the previous chapter, the results are much scarcer. Under simplifying assumptions, the overlaps can be determined approximately [118, 119, 123, 158], or numerically using truncated Hamiltonian methods [94, 120]. Below we elaborate on an alternative analytical approach to the calculation of overlap functions, presenting our work published in Ref. [95]. This approach is motivated by the perturbative expansion of Refs. [40, 121] introduced in the previous section to provide a higher order approximation of the overlap functions.

To contextualise the results, we begin with an introduction of the overlap functions in quantum field theory quenches, with a specific focus on integrable field theories. We discuss how to evaluate these functions in perturbation theory and obtain general formulae in terms of matrix elements of the quenching operator. Although the expressions are expected to hold in a generic quantum field theory, we choose the E_8 model to evaluate them where the matrix elements are known from the form factor bootstrap and the results can be contrasted with the nonperturbative TCSA data for various quantities and different types of quenches.

5.1 Quantum field theory overlaps

The overlaps relate the initial state to the eigenstates of the post-quench Hamiltonian. Formally, this relation is expressed in two-dimensional quantum field theory considering the basis of asymptotic states defined in Eq. (3.4):

$$|\Omega\rangle = \mathcal{N}\left\{ |0\rangle + \sum_{N=1}^{\infty}\sum_{a_1,\dots a_N}\left(\prod_{a=1}^{s}\frac{1}{k_a^{(N)}!}\right)\right. \tag{5.1}$$
$$\left.\left(\prod_{i=1}^{N}\int\frac{\mathrm{d}\vartheta_i}{2\pi}\right)K_{a_1\dots a_N}(\vartheta_1,\dots,\vartheta_N)\,|\vartheta_1\dots\vartheta_N\rangle_{a_1\dots a_N}\right\},$$

where we used $|\Omega\rangle$ to denote the initial state which is the vacuum state of the pre-quench theory. $|0\rangle$ is the vacuum state of the post-quench model, and $\mathcal{N}$ ensures the normalisation of the state. s denotes the number of particle species of the post-quench system, $k_a^{(N)}$ is the number of particles of species a in the state consisting of N particles, and the particle momenta are parameterised by the relativistic rapidity ϑ. The $K_{a_1\dots a_N}(\vartheta_1,\dots,\vartheta_N)$ are called the overlap functions: the characterisation of the initial state amounts to calculating these functions.

For the exactly known overlaps referenced above, the multi-particle functions are factorised in terms of zero-momentum pairs. Formally, this property is expressed most concisely through the cumulants $\bar{K}$ of the overlap functions, defined by:

$$|\Omega\rangle = \mathcal{N}\exp\left\{\sum_{N=1}^{\infty}\sum_{a_1,\dots a_N}\left(\prod_{a=1}^{s}\frac{1}{k_a^{(N)}!}\right)\right. \tag{5.2}$$
$$\left.\left(\prod_{i=1}^{N}\int\frac{\mathrm{d}\vartheta_i}{2\pi}\right)\bar{K}_{a_1\dots a_N}(\vartheta_1,\dots,\vartheta_N)A_{a_1}^{\dagger}(\vartheta_1)\dots A_{a_N}^{\dagger}(\vartheta_N)\right\}|0\rangle\ ,$$

where the $A_a^{\dagger}(\vartheta)$ are the asymptotic particle creation operators. Pair factorisation means that all cumulants with particle number $N > 2$ vanish: this property is trivially satisfied in free quadratic models, and it also holds in a wide class of quenches with integrable post-quench dynamics. Motivated by these results, Refs. [159, 160] coined the term 'integrable quench' to refer to quenches where the post-quench Hamiltonian is integrable and the initial state exhibits pair structure. Applying this criterion to Eq. (5.2) the result is the generalised squeezed state form:

$$|\Psi(0)\rangle = \mathcal{N}\exp\left\{\sum_a\frac{g_a}{2}A_a^{\dagger}(0)+\sum_{a,b}\frac{1}{2}\int\frac{d\vartheta}{2\pi}K_{ab}(\vartheta)A_a^{\dagger}(-\vartheta)A_b^{\dagger}(\vartheta)\right\}|0\rangle\ , \tag{5.3}$$

where g_a are the one-particle overlaps and K_{ab} is nonzero only if $m_a = m_b$. This expression is completely analogous to the integrable boundary states introduced by Ghoshal and Zamolodchikov [161]. Assuming an initial generalised squeezed state form, various traits of the post-quench dynamics can be described analytically [34, 103, 114–119, 162–164].

Eq. (5.3) corresponds to a post-quench initial state with independently created particle pairs (and zero-momentum particles, whenever the one-particle overlap is finite). The most important consequence of this structure is that one- and two-particle overlaps completely characterise the finite density state resulting after the quench, narrowing down the set of overlap functions to be calculated.

The feature that most of the information regarding the initial state is encoded in one- and two-particle overlaps is not unique to integrable quenches. For quenches with small enough post-quench density, i.e. when the average density of particles is smaller than the inverse of the interaction range, one expects on physical grounds that a similar factorisation holds with a very good approximation. It is precisely in this sense that the post-quench expansion [33, 34, 122] considered in the previous section relies on small post-quench density: it uses the vanishing of cumulants with $N > 2$.

The success of the post-quench expansion in describing the post-quench time evolution is a confirmation that for not too large quenches few-body overlaps give an adequate description of the initial state. This motivates the quest to calculate this limited set of functions analytically. Below we present a perturbative calculation for the functions g_a and K_{ab}, corresponding to the one- and two-particle overlaps, respectively:

$$\frac{g_a}{2} = {}_a\langle\{0\}|\Omega\rangle \tag{5.4}$$

$$K_{ab}(\vartheta_1,\vartheta_2) = {}_{ab}\langle\{\vartheta_1,\vartheta_2\}|\Omega\rangle\ . \tag{5.5}$$

Note that in perturbation theory, there is no reason to exclude the two-particle overlap functions K_{ab} with $m_a \neq m_b$. In fact, as we will see below, the perturbative expansions predict that the corresponding overlaps are finite already in leading order. Formally, this is only a small extension of the generalised squeezed state form, such that it remains a very good approximation for the initial state in the small post-quench density regime (cf. the discussion below Eq. (5.3)).

In partial analogy with the pre-quench and post-quench expansions of the previous chapter, these expressions suggest two alternative approaches within perturbation theory to calculate the overlaps: first, expand the initial state $|\Omega\rangle$ on the post-quench basis, and second, expand the post-quench eigenstates $|\{0\}\rangle_a$ and $|\{\vartheta_1,\vartheta_2\}\rangle_{ab}$ on the pre-quench basis, where $|\Omega\rangle$ is the ground state. Note that unlike the previous chapter, here both approaches remain within ordinary perturbation theory. In the hope that these remarks clear up any unwanted confusion, let us adopt a similar terminology in this chapter as well, and let us call the two approaches post-quench perturbative expansion and pre-quench perturbative expansion, respectively. We present the corresponding calculations in this order.

5.2 Post-quench perturbative expansion

In the post-quench expansion the overlaps are computed by expanding the pre-quench vacuum $|\Omega\rangle$ in the basis of post-quench eigenstates. Assuming that the pre- and post-quench Hamiltonians are related by

$$H_{\text{pre}} = H_{\text{post}} + \lambda \int \mathrm{d}x\, \phi(x) \tag{5.6}$$

where ϕ is a local field, we can use ordinary Rayleigh–Schrödinger perturbation theory to express the overlaps in terms of matrix elements of ϕ:

$$\begin{aligned} |\Omega\rangle = |0\rangle - \lambda \sum_{N=1}^{\infty} \sum_{a_1,\dots a_N} \frac{2\pi}{k_a^{(N)}!} \left(\prod_{i=1}^{N} \int_{-\infty}^{\infty} \frac{\mathrm{d}\vartheta_i}{2\pi} \right) \delta \left(\sum_{i=1}^{N} p_{a,i} \right) \times \\ \times \frac{F^{\phi *}_{a_1,\dots a_N}(\vartheta_1,\dots,\vartheta_N)}{\sum_{i=1}^{N} E_{p_{a,i}}} |\vartheta_1,\dots,\vartheta_N\rangle_{a_1,\dots a_N} + O(\lambda^2)\,, \end{aligned} \tag{5.7}$$

where $p_{a,i} = m_{a_i} \sinh\vartheta_i$ and $E_{p_{a,i}} = m_{a_i} \cosh\vartheta_i$, and m_{a_i} is the mass of particle i that is of type a_i. The first order correction includes the following matrix element:

$$\langle k| \int \mathrm{d}x\, \phi(x)\, |0\rangle = 2\pi F^{\phi *}_{a_1,\dots a_N}(\vartheta_1,\dots,\vartheta_N)\delta \left(\sum_{i=1}^{N} p_{a,i} \right)\,, \tag{5.8}$$

where $|k\rangle = |\vartheta_1,\dots,\vartheta_N\rangle_{a_1,\dots a_N}$ and $F^{\phi}_{a_1,\dots a_N}(\vartheta_1,\dots,\vartheta_N)$ is the N-particle form factor of the operator ϕ (cf. Eq. (3.8)), while the Dirac-delta reflects momentum conservation. Note that although Eq. (5.7) contains an infinite summation over states, the scalar product in the overlaps selects only a single term.

The second order contribution to each overlap involves an infinite sum over intermediate states (cf. App. B.1). From Eq. (5.8) it follows that this sum contains an explicit divergence in the diagonal matrix element $\langle 0| \int \mathrm{d}x\, \phi(x)\, |0\rangle$, which is proportional to $\delta(0)$. The perturbed state is not normalised in this convention so all quantities have to be divided by $\mathcal{N} = 1 + \mathcal{O}(\lambda^2)$. However, since we perform overlap calculations up to $\mathcal{O}(\lambda^2)$, the normalisation is immaterial as the leading order contribution to any overlap is of $\mathcal{O}(\lambda)$. Consequently, the divergences can not be removed by dividing with $\mathcal{N}$. Instead, as shown in the following sections, they can be regularised by switching to finite volume.

5.2.1 Finite volume regularisation

Divergences involving $\delta(0)$ originate from the volume integral in Eq. (5.6) and can be handled by switching to finite volume L:

$$\int_{-\infty}^{\infty} \mathrm{d}x\, \phi(x) \longrightarrow \int_{0}^{L} \mathrm{d}x\, \phi(x)\,, \tag{5.9}$$

where for simplicity we impose periodic boundary conditions. Using this prescription, (5.8) is modified as

$$\langle k| \int \mathrm{d}x\, \phi(x)\, |0\rangle = L\, \langle k|\, \phi(0)\, |0\rangle_L\, |_{p_k=0}\,, \tag{5.10}$$

where the L subscript signals that the matrix element is understood in finite volume and $p_k = 0$ makes it explicit that the eigenstate $\langle k|$ has zero overall momentum.

When L is sufficiently large, the finite volume eigenstates can still be described as multi-particle states with rapidities $\{\vartheta_i\}$ that are quantised according to the Bethe–Yang equations:

$$Q_i = mL \sinh\vartheta_i + \sum_{j\neq i} \delta^{\mathrm{ps}}(\vartheta_i - \vartheta_j) = 2\pi I_i\,, \tag{5.11}$$

where the quantum numbers I_i are integers and

$$\delta^{\mathrm{ps}}(\vartheta) = -i \log S(\vartheta) \tag{5.12}$$

is the two-particle scattering phase-shift. As a result, the momentum integrals are replaced by discrete sums running over the quantum numbers or, equivalently, the rapidities labelling different states in finite volume. Matrix elements can be expressed by the finite volume form factor formula [93]:

$$\langle\{\vartheta_i\}|\, \phi\, |\{\vartheta'_j\}\rangle_L = \frac{F^{\phi}_{\{a_i\},\{a_j\}}(\{\vartheta_i - i\pi\}, \{\vartheta'_j\})}{\sqrt{\rho_{\{a_i\}}(\{\vartheta_i\})}\sqrt{\rho_{\{a_j\}}(\{\vartheta'_j\})}}\,, \tag{5.13}$$

where the ρ density factors are defined by the following determinant:

$$\rho_{a_1,\dots a_N}(\vartheta_1,\dots \vartheta_N) = \det\left(\frac{\partial Q_k}{\partial \vartheta_l}\right), \qquad k,l = 1,\dots N\,. \tag{5.14}$$

Note that the N-particle density factor scales as $\mathcal{O}(L^N)$ with respect to the volume. Putting everything together, one obtains for the perturbative expansion up to second order in finite volume

$$\begin{aligned}
|\Omega\rangle_L = |0\rangle_L - \lambda L \sum_{N=1}^{\infty} \left(\prod_{a=1}^{s} \frac{1}{k_a^{(N)}!} \right) \sum_{\{\vartheta_1,\dots\vartheta_N\}} \delta\left(\sum_{i=1}^{N} m_{a_i} \sinh\vartheta_i, 0 \right) \times \\
\times \frac{F^{\phi *}_{a_1,\dots a_N}(\{\vartheta_1,\dots\vartheta_N\})}{\sqrt{\rho_{a_1,\dots a_N}(\vartheta_1,\dots\vartheta_N)} \sum_{i=1}^{N} m_{a_i}\cosh\vartheta_i} |\{\vartheta_1,\dots\vartheta_N\}\rangle_{\{a_i\},L} + \qquad (5.15) \\
+ \lambda^2 |\Omega^{(2)}\rangle_L + O(\lambda^3) ,
\end{aligned}$$

where we introduced the notation $\delta(a,b) \equiv \delta_{ab}$ for the Kronecker delta. Although the first order correction seems to be proportional to L, we will see below that the volume factor is cancelled by the density factor of the finite volume states, so the correction to the overlaps is finite after taking the $L \to \infty$ limit. The second order correction has the explicit form

$$\begin{aligned}
|\Omega^{(2)}\rangle_L = L^2 \sum_{N,M=1}^{\infty} \sum_{\substack{a_1,\dots a_N \\ b_1,\dots b_M}} \left(\prod_{a=1}^{s} \frac{1}{k_a^{(N)}! k_b^{(M)}!} \right) \sum_{\{\vartheta_1,\dots\vartheta_N\}} \sum_{\{\vartheta'_1,\dots\vartheta'_M\}} \\
\delta\left(\sum_{i=1}^{M} m_{b_j} \sinh\vartheta'_j, 0 \right) \delta\left(\sum_{i=1}^{N} m_{a_i} \sinh\vartheta_i, \sum_{j=1}^{M} m_{b_j} \sinh\vartheta'_j \right) \times \\
\times \frac{\langle\{\vartheta'_j\}|\,\phi\,|0\rangle_L \,\langle\{\vartheta_i\}|\,\phi\,|\{\vartheta'_j\}\rangle_L}{\sum_{i=1}^{N} m_{a_i}\cosh\vartheta_i \sum_{j=1}^{M} m_{b_j}\cosh\vartheta'_j} |\{\vartheta_i\}\rangle_{\{a_i\},L} - \qquad (5.16) \\
- L^2 \sum_{N=1}^{\infty} \sum_{a_1,\dots a_N} \left(\prod_{a=1}^{s} \frac{1}{k_a^{(N)}!} \right) \sum_{\{\vartheta_1,\dots\vartheta_N\}} \delta\left(\sum_{i=1}^{N} m_{a_i} \sinh\vartheta_i, 0 \right) \times \\
\times \frac{\langle\phi\rangle_L \,\langle\{\vartheta_i\}|\,\phi\,|0\rangle_L}{\left(\sum_{i=1}^{N} m_{a_i}\cosh\vartheta_i\right)^2} |\{\vartheta_i\}\rangle_{\{a_i\},L} .
\end{aligned}$$

The explicit divergence appears in the last term, since the density factor coming from the finite volume matrix element is insufficient to suppress the L^2 factor. However, the divergence is cancelled by the disconnected part of the finite volume form factor, as shown below.

5.2.2 Results for one-particle overlaps

One-particle overlaps g_a are defined by the scalar product in Eq. (5.4). For simplicity, we suppress the species index here—the generalisation to the case of multiple species is presented later. This reduces the problem to the calculation of a single amplitude g, which is connected to the finite volume scalar product as [165]:

$$\frac{g}{2} = \frac{\langle\{0\}|\Omega\rangle_L}{\sqrt{mL}}\,, \tag{5.17}$$

where the factor of $1/\sqrt{mL}$ results from the relation between the normalisation of the infinite and finite volume states. Using (5.15) we can read off the result of perturbation theory up to the second order:

$$\begin{aligned}\frac{g}{2} =& \frac{1}{\sqrt{mL}}\left[-\lambda L\frac{F_1^\phi}{m\sqrt{mL}} + \lambda^2 L^2\left(-\frac{\langle\phi\rangle\, F_1^\phi}{m^2\sqrt{mL}} + \right.\right. \\ &\left.\left. + \frac{F_1^\phi F_2^\phi(i\pi,0)}{m^2\sqrt{mL}\sqrt{mL}\sqrt{mL}} + \frac{\langle\phi\rangle\, F_1^\phi}{m^2\sqrt{mL}} + \dots\right) + O\left(\lambda^3\right)\right]\,,\end{aligned} \tag{5.18}$$

where the ellipsis denotes the contribution of higher multi-particle form factors, and we used the results for the finite volume form factors derived in [93, 166]:

$$\langle\{0\}|\phi|0\rangle_L = \frac{F_1^\phi}{\sqrt{mL}}\,, \qquad \langle\{0\}|\phi|\{0\}\rangle_L = \frac{F_2^\phi(i\pi,0)}{\sqrt{mL}\sqrt{mL}} + \langle\phi\rangle\,. \tag{5.19}$$

Note that the diagonal form factor includes a disconnected contribution, which exactly cancels the divergent term appearing in the second order of perturbation theory. Eq. (5.18) can be simplified in the form:

$$\frac{g}{2} = -\lambda\frac{F_1^\phi}{m^2} + \lambda^2\left(\frac{F_1^\phi F_2^\phi(i\pi,0)}{m^4} + \dots\right) + O\left(\lambda^3\right)\,. \tag{5.20}$$

The contributions from higher form factors can also be evaluated. The first such term corresponds to the $\{\vartheta'_j\} = \{-\vartheta_1, \vartheta_1\}$ term in Eq. (5.16) and reads

$$\frac{\lambda^2 L^2}{2}\sum_{\vartheta_1}\frac{F_3^\phi(i\pi,-\vartheta_1,\vartheta_1)F_2^{\phi*}(-\vartheta_1,\vartheta_1)}{mL\rho_2(\vartheta_1,-\vartheta_1)2m^2\cosh\vartheta_1}\,, \tag{5.21}$$

where ρ_2 is the density factor defined in (5.14), and overall momentum conservation was used to eliminate one of the rapidity summations. In the infinite volume limit the summation is transformed into an integral

$$\sum_{\vartheta_1} \to \int\frac{\mathrm{d}\vartheta}{2\pi}\tilde{\rho}(\vartheta)\,, \tag{5.22}$$

where $\tilde{\rho}(\vartheta)$ is the density of zero-momentum states, which can be obtained by enforcing zero overall momentum on the Bethe–Yang equations (5.11):

$$\tilde{\rho}_1(\vartheta_1) = \left.\frac{\partial Q_1(\vartheta_1,\vartheta_2)}{\partial\vartheta_1}\right|_{m\sinh\vartheta_1 + m\sinh\vartheta_2 = 0}\,. \tag{5.23}$$

The quotient of these two density factors yields

$$\frac{\tilde{\rho}(\vartheta)}{\rho_2(\vartheta,-\vartheta)} = \frac{1}{mL\cosh\vartheta}\,, \tag{5.24}$$

and so the powers of L cancel, leading to the infinite volume limit

$$\frac{\lambda^2}{2}\int\frac{\mathrm{d}\vartheta}{2\pi}\frac{F_3^{\phi}(i\pi,-\vartheta,\vartheta)F_2^{\phi*}(-\vartheta,\vartheta)}{2m^4\cosh^2\vartheta}\,. \tag{5.25}$$

This expression contains another possible source of divergence due to the kinematic pole (3.13) of the form factors: $F_3(i\pi,-\vartheta,\vartheta)$ has a simple pole for $\vartheta\to 0$. However, $F_2\propto\vartheta$ around the origin due to the two-particle S-matrix satisfying $S(0)=-1$. [1] So the product is regular and the integral is well-defined. Adding this term to Eq. (5.20) results in:

$$\begin{aligned}\frac{g}{2} = &-\lambda\frac{F_1^{\phi}}{m^2}+\lambda^2\left(\frac{F_1^{\phi}F_2^{\phi}(i\pi,0)}{m^4}+\right.\\ &\left.+\frac{1}{2}\int\frac{\mathrm{d}\vartheta}{2\pi}\frac{F_3^{\phi}(i\pi,-\vartheta,\vartheta)F_2^{\phi*}(-\vartheta,\vartheta)}{2m^4\cosh^2\vartheta}+\dots\right)+O\left(\lambda^3\right)\,.\end{aligned} \tag{5.26}$$

The above considerations can easily be generalised to a theory with multiple particle species, resulting in the following expression for the overlap of a particle of species a

$$\begin{aligned}\frac{g_a}{2} = &-\lambda\frac{F_a^{\phi}}{m_a^2}+\lambda^2\left(\sum_{b=1}^{s}\frac{F_b^{\phi}F_{ab}^{\phi}(i\pi,0)}{m_a^2m_b^2}+\right.\\ &\sum_{b\le c}\frac{1}{(2\delta_{bc})!}\int\frac{\mathrm{d}\vartheta}{2\pi}\frac{F_{abc}^{\phi}(i\pi,\vartheta,\vartheta_{bc})}{m_a^2\left(m_b\cosh(\vartheta)+\sqrt{m_c^2+(m_b\sinh\vartheta)^2}\right)}\times\\ &\left.\times\frac{F_{bc}^{\phi*}(\vartheta,\vartheta_{bc})}{\sqrt{m_c^2+(m_b\sinh\vartheta)^2}}+\dots\right)+O\left(\lambda^3\right)\,,\end{aligned} \tag{5.27}$$

with

$$\vartheta_{bc} = -\mathrm{arcsinh}\left(\frac{m_b\sinh\vartheta}{m_c}\right)\,, \tag{5.28}$$

which is a straightforward generalisation of Eq. (5.26). Note that this expression is regular, since F_{aac} does not have a kinematic pole in the case $a\neq c$ for $\vartheta\to 0$ due to $S_{ac}(0)=+1$ for two different species a and c.

---

[1] This reflects an effective exclusion statistics satisfied by these particles, see the exchange axiom of form factors in Eq. (3.11)

5.2.3 Results for two-particle overlaps

The next term in the expansion (5.1) corresponds to two-particle states which have zero total momentum for a global quench (5.6). In the case of a single particle species, their contribution is characterised by a single rapidity-dependent overlap function $K(-\vartheta,\vartheta)$:

$$K(-\vartheta,\vartheta) = \langle\{\vartheta,-\vartheta\}|\Omega\rangle\ , \tag{5.29}$$

which is related to the corresponding finite volume inner product by the relation [165]:

$$K(-\vartheta,\vartheta) = \frac{\tilde{\rho}(\vartheta)\,\langle\{\vartheta,-\vartheta\}|\Omega\rangle_L}{\sqrt{\rho_2(\vartheta,-\vartheta)}}\ . \tag{5.30}$$

The perturbative contributions to $K(-\vartheta,\vartheta)$ can be easily read off from the $n=2$ terms in Eq. (5.15):

$$\begin{aligned} K(-\vartheta,\vartheta) = \frac{\tilde{\rho}(\vartheta)}{\sqrt{\rho_2(\vartheta,-\vartheta)}}\Bigg[&-\lambda L\frac{F_2^{\phi*}(-\vartheta,\vartheta)}{2m\cosh\vartheta\sqrt{\rho_2(\vartheta,-\vartheta)}}+ \\ &+\lambda^2L^2\left(\frac{-\langle\phi\rangle\,F_2^{\phi*}(-\vartheta,\vartheta)}{(2m\cosh\vartheta)^2\sqrt{\rho_2(\vartheta,-\vartheta)}}+\right. \\ &\left.+\frac{F_1^{\phi}F_3^{\phi*}(i\pi,-\vartheta,\vartheta)}{2m^2\cosh\vartheta\sqrt{mL}\sqrt{mL}\sqrt{\rho_2(\vartheta,-\vartheta)}}+\dots\right)+O\left(\lambda^3\right)\Bigg]\ , \end{aligned} \tag{5.31}$$

where the ellipsis again corresponds to higher multi-particle form factor contributions. Using

$$\frac{\tilde{\rho}(\vartheta)}{\rho_2(\vartheta,-\vartheta)} = \frac{1}{mL\cosh\vartheta} \tag{5.32}$$

we obtain

$$\begin{aligned} K(-\vartheta,\vartheta) = &-\lambda\frac{F_2^{\phi*}(-\vartheta,\vartheta)}{2m^2\cosh^2\vartheta}+\lambda^2L\left(-\frac{\langle\phi\rangle\,F_2^{\phi*}(-\vartheta,\vartheta)}{4(m\cosh\vartheta)^3}+\right. \\ &\left.+\frac{F_1^{\phi}F_3^{\phi*}(i\pi,-\vartheta,\vartheta)}{2m^3\cosh^2\vartheta mL}+\dots\right)+O\left(\lambda^3\right)\ . \end{aligned} \tag{5.33}$$

The above expression contains an apparent infinite volume divergence; similarly to the one-particle case, it is expected to cancel with the disconnected piece of the next term in the form factor expansion. The corresponding term is:

$$\sum_{\vartheta'>0}\frac{\langle\{\vartheta,-\vartheta\}|\phi|\{-\vartheta',\vartheta'\}\rangle_L\ \langle\{\vartheta',-\vartheta'\}|\phi|0\rangle_L}{4m^2\cosh\vartheta\cosh\vartheta'}\ , \tag{5.34}$$

where a disconnected piece appears for $\vartheta=\vartheta'$. In this case the relation between the finite volume matrix element and the infinite volume form factors reads as [166]:

$$\begin{aligned}\langle\{\vartheta,-\vartheta\}|\phi|\{-\vartheta,\vartheta\}\rangle_L =&\frac{1}{\rho_2(\vartheta,-\vartheta)}\Big(F_4^{\phi,s}(i\pi+\vartheta,i\pi-\vartheta,-\vartheta,\vartheta)+\\ &+2mL\cosh\vartheta F_2^{\phi}(i\pi,0)+\rho_2(\vartheta,-\vartheta)\,\langle\phi\rangle\Big)\,,\end{aligned}\tag{5.35}$$

where the superscript s denotes that the form factor is evaluated symmetrically at $\vartheta=\vartheta'$, i.e.

$$F_4^{\phi,s}(i\pi+\vartheta,i\pi-\vartheta,-\vartheta,\vartheta)=\lim_{\epsilon\to0}F_4^{\phi}(i\pi+\vartheta+\epsilon,i\pi-\vartheta+\epsilon,-\vartheta,\vartheta)\,,\tag{5.36}$$

which is a regular expression [41, 166]. Note that the last term exactly cancels the term proportional to L in (5.33). The final result for the two-particle overlap is

$$\begin{aligned}K(-\vartheta,\vartheta)=&-\lambda\frac{F_2^{\phi*}(\vartheta,-\vartheta)}{2m^2\cosh^2\vartheta}+\\ &+\lambda^2\left(\frac{F_1^{\phi}F_3^{\phi*}(i\pi,-\vartheta,\vartheta)}{2m^4\cosh^2\vartheta}+\frac{F_2^{\phi*}(-\vartheta,\vartheta)F_2^{\phi}(i\pi,0)}{2m^4\cosh^4\vartheta}+\right.\\ &\left.+\frac{1}{2}\int_{-\infty}^{\infty}\frac{\mathrm{d}\vartheta'}{2\pi}\,\frac{F_4^{\phi,s}(i\pi+\vartheta,i\pi-\vartheta,-\vartheta',\vartheta')F_2^{\phi*}(-\vartheta',\vartheta')}{4m^4\cosh^2\vartheta\cosh^2\vartheta'}+\dots\right)+O\left(\lambda^3\right)\,,\end{aligned}\tag{5.37}$$

The generalisation to multiple particle species is not as straightforward as in the case of one-particle overlaps. The new feature is that in infinite volume divergent disconnected pieces appear even when there is only one particle that appears with the same rapidity on both sides. However, this cannot happen in finite volume, due to the quantisation of rapidities according to Eq. (5.11) [166]. Consequently, it is necessary to be more careful when taking the limit $L\to\infty$. With due care, explicit expressions can be derived both for the overlap functions containing a pair from the same species and a pair from different species. The resulting formulae are similar in structure to Eq. (5.37), but they are more lengthy due to the appearing extra terms. We list them with a detailed derivation in Appendix B.2 for completeness.

At this point we have a second order perturbative expression for the one- and two-particle overlaps generalised to models with multiple particle species. Note that the only assumption these results rely on is that the quench parameter λ is sufficiently small such that a perturbative approach is valid. Under the additional assumption of small post-quench density (which is justified if we are in the perturbative regime), Eqs. (5.26) and (5.37) give an adequate description of the initial state following a global quench of the form (5.6). Moreover, at least formally, this description is valid in a generic quantum field theory.

Naturally, the utility of these expressions is highest when they can be evaluated, i.e. in models where the F_n matrix elements are known. For example, the quenches discussed in the previous chapter that are subject to integrable post-quench dynamics provide an immediate application of Eqs. (5.26) and (5.37). Moreover, the neglect of terms containing higher form factors is justified as well: form factor series in two-dimensional QFT display a rapid convergence in general [3].

We remark that the resulting expression for $K(\vartheta)$ reveals a distinctive feature of the two-particle overlap function, appearing in the second order contribution. That is, for $\vartheta \to 0$ the pair overlap has a simple pole which stems from the $F_3^{\phi *}(i\pi, -\vartheta, \vartheta)$ form factor in the first λ^2 term. The origin of this term is the insertion of a single-particle state in the perturbative expansion. This is a general phenomenon: the pole at the zero-momentum threshold is a consequence of the nonzero single-particle overlap g, which also determines its residue [123]:

$$K(\vartheta) \sim \frac{-ig^2}{2\vartheta} + O(\vartheta^0)\,. \tag{5.38}$$

This relation is satisfied by Eqs. (5.26) and (5.37) up to leading (quadratic) order in λ.

5.3 Pre-quench perturbative expansion

Above we presented a second order perturbative calculation for the overlaps on the post-quench basis. While the formal results are expected to hold true in any quantum field theory, in practice their applicability is more restricted: they apply to quenches with integrable post-quench dynamics. The scope of the perturbative approach can be partially extended by covering the case of integrable pre-quench dynamics. This drives us to pursue a similar approach along the second direction introduced in Sec. 5.1, i.e. to perform an analogous expansion on the pre-quench basis.

Computationally, this amounts to solving a reversed task: in the previous calculations we had to obtain the correction to the pre-quench vacuum order by order, here it is necessary the compute the perturbative correction to each eigenstate, focusing only on the part that is proportional to the pre-quench ground state $|\Omega\rangle$. Apart from this modification, the steps of the calculations are almost identical to the preceding ones so instead of a detailed calculation we focus on the results while commenting on the differences.

5.3.1 One-particle overlaps

For the g amplitudes the major changes compared to Eq. (5.27) are in the denominators: the energy differences appearing in the perturbative expansion are now with respect to the one-particle mass instead of the vacuum. Cancellation of divergent parts is again due to disconnected pieces. Apart from the energy denominators, the only difference appears in the ordering of rapidities in the form factors. The final result is given by:

$$\begin{aligned}\frac{g_a^{(0)}}{2} = &-\lambda\frac{F_a^\phi}{m_a^2} - \lambda^2\left(\sum_{b=1,b\neq a}^{N_{\mathrm{spec}}} \frac{F_b^\phi F_{ab}^\phi(i\pi,0)}{m_a^2 m_b(m_b-m_a)} + \frac{F_{aa}^\phi(i\pi,0)F_a^\phi}{m_a^4}\right.\\ &+\sum_{b\leq c}\frac{1}{(2\delta_{bc})!}\int\frac{\mathrm{d}\vartheta}{2\pi}\,\frac{F^\phi_{bca}(i\pi+\vartheta,i\pi+\vartheta_{bc},0)}{m_a^2\sqrt{m_c^2+(m_b\sinh\vartheta)^2}}\times\\ &\left.\times\,\frac{F^\phi_{bc}(\vartheta,\vartheta_{bc})}{\left(m_b\cosh(\vartheta)+\sqrt{m_c^2+(m_b\sinh\vartheta)^2}-m_a\right)}+\dots\right)+O\left(\lambda^3\right)\,,\end{aligned} \tag{5.39}$$

where now all masses and form factors are those of the pre-quench theory.[2] The ellipsis indicates contributions of intermediate states with more than two particles. Note that if $m_a > m_b + m_c$ then the denominator of the integrand has a zero and the integrand has a pole. This will occur for all one-particle states with mass $m_a > 2m_1$ in one or more such integral terms. This pole is the consequence of a disappearing energy difference between a one-particle state and the two-particle continuum in infinite volume. We postpone the discussion of this singularity after presenting the two-particle overlaps.

5.3.2 Two-particle overlaps

Let us start with the discussion of the K_{aa} function. The first order contribution is simply

$$-\lambda\frac{F^\phi_{aa}(-\vartheta,\vartheta)}{2m_a^2\cosh^2(\vartheta)}\,. \tag{5.40}$$

The second order contribution is given as a sum over eigenstates [c.f. the third term of Eq. (B.5)]. Inserting the vacuum yields a divergent term which is cancelled by the disconnected piece of the diagonal matrix element, analogously to

---

[2] Note that we omitted the (0) superscript from the quantities on the right-hand side for brevity. Also note that for this expression to make sense, the A_a particle state has to be present both in the pre-quench model (where the right-hand side is evaluated) and in the post-quench model (where the overlap is defined).

the argument in Section 5.2. The connected part of the diagonal element disappears in the infinite volume limit due to the corresponding density factor and therefore the only remaining term resulting from inserting the vacuum is

$$-\frac{\lambda^2}{2}\frac{F^{\phi}_{aa}(i\pi,0)F^{\phi}_{aa}(-\vartheta,\vartheta)}{m_a^4\cosh^4(\vartheta)}\,. \tag{5.41}$$

Moving forward and inserting the one-particle states yields

$$\frac{\lambda^2}{2}\sum_{b=1}^{s}\frac{F^{\phi}_{b}F^{\pi}_{baa}(i\pi,-\vartheta,\vartheta)}{m_a^2 m_b\cosh^2(\vartheta)(2m_a\cosh(\vartheta)-m_b)}\,, \tag{5.42}$$

where the aforementioned pole manifests itself as a divergence of the pair overlap function $K_{aa}(\vartheta)$ whenever there is a particle with $m_b > 2m_a$.

Proceeding to the insertion of two-particle states, we can consider inserting a pair of particles A_b with $b \neq a$, in which case the form factor has no pole. In finite volume, the corresponding contribution reads

$$\frac{\lambda^2 L^2}{2}\sum_{\vartheta'}\frac{F^{\phi}_{bb}(-\vartheta',\vartheta')F^{\phi}_{bbaa}(i\pi+\vartheta',i\pi-\vartheta',-\vartheta,\vartheta)}{\rho_{bb}(\vartheta',-\vartheta')2m_a\cosh\vartheta(2m_a\cosh\vartheta-2m_b\cosh\vartheta')m_aL\cosh\vartheta}\,. \tag{5.43}$$

Note that the pole is only present in infinite volume since for any finite L there are no exact degeneracies in the spectrum due to the Bethe-Yang equations (5.11). Hence one might expect that the finite volume regularisation technique detailed in Section 5.2.1 is able to treat its effect properly. In the limit $L\to\infty$ limit the energy difference can be zero at

$$\vartheta_* = \operatorname{arccosh}\left(\frac{m_a\cosh\vartheta}{m_b}\right)\,. \tag{5.44}$$

Note that ϑ_* is imaginary if $\vartheta < \operatorname{arccosh}(m_b/m_a)$. However, for larger ϑ the pole is on the real axis. Eq. (5.43) can be rewritten as

$$\frac{\lambda^2}{8}\sum_{\vartheta'}\frac{F^{\phi}_{bb}(-\vartheta',\vartheta')F^{\phi}_{bbaa}(i\pi+\vartheta',i\pi-\vartheta',-\vartheta,\vartheta)}{\tilde{\rho}_b(\vartheta')m_a^2 m_b\cosh\vartheta'\cosh^2\vartheta(m_a\cosh\vartheta-m_b\cosh\vartheta')}\,. \tag{5.45}$$

The sum can be represented as a sum of contour integrals[3] using

$$\sum_{\vartheta'}\frac{f(\vartheta')}{\tilde{\rho}_b(\vartheta')} = \sum_{\vartheta'}\oint_{\vartheta'}\frac{\mathrm{d}\vartheta}{2\pi}\frac{-f(\vartheta)}{1+e^{i\tilde{Q}_b(\vartheta)}}\,, \tag{5.46}$$

where $f(\vartheta)$ is assumed to be regular at ϑ', and the contours encircle the ϑ' values on the real axis that are given by the quantisation condition

$$\tilde{Q}_b(\vartheta') = m_b L\sinh\vartheta' + \delta^{\mathrm{ps}}_{bb}(2\vartheta') = 2\pi J\,, \tag{5.47}$$

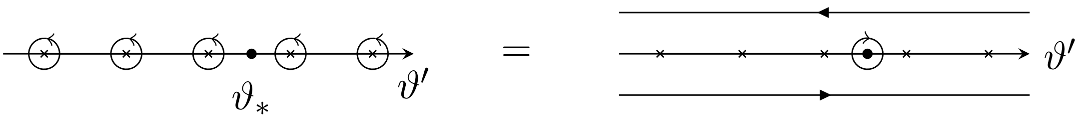

Figure 5.1: Illustration of the contour integrals involved in the finite volume regularisation of an infinite volume pole. The summation goes over the quantised ϑ' (located at the crosses on the axes), and there is an additional pole at ϑ_* (denoted by a dot). The contours can be joined together, but the residue at ϑ_* has to be subtracted.

where J is a half-integer number. The contours can be joined to form two infinite lines below and above the real axis, see Fig. 5.1. On the first the integrand vanishes in the infinite volume limit while the second one yields

$$\frac{\lambda^2}{8}\int_{-\infty+i\epsilon}^{\infty+i\epsilon}\frac{\mathrm{d}\vartheta'}{2\pi}\frac{F^{\phi}_{bb}(-\vartheta',\vartheta')F^{\phi}_{bbaa}(i\pi+\vartheta',i\pi-\vartheta',-\vartheta,\vartheta)}{m_a^2 m_b\cosh^2\vartheta\cosh\vartheta'(m_a\cosh\vartheta-m_b\cosh\vartheta')}\,. \tag{5.48}$$

When joining the contours, it is necessary to subtract the residue of the pole at $\vartheta=\vartheta^*$,

$$\frac{\lambda^2}{8}\frac{iF^{\phi}_{bb}(-\vartheta_*,\vartheta_*)F^{\phi}_{bbaa}(i\pi+\vartheta_*,i\pi-\vartheta_*,-\vartheta,\vartheta)}{m_a^2 m_b\cosh^2\vartheta\cosh\vartheta' m_b\sinh\vartheta_*(1+e^{i\tilde{Q}_b(\vartheta_*)})}\,. \tag{5.49}$$

Even though the result is finite, it does not have a $L\to\infty$ limit due the factor $e^{i\tilde{Q}_b(\vartheta_*)}\sim e^{im_bL\sinh\vartheta_*}$. Consequently, the sum in (5.45) still fails to have a well-defined infinite volume limit.

Therefore the singularities corresponding to vanishing energy denominators are intractable by the method of finite volume regularisation. One may try other ways to circumvent this problem and arrive at a regular expression well defined in the $L\to\infty$ limit, however we failed in all our attempts so far. So the proper treatment of these singularities remains an interesting open question.

Nevertheless, there exist particular quenches which are free of the complications discussed above. If the matrix elements of the operator ϕ are proportional to the energy of the involved states, the divergence is cancelled and the sum can be readily transformed to an integral. For instance, this is the case for Type I quenches considered in the previous chapter, where the quenching operator is $\sigma(x)$. It is proportional to the trace of the energy-momentum tensor [41], and as a consequence all of its form factors are proportional to the total energy of the appropriate states.

The above mathematical reasoning is illuminated by considering the physical picture. Note that in general the pre-quench basis is not an optimal choice to express the dynamics of the post-quench Hamiltonian. For example, heavy particles whose kinematically allowed decays in the pre-quench system are only prohibited

---

[3] Analogously to the treatment of disconnected pieces for the K_{aa} and K_{ab} functions in the post-quench expansion. For more details, see Appendix B.2.

by integrability become unstable. These particles are expected to acquire a finite lifetime which is reflected by the divergent terms of the perturbative series. The resolution would require a resummation, which is expected to shift the singularity away from the real axis. Similarly, two-particle states acquire a finite lifetime due to inelastic processes. The situation is radically different for quenches where the pre-quench and post-quench setting corresponds to the same integrable model. Such a protocol is simply equivalent to a rescaling of parameters describing the spectrum, which retains its structure. Accordingly, one does not expect divergences in perturbation theory and in fact, they are absent—apart from the ones tractable with the method of finite volume regularisation.

Consequently, for this specific class of quenches, we can express the perturbative overlap functions up to second order on the pre-quench basis as well. The explicit formulae for the two-particle overlap functions are once again elaborate, we report them in App. B.3.

5.4 Testing the results in the E_8 Ising field theory

In the previous two sections we presented two applications of perturbation theory to the calculation of post-quench overlaps. In the following we turn to putting these approaches to the test, for which we need a model which satisfies the following important criteria. First, it must be rich enough to test all aspects of our results; second, there must be enough information about its spectrum and form factors for the evaluation of the analytic expressions for the overlaps and third, it must be amenable to an effective alternative treatment.

The E_8 field theory offers an ideal choice. It has 8 stable particles, hence the perturbative predictions can be tested on a wide set of one- and two-particle overlap functions. The matrix elements of its relevant operators can be calculated exactly (cf. Chapter 3), which allows for the numerical evaluation of the perturbative expressions derived above. And finally, the analytic results can be compared with a precise and efficient numerical method, the TCSA, which has been used in a similar setting in the previous chapter.

We consider here the two quench types illustrated in Fig. 4.1, analogously to the case of post-quench time evolution. Let us now turn to the discussion of the results in the two cases.

5.4.1 Integrable post-quench dynamics

We recall that Type I quenches are defined by the action

$$\mathcal{A} = \mathcal{A}_{CFT,\,c=1/2} - h_{\mathrm{i}} \int \sigma(x) \mathrm{d}^2 x - (h_{\mathrm{f}} - h_{\mathrm{i}}) \int \sigma(x) \Theta(t) \mathrm{d}^2 x \,, \tag{5.50}$$

i.e. they correspond to a sudden change of h from the initial h_i to the final h_f at $t = 0$, expressed by the Heaviside function $\Theta(t)$. For $t \leq 0$ the system is in the ground state of the pre-quench Hamiltonian, which is the initial state of the out-of-equilibrium time evolution which happens for $t > 0$. The quench can be characterised by the dimensionless quench magnitude

$$\xi \equiv \frac{h_\mathrm{f} - h_\mathrm{i}}{h_\mathrm{f}}\,. \tag{5.51}$$

These quenches have integrable post-quench dynamics, hence the post-quench expansion provides predictions for the overlap functions in this case. They also belong to the special class of quenches where the pre-quench expansion yields sensible results. As a consequence, the numerical data can be compared with both approaches at the same time. All the TCSA calculations are performed in finite volume, so in order to compare the numerical results to the perturbative predictions it is convenient use the finite volume normalisation of Eqs. (5.17) and (5.30). In the numerical calculations we measure everything in appropriate powers of the post-quench mass gap m_1, so the perturbative parameter λ is obtained by multiplying ξ with the post-quench parameter h_f.

Let us remark that the overlap functions are defined up to a phase factor, since we can freely choose the phase of any quantum state. The TCSA uses a basis in which all vectors are real, consequently the overlaps obtained from this approach are also real. Thus the comparison is performed such that we take the absolute value of the perturbative overlap functions.

Before turning to the discussion of the comparison with TCSA calculations, let us comment on the numerical evaluation of the perturbative formulae. The second order contributions involve a sum over all possible intermediate states, which means an infinite summation over all possible number N of inserted particles. In the above calculations we truncated the infinite sum at pair states with $N = 2$. We observe that the contribution from the terms involving an integral over the momentum of a pair state is very small in most of the cases. Consequently, we argue that the error we make by truncating the form factor expansion at two-particle intermediate states is orders of magnitude smaller than the main contributions in second order. This argument is supported by the numerical evaluation of the various terms presented in Appendix B.4.

Coincidentally, there is another source of truncation in the analytic expansions, related to the large number of particle species in the E_8 model. Currently, the set of available form factors is incomplete already at the three-particle level, hence the full second order contribution cannot be evaluated even for $N \leq 2$ inserted particles. Our calculation presented in Chapter 3 significantly increased the number of available three- and four-particle form factors, reducing the error in the perturbative expansions coming from the truncation of the form factor series.

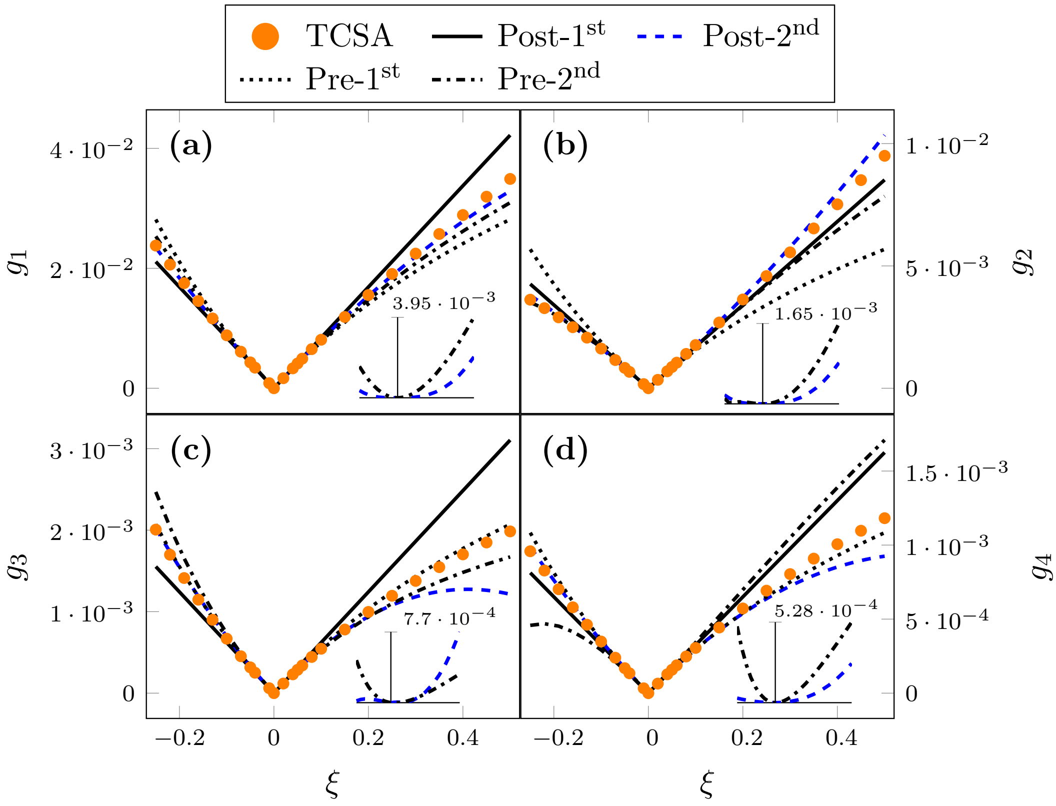

Figure 5.2: Comparison between TCSA overlaps of the lightest four one-particle states and two different perturbative expansions as functions of the quench magnitude ξ for quenches along the E_8 axis in volume $m_1 R = 40$. Dashed lines indicate the first-order predictions of the post-quench expansion and continuous lines depict the sum of the first two orders. The pre-quench result up to the first and second order is shown in dotted and dot-dashed lines, respectively. TCSA data is shown by orange dots. Inset: the absolute deviation of second order results from TCSA. The numbers above the inset indicate the maximal deviation in the plotted ξ interval.

One-particle overlaps

We begin the discussion of the comparison for the case of one-particle overlaps. The g_a functions for the four lowest-lying states are presented in Fig. 5.2. The observation of these functions reveals that the perturbative expressions describe the overlaps very well for a quite wide range of quench magnitudes.

The agreement is most precise for the A_1 and A_2 particles in the top row, while the analytical data is slightly less accurate for the A_3 and A_4 states. This can partially be attributed to the limited knowledge of three-particle form factors remarked above. The largest number of the form factors are accessible for the case of the lightest particle A_1, therefore the agreement is the best for this case and the domain of validity almost covers the whole region of the plot. For heavier

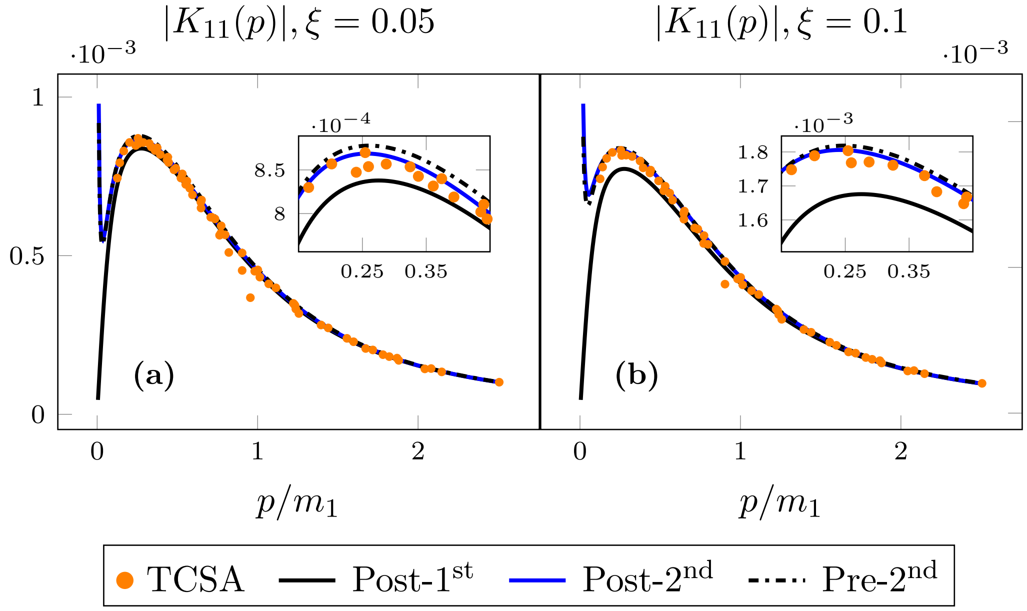

Figure 5.3: Perturbative predictions against the TCSA data for the two-particle overlap K_{11} as a function of the dimensionless momentum p_1/m after quenches of size (a) $\xi = 0.05$, and (b) $\xi = 0.1$. The overlap was determined by TCSA using volumes $m_1 R = 30 \dots 65$.. Black lines correspond to the first-order predictions of the post-quench expansion, and blue continuous lines depict the sum of first two orders. The result of the pre-quench expansion is denoted by black dashdotted lines. The inset shows a magnified section around the local maxima of the curves.

particles it is expected that extending the set of available form factors would result in a better agreement with TCSA data, although the domain of validity presumably remains smaller than for A_1 (see Table B.1).

We also note that including the second order leads to a major improvement of the agreement between the perturbative and TCSA results in almost the whole parameter region presented here. This is valid for both the post- and pre-quench perturbative expansions, but the former gives more accurate predictions, in line with the expectation that the post-quench basis is better suited to describe the quench problem. This is reflected by the figures in the inset which show the absolute deviation of the two perturbative expansions from the overlaps obtained from TCSA: the post-quench curve remains consistently below the pre-quench mismatch in all but one case.

Two-particle overlap functions

The multiple particle species present in the Ising Field Theory provide an opportunity to observe both the K_{aa} and K_{ab} functions. In this case we used the data of quenches at a few different values of ξ and plotted the overlaps as

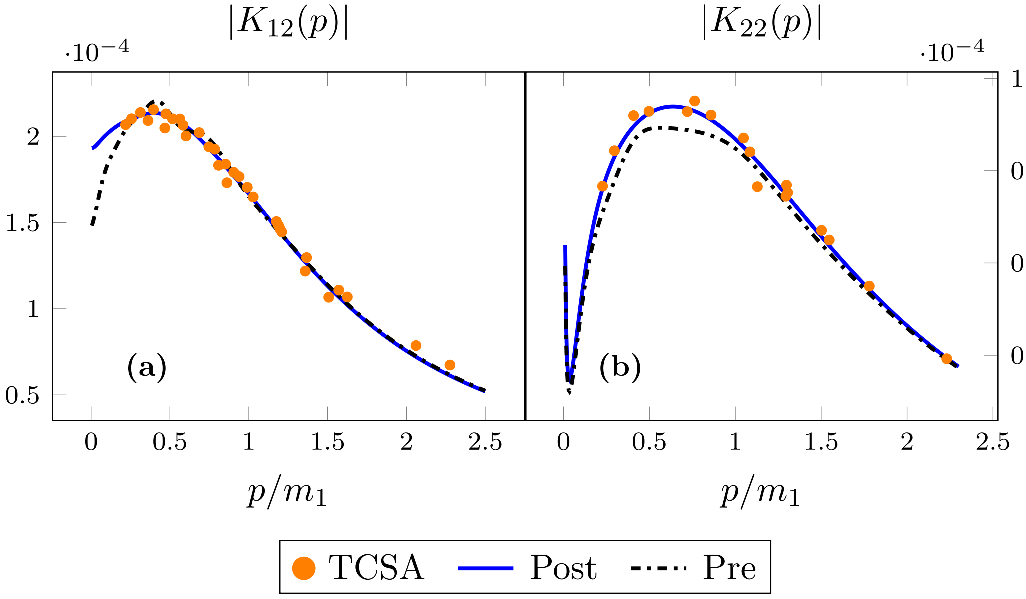

Figure 5.4: Overlap functions of pairs of heavier particles (a) $K_{12}(p)$ and (b) $K_{22}(p)$ after a quench of size $\xi = 0.05$ along the E_8 axis. The first-order results are omitted, all other conventions are as in Fig. 5.3.

functions of the momentum parameterising the particle pair.

The comparison for the overlap function of a pair of the lightest particle is presented in Fig. 5.3, which shows that the perturbative expansion performs well also for pair overlaps in matching the numerical results of TCSA for quenches with $\xi = 0.05$ and $\xi = 0.1$. The change from first to second order is less spectacular as it was in the one-particle case, but it still significantly improves the agreement, more noticeably as the quench magnitude increases, see the inset in Fig. 5.3b. In addition, the second order correction dramatically alters the qualitative behaviour of the overlap since it introduces a pole for zero momentum (cf. the discussion at the end of Sec. 5.2).

It would be worthwhile to extend the numerical data to investigate the presence of the pole. Unfortunately, this is hindered by two reasons: first, to obtain lower momenta, the volume parameter has to be increased to a regime where TCSA becomes less accurate. Second, due to the quantisation condition of $A_1 - A_1$ pair states, their energy gets within touching distance of each other as the volume is increased. Since numerical diagonalisation techniques do not always properly discern between near degenerate states, the resulting overlap will be imprecise. Nevertheless, the agreement shown in Fig. 5.3 is quite convincing.

It is also possible to compare the predictions regarding overlap functions of pair states of heavier particles, as well as that of pairs composed of different species. Fig. 5.4 illustrates that, similar to the case of K_{11}, the analytic prediction still agrees very well with the TCSA numerics, with the difference that there is a slightly bigger difference between the two approaches compared to the case shown in Fig. 5.3. Similarly to the single-particle overlaps, the post-quench approach is closer to the numerical data. As we observe a remarkable agreement between the perturbative expressions and the numerics in Fig. 5.4a, we conclude that Type I quenches, despite the equilibrium models both being integrable, do not meet the criteria (5.3) of integrable quenches. This observation reinforces the similar but purely perturbative argumentation of Ref. [40].

5.4.2 Non-integrable post-quench dynamics

Finally, let us turn to the discussion of Type II quenches leading from an integrable pre-quench Hamiltonian to a non-integrable post-quench dynamics. They are defined by adding the other Ising primary $\epsilon(x)$ field with scaling dimension $x_\epsilon = 1$ to the action (5.50).

$$\mathcal{A} = \mathcal{A}_{CFT,\,c=1/2} - h\int \sigma(x)d^2x - \frac{M}{2\pi}\int \epsilon(x)\Theta(t)d^2x\,, \tag{5.52}$$

The different physics towards the paramagnetic and ferromagnetic directions (corresponding to negative and positive M, respectively) was discussed in Sec. 2.2.1. Here we remain in the perturbative regime close to the E_8 axis, where these differences are less prominent. Still, we remark that in contrast to the symmetric behaviour of the first-order expression we encountered in the previous chapter, the second order perturbative expansion distinguishes between the two directions, promising a more accurate assessment of non-integrable dynamics.

On a less positive note, the applicability of the perturbative calculations is rather restricted in this case. As the post-quench dynamics is non-integrable, the use of the post-quench expansion is excluded. The pre-quench model is integrable, but the quenching operator is not proportional to the energy-momentum tensor, which means that the second order contributions to the overlap functions are plagued with infinities due to zero energy differences in the denominator. However, there are three notable exceptions: the three lowest-lying single particle states are below the two-particle threshold, and consequently escape the above problem. This is related to the stability of the three lightest particles in the non-integrable regime. The test of these three particles is an interesting probe of the effects of integrability breaking with the methods of perturbation theory.

Similarly to the previous chapter, we take the dimensionless parameter η

$$\eta = \frac{M}{|h|^{8/15}} \tag{5.53}$$

to measure the quench magnitude. In the following we work in units of m_1 given by Eq. (2.15) using the coupling h in the integrable pre-quench model, i.e. the mass gap of the pre-quench system. There is an additional modification to the earlier comparison: when we calculate the finite volume normalisation of TCSA

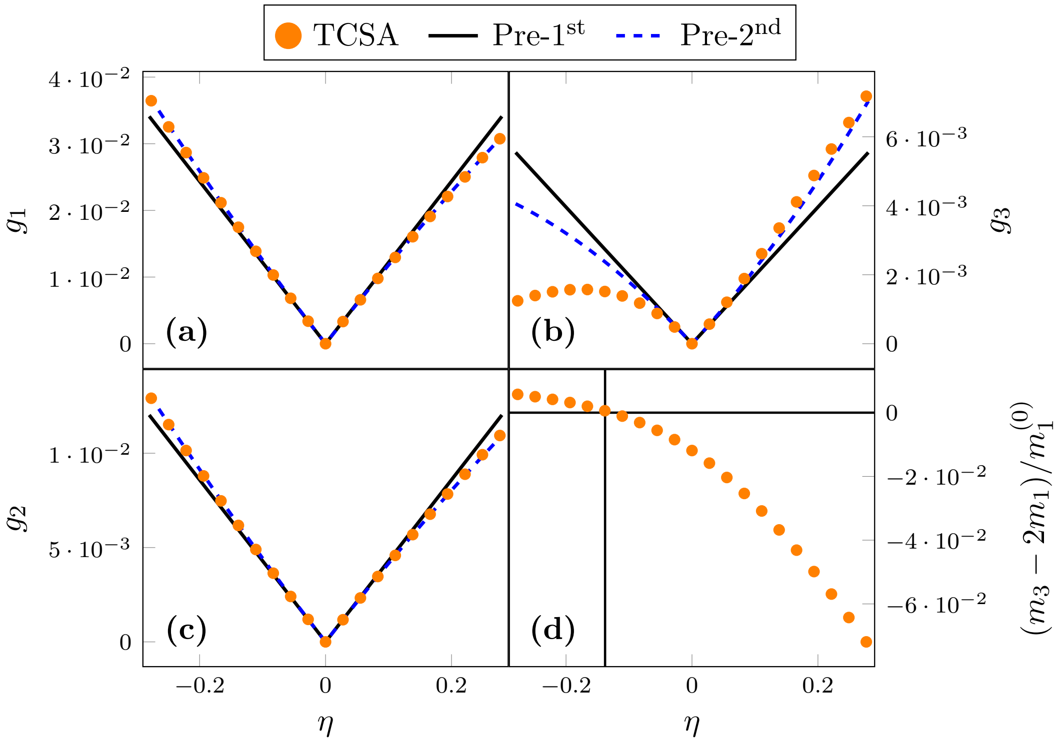

Figure 5.5: The overlaps of the three lowest-lying one-particle states for non-integrable quenches as functions of η (5.53) compared with TCSA data for $m_1^{(0)}R = 40$. Adding the second order yields better agreement in all cases. We observe sizeable deviation only in the case of the third particle in the paramagnetic direction due to the state becoming unstable, i.e. $m_3 > 2m_1$, as it is shown in the bottom right panel. The stability threshold $\eta_3 = -0.138$ is indicated by a grid line.

data given by Eqs. (5.17) we have to use the post-quench masses. These can be obtained from TCSA using a cutoff extrapolation scheme similar to the case of the overlaps.

The overlaps of the first two one-particle states are excellently captured by the perturbative expansion. The third particle shows an asymmetry in terms of agreement with TCSA data: we observe a small deviation from the perturbative result in the ferromagnetic direction, but a sizeable difference in the paramagnetic region. This can be understood in the light of the instability of the third particle in the paramagnetic regime. As η decreases, it crosses a threshold value $\eta_3 = -0.138$ where m_3 becomes smaller than $2m_1$, so the corresponding particle state becomes unstable for $\eta < \eta_3$ [48]. This is a non-perturbative phenomenon which is reflected by the deviation of TCSA data from the perturbative prediction, observable even for small negative η.

5.5 Summary

In this chapter we discussed the application of perturbation theory to construct overlaps of post-quench eigenstates with the ground state of the pre-quench Hamiltonian for quenches between integrable and close to integrable Hamiltonians. As a testing ground for our approach, we used quenches in the scaling Ising field theory (IFT).

We developed two approaches within perturbation theory to address the same question. The first approach is based on a perturbative expansion of the initial state in the basis of post-quench eigenstates. Working in this context, we showed that the divergences resulting from the naive application of ordinary non-degenerate perturbation theory can be handled by putting the system in finite volume using the formalism developed in Refs. [93, 166]. We expanded the one- and two-particle eigenstate functions up to second order in perturbation theory. The second order contribution is given as an infinite sum which is truncated upon numerical evaluation.

This is not a serious limitation, since this approach is effective when the post-quench dynamics is integrable, and the required matrix elements can be obtained as solutions to the form factor bootstrap. Form factor series exhibit fast convergence, leading to reliable results by the inclusion of the first few terms. We used the solution of the E_8 form factor bootstrap presented in Chapter 3 to reduce the residual error even further. The numerical evaluation of the perturbative formulae established that the second order contribution is nearly complete using the available form factors (see Appendix B.4).

The second approach entails a similar calculation on the pre-quench basis. This approach is effective when the pre-quench dynamics is integrable, and is directly related to a recently suggested perturbative approach to describe the post-quench dynamics [40, 121]. The second order calculations revealed a major roadblock in this approach in the shape of divergences intractable by finite volume regularisation. This roadblock is circumvented only by quenches with integrable post-quench dynamics, or, in other cases, by focusing on a limited set of states below the two-particle threshold.

We compared the results of the perturbative calculations with data obtained from the truncated conformal space approach in the IFT for the two types of quenches introduced in the previous chapter. For Type I quenches both expansions performed adequately in comparison with the numerics, with the post-quench expansion having a slight edge, both for single-particle and pair states. Notably, we demonstrated that two-particle states composed of particles of different species are present in the initial state. This violates the property (5.3) of integrable initial states, providing further support for the claim that the quench is not necessarily integrable even if both the pre-quench and post-quench dynamics are [40, 121]. The results for the pair overlap function also showed the appearance of the zero-momentum pole for $K_{aa}(p)$, which is proved to hold generally if there is a non-zero overlap with one-particle states [123].

For the second type of quenches with a non-integrable post-quench Hamiltonian, only the overlaps for the lowest-lying states can be constructed using the pre-quench perturbative expansion. For such overlaps we found good agreement with the numerical TCSA data, where the main limitation is posed by the instability of the third lightest particle. Lifting this limitation amounts to giving a proper description of non-equilibrium integrability breaking in terms of the properties of an integrable model in equilibrium. Whether this description can be found by a perturbative approach or a different take is required is up to future works to decide.

Chapter 6

The chirally factorised truncated space approach

The previous two chapters discussed various aspects of the quench paradigm in quantum field theory. With a specific focus on the Ising field theory, we mustered a set of analytical and numerical approaches to describe the quench dynamics. In particular, on the numerical side, we demonstrated the utility of the nonperturbative TCSA in out-of-equilibrium settings.

Motivated by this success, in this chapter we present the development of a new algorithm, the chirally factorised truncated conformal space approach (CFTCSA), which can be considered an improved version of the TCSA as outlined in Sec. 2.2.2. The aim of this development is twofold. First, to increase the dimensions of the truncated Hilbert space utilising the chiral factorisation of the underlying conformal field theory, and second, to work out a ready-to-use algorithm that can be easily adapted to various problems by physicists with no prior expertise in the method. The first holds the promise to assail more computationally heavy problems in perturbed conformal field theories, and it is fulfilled e.g. by our exploration of the Kibble–Zurek mechanism in the Ising field theory [167] (see Chap. 7 below for a detailed discussion). We aspire to achieve the second goal with our recent preprint [168] accompanied by several example codes realising the new algorithm.[1] In the following we overview the results of the development.

6.1 Ingredients

6.1.1 Formulation

The physical model we want to describe is the same as for the ordinary truncated conformal space approach: a $1+1$-dimensional quantum field theory

---

[1] We remark that a similar idea has been developed independently for a special case: the sinh-Gordon quantum field theory on a truncated free boson Hilbert space [169].

which is defined by perturbing a conformal field theory (CFT) with a relevant field:

$$H = H_{\mathrm{CFT}} + \lambda \int_0^L \mathrm{d}x \mathcal{V}(x) \,, \tag{6.1}$$

where H_{CFT} is the CFT Hamiltonian, $\mathcal{V}(x)$ is the relevant operator and λ is a coupling with positive mass dimension. We remark that it is straightforward to extend this definition by including further relevant fields, we only avoid this to keep the notations simpler. We apply periodic boundary conditions, so the space coordinate is confined to a circle: $x + L \equiv x$, thus the theory is defined on a space-time cylinder. We further assume that the perturbation is translationally invariant.

The Hilbert space employed by the TCSA corresponds to the conformal point, where listing the set of basis vectors amounts to finding all irreducible representations of the conformal algebra. Crucially, in two dimensions the algebra is the product of two decoupled infinite-dimensional chiral parts:

$$\begin{aligned} [L_n, L_m] &= (n-m)L_{n+m} + \frac{c}{12} n(n^2-1)\delta_{n+m,0} \,, \\ \left[\bar{L}_n, \bar{L}_m\right] &= (n-m)\bar{L}_{n+m} + \frac{c}{12} n(n^2-1)\delta_{n+m,0} \,, \\ \left[L_n, \bar{L}_m\right] &= 0 \,. \end{aligned} \tag{6.2}$$

Here c is a constant, the central charge of the algebra, and the L_n and $\bar{L}_n$ operators with $n \in \mathbb{Z}$ are the generators of the left and right chiral parts of the algebra, respectively.[2]

Summing over all irreducible representations of this algebra constructs the conformal Hilbert space:

$$\mathcal{H}_{\mathrm{CFT}} = \bigoplus_{\Phi} \mathcal{W}_{\Phi} \,, \tag{6.3}$$

where we used the Φ primary fields of the CFT to label the representations [170]. The chiral factorisation of the algebra means that each irreducible representation can be further decomposed as a product of left- and right-handed terms:

$$\mathcal{W}_{\Phi} = V_{\mathcal{R}(\Phi)} \otimes V_{\bar{\mathcal{R}}(\Phi)} \,, \tag{6.4}$$

where $\mathcal{R}(\Phi)$ and $\bar{\mathcal{R}}(\Phi)$ are the representations of the fields under left- and right-handed transformations, respectively. The behaviour of primary fields under these conformal transformations can be characterised by their conformal weights (also called primary weights) $(h_{\Phi}, \bar{h}_{\Phi})$. E.g. the usual scaling dimension of a field is simply given as $\Delta_{\Phi} = h_{\Phi} + \bar{h}_{\Phi}$. Notice that there can be fields transforming under different left and right representations. Theories for which all fields satisfy

---

[2] We remark that the principles of the CFTCSA allow for the inclusion of further symmetries, even covering the possibility of different left/right algebras. However, we do not pursue this direction here, as all numerical works in this thesis are related to Eq. (6.2).

$\mathcal{R}(\Phi) = \bar{\mathcal{R}}(\Phi)$ are called diagonal, with an example provided by the Ising field theory.

The representation of the algebra (6.2) can be worked out using the eigenbases of the operators L_0 and $\bar{L}_0$, which generate the chiral conformal scaling transformations. The chiral modules $V_{\mathcal{R}}$ and $V_{\bar{\mathcal{R}}}$ are given as direct sums on these bases:

$$\begin{aligned} V_{\mathcal{R}(\Phi)} &= \bigoplus_{N=0}^{\infty} V_{\mathcal{R}(\Phi)}(N) \;: \quad L_0 \left|v\right\rangle = \left(h_\Phi + N\right) \left|v\right\rangle \quad \forall \left|v\right\rangle \in V_{\mathcal{R}(\Phi)}(N) \\ V_{\bar{\mathcal{R}}(\Phi)} &= \bigoplus_{\bar{N}=0}^{\infty} V_{\bar{\mathcal{R}}(\Phi)}(\bar{N}) \;: \quad \bar{L}_0 \left|\bar{v}\right\rangle = \left(\bar{h}_\Phi + \bar{N}\right) \left|\bar{v}\right\rangle \quad \forall \left|\bar{v}\right\rangle \in V_{\bar{\mathcal{R}}(\Phi)}(\bar{N}) \,. \end{aligned} \tag{6.5}$$

The dimensions of the chiral subspaces at fixed levels are denoted by

$$d_{\mathcal{R}(\Phi)}(N) = \dim V_{\mathcal{R}(\Phi)}(N) \,. \tag{6.6}$$

For each primary Φ the term with $N = \bar{N} = 0$ is called the highest weight subspace, which is spanned by a single vector in the simplest cases. This highest weight vector is created from the conformal vacuum by the action of the primary field Φ. Vectors with non-zero level $N + \bar{N}$ are called descendent vectors, with their chiral descendent levels given by $(N, \bar{N})$.

Finally, using (6.4), the Hilbert space takes the form

$$\mathcal{H}_{\text{CFT}} = \bigoplus_{\Phi, N, \bar{N}} V_{\mathcal{R}(\Phi)}(N) \otimes V_{\bar{\mathcal{R}}(\Phi)}(\bar{N}) \,. \tag{6.7}$$

The full power of the conformal symmetry can be exploited by mapping the theory (6.1) to the the complex plane $(z, \bar{z})$. Starting from the space-time cylinder, let us first continue analytically to imaginary time: $\tau = -it$. By introducing the complex coordinates $w = \tau - ix$ and $\bar{w} = \tau + ix$ we can parameterise the position on the cylinder as $(w, \bar{w})$. The mapping to the complex plane is given by the conformal transformation:

$$z = \exp \frac{2\pi w}{L} \,. \tag{6.8}$$

Under this exponential map, primary fields given on the space-time cylinder transform as [170]

$$\Phi^{\text{cyl}}(w, \bar{w}) = \left(\frac{2\pi z}{L}\right)^{h_\Phi} \left(\frac{2\pi \bar{z}}{L}\right)^{\bar{h}_\Phi} \Phi^{\text{pl}}(z, \bar{z}) \,, \tag{6.9}$$

where the superscripts ‘cyl’ and ‘pl’ correspond to operators given on the space-time cylinder and on the complex plane, respectively.

6.1.2 The gains of chiral factorisation

After introducing the factorisation property of the conformal Hilbert space, let us turn to its application within the truncated conformal space approach. With the notation of the previous subsection, we can express any local operator $\mathcal{O}(x)$ on the cylinder with left/right conformal weights $h_{\mathcal{O}}$ and $\bar{h}_{\mathcal{O}}$ as

$$\begin{aligned}\mathcal{O}(0) = \left(\frac{2\pi}{L}\right)^{h_{\mathcal{O}}+\bar{h}_{\mathcal{O}}} \bigoplus_{\substack{\Phi,N,\bar{N},\\ \Phi',N',\bar{N}'}} \Big[& \mathcal{C}_{\Phi'\Phi}\left(\mathcal{O}\right) \times \\ & \times \mathcal{B}^{\mathcal{O}}(\mathcal{R}(\Phi'),N',\mathcal{R}(\Phi),N) \otimes \bar{\mathcal{B}}^{\mathcal{O}}(\bar{\mathcal{R}}(\Phi'),\bar{N}',\bar{\mathcal{R}}(\Phi),\bar{N}) \Big] ,\end{aligned} \tag{6.10}$$

where $\mathcal{C}_{\Phi'\Phi}(\mathcal{O})$ are the operator product structure constants of the CFT. The only other ingredients are the matrix elements of operator $\mathcal{O}$ on the decomposed Hilbert space (6.7) $\mathcal{B}^{\mathcal{O}}(\mathcal{R}',N',\mathcal{R},N)$ and $\bar{\mathcal{B}}^{\mathcal{O}}(\bar{\mathcal{R}}',\bar{N}',\bar{\mathcal{R}},\bar{N})$. They are called chiral three-point matrices (a.k.a. chiral vertex operators), and they only depend on the representations of the chiral algebra involved in the particular block. Consequently, they can be exactly calculated exploiting the conformal Ward identities [170] which were first used to obtain TCSA matrix elements in Ref. [171]. (For a detailed calculation see Ref. [172], and also Appendix A of Ref. [168].)

The calculation of the operator product structure constants can be reduced to the problem of finding all elementary three-point couplings which relate the primary fields of the CFT to each other. These in turn can be found in the conformal bootstrap approach [170, 173], solving a set of consistency equations satisfied by conformal correlators.

As a net result, all quantities appearing in the Hamiltonian (6.1) can be expressed on the chirally factorised basis (6.7) in the knowledge of the 'conformal field theory data' consisting of the following ingredients:

- the central charge c of the CFT,
- the set of primary fields in the decomposition (6.3) of the CFT Hilbert space,
- the primary three-point couplings,
- and the matrix elements of the chiral three-point matrices

  $$\mathcal{B}^{\mathcal{O}}(\mathcal{R}',N',\mathcal{R},N)_{\alpha'\alpha} \quad \text{and} \quad \bar{\mathcal{B}}^{\mathcal{O}}(\mathcal{R}',\bar{N}',\mathcal{R},\bar{N})_{\bar{\alpha}'\bar{\alpha}} \tag{6.11}$$

  for the perturbing operator $\mathcal{O}=\mathcal{V}$.

The key advantage of the chirally factorised TCSA with respect to earlier realisations is a more economical representation of the operator matrix elements.

This is of major importance, as the main challenge posed to any truncated space approach is the exponential growth of the dimensionality D of the truncated Hilbert space with respect to the cutoff. Since the full space occupied by operator matrix elements grows as D^2, finite data storage places the most severe limitation on the accuracy of TCSA.

However, the chiral factorisation property (6.4) implies that the size of the CFT data, considered as a function of the cutoff, only grows with the square root of the size of the complete (nonchiral) operator matrices, i.e. it is effectively proportional to the dimension D of the truncated Hilbert space instead of D^2. Therefore, by employing chiral factorisation we significantly push the limit of the truncated space approach, even if eventually we are still faced with the same exponential growth. (We note that of the four ingredients listed above, only the matrix elements take up significant space in the memory, and they are the only ones that increase in size with raising the cutoff. For large cutoffs, where memory becomes an issue, the other three ingredients are practically negligible.)

6.2 Implementation

The idea of the chirally factorised TCSA is to set up the numerical algorithm exploiting (6.4), and use it to reduce the size of the CFT input data needed to set up the TCSA. In this setting, the problem is transferred to finding an efficient algorithm to handle the chirally factorised basis. In this section we discuss the solution to this problem.

6.2.1 The core physical quantities

The central object of physical applications is the Hamiltonian (6.1), defined by adding a relevant perturbation to the conformal field theory. The CFT Hamiltonian is given by

$$H_{\mathrm{CFT}} = \frac{2\pi}{L}\left(L_0 + \bar{L}_0 - \frac{c}{12}\right) , \tag{6.12}$$

and it is automatically diagonal in the basis specified by (6.5).

To express the matrix elements of the perturbation we introduce the notation for a general vector in the conformal Hilbert space (6.7)

$$\begin{aligned} |\Psi\rangle = \sum_{\Phi,N,\bar{N}} \sum_{\alpha=1}^{d_{\mathcal{R}(\Phi)}(N)} \sum_{\bar{\alpha}=1}^{d_{\bar{\mathcal{R}}(\Phi)}(\bar{N})} & K_\Psi(\Phi,N,\bar{N})_{\alpha\bar{\alpha}} \times \\ & \times |\mathcal{R}(\Phi),N,\alpha\rangle \otimes \left|\bar{\mathcal{R}}(\Phi),\bar{N},\bar{\alpha}\right\rangle , \end{aligned} \tag{6.13}$$

where α and $\bar{\alpha}$ are indexing the vectors in the degenerate chiral subspaces $V_{\mathcal{R}(\Phi)}(N)$ and $V_{\bar{\mathcal{R}}(\Phi)}(\bar{N})$, while $K_\Psi(\Phi,N,\bar{N})_{\alpha\bar{\alpha}}$ are complex vector coefficients represented as two-index tensors. Choosing an orthonormal basis within the degenerate subspaces we can express the inner product of two vectors as

$$\begin{aligned}\langle\Psi_1|\Psi_2\rangle = \sum_{\Phi,N,\bar{N}}\sum_{\alpha,\bar{\alpha}} K^*_{\Psi_1}(\Phi,N,\bar{N})_{\alpha\bar{\alpha}} K_{\Psi_2}(\Phi,N,\bar{N})_{\alpha\bar{\alpha}} = \\ = \sum_{\Phi,N,\bar{N}} \mathrm{Tr}\left[K_{\Psi_1}(\Phi,N,\bar{N})^\dagger K_{\Psi_2}(\Phi,N,\bar{N})\right]\end{aligned} \tag{6.14}$$

Now let us consider the action of the perturbing operator

$$H_{\text{pert}} = \int_0^L \mathrm{d}x\mathcal{V}(x) \tag{6.15}$$

on a state $|\Psi\rangle$ (6.13). The assumption of translational invariance means that the left and right conformal weights of the operator $\mathcal{V}$ coincide: $h_\mathcal{V} = \bar{h}_\mathcal{V}$. As a consequence, H_{pert} conserves the momentum P, leading to a selection rule within $|\Psi\rangle$. The momentum operator can be expressed as

$$P\left(|\Phi,N,\alpha\rangle \otimes \left|\Phi,\bar{N},\bar{\alpha}\right\rangle\right) = \frac{2\pi}{L}\left(s_\Phi + N - \bar{N}\right)\left(|\Phi,N,\alpha\rangle \otimes \left|\Phi,\bar{N},\bar{\alpha}\right\rangle\right)\,, \tag{6.16}$$

where $s_\Phi = h_\Phi - \bar{h}_\Phi$ is the conformal spin of the primary field Φ. For a state with momentum $2\pi s/L$, its components in the representation (6.13) satisfy the selection rule

$$K_\Psi(\Phi,N,\bar{N}) = 0 \quad \text{for} \quad s_\Phi + N - \bar{N} \neq s\,, \tag{6.17}$$

and taking momentum eigenstates $|\Psi_{1,2}\rangle$ with momentum eigenvalues given by

$$P\,|\Psi_{1,2}\rangle = \frac{2\pi}{L} s(\Psi_{1,2})\,|\Psi_{1,2}\rangle\,, \tag{6.18}$$

the spatial integral in Eq. (6.15) can be performed to give

$$\begin{aligned}&\langle\Psi_1|H_{\text{pert}}|\Psi_2\rangle = \\ &\left(\frac{2\pi}{L}\right)^{2h_\mathcal{V}} \sum_{\Phi_1,\Phi_2} \mathcal{C}_{\Phi_1\Phi_2}(\mathcal{V}) \sum_{N_1,\bar{N}_1}\sum_{N_2,\bar{N}_2} \Bigg\{ L\delta\left(s(\Psi_1),s(\Psi_2)\right) \times \\ &\times \mathrm{Tr}\Bigg[K_{\Psi_1}(\Phi_1,N_1,\bar{N}_1)^\dagger \mathcal{B}^\mathcal{V}(\mathcal{R}(\Phi_1),N_1,\mathcal{R}(\Phi_2),N_2) \\ &\qquad K_{\Psi_2}(\Phi_2,N_2,\bar{N}_2)\bar{\mathcal{B}}^\mathcal{V}(\bar{\mathcal{R}}(\Phi_1),\bar{N}_1,\bar{\mathcal{R}}(\Phi_2),\bar{N}_2)^T\Bigg]\Bigg\}\,,\end{aligned} \tag{6.19}$$

where $\delta(a,b)$ is the Kronecker delta.

As a result, the action of the perturbing operator on a momentum eigenstate $|\Psi\rangle$

$$|\Psi'\rangle = H_{\text{pert}}\,|\Psi\rangle \tag{6.20}$$

gives a state $|\Psi'\rangle$ with the same momentum, and can be written in terms of the vector components as

$$\begin{aligned}
&K_{\Psi'}(\Phi',N',\bar{N}')_{\alpha'\bar{\alpha}'} = \\
&\left(\frac{2\pi}{L}\right)^{2h_{\mathcal{V}}} \sum_{\Phi,N,\bar{N}} L\delta(s',s) \sum_{\substack{\alpha,\bar{\alpha} \\ \alpha',\bar{\alpha}'}} \mathcal{C}_{\Phi'\Phi}(\mathcal{O})\mathcal{B}^{\mathcal{V}}(\mathcal{R}(\Phi'),N',\mathcal{R}(\Phi),N)_{\alpha',\alpha}\times \\
&\times \bar{\mathcal{B}}^{\mathcal{V}}(\bar{\mathcal{R}}(\Phi'),\bar{N}',\bar{\mathcal{R}}(\Phi),\bar{N})_{\bar{\alpha}',\bar{\alpha}} K_{\Psi}(\Phi,N,\bar{N})_{\alpha\bar{\alpha}}\,, \\
&\text{where} \quad s = s_{\Phi} + N - \bar{N} \quad \text{and} \quad s' = s_{\Phi'} + N' - \bar{N}'\,, \qquad (6.21)
\end{aligned}$$

or alternatively in a compact matrix notation as

$$\begin{aligned}
&K_{\Psi'}(\Phi',N',\bar{N}') = \\
&\left(\frac{2\pi}{L}\right)^{2h_{\mathcal{V}}} \sum_{\Phi,N,\bar{N}} L\delta(s',s)\, \mathcal{C}_{\Phi'\Phi}(\mathcal{O})\mathcal{B}^{\mathcal{V}}(\mathcal{R}(\Phi'),N',\mathcal{R}(\Phi),N)\times \\
&\qquad\qquad \times K_{\Psi}(\Phi,N,\bar{N})\bar{\mathcal{B}}^{\mathcal{V}}(\bar{\mathcal{R}}(\Phi'),\bar{N}',\bar{\mathcal{R}}(\Phi),\bar{N})^{T}\,. \qquad (6.22)
\end{aligned}$$

The above expressions are only slightly modified if another translationally invariant quantity is considered in place of H_{pert}. Let us remark that due to the conservation of momentum, for any such quantity the Hilbert space can be limited to states with a fixed value s, corresponding to a subspace with a given total momentum $2\pi s/L$. The vacuum state is in the $s = 0$ sector, hence considering the zero-momentum sector is sufficient in numerous cases, covering every application of TCSA presented in this thesis. Nevertheless, the generalisation to quantities breaking translational invariance is straightforward, although it involves additional momentum sectors and therefore a much larger Hilbert space.

6.2.2 Describing the Hilbert space

The previous subsection showed how to express the Hamiltonian (6.1), and, more generally, any translationally invariant physical quantity using the chiral ingredients introduced in Sec. 6.1. The expressions suggest that the algorithmic realisation of the CFTCSA is essentially equivalent to inventing a clever method to perform the multiple summations over the chirally factorised basis. Put in other words, we have to give an adequate and computationally useful description of the factorised Hilbert space (6.7).

Here we introduce the descriptor structures which fulfil this task on the one hand, and are easily adaptable to various models and physical problems on the other. These descriptors are matrices that encode the decomposition of $\mathcal{H}_{\text{CFT}}$ to chiral subspaces and keep track of the relevant properties of these subspaces. To illustrate their use, we will often reference the Ising field theory, which is a particularly simple example of perturbed CFTs.

Let us begin with the descriptor which performs the latter task, the so-called *Chiral Descriptor*. The Chiral Descriptor summarises the basic information about the chiral subspaces $V_{\mathcal{R}}(N)$. Since for every primary field these spaces are specified by giving the representations $\mathcal{R}_\Phi$ and $\bar{\mathcal{R}}_\Phi$, the independent information needed is to list at each level N the subspaces $V_{\mathcal{R}}(N)$ of all the chiral representations $\mathcal{R}$. These can be ordered by increasing chiral conformal weight (L_0 eigenvalue) $h_{\mathcal{R}} + N$, and the multiindex $(\mathcal{R}, N)$ replaced by their position n in this list (in case of subspaces of equal weight, their order can be chosen in an arbitrary way); however, depending on the problem, other orderings may be more convenient. The CFT data constructed for the purpose of the TCSA computations must contain the basis of the chiral level subspaces to some upper limit $h(\mathcal{R}, N) < h_{\max}$ which is chosen sufficiently high to contain all states that occur in the numerical computations. The Chiral Descriptor is then a two-column matrix listing the conformal weights h_n and dimensions d_n of the chiral level subspaces $V_{\mathcal{R}}(N)$:

$$D_{\mathrm{Ch}} = \begin{pmatrix} h_1 & d_1 \\ h_2 & d_2 \\ h_3 & d_3 \\ \vdots & \vdots \end{pmatrix} , \tag{6.23}$$

with $h_1 \leq h_2 \leq h_3 \leq \dots$.

The primary fields Φ appearing in the decomposition (6.3) can be enumerated in some particular order as

$$\Phi_M \, , \; M = 1, \dots l_{\mathrm{Pr}} \, . \tag{6.24}$$

For CFTs with a finite number of primary fields (so-called rational CFTs), l_{Pr} is a fixed number, but for those with infinitely many primaries (such as the free massless boson) this list must be terminated so that every primary field Φ appearing as a subspace $\mathcal{W}_\Phi$ in the truncated Hilbert space is included. The Ising field theory provides an example of a rational CFT, with three primary fields: the identity $\Phi_1 = \mathbb{I}$, the magnetisation $\Phi_2 = \sigma$ and the energy operator $\Phi_3 = \epsilon$, with conformal dimensions $h_1 = \bar{h}_1 = 0$, $h_2 = \bar{h}_2 = 1/16$ and $h_3 = \bar{h}_3 = 1/2$.

As the Chiral Descriptor contains all information about the chiral algebra, the additional information required to characterise the factorised Hilbert space is how to sew together the primary subspaces from each level. This information is encoded by the *Hilbert Space Descriptor*. The Hilbert Space Descriptor is a three-column matrix with the indices of the left- and right-handed subspaces in its first and second columns, respectively, while the third column contains the index of the primary field corresponding to the subspace. The indices refer to the rows of the Chiral Descriptor and therefore specify the conformal energy and the dimensionality of the subspaces in the product space.

As an illustration, let us consider the zero-momentum subspace of the Hilbert space of the Ising field theory. The first four rows correspond to $V_{\mathcal{R}(\mathbb{I})}(0) \otimes V_{\mathcal{R}(\mathbb{I})}(0)$,

$V_{\mathcal{R}(\sigma)}(0) \otimes V_{\mathcal{R}(\sigma)}(0)$, $V_{\mathcal{R}(\epsilon)}(0) \otimes V_{\mathcal{R}(\epsilon)}(0)$ and $V_{\mathcal{R}(\sigma)}(1) \otimes V_{\mathcal{R}(\sigma)}(1)$, and the Hilbert Space Descriptor takes the form

$$D_{\mathrm{H}} = \begin{pmatrix} 1 & 1 & 1 \\ 2 & 2 & 2 \\ 3 & 3 & 3 \\ 4 & 4 & 2 \\ \vdots & \vdots & \vdots \end{pmatrix} , \tag{6.25}$$

where the first and second column entries refer to the corresponding Chiral Descriptor, the first four lines of which describe the chiral level subspaces $V_{\mathcal{R}(\mathbb{I})}(0)$, $V_{\mathcal{R}(\sigma)}(0)$, $V_{\mathcal{R}(\epsilon)}(0)$ and $V_{\mathcal{R}(\sigma)}(1)$:

$$D_{\mathrm{Ch}} = \begin{pmatrix} 0 & 1 \\ 1/16 & 1 \\ 1/2 & 1 \\ 17/16 & 1 \\ \vdots & \vdots \end{pmatrix} . \tag{6.26}$$

The Hilbert Space Descriptor thus contains all relevant properties of the subspaces its rows correspond to. If the mth row of D_{H} has j, k as its first two elements, then the corresponding subspace has $D_{\mathrm{Ch}}(j, 1) + D_{\mathrm{Ch}}(k, 1)$ total conformal weight, $D_{\mathrm{Ch}}(j, 1) - D_{\mathrm{Ch}}(k, 1)$ conformal spin, and $D_{\mathrm{Ch}}(j, 2) \times D_{\mathrm{Ch}}(k, 2)$ dimension. As the TCSA introduces an upper limit on the total conformal weight, the number of included subspaces are limited to a finite value l_{H}.

The Hilbert Space Descriptor provides the recipe to express the general state vectors (6.13) as

$$|\Psi\rangle = \sum_{m=1}^{l_{\mathrm{H}}} \sum_{\alpha,\bar{\alpha}} K^{\Psi}(m)_{\alpha\bar{\alpha}} \, |m, \alpha, \bar{\alpha}\rangle \ , \tag{6.27}$$

which are most conveniently handled as lists of matrices $K(m)$, $m = 1, \ldots, l_{\mathrm{H}}$ with sizes dictated by D_{H} and D_{Ch}. From (6.14), the inner product of two vectors $|\Psi_1\rangle$ and $|\Psi_2\rangle$ is given in by

$$\langle \Psi_1 | \Psi_2 \rangle = \sum_{m=1}^{l_{\mathrm{H}}} \mathrm{Tr} \left[K^{\Psi_1}(m)^{\dagger} K^{\Psi_2}(m) \right] . \tag{6.28}$$

6.2.3 Describing the action of local operators

The above description of the Hilbert space outlines the method to evaluate the action of local operators, i.e. to perform the summations over the basis states as in Eq. (6.19): one has to simply thread through the Hilbert Space Descriptor which selects the appropriate chiral subspaces by referencing the Chiral Descriptor. It is convenient to exploit this structure completely via the definition of another descriptor type which encodes all the information about a given local operator in a similar manner.

This motivates the introduction of the *Operator Descriptors*. We recall that the ingredients of the CFT data relevant to the action of scaling operators are the three-point couplings between the operator and the primary fields $C_{\Phi\Phi'}(\mathcal{O})$, and the chiral three-point matrices $\mathcal{B}^{\mathcal{O}}(\mathcal{R}, N, \mathcal{R}', N')$. The latter we can abbreviate using $n \equiv (\mathcal{R}, N)$ (recall that n is the row index of the Chiral Descriptor) as $\mathcal{B}^{\mathcal{O}}(n, n')$. Consequently, all matrix elements of an operator $\mathcal{O}$ on the truncated Hilbert space can be arranged in an *Operator List*, which is a list of matrices $\underset{\rightarrow}{\mathcal{B}}$ containing $\mathcal{B}^{\mathcal{O}}(n, n')$ and $\bar{\mathcal{B}}^{\mathcal{O}}(n, n')$.

The Operator Descriptors then merely record the following three pieces of information about the matrices $\mathcal{B}^{\mathcal{O}}(n, n')$: their chiral indices n and n', and their position k in the Operator List. It is convenient to store these three numbers in a matrix format: in a matrix element with value k, whose corresponding row and column indices are related to the chiral indices n and n'. More precisely, the row and column indices refer to the row indices of the Hilbert Space Descriptor, and there are two separate matrices $D^{\mathcal{O},L}_{\mathrm{Op}}$ and $D^{\mathcal{O},R}_{\mathrm{Op}}$ for the left- and right-handed components of the operator action, respectively.

Again, let us illustrate these *Operator Descriptor Matrices* with an example from the Ising field theory. An excerpt from a left descriptor of the σ field is

$$D^{\sigma,L}_{\mathrm{Op}} = \begin{pmatrix} 0 & 1 & 0 & 2 & \cdots \\ 0 & 0 & 9 & 0 & \cdots \\ 0 & 16 & 0 & 0 & \cdots \\ 20 & 0 & 21 & 0 & \cdots \\ \vdots & & \vdots & & \ddots \end{pmatrix} . \tag{6.29}$$

The rows and columns refer to the row indices of the Hilbert Space Descriptor (6.25) that specifies the n and n' chiral indices of $\mathcal{B}^{\sigma}(n, n')$ by referencing the Chiral Descriptor. The values of the matrix elements are position indices in the Operator List: e.g. $\mathcal{B}^{\sigma}(4, 1)$ is the 20th element of $\underset{\rightarrow}{\mathcal{B}}$. We define the zero-index element of this list $\underset{\rightarrow}{\mathcal{B}}(0) = 0$ by convention. Note that the specific numbers are dependent on the truncated Hilbert space: the Operator List and all the descriptors have to be prepared consistently. In practice, it is convenient to create all of them at once for a sufficiently large cutoff, and more stringent truncation can be applied by muting the elements of the descriptors which would refer to subspaces above the smaller cutoff.

Similarly, the matrix elements in the right-handed descriptor $D^{\mathcal{O},R}_{\mathrm{Op}}(n, n')$ specify the position of the right chiral three-point matrices $\bar{\mathcal{B}}^{\mathcal{O}}(\bar{\mathcal{R}}, \bar{N}, \bar{\mathcal{R}}', \bar{N}')$ in the Operator List $\underset{\rightarrow}{\mathcal{B}}$. Note that the left/right blocks are identical for an operator if $\mathcal{R}(\mathcal{O}) = \bar{\mathcal{R}}(\mathcal{O})$, i.e. if both of its chiral parts transform in the same representation. In such a case the two descriptors are identical and can be given by the same matrix: $D_{\mathrm{Op}}^{\mathcal{O},L} = D_{\mathrm{Op}}^{\mathcal{O},R} = D_{\mathrm{Op}}^{\mathcal{O}}$. The dimensions of the Operator Descriptor Matrices are $l_{\mathrm{H}} \times l_{\mathrm{H}}$.

Finally, to further facilitate implementation, we encode the definition of the operator algebra structure constant $\mathcal{C}_{\Phi\Phi'}(\mathcal{O})$ as follows:

$$\mathcal{C}^{\mathcal{O}}(M, M') = \mathcal{C}_{\Phi\Phi'}(\mathcal{O})\,. \tag{6.30}$$

Here Φ and Φ' are primary fields appearing in the decomposition (6.3) of the conformal Hilbert space, and $\mathcal{C}^{\mathcal{O}}(M, M')$ is a rewriting of $\mathcal{C}_{\Phi\Phi'}(\mathcal{O})$ in which the primary fields are indexed according to (6.24) by integers M and $M' > 0$, in accordance with the 3rd row of the Hilbert Space Descriptor. Working in this convention, the structure constants $\mathcal{C}^{\mathcal{O}}(M, M')$ can be stored in a matrix form, which we call the *Structure Constant Matrix*. The non-zero elements at position (M, M') are the actual structure constants connecting the conformal family of the operator $\mathcal{O}$ under consideration and the conformal families associated with Mth and M'th primaries, whose left and right chiral parts, similarly to $\mathcal{O}$ itself, can be different in a generic CFT. Given these considerations, the dimension of this matrix is $l_{\mathrm{Pr}} \times l_{\mathrm{Pr}}$, where l_{Pr} denotes the number of primary fields in the theory.[3] We remark that the case of several operators can be handled on the same footing, providing the above information describing each operator $\mathcal{O}$ analogously.

With these notations, the action (6.22) of an integrated spin-0 field

$$|\Psi'\rangle = \left(\int_0^L \mathrm{d}x \mathcal{V}(x)\right) |\Psi\rangle \tag{6.31}$$

can be computed as

$$\begin{aligned} K_{\Psi'}(m') = \left(\frac{2\pi}{L}\right)^{2h_{\mathcal{V}}} \sum_{m=1}^{l_{\mathrm{H}}} L\delta_{s',s}\, \mathcal{C}^{\mathcal{V}}(D_{\mathrm{H}}(m',3), D_{\mathrm{H}}(m,3)) \times& \\ \times \Bigg[\underset{\rightarrow}{\mathcal{B}} \left(D_{\mathrm{Op}}^{\mathcal{V},L}(m',m)\right) K_{\Psi}(m) \cdot& \\ \cdot \underset{\rightarrow}{\mathcal{B}} \left(D_{\mathrm{Op}}^{\mathcal{V},R}(m',m)\right)^T \Bigg]&\,. \end{aligned} \tag{6.32}$$

6.2.4 An example application: the E_8 spectrum

Finally, let us present an application of the CFTCSA to a specific physical problem. We note that in complete analogy to the earlier versions of TCSA, it can be used in modelling both in- and out-of-equilibrium dynamics of quantum field theories. The next chapter is devoted to the detailed discussion of a nonequilibrium setting, and here we briefly overview a simple equilibrium problem, the spectrum of the E_8 field theory in finite volume. As there are available analytic

Volume $m_1 L$	TBA	Raw CFTCSA	Extrapolated CFTCSA
0.075	-3.490664764718	-3.490664764706	-3.490664764727
0.125	-2.094420612223	-2.094420612172	-2.094420612249
0.475	-0.5521585879901	-0.5521585859634	-0.5521585879800
0.6	-0.4382356381999	-0.4382356343468	-0.4382356381806
0.8	-0.3314363841477	-0.3314363756476	-0.3314363841051
1.2	-0.2307543455439	-0.2307543196153	-0.2307543454197
1.6	-0.1904900446243	-0.1904899873971	-0.1904900443767
2	-0.1777603739145	-0.1777602681131	-0.1777603735367
4	-0.2512909490675	-0.2512902327811	-0.2512909507354
7	-0.4322470994378	-0.4322437272677	-0.4322471438901
9	-0.5555744641670	-0.5555676826358	-0.5555746099325
12	-0.7407438075920	-0.7407286652376	-0.7407443409462

Table 6.1: Ground state energy $E_0(R)$ for various volume parameters. Data in the second column is calculated from Ref. [174]. The third column is obtained by numerical diagonalisation from CFTCSA using 207,809 vectors, while the last column is improved by extrapolating the cut-off dependence.

results for the energies. the spectral problem benchmarks the accuracy of the numerical method.

As is customary, we measure the energy levels in units of the mass gap m_1, while the volume is parameterised by the scaling variable $r = m_1 R$. The ground state energy in finite volume can be expressed as

$$E_0(R) = m_1^2 \mathcal{E}_{\mathrm{E}_8} R - \frac{\pi \tilde{c}(r)}{6R}\,, \tag{6.33}$$

where $\tilde{c}(r)$ is the so-called vacuum scaling function a.k.a. effective central charge, which behaves as e^{-r} for large volume. The coefficient $\mathcal{E}_{\mathrm{E}_8}$ is the bulk energy constant which is exactly known [38]

$$\mathcal{E}_{\mathrm{E}_8} = -\frac{\sin \pi/30}{16 \sin \pi/3 \sin \pi/5 \sin \pi/15}\,. \tag{6.34}$$

The $\tilde{c}(r)$ effective central charge was calculated by Klassen and Melzer [174] using the thermodynamic Bethe Ansatz (TBA) [175], which we use to benchmark our numerical results as shown in Table 6.1. We find a remarkable 10-digit accuracy below $r = 1$, and a still impressive 5-6 digit agreement up until around $r = 10$.

To illustrate the behaviour of low-lying levels, we present results for the energy level $E_1(R)$ of the first excited state E_8 spectrum. This level correspond to the lightest particle with mass m_1, and so $E_1(R) - E_0(R) \to m_1$ as $R \to \infty$, with finite size corrections which were computed up to leading order in Ref. [176] based on the seminal work [177] by Lüscher. We compare the predictions for the finite size corrections (in units $m_1 = 1$) to the CFTCSA results in Table 6.2.

---

[3] On the number of primaries l_{Pr} see the discussion after Eq. (6.24).

Volume m_1R	Δm_1, predicted	Δm_1, raw CFTCSA	Δm_1, extrapolated
12.4613	-2.4860E-03	-2.4281E-03	-2.4274E-03
13.3811	-1.0850E-03	-1.0736E-03	-1.0729E-03
14.2486	-5.0140E-04	-4.9909E-04	-4.9846E-04
15.0722	-2.4220E-04	-2.4194E-04	-2.4139E-04
15.8582	-1.2130E-04	-1.2154E-04	-1.2111E-04
16.6114	-6.2680E-05	-6.2983E-05	-6.2714E-05

Table 6.2: Finite-size corrections to the lowest-lying particle's energy in the E_8 spectrum. KM stands for the analytical results of Klassen and Melzer [176].

6.3 Summary

In this chapter we presented a recent development of the truncated conformal space approach, which utilises the chiral factorisation of the conformal basis. This development allows for a more economical storage of matrix elements on the truncated basis, and consequently for a higher accuracy to be attained by the approach. Besides the structure of the algorithm, we also discussed a specific application of the method and showed that it precisely calculates the finite size corrections to the E_8 energy spectrum.

The results with a range of additional physical applications are available in our preprint [168]. The detailed presentation of the algorithm and the several explicit example codes attached to the paper are aimed at making TCSA a valuable and accessible tool for a wider community of researchers.

Chapter 7

Kibble–Zurek mechanism in the Ising field theory

After taking a detour in numerical modelling in the previous chapter, let us return to the non-equilibrium dynamics of quantum field theories. We already considered a paradigmatic example: quantum quenches, which entail an abrupt change in the parameters of the model. In this chapter we discuss a different protocol, where the parameters of the system are tuned continuously during a finite time period, i.e. the couplings are subject to a ramp.

The ramp protocol is most widely studied in the context of the Kibble–Zurek mechanism (KZM), which paints the picture of a physical system slowly driven through a second-order phase transition towards an ordered phase. As the critical point is approached, the physical scales of the system diverge and adiabatic behaviour inevitably breaks down. Consequently, on the other side of the phase transition the system is in an excited state: ordered domains appear, which are separated by domain walls (defects) [178, 179]. The resulting state carries the imprints of crossing the critical point, as the defect density scales universally with the speed of the ramp, a.k.a. the quench rate [180, 181].

Astonishingly, this simple picture captures universality in an extended set of systems, and is applicable both to classical and quantum phase transitions [9, 74, 182]. The success of this description continues to stimulate research aimed at exploring its limitations and understanding its details. Below we carry out a thorough investigation of the Kibble–Zurek mechanism based on our work in Ref. [167]. First we expand on the simple physical picture of the previous paragraph, and give a brief overview of the vast field of Kibble–Zurek physics, offering various arguments for the universal scaling. Then we explore the various aspects of the KZM within the Ising field theory, focusing on a wide set of quantities from eigenstate dynamics through dynamical scaling to universal work statistics.

7.1 Model and methods

7.1.1 The scenario behind the Kibble–Zurek mechanism

In order to refine the above description of the Kibble–Zurek mechanism, we ought to take a more quantitative approach. In accordance with the topic of this thesis, we focus on quantum critical points (QCPs), where the ramps correspond to tuning the coupling constant λ of some local operator with scaling dimension Δ. We define the coupling constant such that $\lambda = 0$ corresponds to the critical point. To maintain generality, we consider ramps that traverse the critical point with a power-law dependence, i.e. near the QCP

$$\lambda = \lambda_0 \left| \frac{t}{\tau_\mathrm{Q}} \right|^a \mathrm{sgn}(t) \,, \tag{7.1}$$

where τ_Q is the quench rate, parameterising the speed at which the critical point is crossed at $t = 0$.

Near the phase transition, the physical scales of the system grow indefinitely, which entails the divergence of the relaxation time ξ_t, a phenomenon called critical slowing down:

$$\xi_t = C \lambda^{-\nu z} \,, \tag{7.2}$$

where $\nu = (2 - \Delta)^{-1}$ is the critical exponent connecting the diverging correlation length to the coupling λ, and z is the dynamical critical exponent relating the time and length scales to each other, in relativistic models $z = 1$.

If the dynamics were completely adiabatic, the evolution of the relaxation time $\xi_t(t)$ along the ramp would be simply given by substituting (7.1) for the coupling λ. However, due to the critical slowing down, the system is unable to follow an adiabatic path and defects are formed. To estimate the effect of non-adiabatic behaviour, let us introduce the so-called Kibble–Zurek time τ_KZ when the reaction of the system becomes too slow compared to the change in λ. The KZ time can be inferred from comparing the change of ξ_t within a relaxation time to the relaxation time itself: $\dot{\xi}_t \xi_t \sim \xi_t$. When $\dot{\xi}_t(t) \ll 1$, the system can adjust to the change, but it falls behind in the opposite limit. Defining τ_KZ to denote the moment when equality holds gives

$$\tau_\mathrm{KZ} \equiv (a\nu z)^{\frac{1}{a\nu z+1}} \left(\frac{\tau_\mathrm{Q}}{\lambda_0^{1/a}} \right)^{\frac{a\nu z}{a\nu z+1}} . \tag{7.3}$$

More precisely, this expression for the Kibble–Zurek time follows from setting the constant C in the near-critical scaling of the relaxation time (7.2) to 1. This argumentation reveals that strictly speaking τ_KZ is defined only as a scaling relation, i.e. only its power-law dependence on τ_Q is specified. This is not an issue, as its principal use is to express the universal scaling of various quantities.

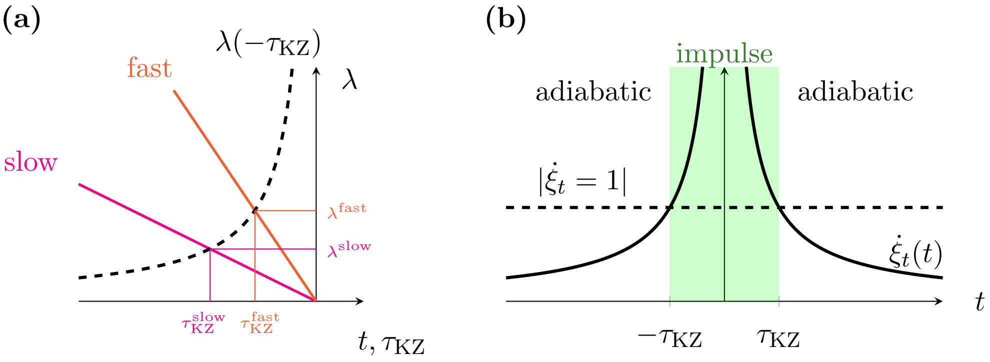

Figure 7.1: The adiabatic-impulse-adiabatic scenario. (a) The impulse regime in terms of the time t and coupling parameter λ. Continuous lines depict the $\lambda(t)$ function for slow/fast linear ramps, while the dashed line denotes the value of λ at the beginning of the impulse regime $-\tau_{\rm KZ}$. (b) Illustration of the region boundaries. Continuous lines depict the time-dependence of the change in the relaxation time $\dot{\xi}_t$, while the green region signals non-adiabatic behaviour, which appears when $\dot{\xi}_t \sim 1$ (dashed line). After crossing the critical point, the system returns to the adiabatic course.

It is worth noting that at the Kibble–Zurek time $\tau_{\rm KZ}$, the correlation time scales with the quench rate $\tau_{\rm Q}$ as $\tau_{\rm KZ}$ itself:

$$\xi_t(-\tau_{\rm KZ}) \propto \left(\frac{\tau_{\rm Q}}{\lambda_0^{1/a}}\right)^{\frac{a\nu z}{a\nu z+1}} \propto \tau_{\rm KZ}\,. \tag{7.4}$$

The above considerations outline a more quantitative (but still hazy) description of the physical scenario behind the KZM. That is, the system is on a completely adiabatic course until $t = -\tau_{\rm KZ}$, then it enters the non-adiabatic or impulse regime, where it remains up until $t = \tau_{\rm KZ}$, i.e. until after crossing the critical point. From then onward, the time evolution is once again adiabatic, but the system is not in its ground state anymore due to the intermediary period.

A depiction of this process is displayed in Fig. 7.1. Note that although the time spent in the non-adiabatic regime is longer for slower quenches (cf. Eq. (7.3)), the distance from the critical point in terms of the coupling parameter λ upon entering the impulse regime decreases as $\tau_{\rm Q}$ increases. In this sense, slower ramps better approach the critical point, even though the duration of the non-adiabatic period grows indefinitely.

The excited state after the impulse period is characterised by a correlation length $\xi_{\rm KZ} = \xi(-\tau_{\rm KZ})$. In the case of the introductory example, $\xi_{\rm KZ}$ is the typical linear size of the ordered domains, so the density of excitations corresponding to defects (domain walls) in spatial dimension d is

$$n_{\text{ex}} \propto \xi_{\text{KZ}}^{-d} \propto \left(\frac{\tau_{\text{Q}}}{\lambda_0^{1/a}}\right)^{-\frac{a\nu d}{a\nu z+1}} . \tag{7.5}$$

We remark that n_{ex} can be defined in more general settings (i.e. not only towards the ordered phase), rendering the KZM a general description of ramps through a critical point.

Eq. (7.5) is the prime example of the so-called Kibble–Zurek scaling. The KZ scaling relies on the assumption is that the only relevant length (time) scale in a system ramped through the critical point is ξ_{KZ} (τ_{KZ}). The initial rationale to underpin this assumption was dubbed the “freeze-out scenario” [180]. This scenario depicts the state in the non-adiabatic interval of time evolution $t \in [-\tau_{\text{KZ}}, \tau_{\text{KZ}}]$ as remaining literally frozen. This entails the freezing of the typical scales and creates a link between n_{ex} measured after the non-adiabatic time evolution and the length scale ξ_{KZ} characterising the state before that.

The freeze-out picture can be refined by taking into account the evolution of the system and the correlation length in the non-adiabatic regime [183–186]. While the inspection of the dynamics reveals that ξ_{KZ} is still the only relevant length scale—so the scaling laws are not altered—it also introduces the KZ scaling into the impulse regime. More precisely, utilising that in the non-adiabatic time window the only relevant time and length scales are τ_{KZ} and ξ_{KZ} for a slow enough ramp, time-dependent correlation functions can be expressed in terms of scaling functions of the rescaled variables t/τ_{KZ} and x/ξ_{KZ}. For example, one- and two-point functions of an operator $\mathcal{O}$ with scaling dimension Δ_O take the form in the impulse regime $t \in [-\tau_{\text{KZ}}, \tau_{\text{KZ}}]$

$$\begin{aligned}\langle \mathcal{O}(x,t)\rangle =& \xi_{\text{KZ}}^{-\Delta_{\mathcal{O}}} F_{\mathcal{O}}(t/\tau_{\text{KZ}})\,,\\ \langle \mathcal{O}(x,t)\mathcal{O}(0,t')\rangle =& \xi_{\text{KZ}}^{-2\Delta_{\mathcal{O}}} G_{\mathcal{O}}\left(\frac{t-t'}{\tau_{\text{KZ}}}, \frac{x}{\xi_{\text{KZ}}}\right)\,,\end{aligned} \tag{7.6}$$

where F and G are scaling functions depending on the operator $\mathcal{O}$ and we assumed translational invariance. Note that for one-point functions the scaling holds in the precedent adiabatic regime $t < -\tau_{\text{KZ}}$ as well, since there the expectation value depends only on the distance from the critical point, which is the function of the dimensionless time t/τ_Q:

$$\langle \mathcal{O}(x,t)\rangle \propto \xi(t)^{-\Delta_{\mathcal{O}}} \propto \left(\frac{t}{\tau_{\text{Q}}}\right)^{a\nu\Delta_{\mathcal{O}}} \propto \left(\frac{t}{\tau_{\text{KZ}}}\right)^{a\nu\Delta_{\mathcal{O}}} \tau_{\text{KZ}}^{-\Delta_{\mathcal{O}}/z}\,, \tag{7.7}$$

where in the last step we used the relation (7.3).

The above arguments seem overly general at first glance. Is it possible that they are an accurate depiction of non-equilibrium quantum dynamics near critical points? A reassuring answer to this question is found in more sophisticated derivations in concrete cases. The first quantum phase transition, where analytic calculations confirmed the scaling relations is that of the free fermionic Ising chain, where the dynamics of low-energy modes can be mapped to the famous Landau–Zener transition problem [186–189]. Contemporaneously, the same problem was treated by a perturbative approach, yielding identical results [190]. This approach, by using adiabatic perturbation theory, predicts the same scaling as the arguments of Kibble–Zurek mechanism in several models besides the Ising chain [190–193]. This formalism is useful to apply the generic scaling arguments outside the non-adiabatic regime for quantities that are beyond the scope of the initial formulation of KZM [194]. Finally, efficient numerical modelling techniques of lattice models found the KZ scaling beyond the applicability of analytic techniques [195–198].

The works cited in the previous paragraph cover only a small portion of the vast literature focusing on the quantum Kibble–Zurek mechanism since the first results came to light less than two decades ago. At the forefront of this “KZ revolution” were the quantum lattice models, while field theories received less attention. Notable exceptions are Refs. [185, 199–201] and applications of the adiabatic perturbation theory approach to the sine–Gordon model [191, 192, 202]. The KZM in relation to field theory also appeared in the context of holography [203–207]. Still, it is desirable to further extend the cases where KZ scaling is demonstrated to genuinely interacting field theories. For this reason, we study different aspects of the quantum Kibble–Zurek mechanism in the paradigmatic Ising field theory, which is a simple but nontrivial field theory.

7.1.2 Ramps in the Ising field theory

The IFT offers an ideal choice in light of the approaches to the quantum KZM presented in the previous subsection (exact analytical calculations, adiabatic perturbation theory and numerical methods), as it admits all three of them in its various settings. Firstly, it includes a free fermionic field theory, where exact results can be obtained. Secondly, it has two integrable directions (the second of which corresponds to a strongly interacting field theory), where the energy spectrum is known and a perturbative approach can be developed. Finally, as already thoroughly demonstrated in this thesis, the non-equilibrium dynamics can be modelled by a very efficient numerical method, the TCSA.

To formulate the specific non-equilibrium setting that we use to study the KZM, let us recall the expression of the IFT Hamiltonian:

$$H_{\mathrm{IFT}} = H_{\mathrm{CFT},c=1/2} + \frac{M}{2\pi}\int_0^L \epsilon(x)\mathrm{d}x + h\int_0^L \sigma(x)\mathrm{d}x\,. \tag{7.8}$$

As illustrated in Fig. 7.2, we perform ramps along the two integrable lines of the model, equivalent to setting one of the two couplings to zero. For $h = 0$, called the free fermion line, the Hamiltonian describes the dynamics of a free Majorana

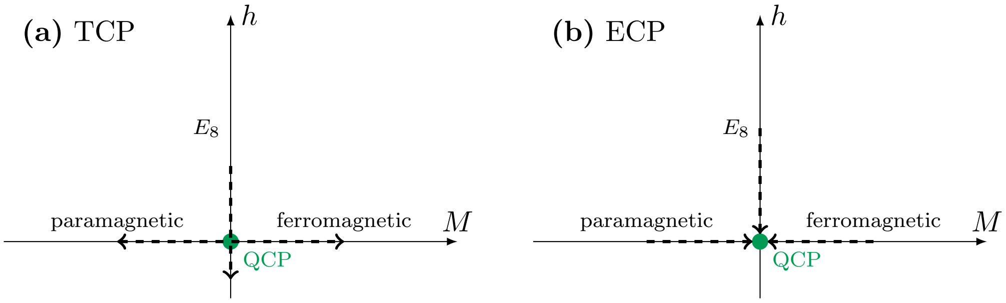

Figure 7.2: The two types of ramp protocols considered in this chapter, denoted by dashed arrows in the parameter space of the Ising model. On the free fermion line both directions were explored. Trans-critical protocols (TCP) traverse the critical point, while end-critical protocols (ECP) end in the QCP, and give rise to a different scaling.

fermionic field with mass $|M|$. The QCP at $M = 0$ separates the ferromagnetic phase $M > 0$ from the paramagnetic phase $M < 0$. The coupling is proportional to the mass gap and since the correlation length is the inverse of the gap, $\nu = 1$.

The other integrable direction, corresponding to $M = 0$ is the E_8 integrable line. The correlation length critical exponent is different in this direction, we have $\nu = 8/15$. Consequently, the predictions of the KZM can be tested independently in the two directions as the scaling laws depend on ν.

To perform an exhaustive investigation of the Kibble–Zurek physics in the Ising field theory, we follow Ref. [185] and introduce two different types of ramp protocols, indicated by dashed arrows in the two panels of Fig. 7.2. We distinguish between the protocols based on the initial and final values of the tuned coupling parameter λ. Protocols with λ_i and λ_f corresponding to different phases of the model (ramp crossing the critical point) are instances of a trans-critical protocol (TCP), while ramps with $\lambda_\mathrm{f} = 0$ (ramp ending at the critical point) realise the end-critical protocol (ECP). Certain observables exhibit markedly different behaviour depending on the protocol [194], hence the concurrent exploration of the two settings is a profound probe of the Kibble–Zurek scaling.

We focus our attention on linear ramps, where one of the couplings is varied such that the system reaches or crosses the critical point at a constant rate,

$$\lambda(t) = -\lambda_0 \frac{t}{\tau_\mathrm{Q}}\,, \tag{7.9}$$

where λ stands for M or h and the other coupling is set to zero. τ_Q is the duration of the ramp that takes place in the time interval $t \in [-\tau_\mathrm{Q}/2, \tau_\mathrm{Q}/2]$ for a TCP ramp and $t \in [-\tau_\mathrm{Q}, 0]$ for an ECP ramp.

Ramps along the free fermion line ($h = 0$) have been studied extensively, especially in the spin chain. The time evolution of the free fermion modes with different momentum magnitudes decouple and only modes of opposite momenta

$\{k, -k\}$ are coupled by the evolution equation. One can make progress either by invoking the Landau–Zener description of transitions between energy levels or by numerically solving the set of two-variable differential equations. Even analytical solutions are known for various ramp profiles [182, 201]. These solutions are easily generalised to the continuum field theory, providing us with an analytical tool to examine the KZ scaling and offering a benchmark for our numerical method. The detailed calculations are in Appendix C.2.

The Kibble–Zurek mechanism has not been studied along the other integrable axis $M = 0$. As we noted above, in this direction $\nu = 8/15$, so the KZ scaling is modified with respect to the well-investigated free fermion case. Although the model is integrable, the time evolution cannot be solved analytically, which highlights the importance of the non-perturbative numerical method that exploits the conformal symmetry of the critical model: the Truncated Conformal Space Approach (TCSA). Nevertheless, as standard KZ arguments rely only on typical energy and distance scales of the model, they should apply regardless of the presence of interactions. The scaling arguments can also be supported by the analysis of the exactly known form factors of the model in the context of the adiabatic perturbation theory, to which we turn now.

7.1.3 Adiabatic perturbation theory

The adiabatic perturbation theory (APT) is a standard approach to study the response to a slow perturbation [9, 208]. Assume that we want to solve the time-dependent Schrödinger equation:

$$i\frac{\mathrm{d}}{\mathrm{d}t}\left|\Psi(t)\right\rangle = H(t)\left|\Psi(t)\right\rangle \tag{7.10}$$

in a time interval $t \in [t_\mathrm{i}, t_\mathrm{f}]$. Using the basis of eigenstates of $H(t)$ that are going to be called instantaneous eigenstates $\left|n(t)\right\rangle$,

$$H(t)\left|n(t)\right\rangle = E_n(t)\left|n(t)\right\rangle \ , \tag{7.11}$$

we can expand the time evolved state with coefficients $\alpha_n(t)$:

$$\left|\Psi(t)\right\rangle = \sum_n \alpha_n(t) \exp\{-i\Theta_n(t)\} \left|n(t)\right\rangle \ , \tag{7.12}$$

where the dynamical phase factor $\Theta_n(t) = \int_{t_\mathrm{i}}^t E_n(t')\,\mathrm{d}t'$ is already included. The initial condition is that at t_i the system is in its ground state $\left|0(t_\mathrm{i})\right\rangle$.

In the context of APT we assume that the explicit time dependence of the Hamiltonian is of the form $H(t) = H_0 + \lambda(t)V$, where the parameter λ changes slowly and monotonously. The small parameter of perturbation theory is $\dot{\lambda}$, and plugging (7.12) into (7.10) we can express the α_n coefficients in terms of the coupling up to leading order as

$$\alpha_n(\lambda) \approx \int_{\lambda_\mathrm{i}}^{\lambda} \mathrm{d}\lambda' \left\langle n(\lambda')\right| \partial_{\lambda'} \left|0(\lambda')\right\rangle \exp\{i(\Theta_n(\lambda') - \Theta_0(\lambda'))\} \, , \tag{7.13}$$

where the dynamical phase $\Theta_n(\lambda) = \int^{\lambda} E_n(\lambda')/\dot{\lambda}'\,\mathrm{d}\lambda'$ is expressed in terms of the coupling with $\lambda = \lambda(t)$, and we assumed that there is no Berry phase. The integrand strongly oscillates in the adiabatic limit $\dot{\lambda} \to 0$, so the integral can be approximated to read at the end of the time evolution t_f

$$\alpha_n(\lambda_\mathrm{f}) \approx i\dot{\lambda}' \frac{\langle n(\lambda')|\,\partial_{\lambda'}\,|0(\lambda')\rangle}{E_n(\lambda') - E_0(\lambda')} \exp\{i(\Theta_n(\lambda') - \Theta_0(\lambda'))\}\Big|_{\lambda_\mathrm{i}}^{\lambda_\mathrm{f}}\,, \tag{7.14}$$

where we neglected a non-analytic contribution, which is exponentially small in the inverse of $\dot{\lambda}$. The result is essentially a switch-on/off effect: it is proportional to the time derivative of λ at the initial and final moments. If the ramp is initiated and finished more smoothly, this effect is suppressed: in general, a discontinuity in the ath derivative brings about the scaling $\alpha \propto \tau_\mathrm{Q}^{-a}$ with the time parameter of the ramp τ_Q [182]. We consider linear ramps (cf. Eq. (7.9)) so higher derivatives disappear and the small parameter of the perturbative expansion is $1/\tau_\mathrm{Q}$.

Note that the coefficients $\alpha_{n\neq 0}$ measure the non-adiabaticity of the process, and they are required to be small by the standard arguments of perturbation theory. Therefore, naively, APT is expected to break down completely for ramps that pass the critical point, as the gap disappears and the fraction in Eq. (7.14) is divergent. Quite surprisingly, by relaxing the $\alpha_0 \approx 1$ requirement of elementary perturbation theory, Ref. [190] reproduced the KZ scaling for the density of defects in the quantum Ising chain, followed by the APT treatment of a wider variety of scaling quantities in different models [191–194, 209–211].

As we generalise this approach to the case of the Ising field theory, it is worthwhile to reiterate the basic arguments introducing adiabatic perturbation theory to Kibble–Zurek physics, following Ref. [193]. In essence, the APT calculation makes an appeal to low density, analogously to our argumentation in Chap. 5 regarding the post-quench initial state, but with a different mindset. The rationale is that for small intensive quantities in the thermodynamic limit, a perturbative approach should be feasible even if the resulting state does not have substantial overlap with the instantaneous ground state. This is motivated by the consideration that exciting even a single quasi-particle results in an orthogonal state, even though it corresponds to a vanishing energy and particle density in the thermodynamic limit.

The perturbative calculation is based on the above reasoning. For a specific example, we consider the transverse field Ising chain, where all quasi-particles are created in pairs $\{k, -k\}$, so we can use their momentum k to enumerate them, and express the density of defects as[1]

$$n_\mathrm{ex} = \lim_{L\to\infty} \frac{2}{L} \sum_{k>0} |\alpha_k|^2 = \int_{-\pi}^{\pi} \frac{\mathrm{d}k}{2\pi} |\alpha_k|^2\,, \tag{7.15}$$

---

[1] The model is quadratic, hence the density of excitations is given by summing the independently created pairs.

where $\alpha_k = \alpha_k(\lambda_\mathrm{f})$ is the coefficient of a particle pair state $|k, -k\rangle$ given by Eq. (7.13). The KZ scaling can be derived through an appropriate rescaling of the momentum and coupling variables:

$$\eta = k\tau_\mathrm{Q}^{\frac{\nu}{1+z\nu}}\,, \qquad \zeta = \lambda\tau_\mathrm{Q}^{\frac{1}{1+z\nu}}\,, \tag{7.16}$$

which removes the dependence on the small parameter $1/\tau_\mathrm{Q}$ from the exponent of Eq. (7.13). The observation that lies at the heart of the APT treatment of KZ scaling is that near the phase transition the energy difference and matrix element appearing in the expression of α_k take the following scaling forms:

$$E_k(\lambda) - E_0(\lambda) = |\lambda|^{z\nu} F(k/|\lambda|^\nu) \tag{7.17}$$

$$\langle\{k, -k\}(\lambda)|\, \partial_\lambda\, |0(\lambda)\rangle = \lambda^{-1} G(k/|\lambda|^\nu)\,, \tag{7.18}$$

with the asymptotic behaviour $F(x) \propto x^z$ and $G(x) \propto x^{-1/\nu}$ as $x \to \infty$. These considerations yield that

$$n_\mathrm{ex} = \tau_\mathrm{Q}^{-\frac{\nu}{1+z\nu}} \int \frac{\mathrm{d}\eta}{2\pi} K(\eta)\,, \tag{7.19}$$

with

$$K(\eta) = \left|\int_{\zeta_\mathrm{i}}^{\zeta_\mathrm{f}} \mathrm{d}\zeta\, \frac{G(\eta/\zeta^\nu)}{\zeta} \exp\!\left(i\int_{\zeta_\mathrm{i}}^{\zeta} \mathrm{d}\zeta'\, \zeta'^{z\nu} F(\eta/\zeta'^\nu)\right)\right|^2 . \tag{7.20}$$

At this point supposedly all power-like dependence on the quench rate is gathered into the prefactor, at the cost of extending the boundaries of the momentum integral. The scaling of the defect density is then given by the prefactor if the integral over η is convergent in the limit $\tau_\mathrm{Q} \to \infty$. In that case the limits of the integral over η are sent to $\pm\infty$, and its convergence properties can be deducted from the asymptotics of $K(\eta)$. Substituting Eqs. (7.17) and (7.18) one can perform the integral in (7.20) in the limit $\eta \gg \zeta_\mathrm{i,f}^\nu$ to determine the asymptotic behaviour

$$K(\eta) \propto \eta^\beta \equiv \eta^{-2z-2/\nu}\,. \tag{7.21}$$

The criterion for convergence then is $2z + 2/\nu > 1$, or, equivalently $\frac{\nu}{1+z\nu} < 2$ [210]. In the opposite case the integral is divergent, indicating that to discard the contribution from high-energy modes in the limit $\tau_\mathrm{Q} \to \infty$ is not justified. The scaling brought about by all energy scales is quadratic τ_Q^{-2} due to the discontinuity of $\dot\lambda$, cf. Eq. (7.14). Consequently, the case of equality $\frac{\nu}{1+z\nu} = 2$ separates between the Kibble–Zurek scaling determined by the exponent of τ_Q in Eq. (7.19) and the quadratic scaling.

We note that even if in a strict sense adiabatic perturbation theory breaks down in the impulse regime, the above extension of the APT indeed gives the correct scaling in several cases, and notably, makes only 10% error in the prefactor C in $n_\mathrm{ex} = C\tau_\mathrm{Q}^{-1/2}$ in the transverse field Ising chain [190]. This motivates its application in the Ising field theory as well.

7.1.4 The APT in the Ising field theory

The APT can be used to model ramps in the Ising field theory in two separate directions corresponding to the ramps along the two integrable directions of the model. In the case of the free field theory the generalisation of the arguments above is straightforward and it yields the same result as for the free fermion Ising chain. The application of the reasoning to the E_8 integrable model requires a bit of extra work. To some extent, the complications are technical, these details are presented in App. C.1. Here we comment on the key assumptions of the arguments.

The application of the APT to the Kibble–Zurek scaling heavily relies on the assumption that the ramp induces a low-density state. This is justified in the limit $\tau_\mathrm{Q} \to \infty$: the slower we cross the critical point, the less defects are created. Coincidentally, it has a profound consequence in the case of the E_8 model: based on the reasoning following Eq. (5.3) we expect that the non-equilibrium state essentially factorises to a product of few-particle states. Note that in contrast to the free fermion case, this factorisation is not exact, but a very accurate approximation given that the energy density of the non-equilibrium state is low [49, 119, 120] compared to the natural scale set by the final mass gap.

Based on these assumptions, we can show that the arguments of APT generalise to an interacting field theory as well. To formulate the arguments, let us have in mind a specific quantity, the excess heat density w that can be expressed as

$$w(\lambda_\mathrm{f}) = \lim_{L\to\infty} \frac{1}{L} \sum_n E_n(\lambda_\mathrm{f}) |\alpha_n(\lambda_\mathrm{f})|^2 \,. \tag{7.22}$$

In the calculation of the energy density, the machinery of APT introduced above is applicable despite the interacting nature of the E_8 model, with two important caveats. The first is the role of one-particle states. Since there is only a finite number of them, they cannot contribute to intensive quantities in the thermodynamic limit, however, they cannot be entirely discarded either. As we will see below in the case of E_8 ramps, for any finite L increasing the quench time τ_Q eventually results in a state where single-particle states contribute dominantly to the energy density. This issue is related to the order of the limits $\tau_\mathrm{Q} \to \infty$ and $L \to \infty$, and it is not clear at first glance whether the KZ scaling should apply here.

To gain some insight, let us take a small diversion to the discussion of finite volume effects in regard of the Kibble–Zurek mechanism. As the KZ arguments rely on a divergent length scale ξ_KZ, it is clear that finite volume can bring about adiabatic behaviour if

$$\xi_\mathrm{KZ} \simeq L \quad \Rightarrow \quad (\tau_\mathrm{Q}/\xi_t)^{\frac{a\nu}{a\nu z+1}} \simeq L/\xi \,, \tag{7.23}$$

where ξ and ξ_t are the correlation length and time in the ground state of the initial Hamiltonian. If the quench rate τ_Q is significantly larger than this, the transition is adiabatic due to the fact that finite volume opens the gap.

In light of Eq. (7.23) we are ready to pose the question: do zero-momentum single-particle states provide a "shortcut to adiabaticity", or are they subject to the same Kibble–Zurek scaling as the moving particle pairs? We note that this issue is unique to models with stable one-particle states, and hence is absent from previous APT calculations.[2] Remarkably, the finite volume calculation (for details see App. C.1.1) predicts that one-particle states contribute to the energy density with the right KZ exponent $\tau_{\mathrm{Q}}^{-\frac{\nu}{\nu+1}}$. We will comment on this result later in comparison with the numerics.

The second caveat is that for two-particle states there are separate branches of excitations corresponding to the different $A_a A_b$ pairings of the multiple species, each branch with a nontrivial density of states due to the interactions between the particles. However, in the thermodynamic limit the effects of the interactions are of $\mathcal{O}(1/L)$ and disappear as $L \to \infty$,[3] while the separate branches are independent due to the approximate factorisation and can be simply summed up. Consequently, the derivation is identical to the free fermion case, although one has to check whether the scaling forms (7.17) and (7.18) apply for the dispersion and the matrix elements of the E_8 theory as well. Observing that $\vartheta = \operatorname{arcsinh}(p/m_a) = \operatorname{arcsinh}\left[p/\left(c|\lambda|^{\nu}\right)\right]$ with some constant c, one can see that the former is trivially satisfied with the right asymptotic $F(x) \propto x^z$. The latter equation regarding the scaling and the high-energy behaviour of the matrix element also holds in general, as one can verify in the E_8 model (see Appendix C.1). Hence, as long as the initial assumptions of low energy and approximate pair factorisation are valid, the adiabatic perturbation theory predicts KZ scaling of intensive quantities in the E_8 theory as well.

7.1.5 Realisation in the truncated conformal space approach

Finally, let us briefly discuss the modelling of the ramp protocols with the CFTCSA introduced in the previous chapter. The dimensionless form of the Hamiltonian used for the calculations (2.18) is expressed in Sec. 2.2.2. Throughout this chapter, we work along the integrable lines, which corresponds to setting $\tilde{\kappa}_1$ or $\tilde{\kappa}_2$ to zero in Eq. (2.18). The energy scale is set by the unit $\Delta = m$ for the free fermion field theory, and $\Delta = m_1$ in the E_8 model. We measure every physical quantity in appropriate powers of Δ_{i}, the mass gap in the pre-ramp model.

The ramping protocol is realised in the CFTCSA by tuning the nonzero $\tilde{\kappa}$

---

[2] With the only exception of the attractive regime of the sine–Gordon model studied in Ref. [192], where non-moving breathers are present. Unfortunately, it is unclear whether this issue was explored there, cf. Sec. IV. in Ref. [192], and especially footnote 64 therein.

[3] This counters the intuition coming from thermodynamical Bethe Ansatz calculations, but note that the state is composed of only two particles, so no "backflow" can survive the thermodynamic limit.

linearly in the dimensionless time $\Delta_\mathrm{i} t$. The dynamics is obtained by numerically integrating the time-dependent Schrödinger equation

$$i\partial_t \left|\Psi\right\rangle = H(t) \left|\Psi\right\rangle \, . \tag{7.24}$$

To apply the CFTCSA, we need an algorithm for numerical integration that operates without having direct access to the elements of the matrix $H(t)$. In MATLAB [212], there are several efficient built-in numerical routines available to solve this task, hence we used this software in this case.

In this section we introduced the general arguments underpinning the Kibble–Zurek scaling, and enumerated a set of analytical and numerical approaches to test the mechanism in the context of the Ising field theory. Collectedly, these tools allow for an in-depth exploration of the Kibble–Zurek mechanism, from the microscopic level of eigenstates to more recently developed themes in the literature: the universal dynamical scaling (7.6), and the scaling behaviour of the higher cumulants of the work. We present the results of the exploration in this order.

7.2 Eigenstate dynamics

Perhaps the most intriguing characteristic of the Kibble–Zurek mechanism is that it can be explained by a simple-minded scenario, the adiabatic-impulse-adiabatic approximation. The overwhelming success of this "cartoon picture" begs the question whether it is an accurate depiction of the dynamics even at the microscopic level. For a quantum model, the fundamental level is that of the eigenstates, and the question is equivalent to the enquiry whether all change in the population of eigenstates is localised to the impulse regime. While the predicted scaling relations are heavily analysed in the literature, the microscopic dynamics is a relatively unexplored territory. Our aim here is to exploit the fact that through the TCSA we have a direct access to the eigenstate dynamics, so we are able to test the Kibble–Zurek scenario at the most fundamental level. At the same time, this is a nontrivial check of the claims of the adiabatic perturbation theory, since the key players of APT are the $|\alpha_n|^2$ probabilities to be in a given excited state.

To quantify the above considerations, we work in the basis of the eigenstates $|n(t)\rangle$ corresponding to the time-dependent Hamiltonian $H(t)$ (the instantaneous eigenstates) introduced in Eq. (7.11). We use them to generalise the statistics of work function [213] to each time instance along the course of the ramp, defining an instantaneous statistics of work function

$$\tilde{P}(W,t) = \sum_n \delta\left(W - \left[E_n(t) - E_0(t_\mathrm{i})\right]\right) \left|g_n(t)\right|^2 , \tag{7.25}$$

where the summation is over $|n(t)\rangle$, and $g_n(t)$ are the overlaps of the time-evolved state with the instantaneous eigenstates:

$$g_n(t) = \langle n(t)|\Psi(t)\rangle \ . \tag{7.26}$$

W is called to the total work performed by the non-equilibrium protocol. $\tilde{P}(W,t)$ is zero for $W < E_0(t) - E_0(0)$. In the following we focus only on the statistics of the excess work $P(W,t) = \tilde{P}(W - [E_0(t) - E_0(t_\mathrm{i})],t)$ so $P(W,t)$ is zero if $W < 0$. In the following we analyse $P(W,t)$ from two main aspects for ramps along the two integrable directions in the Ising field theory. On the free fermion line, our primary focus will be on the $g_n(t)$ overlap functions. They provide a benchmark to the TCSA calculations by comparing them to the exact results, and they are perfect indicators of non-adiabatic behaviour. On the E_8 line, where only the numerical approach works for $P(W,t)$, we concentrate on the structure of excitations after the ramp.

However, to accept the TCSA as a reliable method to model the Kibble–Zurek physics, it is necessary to outline the parameter region in terms of the quench rate τ_Q, where it is able to capture the universal KZ scaling. It is clear that this region is limited from above due to finite volume effects (cf. the discussion around Eq. (7.23)), and also from below, as fast ramps excite high-energy modes, enhancing truncation errors. Let us turn to this question first.

7.2.1 Probability of adiabaticity

A control quantity that can be used to fix the domain of τ_Q where the Kibble–Zurek scaling applies is the probability to be adiabatic after the ramp, $|g_0(t_\mathrm{f})|^2$, where $g_0(t)$ is the overlap with the instantaneous ground state. This overlap is exponentially suppressed with the volume in the KZ scaling regime, but its logarithm is proportional to the density of quasiparticles n_ex, such that $-\log(|g_0|)/L \propto n_\mathrm{ex}$ (cf. Eq. (7.15)). Within the domain of validity of the Kibble–Zurek scaling the density scales according to Eq. (7.5), i.e. it decays as a power law with τ_Q. However, at the onset of adiabaticity it is exponentially suppressed [214, 215]. To explore the time scale mentioned above for the volume parameters available in our calculation, we investigate the logarithm of the ground state overlap $P(0)$ after a TCP ramp crossing the critical point.

We begin with ramps along the free fermion line. In this case, besides the numerical treatment of TCSA, the dynamics admits an exact analytic solution as well. The field theory calculation is completely analogous to the lattice case: starting from an equilibrium ground state, only states consisting of zero-momentum particle pairs have nonzero overlap with the time evolved state, moreover, the different pairs of momentum modes $\{p,-p\}$ decouple completely. In finite volume L the momentum is quantised as $p_n = 2\pi n/L$, where n is a half-integer in the Neveu–Schwarz (NS) sector and integer in the Ramond (R) sector (cf. Sec. 2.2.1). To solve the dynamics we follow the approach of Ref. [201] and use the

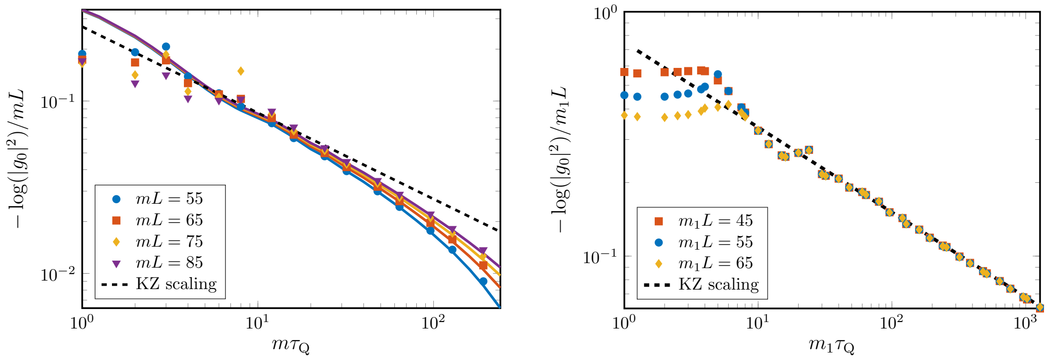

(a) Free fermion line

(b) E_8 line

Figure 7.3: Logarithm of the probability of adiabaticity after a linear ramp along the two integrable lines of the Ising Field Theory. (a) Continuous lines and symbols of the same colour denote analytical and extrapolated TCSA data, respectively, for various volume parameters. Black dashed line denotes the KZ scaling. At the onset of adiabaticity finite volume results deviate from the KZ slope and each other in a more pronounced manner. (b) Symbols stand for extrapolated TCSA data and the slope of the dashed line signals the KZ scaling exponent.

Ansatz:

$$|\Psi(t)\rangle = \bigotimes_p |\Psi(t)\rangle_p \,, \qquad \text{with} \qquad |\Psi(t)\rangle_p = a_p(t)\,|0\rangle_{p,t} + b_p(t)\,|1\rangle_{p,t} \,, \tag{7.27}$$

where $|0\rangle_{p,t}$ and $|1\rangle_{p,t}$ denote the instantaneous ground and excited states of the two-level system at time t along the ramp. The coefficients $a_p(t)$ and $b_p(t)$ satisfy $|a_p(t)|^2 + |b_p(t)|^2 = 1$, and they can be expressed via the solutions of two coupled first order differential equations (for details see Appendix C.2). The population of mode p is given by $n_p(t) = |b_p(t)|^2$. Although the equations can be solved exactly, numerical integration is more suitable for our purposes. Hence, strictly speaking, referring to this solution as 'analytical' is not entirely precise. From now on, when we use the term 'analytical' we mean the "numerically exact" procedure outlined above. The probability to remain in the ground state is readily given by the product over momenta:

$$|g_0(t)|^2 = \prod_p (1 - n_p(t)) \,. \tag{7.28}$$

Although there are infinitely many terms in this product, n_p is suppressed as $n_p \propto \exp(-\pi\tau_Q p^2/m)$, so we can safely truncate it at some $p_{\max}$ upon evaluation.

The analytical results for a ramp starting in the paramagnetic phase are compared with TCSA data in Fig. 7.3a, with the slope of the KZ scaling as a guide to the eye. The lower time limit of TCSA is signalled by the deviation from the exact solution for $m\tau_Q < 5$. To identify the upper time limit of TCSA in application to the KZ scaling, we note that the onset of adiabaticity occurs at different quench times τ_{Q} depending on the volume parameter. Therefore, the claim that for a given volume L we can observe the KZ scaling—as opposed to adiabatic behaviour—can be supported by the observation that changing the volume does not alter the KZ scaling. We note that the onset of adiabaticity signalled by the strong deviation of different volume curves from each other and from the $\tau_{\mathrm{Q}}^{-1/2}$ line is not an abrupt change but rather a smooth crossover, which prohibits a precise estimate of the upper time limit. Nevertheless, we can identify that for $m\tau_{\mathrm{Q}} \approx 5 \cdot 10^0 \dots 10^2$ the Kibble–Zurek scaling is satisfied to a good precision using the volume parameters available to the numerical method.

The results of the same enquiry are presented in Fig. 7.3b for the E_8 model, where we have to resort to the results of TCSA. The comparison with the slope of the predicted KZ scaling shows that the logarithm of the ground state overlap scales as the density of quasiparticles for large enough τ_{Q}. Although the KZ scaling sets in later, i.e. for larger τ_{Q} than in the free fermion case, it is persistent up to the maximum ramp duration available to our numerical method. This can be understood in light of the fact that the exponent appearing in Eq. (7.23) is larger for the E_8 model, and consequently the onset of adiabaticity occurs for a slower ramp in the same volume.

The analysis of adiabatic behaviour established that our numerical method is applicable to address the KZM for a fairly wide range of parameters. Consequently, we are ready to utilise it to explore the microscopic dynamics behind the KZM, i.e. to observe how excitations form at the level of instantaneous eigenstates. Below we discuss the results for the free fermion line and the E_8 direction, respectively.

7.2.2 Ramps along the free fermion line

As already noted, the ramp dynamics along the free fermion line is exactly solvable; we exploit this fact to draw a robust picture of eigenstate dynamics by comparing the analytical and numerical results. We perform linear ramps of the type (7.9), with the role of the coupling parameter λ played by the time-dependent fermion mass M :

$$M(t) = -2M_{\mathrm{i}}t/\tau_{\mathrm{Q}}\,, \tag{7.29}$$

where M_{i} is the initial value of the coupling at $t = -\tau_{\mathrm{Q}}/2$. As discussed in Sec. 7.1.2, the critical exponents in this case are $\nu = 1$, $z = 1$, so the Kibble–Zurek time (7.3) scales as $\tau_{\mathrm{KZ}} \sim \sqrt{\tau_{\mathrm{Q}}}$. To test the adiabatic-impulse-adiabatic scenario, we need to have a specified value of τ_{KZ} which we simply set as

$$m\tau_{\mathrm{KZ}} = \sqrt{m\tau_{\mathrm{Q}}}\,, \tag{7.30}$$

where $m = |M_{\mathrm{i}}|$ is the mass gap at the start of the ramp. Depending on the sign of M_{i}, the ramp is either towards the ferromagnetic phase or the paramagnetic phase; we are going to present our results in this order.

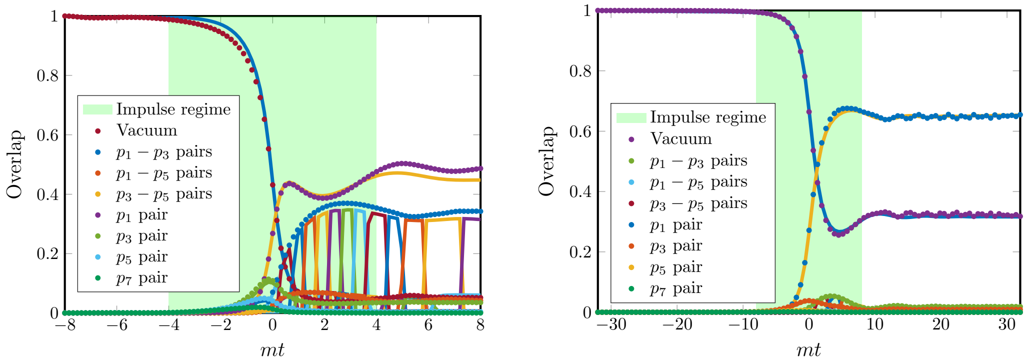

(a) $m\tau_\mathrm{Q} = 16$

(b) $m\tau_\mathrm{Q} = 64$

Figure 7.4: Overlaps of the evolving wave function with instantaneous eigenstates for two different ramps from the paramagnetic to the ferromagnetic phase with $m\tau_\mathrm{Q} = 16$ and $m\tau_\mathrm{Q} = 64$ for $mL = 50$. The green region indicates the non-adiabatic regime. Solid lines are TCSA data for $N_\mathrm{cut} = 25$ while dots are obtained from the numerical solution of the exact differential equations. Analytical results are plotted only for the few low-momentum states with the most substantial overlap. Lower indices in the legends refer to the quantum numbers of the modes present in the many-body eigenstate: $p_n = n\pi/L$. The composite structure of some lines is caused by level crossings experienced by multiparticle states.

The paramagnetic-ferromagnetic (PF) direction

Ramps starting from the paramagnetic phase are defined by $M_\mathrm{i} < 0$. In this case the ground state is non-degenerate and lies in the Neveu–Schwarz sector, so the time evolved state is orthogonal to the Ramond sector subspace for all times.

As noted above, the solution of the dynamics amounts to finding the $a_p(t)$ and $b_p(t)$ coefficients characterising the decoupled particle pairs with momenta $\{p, -p\}$. Consequently, each excited state is specified as a set of p momentum modes. The elementary overlaps g_p corresponding to a state with a single momentum mode can be expressed as

$$|\langle p, -p|\Psi(t)\rangle|^2 \equiv |g_p(t)|^2 = n_p(t) \prod_{p' \neq p} (1 - n_{p'}(t)) \,, \tag{7.31}$$

where $n_p = |b_p|^2$ and the product goes over the quantised momenta, which are odd multiples of π/L in the NS sector. The extension to states with multiple particle pairs is straightforward.

The comparison of these results with the numerical data involves a subtlety. TCSA constructs the eigenstates and the time-evolved state such that they are normalised to 1, and as a result, the overlaps $|g_n|^2$ are highly sensitive to the number of states kept after truncation. As there is no direct correspondence between the single-mode momentum cutoff applied to the infinite product of Eq. (7.31) and the many-body TCSA energy cutoff, we set the latter such that the

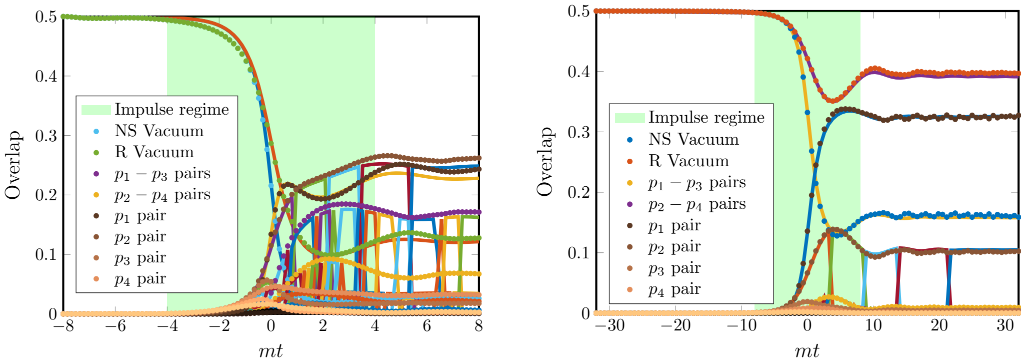

(a) $m\tau_{\mathrm{Q}} = 16$ (b) $m\tau_{\mathrm{Q}} = 64$

Figure 7.5: Overlaps of the evolving wave function with instantaneous eigenstates for two different ramps from the ferromagnetic to the paramagnetic phase with $m\tau_{\mathrm{Q}} = 16$ and $m\tau_{\mathrm{Q}} = 64$ for $mL = 50$. The green region indicates the non-adiabatic regime. Solid lines are TCSA data for $N_{\mathrm{cut}} = 31$ while dots are obtained from the numerical solution of the exact differential equations.

match between the analytical and numerical results is optimal. Note that this is a single parameter for all the states.

The time evolution of the overlaps is presented in Fig. 7.4. Dots are calculated from the exact solution (7.31) and continuous lines denote TCSA data obtained by solving the many-body dynamics numerically. Fig. 7.4a depicts a curious behaviour of the second largest overlap in TCSA: the corresponding line seemingly consists of many different segments. This is a consequence of level crossings and the errors of numerical diagonalisation near these crossings. The state in question consists of two two-particle pairs, and as the mass scale M is ramped, its energy increases steeper than that of high-momentum states with only a single pair, hence the level crossings. At each crossing the numerical diagonalisation cannot resolve precisely levels in the degenerate subspace, so the resulting overlap is not accurate. This accounts for the most prominent difference between the numerical and analytical results. Apart from that, the agreement is quite satisfactory.

The light green background corresponds to the naive impulse regime $t \in [-\tau_{\mathrm{KZ}},\ \tau_{\mathrm{KZ}}]$. Of course this is only a crude estimate for the time when adiabaticity breaks down, as strictly speaking Eq. (7.30) is valid only as a scaling relation. Nevertheless, most of the change in each state population indeed happens within this coloured region. This statement is even more accentuated by Fig. 7.4b, that is, for a slower ramp. Comparing the two panels of Fig. 7.4 we observe that increasing the ramp time the probability of adiabaticity increases while the weight of the multiparticle states are suppressed. Note that although the two lowest available levels (the ground state and the first excited state) dominate the time-evolved state, the dynamics is far from being completely adiabatic, meaning no excitations at all. Hence, in accordance with the remarks concerning finite size effects in the previous subsection, we are within the regime of Kibble–Zurek

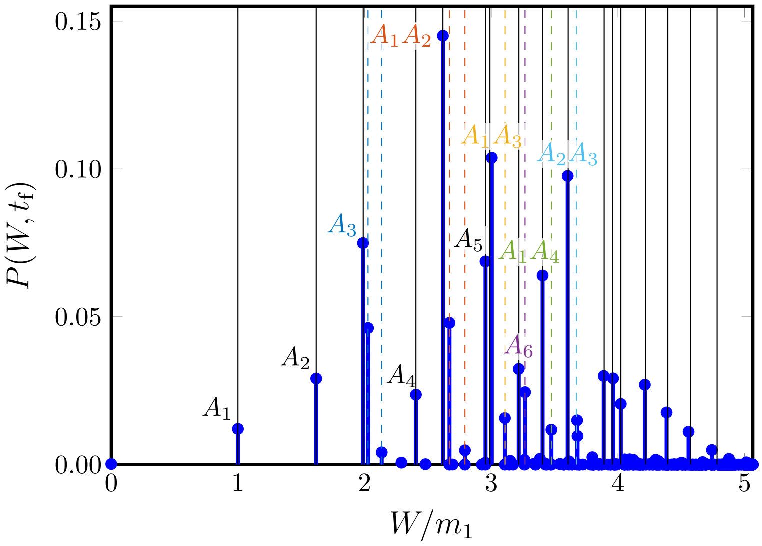

Figure 7.6: Statistics of work after the ramp $P(W, t = \tau_\mathrm{Q}/2)$ along the E_8 direction with $m_1\tau_\mathrm{Q} = 32$, $m_1L = 40$, and $N_\mathrm{cut} = 45$. States containing only zero-momentum particles are denoted by continuous lines, while dashed lines denote moving multiparticle states, different colours correspond to a different A_aA_b branch. The particle content is expressed as a label near the overlap of the most prominent states, with the same convention for colouring. The colour of the single-particle labels A_3 and A_6 reflects that they can be viewed as the bound states of A_1A_1 and A_2A_2, respectively, with a small binding energy (cf. Table A.1).

scaling instead of being adiabatic.

The ferromagnetic-paramagnetic (FP) direction

The ferromagnetic ground state is twofold degenerate in infinite volume. For the initial state we choose the state with maximal magnetisation corresponding to the infinite volume symmetry breaking state: $|\Psi_0\rangle = \frac{1}{\sqrt{2}}\left(|0\rangle_\mathrm{R} + |0\rangle_\mathrm{NS}\right)$. As both sectors are present in the initial state, the time-evolved state also overlaps with both sectors. This provides yet another benchmark for our numerical approach and also a somewhat richer landscape of the overlap functions.

As one can see in Fig. 7.5, the dynamics are very similar to the PF case with the main difference coming from the fact that both sectors contribute. We also note that the number of level crossings is substantially increased, due to the gap developed between the two sectors in the paramagnetic phase. The different behaviour of the two vacua stems from the different available momentum modes in each sector: in the Ramond sector the momenta are larger in the lowest available modes and consequently they are less likely to be excited.

7.2.3 Ramps along the E_8 line

After investigating the free fermion line, we now turn to the behaviour of overlaps in the other integrable direction, i.e. for ramps along the E_8 axis defined by the protocol

$$h(t) = -2h_{\mathrm{i}}t/\tau_{\mathrm{Q}} \tag{7.32}$$

for $t \in [-\tau_{\mathrm{Q}}/2, \tau_{\mathrm{Q}}/2]$. The scaling dimension of the perturbing operator σ is $\Delta_\sigma = 1/8$, so critical exponent ν is different in this direction from the free fermion case: $\nu = 1/(2-\Delta_\sigma) = 8/15$ (cf. Eq.(2.15)). This implies that the Kibble–Zurek time (7.3) is given by

$$m_1\tau_{\mathrm{KZ}} = (m_1\tau_{\mathrm{Q}})^{8/23}\ , \tag{7.33}$$

where, similarly to the free fermion case, the choice of the proportionality factor being 1 is just a convention.

Due to the lack of exact results for the evolution of energy levels, we consider another aspect of the instantaneous work function compared to the free fermion case, i.e. we calculate $P(W)$ at a specific moment: the end of the ramp. From the defining relation Eq. (7.25) it is clear that $P(W)$ has peaks at the discrete finite volume energy levels of the E_8 spectrum. By virtue of the E_8 particle spectrum (2.16), many of these peaks correspond to states composed of one or more zero-momentum particles, denoted by A_a, where a is the particle species index. Similarly to the free fermion line, pair states of moving particles are present as well, their quantisation is dictated by the zero-momentum Bethe–Yang equations (B.8) accounting for the interactions between the two particles in the pair state. As a result, we can identify the particle content of all states in the spectrum by their energy, and have a detailed picture of excitations created by the ramp.

First, we present $P(W)$ following a ramp at the onset of the KZ scaling regime (cf. Fig. 7.3b), $m_1\tau_{\mathrm{Q}} = 32$. States with visible overlap in Fig. 7.6 are marked with gridlines: continuous lines for states built up from zero-momentum particles, and dashed lines for moving particle pairs. We labelled the most prominent overlaps with the A_a particle content: note that most of the post-ramp weight is carried by zero-momentum particles, and only a few dashed lines are present, each marking a state with comparatively small overlap. Moreover, in each moving branch, the pair with the lowest momentum stands out, indicating an effective "momentum-cutoff". This is very much in line with the traditional KZ arguments, as the dominant role of low-momentum modes is the consequence of the large Kibble–Zurek length scale ξ_{KZ}. The distribution of the overlaps of states composed of zero-momentum particles indicates an akin tendency in terms of the overall energy of the states, as high-energy modes are similarly suppressed.

This suppression is even more drastic for a slower ramp with $m_1\tau_{\mathrm{Q}} = 128$, presented in Fig. 7.7. Note that there is a single pair overlap which is at least barely visible on the y scale of the figure, all others are practically negligible, meaning that the post-ramp state is almost exclusively composed of zero-momentum particles. These in turn exhibit a shift towards lower energies compared to the

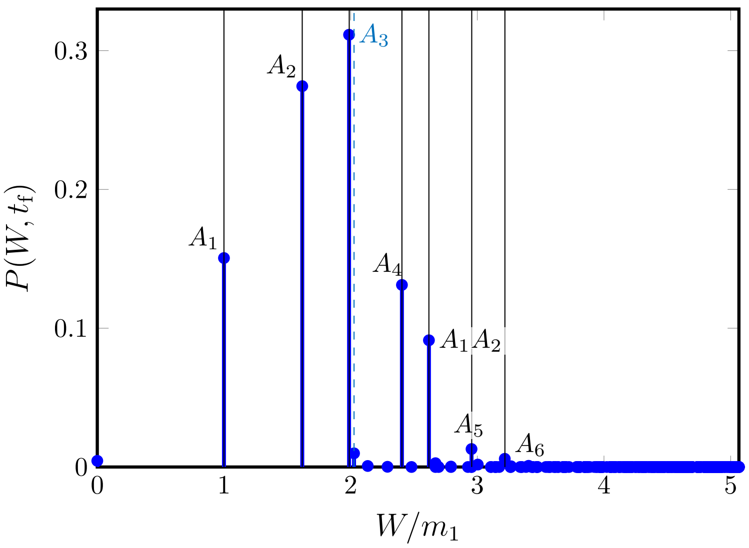

Figure 7.7: Statistics of work after the ramp $P(W, t = \tau_\mathrm{Q}/2)$ along the E_8 direction with $m_1\tau_\mathrm{Q} = 128$, $m_1L = 40$, and $N_\mathrm{cut} = 45$. The conventions are the same as in Fig. 7.6.

faster ramp (note the drop in the number of continuous gridlines). Altogether, the indication of the statistics of work function is that the customary Kibble-Zurek arguments, stating the sole importance of low-momentum modes by virtue of the increasing ξ_KZ length scale, identically apply in regard of the large time scale ξ_t and the prominence of low-energy excitations. We remark that to our knowledge, albeit well within the KZ motif, this is the first case where the unique role of low-energy excitations is demonstrated on a different footing than that of low-momentum modes.

The dominant role of zero-momentum particles prompts us to return to the point made in Sec. 7.1.4 regarding the scaling brought about by single-particle states. We recall that in the thermodynamic limit they cannot contribute to intensive quantities, but it is equally clear that in the finite volume parameter regime available by TCSA their contribution is in fact dominant. A comparison of the τ_Q values of Figs. 7.6-7.7 to the x scale in Fig. 7.3b indicates that we are well within the KZ scaling regime, which was identified by looking at the scaling of the probability of remaining adiabatic. It is desirable to have an analytic argument to explain the observed scaling in this case, where it must be attributed to single-particle states. Apparently, the APT calculation provides one, as it predicts that each single-particle overlap $|\alpha_a|^2$ scales as $\tau_\mathrm{Q}^{-8/23}$ separately, i.e. they are subject to the "correct" KZ scaling (cf. App. C.1.1). However, a more careful inspection of Figs. 7.6-7.7 reveals that this prediction cannot hold exactly. For instance, the overlap of the first particle (located at 1 on the horizontal axis in the figures) increases with increasing τ_Q instead of the monotonously decreasing behaviour predicted by the scaling form.

This ambiguity does not come as a surprise, as the application of the APT to the KZ scaling far exceeds the conventional boundaries of perturbation theory, hence not all aspects of its conclusions are warranted. This is not to say that the KZ scaling itself is in question: we are well within the τ_{Q} regime where the KZ scaling is spectacularly satisfied. To sum up, even if the APT arguments do not describe them properly, our numerical data verifies that one-particle states in fact comply with the usual KZ scaling arguments and reproduce the expected scaling relations for various quantities. This was already seen for the probability of adiabaticity, and will be demonstrated below for further quantities. In regard of the conflicting predictions of the perturbative approach, a remote analogy can be drawn with the form factor series expansion calculation of the central charge in integrable perturbed conformal field theories, where the result of the sum over multiparticle states is fixed by the c-theorem, while the separate terms vary greatly due to the details of the interaction [89].

7.3 Dynamical scaling in the impulse regime

In this section we explore the dynamical scaling aspect of the Kibble–Zurek mechanism in the Ising field theory considering two one-point functions. We focus on the energy density and the magnetisation, both of which are important observables in the theory.

7.3.1 Energy density

The energy density over the instantaneous vacuum or the excess heat density is defined as

$$w(t) = \frac{1}{L} \left\langle \Psi(t) | H(t) - E_0(t) | \Psi(t) \right\rangle , \tag{7.34}$$

where the Hamiltonian $H(t)$ has an explicit time dependence governed by the ramping protocol and $E_0(t)$ is the ground state of the instantaneous Hamiltonian $H(t)$. In accordance with Eq. (7.6), the excess heat for different ramp rates is expected to collapse to a single scaling function:

$$w(t/\tau_{\mathrm{KZ}}) = \xi_{\mathrm{KZ}}^{-d-\Delta_H} F_H(t/\tau_{\mathrm{KZ}}) = \tau_{\mathrm{KZ}}^{-d/z-1} F_H(t/\tau_{\mathrm{KZ}}) = \tau_{\mathrm{KZ}}^{-2} F_H(t/\tau_{\mathrm{KZ}}) \,, \tag{7.35}$$

where $d = 1$ is the spatial dimension, $\Delta_H = z$ is the scaling dimension of the energy and the second equation follows from $\tau_{\mathrm{KZ}} = \xi_{\mathrm{KZ}}^z$. For ramps along the free fermion line the energy density can be obtained from the solution of the exact differential equations using the mapping to free fermions, yielding essentially exact results. For the E_8 line, it is easily extracted from the numerical data, as it merely amounts to taking the expectation value of the Hamiltonian.

In Fig. 7.8 we examine the scaling behaviour (7.35) for several ramps in both integrable directions. In the free fermion case, the analytic calculations and the

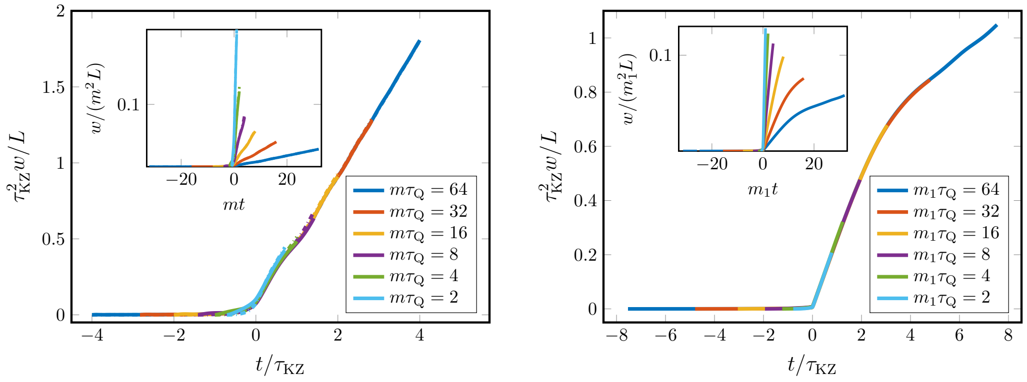

(a) PF ramp (b) E_8 ramp

Figure 7.8: Dynamical scaling of the energy density for ramps along the two integrable directions. The insets illustrate the effects of rescaling. (a) The free fermion line, where solid lines denote exact analytical solution while dot-dashed lines represent TCSA results for $mL = 50$ extrapolated in the cutoff. (b) The E_8 direction, where extrapolated TCSA data obtained for $m_1L = 50$ is in solid lines.

extrapolated TCSA data are practically indistinguishable. The insets show that the non-rescaled curves deviate substantially from each other, reflecting that the dynamical scaling of Eq. (7.35) is retained in both directions. Notably, the collapse of the curves is perfect well beyond the impulse regime $|t/\tau_{\rm KZ}| < 1$. This can be understood in light of the eigenstate dynamics investigated in Sec. 7.2. As we observed, the population of the instantaneous eigenstates is approximately constant after the non-adiabatic period. The subsequent increase in energy density then is merely due to the increasing gap $\Delta(t)$ as the coupling is ramped. The energy scale increases identically for all quench rates which in turn leads to the collapse of different curves. This argument can be formalised for the general set-up of Sec. 7.1.1 as

$$w(t \gg \tau_{\rm KZ}) \approx n_{\rm ex}(t)\cdot\Delta(t) \propto \tau_{\rm KZ}^{-d/z}\left(\frac{t}{\tau_{\rm Q}}\right)^{a\nu z} \propto \tau_{\rm KZ}^{-d/z}\left(\frac{t}{\tau_{\rm KZ}}\right)^{a\nu z}\tau_{\rm KZ}^{-1}\,, \qquad (7.36)$$

where $n_{\rm ex}$ is the density of defects that is constant well beyond the impulse regime and scales as $\tau_{\rm KZ}^{-d/z}$. The gap scales as $(t/\tau_{\rm Q})^{z\nu}$ and we used that $(\tau_{\rm KZ}/\tau_{\rm Q})^{a\nu z} \propto \tau_{\rm KZ}^{-1}$. The result shows that $w(t \gg \tau_{\rm KZ})$ is a function of $t/\tau_{\rm KZ}$. To conclude, we expect the rescaled energy density to grow as $(t/\tau_{\rm KZ})^{a\nu z}$ in the final adiabatic period, and this is in fact what we observe in Fig. 7.8.

7.3.2 Magnetisation

The magnetisation operator σ that corresponds to the order parameter has scaling dimension $\Delta_\sigma = 1/8$ hence is expected to satisfy the following scaling in

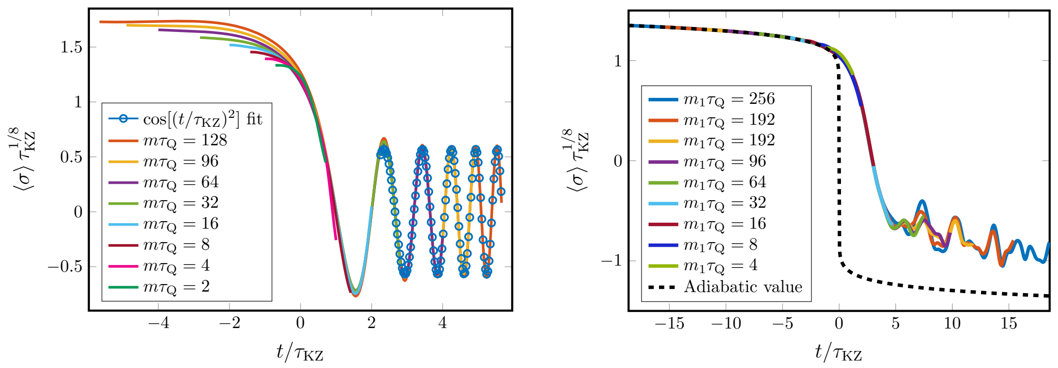

(a) FP ramp (b) E_8 ramp

Figure 7.9: Dynamical scaling of the magnetisation for two different ramps. The extrapolated TCSA results are obtained using dimensionless volume $l = 50$. (a) Ramps from the ferromagnetic phase in the free fermion model. The fitted function corresponding to the instantaneous one-particle oscillation is $f(t/\tau_{\mathrm{KZ}}) = 0.612(2)\,\cos\left((t/\tau_{\mathrm{KZ}})^2 + 0.830(3)\right)$. (Note that $(t/\tau_{\mathrm{KZ}})^2 = m(t)t$.) (b) Ramps along the E_8 axis. The dashed black line shows the exact adiabatic value [138]: $\langle\sigma\rangle_{\mathrm{ad}} = (-1.277578\dots)\cdot\mathrm{sgn}(h)|h|^{1/15}$.

the impulse regime ($z = 1$):

$$\langle\sigma(t/\tau_{\mathrm{KZ}})\rangle = \tau_{\mathrm{KZ}}^{-1/8}F_\sigma(t/\tau_{\mathrm{KZ}})\,. \tag{7.37}$$

In contrast to the energy density, the magnetisation is much harder to calculate even in the free fermion case as it is a highly non-local operator in terms of the fermions. Consequently, we have to resort to TCSA calculations in both directions.

The scaling behaviour of the magnetisation (7.37) is checked in Fig. 7.9. Let us begin with the discussion of the free fermion case, presented in Fig. 7.9a. To have a nonzero magnetisation, we initiate the ramp in the ferromagnetic phase. The scaling is present most notably in terms of the frequency of the oscillations beyond the non-adiabatic window. Due to truncation errors of the TCSA method (see Appendix D), the predicted scaling is not reproduced perfectly in terms of the amplitudes and neither in the first half of the non-adiabatic regime. This is also the reason why the various curves do not collapse perfectly for times $t < -\tau_{\mathrm{KZ}}$ where the scaling should also hold according to Eq. (7.7). This is in contrast with the E_8 results presented in Fig. 7.9b, where TCSA has better convergence properties and the curves precisely reproduce the initial adiabatic behaviour.

Returning to the free fermion ramp, we observe that the frequency of the late time oscillations is increasing with time. The oscillations can be fitted with the function $f(t) = A\cos\left[m(t)\cdot t + \phi\right]$ which demonstrates that the oscillations originate from one-particle states whose masses and thus the frequency increases in time with the gap. We remark that this is analogous to sudden quenches in the Ising field theory (cf. Chapter 4) where the presence of one-particle oscillations is supported by analytical and numerical evidence [33, 49, 94]. The oscillations appear undamped well after the impulse regime $t/\tau_{\mathrm{KZ}} \gg 1$. We remark that for sudden quenches the decay rate of the oscillations depends on the post-quench energy density [33, 216]. We expect the same to apply for ramps as well, but here the energy density is suppressed for slower ramps so the damping cannot be observed during a finite ramp. In contrast, the decay of oscillations in the dynamics of the order parameter after the ramp is observed in Ref. [198] in the spin chain.

In the E_8 direction we observe that the collapse in the early adiabatic regime is perfect, but the curves slightly deviate after the non-adiabatic regime. The oscillations appearing afterwards are once again expected to be related to the single-particle states. Unfortunately, to verify this expectation by a similar fitting procedure is not viable, due to the fact that there are eight of them.

7.4 Cumulants of work

So far we have gained insight in the KZM by examining the instantaneous spectrum directly and demonstrated the relevance of the Kibble–Zurek time scale in dynamical scaling functions of local observables. In this section we aim to demonstrate that the Kibble–Zurek scaling is present in an even wider variety of quantities: the full statistics of the excess heat (or work) during the ramp is subject to scaling laws of the KZ type as well.

A particularly interesting result of the free fermion chain (already tested experimentally, cf. Ref. [65]) is that apart from the average density of defects and excess heat, their full counting statistics is also universal in the KZ sense: all higher cumulants of the respective distribution functions scale according to the Kibble–Zurek laws [194, 217]. The scaling exponents depend on the protocol in the sense that they are different for ramps ending at the critical point (ECP) and those crossing it (TCP). As Ref. [218] demonstrates, the universal scaling of cumulants can be observed in models apart from the transverse field Ising spin chain, hence it is natural to explore their behaviour in the Ising Field Theory.

The cumulants of excess work are defined via a generating function $\ln G(s)$:

$$G(s) = \langle \exp[s(H(t) - E_0(t))] \rangle \tag{7.38}$$

where the expectation value is taken with respect to the time-evolved state. The cumulants κ_j are the coefficients appearing in the expansion of the logarithm:

$$\ln G(s) = \sum_{j=1}^{\infty} \frac{s^j}{j!} \kappa_j \,. \tag{7.39}$$

The first three cumulants coincide with the mean, and the second and third central moments, respectively. Assuming that the generating functions satisfy a large deviation principle [194, 219], all of the cumulants are extensive $\propto L$. To have a more robust numerical estimate of the cumulants by comparing results using various volume parameters, we are going to focus on the κ_j/L cumulant densities.

Elaborating on the framework of adiabatic perturbation theory presented in Sec. 7.1.3, we argue that the scaling behaviour of the cumulants of the excess heat are not sensitive to the presence of interactions in the E_8 model and take a route analogous to Ref. [194] to obtain the KZ exponents. The core of the argument is the following: the Kibble–Zurek scaling within the context of APT stems from the rescaling of variables (7.16) which yields Eq. (7.19) from Eq. (7.15). The rescaling concerns the momentum variable that originates from the summation over pair states.

Now consider that cumulants can be expressed as a polynomial of the moments of the distribution:

$$\kappa_n = \mu_n + \sum_{\lambda \vdash n} \alpha_\lambda \prod_{j=1}^{k} \mu_{m_j} \tag{7.40}$$

where $\lambda = \{m_1, m_2, \ldots, m_k\}$ is a partition of the integer index n with $|\lambda| = k \geq 2$, and α_λ are integer coefficients. The moments are defined for the excess heat as

$$\mu_n = \langle [H - E_0]^n \rangle \ . \tag{7.41}$$

Let us note that the integration variable subject to rescaling in Eq. (7.16) originates from taking the expectation value. Consequently, in the limit $\tau_\mathrm{Q} \to \infty$ terms consisting of powers of lower moments are suppressed compared to μ_n, because they are the product of multiple integrals of the form (7.19). So the scaling behaviour of κ_n equals that of μ_n, which is defined with a single expectation value, hence its scaling behaviour is given by the calculation in Sec. 7.1.3. We remark that this line of thought is completely analogous to the arguments of Ref. [194]. According to the above reasoning, all cumulants of the work and quasiparticle distributions in the E_8 model should decay with the same power law as $\tau_\mathrm{Q} \to \infty$.

To put the claims above to test, we follow the presentation of Ref. [194] and we discuss the two different scaling for the cumulants: first considering ramps that end at the critical point then examining ramps that navigate through the phase transition.

7.4.1 ECP protocol: ramps ending at the critical point

For ramps that end at the critical point one may apply the scaling form in (7.6) since the final time of such protocols corresponds to a fixed $t/\tau_\mathrm{KZ} = 0$. The

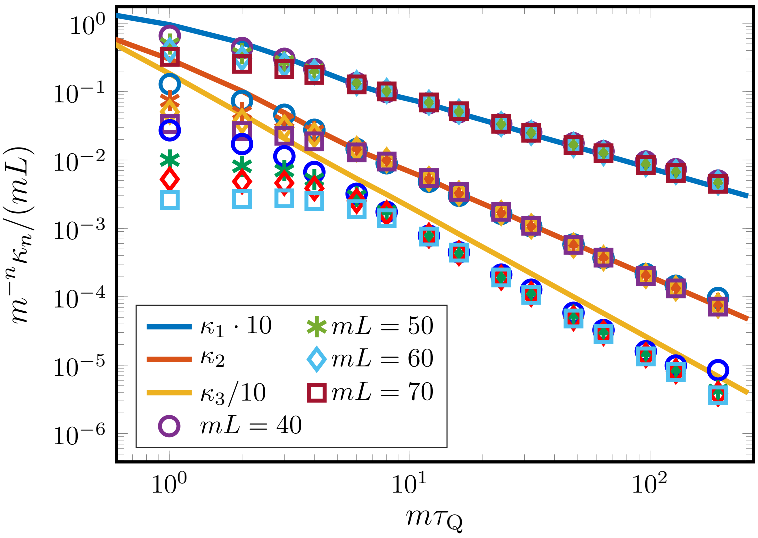

Figure 7.10: Cumulant densities for linear ramps on the free fermion line starting in the paramagnetic phase and ending at the QCP: a comparison between the numerically exact solution (solid lines) in the thermodynamic limit and cutoff-extrapolated TCSA data in different volumes (symbols). For both approaches κ_3/L is plotted a decade lower for better visibility.

resulting naive scaling dimension of a work cumulant κ_n is then easily obtained since it contains the product of n Hamiltonians with dimension $\Delta_H = z = 1$. Consequently, we expect

$$\kappa_n/L \propto \tau_{\mathrm{KZ}}^{-d/z-n} \propto \tau_{\mathrm{Q}}^{-\frac{a\nu(d+nz)}{a\nu z+1}}, \tag{7.42}$$

where we used Eq. (7.3). However, the arguments of adiabatic perturbation theory [194] as outlined in Sec. 7.1.3 demonstrate that this naive scaling is true only if the corresponding quantity is not sensitive to the high-energy modes. However, using APT one can express the cumulants similarly to the defect density in Eq. (7.19). If the corresponding rescaled integral does not converge that means the contribution from high-energy modes cannot be discarded and the resulting scaling is quadratic with respect to the ramp velocity: τ_{Q}^{-2}. The crossover happens when $a\nu(d+nz)/(a\nu z+1) = 2$; for smaller n the KZ scaling applies while for larger n quadratic scaling applies with logarithmic corrections at equality [210].

For the free fermion line $\nu = 1$ $(a = d = z = 1)$, and the crossover cumulant index is $n = 3$. Fig. 7.10 justifies the above expectations for the three lowest cumulants by comparing the numerically exact solutions to TCSA results. TCSA is most precise for moderately slow quenches and the first two cumulants. There is notable deviation from the exact results in the case of the third cumulant although the scaling behaviour is intact. The deviation does not come as a surprise, since the fact that the integral of adiabatic perturbation theory does not converge means that there is substantial contribution from all energy scales,

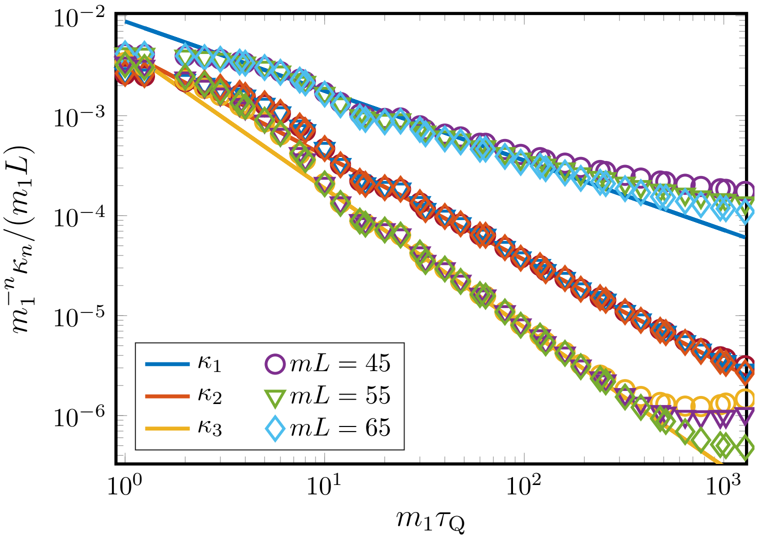

Figure 7.11: Cumulant densities for ECP ramps on the E_8 integrable line: cutoff-extrapolated TCSA data and the expected KZ scaling from dimension counting. The scaling exponents are 16/23, 24/23 and 32/23, respectively.

including those that fall victim to the truncation.

Fig. 7.10 also demonstrates that for very slow quenches finite size effects can spoil the agreement between exact results and TCSA. This is the result of the onset of adiabaticity (cf. Fig. 7.3a).

We expect identical scaling behaviour from the other integrable direction of the Ising Field Theory in terms of τ_{KZ} that translates to a different power-law dependence on τ_{Q}. Indeed this is what we observe in Fig. 7.11. In this case there is no exact solution available, hence solid lines denote the expected scaling law instead of the analytic result. The figure is indicative of the correct scaling although finite volume effects are more pronounced as the duration of the ramps is larger than earlier.

7.4.2 TCP protocol: ramps crossing the critical point

For slow enough ramps that cross the critical point, and terminate at a given finite value of the coupling which lies far from the non-adiabatic regime where (7.6) applies, the excess work density scales identically to the defect density. This is due to the fact that the gap that defines the typical energy of the defects is the same for ramps with different τ_{Q} and the excess energy equals energy scale times defect density. It is demonstrated in Ref. [194] that higher cumulants of the excess work share a similar property: their scaling dimension coincides with that of the mean excess work, consequently all cumulants of the defect number and the excess work scale with the same exponent. As we argued above, this claim is expected to hold more generally than the free model considered in Ref.

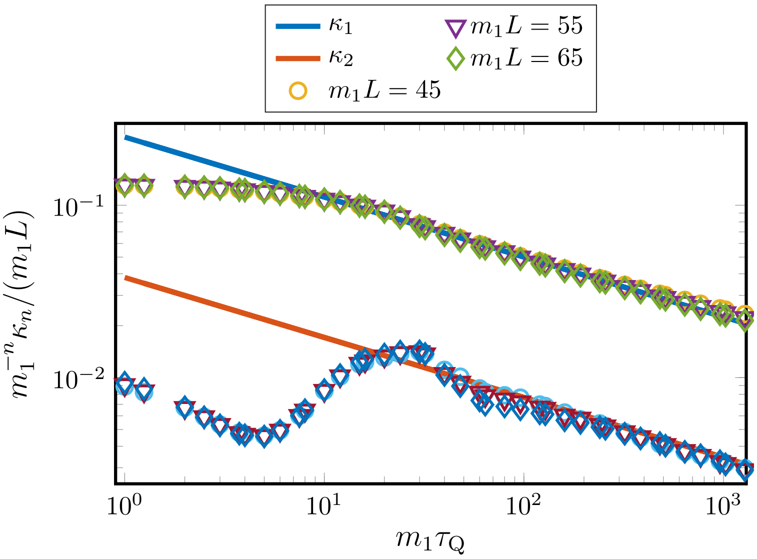

Figure 7.12: The first two cumulant densities for linear ramps crossing the QCP along the E_8 integrable line: the symbols represent cutoff-extrapolated TCSA data while the solid lines show the expected KZ scaling $\sim \tau_Q^{-8/23}$.

[194], and in particular we claimed that it holds in the E_8 model.

Fig. 7.12 demonstrates the validity of this statement for the second cumulant. In line with the reasoning presented earlier (cf. Eq. (7.40) and below), the subleading terms are more prominent than in the case of the first cumulant (i.e. the excess heat) and KZ scaling is observable only for larger τ_Q. Higher cumulants do not exhibit the same scaling within the quench time window available for TCSA calculations. Due to the increasing number of terms in the expressions with moments for the nth cumulant κ_n, we expect that the Kibble–Zurek scaling occurs for larger and larger τ_Q, on time scales that are not amenable to effective numerical treatment as of now. Nevertheless, the behaviour of the second cumulant still serves as a nontrivial check of the assumptions that were used in Sec. 7.1.4 to apply APT to the E_8 model. As the argumentation did not rely explicitly on the details of the interactions in the E_8 theory, rather on the more general scaling behaviour of the gap (7.17) and the matrix element (7.18), we expect that a similar behaviour of the cumulants is observable in other interacting models exhibiting a phase transition.

7.5 Summary

In this chapter we explored the Kibble–Zurek mechanism in the Ising field theory. This model accommodates two types of universality, predicting different KZ scaling for ramps along the free fermion line and the E_8 integrable line, caused by the different universal scaling exponent ν for the two cases. The lattice counterpart of the free fermion model is thoroughly studied in the literature, as the dynamics can be solved exactly. Taking the scaling limit, we obtained an exact solution in the field theory and showed that the KZ scaling is intact. At the same time, the exact calculation proved the validity of our numerical approach, the TCSA, in the context of the Kibble–Zurek mechanism. In the E_8 model, we could only rely on the latter method, supplemented by arguments from adiabatic perturbation theory.

We investigated three main aspects of the Kibble–Zurek physics. The first is the dynamics at the microscopic level, which can be obtained from the numerical diagonalisation, and from the exact results, where available. Remarkably, we found that the simple scenario explaining the KZ scaling is followed almost to the letter even at the most fundamental level, which means that most of the change in the population of eigenstates is localised to the non-adiabatic period. Moreover, in the interacting E_8 model, we demonstrated that the behaviour of low-energy zero-momentum particles is analogous to the low-momentum modes of the free fermion model. In the second part we introduced a new perspective on the impulse regime of the time evolution, where we demonstrated the validity of a dynamical scaling law for the one-point functions of the theory. Finally, we extended on a recent theme of the literature, the universality of the full counting statistics of excitations after the ramp. More precisely, we focused on the cumulants of the distribution of the excess heat, and offered an argument in the context of adiabatic perturbation theory that all of the cumulants obey the KZ scaling even in an interacting model. We demonstrated this claim in the E_8 model for the first three cumulants in the case of ramp protocols ending in the critical point, and for the first two cumulants in the case of ramps crossing it.

Altogether, the results of this chapter serve as a robust demonstration of the KZ scaling laws in a nontrivial field theory. The observed scaling indicates that the arguments behind the Kibble–Zurek mechanism should apply to a generic field theory setting as well. In the case of the full distribution of excess heat, our numerical results and perturbative arguments provide particularly strong indications. Importantly, this quantity is available to experiments, e.g. using Rydberg atoms [220] to explore the Ising universality class, or in cold-atomic gases realising an interacting field theory [221]. We remark that in terms of the higher cumulants of the kink distribution in the free model, the universal scaling is already verified experimentally [65].

Chapter 8

Thesis statements

The works presented in this thesis describe the quantum many-body dynamics in low dimensions in terms of quantum field theory models both in and out of equilibrium. As a conclusion, let us summarise the novel results by the following statements:

1. I worked out the solution of the form factor bootstrap in the E_8 integrable quantum field theory. I performed a re-derivation of the recurrence relations generating the multi-particle form factors, and by solving them extended the set of matrix elements available in the earlier literature. The solution for the σ field was published in Ref. [95], while the analogous results for the ϵ operator were published in Ref. [96] with a synopsis of the form factor bootstrap. Finally, my results provided theoretical support for the experimental observation of the E_8 particle spectrum, published in Ref. [77].

2. I analysed the time evolution following a global quantum quench in the E_8 field theory. With the tools of numerical modelling I compared two analytical approaches to the post-quench dynamics with each other, and argued that the expansion on the post-quench basis is more suited to describe the time evolution, which carries the fingerprints of the equilibrium post-quench model. Most notably, I pointed out the prominent role of single-particle oscillations in the dynamical one-point functions, originating from the particle states in the post-quench spectrum. I demonstrated the validity of this claim both for integrable and non-integrable post-quench dynamics. The results were published in Ref. [94].

3. I derived a second-order perturbative expansion to post-quench overlaps applicable to generic quantum field theories in principle, and to models with at most a small integrability breaking in practice. In comparison with the numerical data I have justified the perturbative approach for quenches of moderate size in the E_8 model for one- and two-particle states. Importantly, the presence of pairs composed of different particles indicated that the

initial state is not of an integrable form. I applied the expansion to quenches with non-integrable dynamics for the lightest particles and found serious limitations otherwise. The results were published in Ref. [95].

4. I investigated the Kibble–Zurek mechanism in the Ising field theory. Exploring the parameter space, by numerically modelling ramps slowly approaching and crossing the critical point, I verified the distinct scaling predictions corresponding to the two integrable directions. In particular, I found strong evidence for the general arguments behind the Kibble–Zurek scaling in terms of various quantities from the microscopic level to dynamical scaling functions. The unique spectrum of the E_8 model allowed for a nontrivial demonstration of the scaling brought about by single-particle states. Furthermore, I offered a set of numerical and analytical arguments in support of the universal scaling of the full distribution of the excess heat induced by the non-equilibrium protocol. The results were published in Ref. [167].

Bibliography

[1] M. Planck, "Über das Gesetz der Energieverteilung im Normalspectrum," *Annalen der Physik* **309** (1901) 553–563.

[2] M. E. Peskin and D. V. Schroeder, *An Introduction to Quantum Field Theory*. Addison-Wesley, Reading, USA, 1995.

[3] G. Mussardo, *Statistical field theory: an introduction to exactly solved models in statistical physics*. Oxford Univ. Press, New York, NY, 2010.

[4] S. Sachdev, *Quantum Phase Transitions*. Cambridge University Press, 2011.

[5] B. Sutherland, *Beautiful Models: 70 Years of Exactly Solved Quantum Many-Body Problems*. World Scientific, River Edge, NJ, 2004.

[6] T. Langen, R. Geiger, and J. Schmiedmayer, "Ultracold Atoms Out of Equilibrium," *Annual Review of Condensed Matter Physics* **6** (2015) 201–217, `arXiv:1408.6377 [cond-mat.quant-gas]`.

[7] P. Calabrese, F. H. L. Essler, and G. Mussardo, "Introduction to "Quantum Integrability in Out of Equilibrium Systems"," *Journal of Statistical Mechanics: Theory and Experiment* **6** (2016) 064001.

[8] P. Calabrese and J. Cardy, "Time Dependence of Correlation Functions Following a Quantum Quench," *Physical Review Letters* **96** (2006) 136801, `cond-mat/0601225`.

[9] A. Polkovnikov, K. Sengupta, A. Silva, and M. Vengalattore, "Colloquium: Nonequilibrium dynamics of closed interacting quantum systems," *Reviews of Modern Physics* **83** (2011) 863–883, `arXiv:1007.5331 [cond-mat.stat-mech]`.

[10] J. M. Deutsch, "Quantum statistical mechanics in a closed system," *Physical Review A* **43** (1991) 2046–2049.

[11] M. Srednicki, "Chaos and quantum thermalization," *Physical Review E* **50** (1994) 888–901, `cond-mat/9403051`.

[12] L. D'Alessio, Y. Kafri, A. Polkovnikov, and M. Rigol, "From quantum chaos and eigenstate thermalization to statistical mechanics and thermodynamics," *Advances in Physics* **65** (2016) 239–362, `arXiv:1509.06411 [cond-mat.stat-mech]`.

[13] M. Rigol, V. Dunjko, and M. Olshanii, "Thermalization and its mechanism for generic isolated quantum systems," *Nature* **452** (2008) 854–858, `arXiv:0708.1324 [cond-mat.stat-mech]`.

[14] J. R. Garrison and T. Grover, "Does a Single Eigenstate Encode the Full Hamiltonian?," *Physical Review X* **8** (2018) 021026, `arXiv:1503.00729 [cond-mat.str-el]`.

[15] M. Rigol, V. Dunjko, V. Yurovsky, and M. Olshanii, "Relaxation in a Completely Integrable Many-Body Quantum System: An AbInitio Study of the Dynamics of the Highly Excited States of 1D Lattice Hard-Core Bosons," *Physical Review Letters* **98** (2007) 050405, `cond-mat/0604476`.

[16] T. Kinoshita, T. Wenger, and D. S. Weiss, "A quantum Newton's cradle," *Nature* **440** (2006) 900–903.

[17] M. Gring, M. Kuhnert, T. Langen, T. Kitagawa, B. Rauer, M. Schreitl, I. Mazets, D. A. Smith, E. Demler, and J. Schmiedmayer, "Relaxation and Prethermalization in an Isolated Quantum System," *Science* **337** (2012) 1318, `arXiv:1112.0013 [cond-mat.quant-gas]`.

[18] T. Langen, S. Erne, R. Geiger, B. Rauer, T. Schweigler, M. Kuhnert, W. Rohringer, I. E. Mazets, T. Gasenzer, and J. Schmiedmayer, "Experimental observation of a generalized Gibbs ensemble," *Science* **348** (2015) 207–211, `arXiv:1411.7185 [cond-mat.quant-gas]`.

[19] J. Berges, S. Borsányi, and C. Wetterich, "Prethermalization," *Physical Review Letters* **93** (2004) 142002, `hep-ph/0403234`.

[20] M. Kollar, F. A. Wolf, and M. Eckstein, "Generalized Gibbs ensemble prediction of prethermalization plateaus and their relation to nonthermal steady states in integrable systems," *Physical Review B* **84** (2011) 054304, `arXiv:1102.2117 [cond-mat.str-el]`.

[21] B. Bertini and M. Fagotti, "Pre-relaxation in weakly interacting models," *Journal of Statistical Mechanics: Theory and Experiment* **7** (2015) 07012, `arXiv:1501.07260 [cond-mat.stat-mech]`.

[22] B. Bertini, F. H. L. Essler, S. Groha, and N. J. Robinson, "Prethermalization and Thermalization in Models with Weak Integrability Breaking," *Physical Review Letters* **115** (2015) 180601, `arXiv:1506.02994 [cond-mat.stat-mech]`.

[23] K. Mallayya, M. Rigol, and W. De Roeck, "Prethermalization and Thermalization in Isolated Quantum Systems," *Physical Review X* **9** (2019) 021027, `arXiv:1810.12320 [cond-mat.stat-mech]`.

[24] E. Barouch, B. M. McCoy, and M. Dresden, "Statistical Mechanics of the XY Model. I," *Phys. Rev. A* **2** (1970) 1075–1092.

[25] P. Calabrese and J. Cardy, "Quantum quenches in extended systems," *Journal of Statistical Mechanics: Theory and Experiment* **6** (2007) 06008, `arXiv:0704.1880 [cond-mat.stat-mech]`.

[26] P. Calabrese and J. Cardy, "Evolution of entanglement entropy in one-dimensional systems," *Journal of Statistical Mechanics: Theory and Experiment* **4** (2005) 04010, `cond-mat/0503393`.

[27] F. H. L. Essler and M. Fagotti, "Quench dynamics and relaxation in isolated integrable quantum spin chains," *Journal of Statistical Mechanics: Theory and Experiment* **6** (2016) 064002, `arXiv:1603.06452 [cond-mat.quant-gas]`.

[28] V. Alba and P. Calabrese, "Entanglement dynamics after quantum quenches in generic integrable systems," *SciPost Physics* **4** (2018) 017, `arXiv:1712.07529 [cond-mat.stat-mech]`.

[29] M. Kormos, M. Collura, G. Takács, and P. Calabrese, "Real-time confinement following a quantum quench to a non-integrable model," *Nature Physics* **13** (2017) 246–249, `arXiv:1604.03571 [cond-mat.stat-mech]`.

[30] J.-S. Caux and F. H. L. Essler, "Time Evolution of Local Observables After Quenching to an Integrable Model," *Physical Review Letters* **110** (2013) 257203, `arXiv:1301.3806 [cond-mat.stat-mech]`.

[31] J. De Nardis, L. Piroli, and J. S. Caux, "Relaxation dynamics of local observables in integrable systems," *Journal of Physics A Mathematical General* **48** (2015) 43FT01, `arXiv:1505.03080 [cond-mat.quant-gas]`.

[32] J.-S. Caux, "The Quench Action," *Journal of Statistical Mechanics: Theory and Experiment* **6** (2016) 064006, `arXiv:1603.04689 [cond-mat.str-el]`.

[33] D. Schuricht and F. H. L. Essler, "Dynamics in the Ising field theory after a quantum quench," *Journal of Statistical Mechanics: Theory and Experiment* **4** (2012) 04017, `arXiv:1203.5080 [cond-mat.str-el]`.

[34] B. Bertini, D. Schuricht, and F. H. L. Essler, "Quantum quench in the sine-Gordon model," *Journal of Statistical Mechanics: Theory and Experiment* **10** (2014) 10035, `arXiv:1405.4813 [cond-mat.stat-mech]`.

[35] E. Lieb, T. Schultz, and D. Mattis, "Two soluble models of an antiferromagnetic chain," *Annals of Physics* **16** (1961) 407–466.

[36] P. Pfeuty, "The one-dimensional Ising model with a transverse field," *Annals of Physics* **57** (1970) 79–90.

[37] J. B. Zuber and C. Itzykson, "Quantum field theory and the two-dimensional Ising model," Phys. Rev. D **15** (1977) 2875–2884.

[38] V. A. Fateev, "The exact relations between the coupling constants and the masses of particles for the integrable perturbed conformal field theories," *Physics Letters B* **324** (1994) 45–51.

[39] A. B. Zamolodchikov, "Integrals of Motion and S-Matrix of the (scaled) $T = T_c$ Ising Model with Magnetic Field," *International Journal of Modern Physics A* **4** (1989) 4235–4248.

[40] G. Delfino and J. Viti, "On the theory of quantum quenches in near-critical systems," *Journal of Physics A Mathematical General* **50** (2017) 084004, `arXiv:1608.07612 [cond-mat.stat-mech]`.

[41] G. Delfino, G. Mussardo, and P. Simonetti, "Non-integrable quantum field theories as perturbations of certain integrable models," *Nuclear Physics B* **473** (1996) 469–508, `hep-th/9603011`.

[42] G. Delfino, P. Grinza, and G. Mussardo, "Decay of particles above threshold in the Ising field theory with magnetic field," *Nuclear Physics B* **737** (2006) 291–303, `hep-th/0507133`.

[43] B. Pozsgay and G. Takács, "Characterization of resonances using finite size effects," *Nuclear Physics B* **748** (2006) 485–523, `hep-th/0604022`.

[44] B. M. McCoy and T. T. Wu, "Two-dimensional Ising field theory in a magnetic field: Breakup of the cut in the two-point function," *Physical Review D* **18** (1978) 1259–1267.

[45] S. B. Rutkevich, "Large-n Excitations in the Ferromagnetic Ising Field Theory in a Weak Magnetic Field: Mass Spectrum and Decay Widths," *Physical Review Letters* **95** (2005) 250601, `hep-th/0509149`.

[46] P. Fonseca and A. Zamolodchikov, "Ising Spectroscopy I: Mesons at $T < T_c$," *ArXiv High Energy Physics - Theory e-prints* (2006) , `hep-th/0612304`.

[47] S. B. Rutkevich, "Formfactor perturbation expansions and confinement in the Ising field theory," *Journal of Physics A Mathematical General* **42** (2009) 304025, `arXiv:0901.1571 [cond-mat.stat-mech]`.

[48] A. Zamolodchikov, "Ising Spectroscopy II: Particles and poles at $T > T_c$," *ArXiv e-prints* (2013) , `arXiv:1310.4821 [hep-th]`.

[49] T. Rakovszky, M. Mestyán, M. Collura, M. Kormos, and G. Takács, "Hamiltonian truncation approach to quenches in the Ising field theory," *Nuclear Physics B* **911** (2016) 805–845, `arXiv:1607.01068 [cond-mat.stat-mech]`.

[50] A. LeClair and G. Mussardo, "Finite temperature correlation functions in integrable QFT," *Nuclear Physics B* **552** no. 3, (July, 1999) 624–642, `arXiv:hep-th/9902075 [hep-th]`.

[51] B. Doyon, "Finite-Temperature Form Factors: a Review," *SIGMA* **3** (2007) 011, `arXiv:hep-th/0611066 [hep-th]`.

[52] B. Pozsgay and G. Takács, "Form factor expansion for thermal correlators," *Journal of Statistical Mechanics: Theory and Experiment* **2010** no. 11, (Nov., 2010) 11012, `arXiv:1008.3810 [hep-th]`.

[53] A. J. A. James, R. M. Konik, P. Lecheminant, N. J. Robinson, and A. M. Tsvelik, "Non-perturbative methodologies for low-dimensional strongly-correlated systems: From non-Abelian bosonization to truncated spectrum methods," *Reports on Progress in Physics* **81** (2018) 046002, `arXiv:1703.08421 [cond-mat.str-el]`.

[54] P. Fonseca and A. Zamolodchikov, "Ising field theory in a magnetic field: analytic properties of the free energy," *ArXiv High Energy Physics - Theory e-prints* (2001) , `hep-th/0112167`.

[55] V. P. Yurov and A. B. Zamolodchikov, "Truncated Comformal Space Approach to Scaling Lee-Yang Model," *International Journal of Modern Physics A* **5** (1990) 3221–3245.

[56] V. P. Yurov and A. B. Zamolodchikov, "Truncated-Fermionic Approach to the Critical 2d Ising Model with Magnetic Field," *International Journal of Modern Physics A* **6** (1991) 4557–4578.

[57] M. Kormos, "Boundary renormalisation group flows of the supersymmetric Lee Yang model and its extensions," *Nuclear Physics B* **772** (2007) 227–248, `arXiv:hep-th/0701061 [hep-th]`.

[58] P. Giokas and G. Watts, "The renormalisation group for the truncated conformal space approach on the cylinder," *ArXiv e-prints* (2011) , `arXiv:1106.2448 [hep-th]`.

[59] I. M. Szécsényi, G. Takács, and G. M. T. Watts, "One-point functions in finite volume/temperature: a case study," *Journal of High Energy Physics* **8** (2013) 94, `arXiv:1304.3275 [hep-th]`.

[60] M. Lencsés and G. Takács, "Excited state TBA and renormalized TCSA in the scaling Potts model," *J. High Energy Phys.* **2014** (2014) 52, `arXiv:1405.3157`.

[61] M. Hogervorst, S. Rychkov, and B. C. van Rees, "Truncated conformal space approach in d dimensions: A cheap alternative to lattice field theory?," *Physical Review D* **91** (2015) 025005, `arXiv:1409.1581 [hep-th]`.

[62] S. Rychkov and L. G. Vitale, "Hamiltonian truncation study of the ϕ^4 theory in two dimensions," *Physical Review D* **91** (2015) 085011, `arXiv:1412.3460 [hep-th]`.

[63] S. Rychkov and L. G. Vitale, "Hamiltonian truncation study of the ϕ^4 theory in two dimensions. II. The Z_2 -broken phase and the Chang duality," *Physical Review D* **93** (2016) 065014, `arXiv:1512.00493 [hep-th]`.

[64] M. Lencsés and G. Takács, "Confinement in the q-state Potts model: an RG-TCSA study," *Journal of High Energy Physics* **9** (2015) 146, `arXiv:1506.06477 [hep-th]`.

[65] J.-M. Cui, F. J. Gómez-Ruiz, Y.-F. Huang, C.-F. Li, G.-C. Guo, and A. del Campo, "Experimentally testing quantum critical dynamics beyond the Kibble-Zurek mechanism," *Commun. Phys.* **3** (2020) 44, `arXiv:1903.02145`.

[66] J. Knaute and P. Hauke, "Relativistic meson spectra on ion-trap quantum simulators," *Phys. Rev. A* **105** (2022) 022616, `arXiv:2107.09071 [cond-mat.str-el]`.

[67] J. Simon, W. S. Bakr, R. Ma, M. E. Tai, P. M. Preiss, and M. Greiner, "Quantum simulation of antiferromagnetic spin chains in an optical lattice," *Nature* **472** (2011) 307–312, `arXiv:1103.1372 [cond-mat.quant-gas]`.

[68] F. Meinert, M. J. Mark, E. Kirilov, K. Lauber, P. Weinmann, A. J. Daley, and H.-C. Nägerl, "Quantum Quench in an Atomic One-Dimensional Ising Chain," *Physical Review Letters* **111** (2013) 053003, `arXiv:1304.2628 [cond-mat.quant-gas]`.

[69] S. Trotzky, Y.-A. Chen, A. Flesch, I. P. McCulloch, U. Schollwöck, J. Eisert, and I. Bloch, "Probing the relaxation towards equilibrium in an isolated strongly correlated one-dimensional Bose gas," *Nature Physics* **8** (2012) 325–330, `arXiv:1101.2659 [cond-mat.quant-gas]`.

[70] A. M. Kaufman, M. E. Tai, A. Lukin, M. Rispoli, R. Schittko, P. M. Preiss, and M. Greiner, "Quantum thermalization through entanglement in an isolated many-body system," *Science* **353** (2016) 794–800, `arXiv:1603.04409 [quant-ph]`.

[71] S. Hofferberth, I. Lesanovsky, B. Fischer, T. Schumm, and J. Schmiedmayer, "Non-equilibrium coherence dynamics in one-dimensional Bose gases," *Nature* **449** (2007) 324–327, `arXiv:0706.2259`.

[72] T. Langen, R. Geiger, M. Kuhnert, B. Rauer, and J. Schmiedmayer, "Local emergence of thermal correlations in an isolated quantum many-body system," *Nature Physics* **9** (2013) 640–643, `arXiv:1305.3708 [cond-mat.quant-gas]`.

[73] T. Schweigler, V. Kasper, S. Erne, I. Mazets, B. Rauer, F. Cataldini, T. Langen, T. Gasenzer, J. Berges, and J. Schmiedmayer, "Experimental characterization of a quantum many-body system via higher-order correlations," Nature **545** (2017) 323–326, `arXiv:1505.03126 [cond-mat.quant-gas]`.

[74] A. del Campo and W. H. Zurek, "Universality of Phase Transition Dynamics: Topological Defects from Symmetry Breaking," *Int. J. Mod. Phys. A* **29** (2014) 1430018, `arXiv:1310.1600`.

[75] R. Coldea, D. A. Tennant, E. M. Wheeler, E. Wawrzynska, D. Prabhakaran, M. Telling, K. Habicht, P. Smeibidl, and K. Kiefer, "Quantum Criticality in an Ising Chain: Experimental Evidence for Emergent E_8 Symmetry," *Science* **327** (2010) 177, `arXiv:1103.3694 [cond-mat.str-el]`.

[76] Q. Faure, *Quantum phase transitions in the quasi-1D Ising-like antiferromagnet BaCo2V2O8*. Theses, Université Grenoble Alpes, 2018. `https://tel.archives-ouvertes.fr/tel-02063688`.

[77] H. Zou, Y. Cui, X. Wang, Z. Zhang, J. Yang, G. Xu, A. Okutani, M. Hagiwara, M. Matsuda, G. Wang, G. Mussardo, K. Hódsági, M. Kormos, Z. He, S. Kimura, R. Yu, W. Yu, J. Ma, and J. Wu, "E_8 Spectra of Quasi-One-Dimensional Antiferromagnet $BaCo_2V_2O_8$ under Transverse Field," *Phys. Rev. Lett.* **127** (2021) 077201, `arXiv:2005.13302 [cond-mat.str-el]`.

[78] K. Amelin, J. Engelmayer, J. Viirok, U. Nagel, T. Rõõm, T. Lorenz, and Z. Wang, "Experimental observation of quantum many-body excitations of E_8 symmetry in the Ising chain ferromagnet $CoNb_2O_6$," Phys. Rev. B **102** (2020) 104431, `arXiv:2006.12956 [cond-mat.str-el]`.

[79] P. Dorey, “Exact S-matrices,” *arXiv e-prints* (1998) hep–th/9810026, `arXiv:hep-th/9810026 [hep-th]`.

[80] S. Coleman and J. Mandula, “All Possible Symmetries of the S Matrix,” *Physical Review* **159** (1967) 1251–1256.

[81] A. B. Zamolodchikov and A. B. Zamolodchikov, “Factorized S-matrices in two dimensions as the exact solutions of certain relativistic quantum field theory models,” *Annals of Physics* **120** (1979) 253–291.

[82] A. B. Zamolodchikov, “Integrable field theory from conformal field theory,” *Adv. Stud. Pure Math.* **19** (1989) 641–674.

[83] V. A. Fateev and A. B. Zamolodchikov, “Conformal Field Theory and Purely Elastic S-Matrices,” *International Journal of Modern Physics A* **5** (1990) 1025–1048.

[84] K. M. Watson, “Some General Relations between the Photoproduction and Scattering of π Mesons,” *Physical Review* **95** (1954) 228–236.

[85] F. A. Smirnov, “Form Factors In Completely Integrable Models Of Quantum Field Theory.” Advanced series in mathematical physics: Vol. 14, 1992.

[86] M. Karowski and P. Weisz, “Exact form factors in (1+1)-dimensional field theoretic models with soliton behaviour,” *Nuclear Physics B* **139** (1978) 455–476.

[87] M. Karowski, “On the bound state problem in 1+1 dimensional field theories,” *Nuclear Physics B* **153** (1979) 244–252.

[88] B. Berg, M. Karowski, and P. Weisz, “Construction of Green’s functions from an exact S matrix,” Phys. Rev. D **19** (1979) 2477–2479.

[89] G. Delfino and G. Mussardo, “The spin-spin correlation function in the two-dimensional Ising model in a magnetic field at $\mathrm{T} = \mathrm{T}_c$,” *Nuclear Physics B* **455** (1995) 724–758, `arXiv:hep-th/9507010 [hep-th]`.

[90] J. L. Cardy and G. Mussardo, “Form-factors of Descendent Operators in Perturbed Conformal Field Theories,” *Nucl. Phys. B* **340** (1990) 387–402.

[91] G. Delfino and P. Simonetti, “Correlation functions in the two-dimensional Ising model in a magnetic field at $\mathrm{T} = \mathrm{T}_c$,” *Physics Letters B* **383** (1996) 450–456, `hep-th/9605065`.

[92] `https://people.sissa.it/~delfino/isingff.html`.

[93] B. Pozsgay and G. Takács, "Form factors in finite volume I: Form factor bootstrap and truncated conformal space," *Nuclear Physics B* **788** (2008) 167–208, `arXiv:0706.1445 [hep-th]`.

[94] K. Hódsági, M. Kormos, and G. Takács, "Quench dynamics of the Ising field theory in a magnetic field," *SciPost Physics* **5** (2018) 027, `arXiv:1803.01158 [cond-mat.stat-mech]`.

[95] K. Hódsági, M. Kormos, and G. Takács, "Perturbative post-quench overlaps in quantum field theory," *Journal of High Energy Physics* **2019** (2019) 47, `arXiv:1905.05623 [cond-mat.stat-mech]`.

[96] X. Wang, H. Zou, K. Hódsági, M. Kormos, G. Takács, and J. Wu, "Cascade of singularities in the spin dynamics of a perturbed quantum critical Ising chain," *Phys. Rev. B* **103** (2021) 235117, `arXiv:2103.09128 [cond-mat.str-el]`.

[97] A. B. Zamolodchikov, ""Irreversibility" of the flux of the renormalization group in a 2D field theory," *ZhETF Pisma Redaktsiiu* **43** (1986) 565.

[98] J. L. Cardy, "Central charge and universal combinations of amplitudes in two-dimensional theories away from criticality," *Phys. Rev. Lett.* **60** (1988) 2709–2711.

[99] Wolfram Research, Inc., "Mathematica, Version 12.3.1." `https://www.wolfram.com/mathematica`. Champaign, IL, 2021.

[100] G. Delfino, P. Simonetti, and J. L. Cardy, "Asymptotic factorisation of form factors in two-dimensional quantum field theory," *Physics Letters B* **387** (1996) 327–333, `arXiv:hep-th/9607046 [hep-th]`.

[101] M. A. Cazalilla, "Effect of Suddenly Turning on Interactions in the Luttinger Model," *Physical Review Letters* **97** (2006) 156403, `cond-mat/0606236`.

[102] S. Sotiriadis, P. Calabrese, and J. Cardy, "Quantum quench from a thermal initial state," *EPL (Europhysics Letters)* **87** (2009) 20002.

[103] D. Fioretto and G. Mussardo, "Quantum quenches in integrable field theories," *New Journal of Physics* **12** (2010) 055015, `arXiv:0911.3345 [cond-mat.stat-mech]`.

[104] B. Dóra, M. Haque, and G. Zaránd, "Crossover from Adiabatic to Sudden Interaction Quench in a Luttinger Liquid," *Physical Review Letters* **106** (2011) 156406, `arXiv:1011.6655 [cond-mat.str-el]`.

[105] M. Kormos, M. Collura, and P. Calabrese, "Analytic results for a quantum quench from free to hard-core one-dimensional bosons," *Physical Review A* **89** (2014) 013609, `arXiv:1307.2142 [cond-mat.quant-gas]`.

[106] S. Sotiriadis and P. Calabrese, "Validity of the GGE for quantum quenches from interacting to noninteracting models," *Journal of Statistical Mechanics: Theory and Experiment* **7** (2014) 07024, `arXiv:1403.7431 [cond-mat.stat-mech]`.

[107] S. Sotiriadis, "Memory-preserving equilibration after a quantum quench in a one-dimensional critical model," *Physical Review A* **94** (2016) 031605, `arXiv:1507.07915 [cond-mat.stat-mech]`.

[108] S. Evangelisti, "Semi-classical theory for quantum quenches in the O(3) non-linear sigma model," *Journal of Statistical Mechanics: Theory and Experiment* **4** (2013) 04003, `arXiv:1210.4028 [cond-mat.stat-mech]`.

[109] M. Kormos and G. Zaránd, "Quantum quenches in the sine-Gordon model: A semiclassical approach," *Physical Review E* **93** (2016) 062101, `arXiv:1507.02708 [cond-mat.stat-mech]`.

[110] C. P. Moca, M. Kormos, and G. Zaránd, "Hybrid semiclassical theory of quantum quenches in one-dimensional systems," *Phys. Rev. Lett.* **119** (2016) 100603, `arXiv:1609.00974 [cond-mat.stat-mech]`.

[111] S. Sotiriadis and J. Cardy, "Quantum quench in interacting field theory: A self-consistent approximation," Phys. Rev. B **81** (2010) 134305, `arXiv:1002.0167 [quant-ph]`.

[112] Y. D. van Nieuwkerk and F. H. L. Essler, "Self-consistent time-dependent harmonic approximation for the sine-Gordon model out of equilibrium," *Journal of Statistical Mechanics: Theory and Experiment* **8** (2019) 084012, `arXiv:1812.06690 [cond-mat.quant-gas]`.

[113] Y. D. van Nieuwkerk and F. Essler, "On the low-energy description for tunnel-coupled one-dimensional Bose gases," *SciPost Physics* **9** (2020) 025, `arXiv:2003.07873 [cond-mat.quant-gas]`.

[114] G. Mussardo, "Infinite-Time Average of Local Fields in an Integrable Quantum Field Theory After a Quantum Quench," *Physical Review Letters* **111** (2013) 100401, `arXiv:1308.4551 [cond-mat.stat-mech]`.

[115] B. Bertini, L. Piroli, and P. Calabrese, "Quantum quenches in the sinh-Gordon model: steady state and one-point correlation functions," *Journal of Statistical Mechanics: Theory and Experiment* **6** (2016) 063102, `arXiv:1602.08269 [cond-mat.stat-mech]`.

[116] F. H. L. Essler, G. Mussardo, and M. Panfil, "On truncated generalized Gibbs ensembles in the Ising field theory," *Journal of Statistical Mechanics: Theory and Experiment* **1** (2017) 013103, `arXiv:1610.02495 [cond-mat.stat-mech]`.

[117] S. Sotiriadis, D. Fioretto, and G. Mussardo, "Zamolodchikov-Faddeev algebra and quantum quenches in integrable field theories," *Journal of Statistical Mechanics: Theory and Experiment* **2** (2012) 02017, `arXiv:1112.2963 [cond-mat.stat-mech]`.

[118] S. Sotiriadis, G. Takacs, and G. Mussardo, "Boundary state in an integrable quantum field theory out of equilibrium," *Physics Letters B* **734** (2014) 52–57, `arXiv:1311.4418 [cond-mat.stat-mech]`.

[119] D. X. Horváth, S. Sotiriadis, and G. Takács, "Initial states in integrable quantum field theory quenches from an integral equation hierarchy," *Nuclear Physics B* **902** (2016) 508–547, `arXiv:1510.01735 [cond-mat.stat-mech]`.

[120] D. X. Horváth and G. Takács, "Overlaps after quantum quenches in the sine-Gordon model," *Physics Letters B* **771** (2017) 539–545, `arXiv:1704.00594 [cond-mat.stat-mech]`.

[121] G. Delfino, "Quantum quenches with integrable pre-quench dynamics," *Journal of Physics A Mathematical General* **47** (2014) 402001, `arXiv:1405.6553 [cond-mat.stat-mech]`.

[122] A. Cortés Cubero and D. Schuricht, "Quantum quench in the attractive regime of the sine-Gordon model," *Journal of Statistical Mechanics: Theory and Experiment* **10** (2017) 103106, `arXiv:1707.09218 [cond-mat.stat-mech]`.

[123] D. X. Horváth, M. Kormos, and G. Takács, "Overlap singularity and time evolution in integrable quantum field theory," *Journal of High Energy Physics* **2018** (2018) 170, `arXiv:1805.08132 [cond-mat.stat-mech]`.

[124] M. Lässig, G. Mussardo, and J. L. Cardy, "The scaling region of the tricritical Ising model in two dimensions," *Nuclear Physics B* **348** (1991) 591–618.

[125] G. Feverati, F. Ravanini, and G. Takács, "Truncated conformal space at c=1, nonlinear integral equation and quantization rules for multi-soliton states," *Physics Letters B* **430** (1998) 264–273, `hep-th/9803104`.

[126] A. Coser, M. Beria, G. P. Brandino, R. M. Konik, and G. Mussardo, "Truncated conformal space approach for 2D Landau-Ginzburg theories," *Journal of Statistical Mechanics: Theory and Experiment* **12** (2014) 12010, `arXiv:1409.1494 [hep-th]`.

[127] Z. Bajnok and M. Lajer, "Truncated Hilbert space approach to the 2d ϕ^4 theory," *J. High Energy Phys.* **2016** (2016) 50, `arXiv:1512.06901`.

[128] M. Beria, G. P. Brandino, L. Lepori, R. M. Konik, and G. Sierra, "Truncated conformal space approach for perturbed Wess-Zumino-Witten SU(2 models," *Nuclear Physics B* **877** (2013) 457–483, `arXiv:1301.0084 [hep-th]`.

[129] R. M. Konik, T. Pálmai, G. Takács, and A. M. Tsvelik, "Studying the perturbed Wess-Zumino-Novikov-Witten $SU(2)_k$ theory using the truncated conformal spectrum approach," *Nuclear Physics B* **899** (2015) 547–569, `arXiv:1505.03860 [cond-mat.str-el]`.

[130] P. Azaria, R. M. Konik, P. Lecheminant, T. Pálmai, G. Takács, and A. M. Tsvelik, "Particle formation and ordering in strongly correlated fermionic systems: Solving a model of quantum chromodynamics," Phys. Rev. D **94** (2016) 045003, `arXiv:1601.02979 [hep-th]`.

[131] G. P. Brandino, J.-S. Caux, and R. M. Konik, "Glimmers of a Quantum KAM Theorem: Insights from Quantum Quenches in One-Dimensional Bose Gases," *Physical Review X* **5** (2015) 041043, `arXiv:1407.7167 [cond-mat.str-el]`.

[132] A. J. A. James and R. M. Konik, "Quantum quenches in two spatial dimensions using chain array matrix product states," *Physical Review B* **92** (2015) 161111, `arXiv:1504.00237 [cond-mat.stat-mech]`.

[133] I. Kukuljan, S. Sotiriadis, and G. Takacs, "Correlation Functions of the Quantum Sine-Gordon Model in and out of Equilibrium," Phys. Rev. Lett. **121** (2018) 110402, `arXiv:1802.08696 [cond-mat.stat-mech]`.

[134] A. J. A. James, R. M. Konik, and N. J. Robinson, "Nonthermal States Arising from Confinement in One and Two Dimensions," *Phys. Rev. Lett.* **122** (2019) 130603, `arXiv:1804.09990`.

[135] I. Kukuljan, S. Sotiriadis, and G. Takács, "Out-of-horizon correlations following a quench in a relativistic quantum field theory," *Journal of High Energy Physics* **2020** (2020) 224, `arXiv:1906.02750 [cond-mat.stat-mech]`.

[136] D. X. Horváth, M. Kormos, S. Sotiriadis, and G. Takács, "Inhomogeneous quantum quenches in the sine-Gordon theory," *arXiv e-prints* (2021) arXiv:2109.06869, `arXiv:2109.06869 [cond-mat.str-el]`.

[137] D. Szász-Schagrin, I. Lovas, and G. Takács, "Quantum quenches in an interacting field theory: Full quantum evolution versus semiclassical approximations," Phys. Rev. B **105** (2022) 014305, `arXiv:2110.01636 [cond-mat.stat-mech]`.

[138] V. Fateev, S. Lukyanov, A. Zamolodchikov, and A. Zamolodchikov, "Expectation values of local fields in the Bullough-Dodd model and integrable perturbed conformal field theories," *Nuclear Physics B* **516** (1998) 652–674, `hep-th/9709034`.

[139] J. Loschmidt, "Über den Zustand des Wärmegleichgewichts eines Systems von Körpern mit Rücksicht auf die Schwerkraft," *Sitzungsberichte der Akademie der Wissenschaften, Wien* **II. 73** (1876) 128–142.

[140] M. Heyl, A. Polkovnikov, and S. Kehrein, "Dynamical Quantum Phase Transitions in the Transverse-Field Ising Model," *Physical Review Letters* **110** (2013) 135704, `arXiv:1206.2505 [cond-mat.stat-mech]`.

[141] K. K. Kozlowski and B. Pozsgay, "Surface free energy of the open XXZ spin-1/2 chain," *Journal of Statistical Mechanics: Theory and Experiment* **5** (2012) 05021, `arXiv:1201.5884 [nlin.SI]`.

[142] J. De Nardis, B. Wouters, M. Brockmann, and J.-S. Caux, "Solution for an interaction quench in the Lieb-Liniger Bose gas," *Physical Review A* **89** (2014) 033601, `arXiv:1308.4310 [cond-mat.stat-mech]`.

[143] B. Wouters, J. De Nardis, M. Brockmann, D. Fioretto, M. Rigol, and J.-S. Caux, "Quenching the Anisotropic Heisenberg Chain: Exact Solution and Generalized Gibbs Ensemble Predictions," *Physical Review Letters* **113** (2014) 117202, `arXiv:1405.0172 [cond-mat.str-el]`.

[144] M. Brockmann, B. Wouters, D. Fioretto, J. De Nardis, R. Vlijm, and J.-S. Caux, "Quench action approach for releasing the Néel state into the spin-1/2 XXZ chain," *Journal of Statistical Mechanics: Theory and Experiment* **12** (2014) 12009, `arXiv:1408.5075 [cond-mat.str-el]`.

[145] M. Brockmann, J. De Nardis, B. Wouters, and J.-S. Caux, "A Gaudin-like determinant for overlaps of Néel and XXZ Bethe states," *Journal of Physics A Mathematical General* **47** (2014) 145003, `arXiv:1401.2877 [cond-mat.stat-mech]`.

[146] B. Pozsgay, "Overlaps between eigenstates of the XXZ spin-1/2 chain and a class of simple product states," *Journal of Statistical Mechanics: Theory and Experiment* **6** (2014) 06011, `arXiv:1309.4593 [cond-mat.stat-mech]`.

[147] M. Brockmann, "Overlaps of q-raised Néel states with XXZ Bethe states and their relation to the Lieb-Liniger Bose gas," *Journal of Statistical Mechanics: Theory and Experiment* **5** (2014) 05006, `arXiv:1402.1471 [cond-mat.stat-mech]`.

[148] M. Brockmann, J. De Nardis, B. Wouters, and J.-S. Caux, "Néel-XXZ state overlaps: odd particle numbers and Lieb-Liniger scaling limit," *Journal of Physics A Mathematical General* **47** (2014) 345003, `arXiv:1403.7469 [cond-mat.stat-mech]`.

[149] L. Piroli, P. Calabrese, and F. H. L. Essler, "Multiparticle Bound-State Formation following a Quantum Quench to the One-Dimensional Bose Gas with Attractive Interactions," *Physical Review Letters* **116** (2016) 070408, `arXiv:1509.08234 [cond-mat.quant-gas]`.

[150] M. Mestyán, B. Bertini, L. Piroli, and P. Calabrese, "Exact solution for the quench dynamics of a nested integrable system," *Journal of Statistical Mechanics: Theory and Experiment* **8** (2017) 083103, `arXiv:1705.00851 [cond-mat.stat-mech]`.

[151] B. Pozsgay, "Overlaps with arbitrary two-site states in the XXZ spin chain," *Journal of Statistical Mechanics: Theory and Experiment* **5** (2018) 053103, `arXiv:1801.03838 [cond-mat.stat-mech]`.

[152] Y. Jiang and B. Pozsgay, "On exact overlaps in integrable spin chains," *Journal of High Energy Physics* **2020** (2020) 22, `arXiv:2002.12065 [cond-mat.stat-mech]`.

[153] T. Gombor and B. Pozsgay, "On factorized overlaps: Algebraic Bethe Ansatz, twists, and separation of variables," *Nuclear Physics B* **967** (2021) 115390, `arXiv:2101.10354 [cond-mat.stat-mech]`.

[154] M. de Leeuw, C. Kristjansen, and K. Zarembo, "One-point functions in defect CFT and integrability," *Journal of High Energy Physics* **2015** (2015) 98, `arXiv:1506.06958 [hep-th]`.

[155] O. Foda and K. Zarembo, "Overlaps of Partial Neel States and Bethe States," *Journal of Statistical Mechanics* **1602** (2016) 023107, `arXiv:1512.02533 [hep-th]`.

[156] I. Buhl-Mortensen, M. de Leeuw, C. Kristjansen, and K. Zarembo, "One-point functions in AdS/dCFT from matrix product states," *Journal of High Energy Physics* **2016** (2016) 52, `arXiv:1512.02532 [hep-th]`.

[157] M. de Leeuw, C. Kristjansen, and S. Mori, "AdS/dCFT one-point functions of the SU(3) sector," *Physics Letters B* **763** (2016) 197–202, `arXiv:1607.03123 [hep-th]`.

[158] P. Ruggiero, P. Calabrese, L. Foini, and T. Giamarchi, "Quenches in initially coupled Tomonaga-Luttinger Liquids: a conformal field theory approach," *SciPost Physics* **11** (2021) 055, `arXiv:2103.08927 [cond-mat.stat-mech]`.

[159] L. Piroli, B. Pozsgay, and E. Vernier, “What is an integrable quench?,” *Nuclear Physics B* **925** (2017) 362–402, `arXiv:1709.04796 [cond-mat.stat-mech]`.

[160] B. Pozsgay, L. Piroli, and E. Vernier, “Integrable Matrix Product States from boundary integrability,” *SciPost Physics* **6** (2019) 062, `arXiv:1812.11094 [cond-mat.stat-mech]`.

[161] S. Ghoshal and A. Zamolodchikov, “Boundary S Matrix and Boundary State in Two-Dimensional Integrable Quantum Field Theory,” *International Journal of Modern Physics A* **9** (1994) 3841–3885, `hep-th/9306002`.

[162] D. Schuricht, “Quantum quenches in integrable systems: constraints from factorisation,” *Journal of Statistical Mechanics: Theory and Experiment* **11** (2015) 11004, `arXiv:1509.00435 [cond-mat.stat-mech]`.

[163] A. Cortés Cubero, G. Mussardo, and M. Panfil, “Quench dynamics in two-dimensional integrable SUSY models,” *Journal of Statistical Mechanics: Theory and Experiment* **3** (2016) 033115, `arXiv:1511.02712 [cond-mat.stat-mech]`.

[164] A. Cortés Cubero, “Planar quantum quenches: computation of exact time-dependent correlation functions at large N,” *Journal of Statistical Mechanics: Theory and Experiment* **8** (2016) 083107, `arXiv:1604.03879 [cond-mat.stat-mech]`.

[165] M. Kormos and B. Pozsgay, “One-point functions in massive integrable QFT with boundaries,” *Journal of High Energy Physics* **4** (2010) 112, `arXiv:1002.2783 [hep-th]`.

[166] B. Pozsgay and G. Takács, “Form factors in finite volume II: Disconnected terms and finite temperature correlators,” *Nuclear Physics B* **788** (2008) 209–251, `arXiv:0706.3605 [hep-th]`.

[167] K. Hódsági and M. Kormos, “Kibble–Zurek mechanism in the Ising Field Theory,” *SciPost Physics* **9** (2020) 055, `arXiv:2007.08990 [cond-mat.stat-mech]`.

[168] D. X. Horvath, K. Hodsagi, and G. Takacs, “Chirally Factorised Truncated Conformal Space Approach,” *arXiv e-prints* (2022) arXiv:2201.06509, `arXiv:2201.06509 [hep-th]`.

[169] R. Konik, M. Lájer, and G. Mussardo, “Approaching the self-dual point of the sinh-Gordon model,” *JHEP* **2021** (2021) 14, `arXiv:2007.00154 [hep-th]`.

[170] A. A. Belavin, A. M. Polyakov, and A. B. Zamolodchikov, "Infinite conformal symmetry in two-dimensional quantum field theory," *Nuclear Physics B* **241** (1984) 333–380.

[171] H. Kausch, G. Takács, and G. Watts, "On the relation between $\Phi_{(1,2)}$ and $\Phi_{(1,5)}$ perturbed minimal models and unitarity," *Nucl. Phys. B* **489** (1997) 557–579, `arXiv:hep-th/9605104 [hep-th]`.

[172] M. Kormos, "Boundary renormalisation group flows of unitary superconformal minimal models," *Nucl. Phys. B* **744** (2006) 358–379, `arXiv:hep-th/0512085 [hep-th]`.

[173] A. M. Polyakov, "Nonhamiltonian approach to conformal quantum field theory," *Zh. Eksp. Teor. Fiz.* **66** (1974) 23–42.

[174] T. R. Klassen and E. Melzer, "The thermodynamics of purely elastic scattering theories and conformal perturbation theory," *Nucl. Phys. B* **350** (1991) 635–689.

[175] A. B. Zamolodchikov, "Thermodynamic Bethe Ansatz in Relativistic Models. Scaling Three State Potts and Lee-yang Models," *Nucl. Phys. B* **342** (1990) 695–720.

[176] T. R. Klassen and E. Melzer, "On the relation between scattering amplitudes and finite-size mass corrections in QFT," *Nucl. Phys. B* **362** (1991) 329–388.

[177] M. Luscher, "Volume Dependence of the Energy Spectrum in Massive Quantum Field Theories. 1. Stable Particle States," *Commun. Math. Phys.* **104** (1986) 177.

[178] T. W. B. Kibble, "Topology of cosmic domains and strings," *J. Phys. A. Math. Gen.* **9** (1976) 1387–1398.

[179] T. W. B. Kibble, "Some implications of a cosmological phase transition," *Phys. Rep.* **67** (1980) 183–199.

[180] W. H. Zurek, "Cosmological experiments in superfluid helium?," *Nature* **317** (1985) 505–508.

[181] W. H. Zurek, "Cosmological experiments in condensed matter systems," *Phys. Rep.* **276** (1996) 177–221.

[182] J. Dziarmaga, "Dynamics of a quantum phase transition and relaxation to a steady state," *Adv. Phys.* **59** (2010) 1063–1189, `arXiv:0912.4034`.

[183] S. Deng, G. Ortiz, and L. Viola, "Dynamical non-ergodic scaling in continuous finite-order quantum phase transitions," *EPL (Europhysics Lett.* **84** (2008) 67008, `arXiv:0809.2831`.

[184] M. Kolodrubetz, B. K. Clark, and D. A. Huse, “Nonequilibrium Dynamic Critical Scaling of the Quantum Ising Chain,” *Phys. Rev. Lett.* **109** (2012) 015701, `arXiv:1112.6422`.

[185] A. Chandran, A. Erez, S. S. Gubser, and S. L. Sondhi, “The Kibble-Zurek Problem: Universality and the Scaling Limit,” *Phys. Rev. B* **86** (2012) 064304, `arXiv:1202.5277`.

[186] A. Francuz, J. Dziarmaga, B. Gardas, and W. H. Zurek, “Space and time renormalization in phase transition dynamics,” *Phys. Rev. B* **93** (2016) 075134, `arXiv:1510.06132`.

[187] C. Zener, “Non-Adiabatic Crossing of Energy Levels,” *Proceedings of the Royal Society of London Series A* **137** (1932) 696–702.

[188] B. Damski, “The simplest quantum model supporting the Kibble-Zurek mechanism of topological defect production: Landau-Zener transitions from a new perspective.,” *Phys. Rev. Lett.* **95** (2005) 035701.

[189] J. Dziarmaga, “Dynamics of quantum phase transition: exact solution in quantum Ising model,” *Phys. Rev. Lett.* **95** (2005) 245701, `arXiv:0509490 [cond-mat]`.

[190] A. Polkovnikov, “Universal adiabatic dynamics in the vicinity of a quantum critical point,” *Phys. Rev. B* **72** (2005) 161201.

[191] C. De Grandi, R. A. Barankov, and A. Polkovnikov, “Adiabatic nonlinear probes of one-dimensional bose gases.,” *Phys. Rev. Lett.* **101** (2008) 230402.

[192] C. De Grandi, V. Gritsev, and A. Polkovnikov, “Quench dynamics near a quantum critical point: Application to the sine-Gordon model,” *Phys. Rev. B* **81** (2010) 224301, `arXiv:0910.0876`.

[193] C. De Grandi, V. Gritsev, and A. Polkovnikov, “Quench dynamics near a quantum critical point,” *Physical Review B* **81** (2010) 012303.

[194] Z. Fei, N. Freitas, V. Cavina, H. T. Quan, and M. Esposito, “Work Statistics across a Quantum Phase Transition,” *Physical Review Letters* **124** (2020) 170603, `arXiv:2002.07860`.

[195] F. Pollmann, S. Mukerjee, A. G. Green, and J. E. Moore, “Dynamics after a sweep through a quantum critical point,” *Phys. Rev. E* **81** (2010) 020101, `arXiv:0907.3206`.

[196] P. Silvi, G. Morigi, T. Calarco, and S. Montangero, “Crossover from Classical to Quantum Kibble-Zurek Scaling,” Phys. Rev. Lett. **116** (2016) 225701, `arXiv:1510.07941 [quant-ph]`.

[197] M. Gerster, B. Haggenmiller, F. Tschirsich, P. Silvi, and S. Montangero, "Dynamical Ginzburg criterion for the quantum-classical crossover of the Kibble-Zurek mechanism," Phys. Rev. B **100** (2019) 024311, `arXiv:1807.10611 [quant-ph]`.

[198] D. M. Kennes, C. Karrasch, and A. J. Millis, "Loschmidt-amplitude wave function spectroscopy and the physics of dynamically driven phase transitions," *Phys. Rev. B* **101** (2020) 081106, `arXiv:1809.00733`.

[199] P. Smacchia and A. Silva, "Work distribution and edge singularities for generic time-dependent protocols in extended systems," *Phys. Rev. E* **88** (2013) 042109, `arXiv:1305.2822`.

[200] S. R. Das, D. A. Galante, and R. C. Myers, "Quantum quenches in free field theory: universal scaling at any rate," *J. High Energy Phys.* **2016** (2016) 164, `arXiv:1602.08547`.

[201] D. Schuricht and T. Puskarov, "Time evolution during and after finite-time quantum quenches in the transverse-field Ising chain," *SciPost Phys.* **1** (2016) 003, `arXiv:1608.05584`.

[202] E. G. D. Torre, E. Demler, and A. Polkovnikov, "Universal Rephasing Dynamics after a Quantum Quench via Sudden Coupling of Two Initially Independent Condensates," *Phys. Rev. Lett.* **110** (2012) 090404, `arXiv:1211.5145`.

[203] P. Basu and S. R. Das, "Quantum Quench across a Holographic Critical Point," *J. High Energy Phys.* **2012** (2011) 103, `arXiv:1109.3909`.

[204] P. Basu, D. Das, S. R. Das, and T. Nishioka, "Quantum Quench Across a Zero Temperature Holographic Superfluid Transition," `arXiv:1211.7076`.

[205] P. Basu, D. Das, S. R. Das, and K. Sengupta, "Quantum Quench and Double Trace Couplings," `arXiv:1308.4061`.

[206] J. Sonner, A. del Campo, and W. H. Zurek, "Universal far-from-equilibrium Dynamics of a Holographic Superconductor," `arXiv:1406.2329`.

[207] M. Natsuume and T. Okamura, "Kibble-Zurek scaling in holography," *Phys. Rev. D* **95** (2017) 106009, `arXiv:1703.00933`.

[208] G. Rigolin, G. Ortiz, and V. H. Ponce, "Beyond the quantum adiabatic approximation: Adiabatic perturbation theory," *Phys. Rev. A* **78** (2008) 052508, `arXiv:0807.1363 [quant-ph]`.

[209] V. Gritsev and A. Polkovnikov, "Universal Dynamics Near Quantum Critical Points," `arXiv:0910.3692`.

[210] C. D. Grandi and A. Polkovnikov, "Adiabatic perturbation theory: from Landau-Zener problem to quenching through a quantum critical point," in *Quantum Quenching, Annealing and Computation*, A. K. Chandra, A. Das, and B. K. Chakrabarti, eds., vol. 802 of *Lecture Notes in Physics*, pp. 75–114. Springer Berlin Heidelberg, Berlin, Heidelberg, 2010.

[211] C. De Grandi, A. Polkovnikov, and A. W. Sandvik, "Universal nonequilibrium quantum dynamics in imaginary time," *Phys. Rev. B* **84** (2011) 224303.

[212] The MathWorks Inc., "Matlab, Version 9.9.0 (r2020b)." `https://www.mathworks.com/products/matlab.html`. Natick, MA, 2020.

[213] M. Campisi, P. Hänggi, and P. Talkner, "Colloquium: Quantum fluctuation relations: Foundations and applications," *Reviews of Modern Physics* **83** (2011) 771–791, `arXiv:1012.2268 [cond-mat.stat-mech]`.

[214] W. H. Zurek, U. Dorner, and P. Zoller, "Dynamics of a Quantum Phase Transition," *Phys. Rev. Lett.* **95** (2005) 105701.

[215] L. Cincio, J. Dziarmaga, M. Rams, and W. Zurek, "Entropy of entanglement and correlations induced by a quench: Dynamics of a quantum phase transition in the quantum Ising model," *Phys. Rev. A* **75** (2007) 052321, `arXiv:0701768 [cond-mat]`.

[216] P. Calabrese, F. H. L. Essler, and M. Fagotti, "Quantum quench in the transverse field Ising chain: I. Time evolution of order parameter correlators," *Journal of Statistical Mechanics: Theory and Experiment* **7** (2012) 07016, `arXiv:1204.3911 [cond-mat.quant-gas]`.

[217] A. del Campo, "Universal Statistics of Topological Defects Formed in a Quantum Phase Transition," *Phys. Rev. Lett.* **121** (2018) 200601, `arXiv:1806.10646`.

[218] F. J. Gómez-Ruiz, J. J. Mayo, and A. del Campo, "Full Counting Statistics of Topological Defects after Crossing a Phase Transition," *Physical Review Letters* **124** (2020) 240602, `arXiv:1912.04679`.

[219] P. Smacchia and A. Silva, "Universal Energy Distribution of Quasiparticles Emitted in a Local Time-Dependent Quench," *Phys. Rev. Lett.* **109** (2012) 037202, `arXiv:1203.1815`.

[220] A. Keesling, A. Omran, H. Levine, H. Bernien, H. Pichler, S. Choi, R. Samajdar, S. Schwartz, P. Silvi, S. Sachdev, P. Zoller, M. Endres, M. Greiner, V. Vuletić, and M. D. Lukin, "Quantum Kibble–Zurek mechanism and critical dynamics on a programmable Rydberg simulator," *Nature* **568** (2019) 207–211.

[221] M. Pigneur, T. Berrada, M. Bonneau, T. Schumm, E. Demler, and J. Schmiedmayer, “Relaxation to a Phase-Locked Equilibrium State in a One-Dimensional Bosonic Josephson Junction,” *Physical Review Letters* **120** (2018) 173601, `arXiv:1711.06635`.

[222] T. R. Klassen and E. Melzer, “Purely Elastic Scattering Theories and their Ultraviolet Limits,” *Nucl. Phys. B* **338** (1990) 485–528.

Appendix A

Details of the E_8 bootstrap

A.1 Elementary building blocks

As discussed in the main text, the form factor bootstrap builds on the exactly known S-matrix, calculated in the context of S-matrix bootstrap. In the E_8 model all scatterings are diagonal, hence the complete S-matrix is built up of $8 \cdot (8-1)/2 = 56$ blocks: this is the number of possible pairings between the 8 particles. The full S-matrix of the E_8 model was conjectured by Zamolodchikov [39, 82] and later on verified through thermodynamic Bethe Ansatz calculations by Klaasen and Melzer [222]. The two-body scatterings factorise to products of the elementary function [89]

$$(k)_\vartheta = \frac{\sinh \vartheta + i \sin \pi k/30}{\sinh \vartheta - i \sin \pi k/30} \,. \tag{A.1}$$

We present the full S-matrix in Table A.1. For each possible pairing ab we list the (k) factors appearing in the corresponding S-matrix block S_{ab}. When a particle A_c is a bound state of the ab pairing, a bold number **c** is printed in the overset of the (k) factor which determines the so-called fusion angle, the rapidity difference where the bound state pole appears. Most notable are the bound states of various pairings of the three lightest particles, as they were used repeatedly in the construction of the new form factors. In many cases, the same (k) factor appears multiple times in a single S_{ab} block, this is denoted by superscript: when calculating the S-matrix, the appropriate power must be taken. Formally, S_{ab} can be expressed as

$$S_{ab}(\vartheta) = \prod_{k \in \mathcal{A}_{ab}} \left[(k)_\vartheta\right]^{p_k} \,, \tag{A.2}$$

where $\mathcal{A}_{ab}$ denotes that the product is taken over the entries in the cell corresponding to the ab pairing of Table A.1, and p_k are the multiplicities of a single k block, i.e. the superscripts appearing in the table.

Calculating the S-matrix pins down the minimal form factors introduced in the main text. More precisely, they are completely fixed as those solutions of

$a\,b$	$\mathcal{A}_{ab}$	$a\,b$	$\mathcal{A}_{ab}$
1 1	$\overset{\mathbf{1}}{(20)}\ \overset{\mathbf{2}}{(12)}\ \overset{\mathbf{3}}{(2)}$	3 6	$\overset{\mathbf{2}}{(26)}\ \overset{\mathbf{3}}{(24)}^3\ \overset{\mathbf{6}}{(18)}^3\ \overset{\mathbf{8}}{(8)}^3\ (10)^2\ (16)^4$
1 2	$\overset{\mathbf{1}}{(24)}\ \overset{\mathbf{2}}{(18)}\ \overset{\mathbf{3}}{(14)}\ \overset{\mathbf{4}}{(8)}$	3 7	$\overset{\mathbf{3}}{(28)}\ \overset{\mathbf{5}}{(22)}^3\ (4)^2\ (6)^2\ (10)^4\ (12)^4\ (16)^4$
1 3	$\overset{\mathbf{1}}{(29)}\ \overset{\mathbf{2}}{(21)}\ \overset{\mathbf{4}}{(13)}\ \overset{\mathbf{5}}{(3)}\ (11)^2$	3 8	$\overset{\mathbf{5}}{(27)}\ \overset{\mathbf{6}}{(25)}^3\ \overset{\mathbf{8}}{(17)}^5\ (7)^4\ (9)^4\ (11)^2\ (15)^3$
1 4	$\overset{\mathbf{2}}{(25)}\ \overset{\mathbf{3}}{(21)}\ \overset{\mathbf{4}}{(17)}\ \overset{\mathbf{5}}{(11)}\ \overset{\mathbf{6}}{(7)}\ (15)$	4 4	$\overset{\mathbf{1}}{(26)}\ \overset{\mathbf{4}}{(20)}^3\ \overset{\mathbf{6}}{(16)}^3\ \overset{\mathbf{7}}{(12)}^3\ \overset{\mathbf{8}}{(2)}\ (6)^2\ (8)^2$
1 5	$\overset{\mathbf{3}}{(28)}\ \overset{\mathbf{4}}{(22)}\ \overset{\mathbf{6}}{(14)}\ \overset{\mathbf{7}}{(4)}\ (10)^2\ (12)^2$	4 5	$\overset{\mathbf{1}}{(27)}\ \overset{\mathbf{3}}{(23)}^3\ \overset{\mathbf{5}}{(19)}^3\ \overset{\mathbf{8}}{(9)}^3\ (5)^2\ (13)^4\ (15)^2$
1 6	$\overset{\mathbf{4}}{(25)}\ \overset{\mathbf{5}}{(19)}\ \overset{\mathbf{7}}{(9)}\ (7)^2\ (13)^2\ (15)$	4 6	$\overset{\mathbf{1}}{(28)}\ \overset{\mathbf{4}}{(22)}^3\ (4)^2\ (6)^2\ (10)^4\ (12)^4\ (16)^4$
1 7	$\overset{\mathbf{5}}{(27)}\ \overset{\mathbf{6}}{(23)}\ \overset{\mathbf{8}}{(5)}\ (9)^2\ (11)^2\ (13)^2\ (15)$	4 7	$\overset{\mathbf{2}}{(28)}\ \overset{\mathbf{4}}{(24)}^3\ \overset{\mathbf{7}}{(18)}^5\ \overset{\mathbf{8}}{(14)}^5\ (4)^2\ (8)^4\ (10)^4$
1 8	$\overset{\mathbf{7}}{(26)}\ \overset{\mathbf{8}}{(16)}^3\ (6)^2\ (8)^2\ (10)^2\ (12)^2$	4 8	$\overset{\mathbf{4}}{(29)}\ \overset{\mathbf{5}}{(25)}^3\ \overset{\mathbf{7}}{(21)}^5\ (3)^2\ (7)^4\ (11)^6\ (13)^6\ (15)^3$
2 2	$\overset{\mathbf{1}}{(24)}\ \overset{\mathbf{2}}{(20)}\ \overset{\mathbf{4}}{(14)}\ \overset{\mathbf{5}}{(8)}\ \overset{\mathbf{6}}{(2)}\ (12)^2$	5 5	$\overset{\mathbf{4}}{(22)}^3\ \overset{\mathbf{5}}{(20)}^5\ \overset{\mathbf{8}}{(12)}^5\ (2)^2\ (4)^2\ (6)^2\ (16)^4$
2 3	$\overset{\mathbf{1}}{(25)}\ \overset{\mathbf{3}}{(19)}\ \overset{\mathbf{6}}{(9)}\ (7)^2\ (13)^2\ (15)$	5 6	$\overset{\mathbf{1}}{(27)}\ \overset{\mathbf{2}}{(25)}^3\ \overset{\mathbf{7}}{(17)}^5\ (7)^4\ (9)^4\ (11)^4\ (15)^3$
2 4	$\overset{\mathbf{1}}{(27)}\ \overset{\mathbf{2}}{(23)}\ \overset{\mathbf{7}}{(5)}\ (9)^2\ (11)^2\ (13)^2\ (15)$	5 7	$\overset{\mathbf{1}}{(29)}\ \overset{\mathbf{3}}{(25)}^3\ \overset{\mathbf{6}}{(21)}^5\ (3)^2\ (7)^4\ (11)^6\ (13)^6\ (15)^3$
2 5	$\overset{\mathbf{2}}{(26)}\ \overset{\mathbf{6}}{(16)}^3\ (6)^2\ (8)^2\ (10)^2\ (12)^2$	5 8	$\overset{\mathbf{3}}{(28)}\ \overset{\mathbf{4}}{(26)}^3\ \overset{\mathbf{5}}{(24)}^5\ \overset{\mathbf{8}}{(18)}^7\ (8)^6\ (10)^6\ (16)^8$
2 6	$\overset{\mathbf{2}}{(29)}\ \overset{\mathbf{3}}{(25)}\ \overset{\mathbf{5}}{(19)}^3\ \overset{\mathbf{7}}{(13)}^3\ \overset{\mathbf{8}}{(3)}\ (7)^2\ (9)^2\ (15)$	6 6	$\overset{\mathbf{3}}{(24)}^3\ \overset{\mathbf{6}}{(20)}^5\ \overset{\mathbf{8}}{(14)}^5\ (2)^2\ (4)^2\ (8)^4\ (12)^6$
2 7	$\overset{\mathbf{4}}{(27)}\ \overset{\mathbf{6}}{(21)}^3\ \overset{\mathbf{7}}{(17)}^3\ \overset{\mathbf{8}}{(11)}^3\ (5)^2\ (7)^2\ (15)^2$	6 7	$\overset{\mathbf{1}}{(28)}\ \overset{\mathbf{2}}{(26)}^3\ \overset{\mathbf{5}}{(22)}^5\ \overset{\mathbf{8}}{(16)}^7\ (6)^4\ (10)^6\ (12)^6$
2 8	$\overset{\mathbf{6}}{(28)}\ \overset{\mathbf{7}}{(22)}^3\ (4)^2\ (6)^2\ (10)^4\ (12)^4\ (16)^4$	6 8	$\overset{\mathbf{2}}{(29)}\ \overset{\mathbf{3}}{(27)}^3\ \overset{\mathbf{6}}{(23)}^5\ \overset{\mathbf{7}}{(21)}^7\ (5)^4\ (11)^8\ (13)^8\ (15)^4$
3 3	$\overset{\mathbf{2}}{(22)}\ \overset{\mathbf{3}}{(20)}^3\ \overset{\mathbf{5}}{(14)}\ \overset{\mathbf{6}}{(12)}^3\ \overset{\mathbf{7}}{(4)}\ (2)^2$	7 7	$\overset{\mathbf{2}}{(26)}^3\ \overset{\mathbf{4}}{(24)}^5\ \overset{\mathbf{7}}{(20)}^7\ (2)^2\ (8)^6\ (12)^8\ (16)^8$
3 4	$\overset{\mathbf{1}}{(26)}\ \overset{\mathbf{5}}{(16)}^3\ (6)^2\ (8)^2\ (10)^2\ (12)^2$	7 8	$\overset{\mathbf{1}}{(29)}\ \overset{\mathbf{2}}{(27)}^3\ \overset{\mathbf{4}}{(25)}^5\ \overset{\mathbf{6}}{(23)}^7\ \overset{\mathbf{8}}{(19)}^9\ (9)^8\ (13)^{10}\ (15)^5$
3 5	$\overset{\mathbf{1}}{(29)}\ \overset{\mathbf{3}}{(23)}\ \overset{\mathbf{4}}{(21)}^3\ \overset{\mathbf{7}}{(13)}^3\ \overset{\mathbf{8}}{(5)}\ (3)^2\ (11)^4\ (15)$	8 8	$\overset{\mathbf{1}}{(28)}^3\ \overset{\mathbf{3}}{(26)}^5\ \overset{\mathbf{5}}{(24)}^7\ \overset{\mathbf{7}}{(22)}^9\ \overset{\mathbf{8}}{(20)}^{11}\ (12)^{12}\ (16)^{12}$

Table A.1: The full S-matrix of the E_8 model. For each pairing the scattering matrix is the product of $(k)_\vartheta$ factors denoted by parentheses. Superscript stands for the appropriate power, while the bold number $\mathbf{c}$ in the overset signals the presence of a bound state A_c in the A_aA_b channel, at the rapidity difference where the corresponding (k) factor has a pole.

Watson's equations for $n = 2$, that fulfil the following criteria: first, they have no poles nor zeros in the strip $\mathrm{Im}\,\vartheta \in (0, 2\pi)$, and second, they are minimally increasing as $|\vartheta| \to \infty$ [89]. These constraints identify the minimal form factors to be

$$F_{ab}^{\min}(\vartheta) = \left(-i\sinh\frac{\vartheta}{2}\right)^{\delta_{ab}} \prod_{k\in S_{ab}} \left[G_{k/30}(\vartheta)\right]^{p_k} , \tag{A.3}$$

where δ_{ab} is the Kronecker delta, and otherwise the notation is analogous to Eq. (A.2). The G_λ functions have the integral representation

$$G_\lambda(\vartheta) = \exp\left\{ 2\int_0^\infty \frac{dt}{t} \frac{\cosh\left(\lambda - \frac{1}{2}\right)t}{\cosh t/2 \sinh t} \sin^2 \frac{i\pi - \vartheta}{2\pi} \right\}. \tag{A.4}$$

They satisfy various functional identities, two of which are repeatedly used to derive the recurrence relations:

$$G_\lambda(\vartheta + i\pi\alpha)G_\lambda(\vartheta - i\pi\alpha) = \frac{G_\lambda(i\pi\alpha)G_\lambda(-i\pi\alpha)}{G_{\lambda+\alpha}(0)G_{\lambda-\alpha}(0)} G_{\lambda+\alpha}(\vartheta)G_{\lambda-\alpha}(\vartheta)\,, \tag{A.5}$$

$$G_{1-\lambda}(\vartheta)G_\lambda(\vartheta) = \frac{\sinh(1/2(\vartheta - i(\lambda-1)\pi))\sinh(1/2(\vartheta + i(\lambda+1)\pi))}{\sin^2(\pi\lambda/2)}\,. \tag{A.6}$$

A.2 Derivation of the recurrence relation

To construct solutions to the form factor equations, one takes the following Ansatz for the n-particle form factors containing only the lightest particle:

$$\begin{aligned} F_n^{\mathcal{O}}(\vartheta_1, \vartheta_2, \ldots \vartheta_n) &\equiv F^{\mathcal{O}}_{\underbrace{1\ldots1}_{n}}(\vartheta_1, \vartheta_2, \ldots \vartheta_n) \\ &= H_n \frac{\Lambda_n(x_1, \ldots, x_n)}{(\omega_n(x_1, \ldots, x_n))^n} \prod_{i<j}^{n} \frac{F_{11}^{\min}(\vartheta_i - \vartheta_j)}{D_{11}(\vartheta_i - \vartheta_j)(x_i + x_j)}\,, \end{aligned} \tag{A.7}$$

where $x \equiv \exp(\vartheta)$ and ω_n denotes the elementary symmetric polynomials generated by

$$\prod_{k=1}^{n}(x + x_k) = \sum_{j=0}^{n} x^{n-j}\omega_j(x_1, \ldots, x_n)\,, \tag{A.8}$$

and the operator-dependence is carried by the H_n constant factor and the Λ_n n-variable symmetric polynomial. Λ_n can be expressed in terms of the elementary symmetric polynomials ω.

Using the above Ansatz, Eqs. (3.13) and (3.14) yield recurrence relations for Λ_n. Here we derive the recursion corresponding to the the bound state pole equation (3.14) which can be written as

$$\begin{aligned} &-i \lim_{\vartheta_{ab}\to 2i\pi/3} (\vartheta_{ab} - 2i\pi/3) H_{n+2} \frac{\Lambda_{n+2}(x_a, x_b, x_1, \ldots, x_n)}{(\omega_{n+2})^{n+2}} \times \\ &\times \prod_{i=1}^{n} \frac{F_{11}^{\min}(\vartheta_a - \vartheta_j)F_{11}^{\min}(\vartheta_b - \vartheta_j)}{D_{11}(\vartheta_a - \vartheta_j)D_{11}(\vartheta_b - \vartheta_j)(x_a + x_j)(x_b + x_j)} \frac{F_{11}^{\min}(\vartheta_a - \vartheta_b)}{D_{11}(\vartheta_a - \vartheta_b)(x_a + x_b)} = \\ &= \Gamma_{11}^{1} H_{n+1} \frac{\Lambda_{n+1}(x_c, x_1, \ldots, x_n)}{(\omega_{n+1})^{n+1}} \prod_{i=1}^{n} \frac{F_{11}^{\min}(\vartheta_c - \vartheta_j)}{D_{11}(\vartheta_c - \vartheta_j)(x_c + x_j)}\,. \end{aligned} \tag{A.9}$$

We can parameterise $\vartheta_a = \vartheta + i\pi/3$, $\vartheta_b = \vartheta - i\pi/3$ and $\vartheta_c = \vartheta$. The bound state poles are encoded in the factors D_{11} which can be expressed as

$$D_{11}(\vartheta) = P_{2/3}(\vartheta)P_{2/5}(\vartheta)P_{1/15}(\vartheta)\,, \tag{A.10}$$

where

$$P_\gamma(\vartheta) = \frac{\cos(\pi\gamma) - \cosh(\vartheta)}{2\cos^2\left(\frac{\pi\gamma}{2}\right)}\,. \tag{A.11}$$

The residue can be calculated using l'Hospital's rule,

$$-i \lim_{\vartheta_{ab}\to 2i\pi/3} (\vartheta_{ab} - 2i\pi/3)P_{2/3}(\vartheta_{ab}) = \frac{2\cos^2(\pi/3)}{\sin(2\pi/3)}\,, \tag{A.12}$$

resulting in

$$\begin{aligned}
&\frac{2\cos^2(\pi/3)}{\sin(2\pi/3)}\,\frac{H_{n+2}}{H_{n+1}}\,\frac{\Lambda_{n+2}(xe^{i\pi/3}, xe^{-i\pi/3}, x_1, \ldots, x_n)}{(\omega_{n+2})^{n+2}}\times\\
&\times\prod_{i=1}^{n}\frac{F_{11}^{\mathrm{min}}(\vartheta + i\pi/3 - \vartheta_j)F_{11}^{\mathrm{min}}(\vartheta - i\pi/3 - \vartheta_j)}{D_{11}(\vartheta + i\pi/3 - \vartheta_j)D_{11}(\vartheta - i\pi/3 - \vartheta_j)(xe^{i\pi/3} + x_j)(xe^{-i\pi/3} + x_j)}\times\\
&\frac{F_{11}^{\mathrm{min}}(2\pi i/3)}{P_{2/5}(2\pi i/3)P_{1/15}(2\pi i/3)(xe^{i\pi/3} + xe^{-i\pi/3})} =\\
&= \Gamma_{11}^{1}\frac{\Lambda_{n+1}(x, x_1, \ldots, x_n)}{(\omega_{n+1})^{n+1}}\prod_{i=1}^{n}\frac{F_{11}^{\mathrm{min}}(\vartheta - \vartheta_j)}{D_{11}(\vartheta - \vartheta_j)(x + x_j)}\,.
\end{aligned} \tag{A.13}$$

The minimal form factor can be written in the form

$$F_{11}^{\mathrm{min}}(\vartheta) = -i\sinh(\vartheta/2)G_{2/3}(\vartheta)G_{2/5}(\vartheta)G_{1/15}(\vartheta)\,. \tag{A.14}$$

with the G_λ functions defined in Eq. (A.4).

We can then compute

$$\begin{aligned}
&\frac{F_{11}^{\mathrm{min}}(\vartheta + i\pi/3 - \vartheta_j)F_{11}^{\mathrm{min}}(\vartheta - i\pi/3 - \vartheta_j)}{F_{11}^{\mathrm{min}}(\vartheta - \vartheta_j)} =\\
&\qquad \frac{1}{\gamma}\prod_{\sigma_1,\sigma_2=\pm}\sinh((\vartheta - \vartheta_j)/2 + i\pi\sigma_1/6)\frac{\sinh\left(\frac{1}{2}(\vartheta - \vartheta_j + 4i\pi\sigma_2/15)\right)}{\sin^2(11\pi/30)}\,,
\end{aligned} \tag{A.15}$$

where we used the identity $G_1(\vartheta) = -i\sinh(\vartheta/2)$, and denoted

$$\frac{1}{\gamma} \equiv \frac{\prod_{\sigma_1,\sigma_2=\pm} G_{1/15}(\sigma_1 i\pi/3)G_{2/5}(\sigma_2 i\pi/3)G_{2/3}(2i\pi/3)G_{2/3}(0)}{G_1(i\pi/3)G_{1/3}(i\pi/3)G_{11/15}(0)G_{1/15}(0)G_{2/5}(0)G_{-4/15}(0)}\,. \tag{A.16}$$

Introducing further the function

$$G_{11}(\vartheta) = G_{1/15}(\vartheta)G_{2/5}(\vartheta)G_{2/3}(\vartheta)\,, \tag{A.17}$$

one obtains

$$\begin{aligned}
&\frac{H_{n+2}}{H_{n+1}}\,\frac{\Lambda_{n+2}(xe^{i\pi/3}, xe^{-i\pi/3}, x_1, \dots, x_n)}{x^{n+4}\omega_n}\,\frac{G_{11}(2\pi i/3)}{P_{2/5}(2\pi i/3)P_{1/15}(2\pi i/3)}\times\\
&\times\prod_{i=1}^{n}\left[\frac{\prod_{\sigma_1=\pm}\sinh((\vartheta-\vartheta_j)/2+i\pi\sigma_1/6)}{D_{11}(\vartheta+i\pi/3-\vartheta_j)D_{11}(\vartheta-i\pi/3-\vartheta_j)\sin^2(11\pi/30)\gamma}\times\right.\\
&\left.\times\frac{\prod_{\sigma_2=\pm}\sinh\left(\frac{1}{2}(\vartheta-\vartheta_j+4i\pi\sigma_2/15)\right)}{(xe^{i\pi/3}+x_j)(xe^{-i\pi/3}+x_j)}\right]=\\
&=\frac{1}{2\cos^2(\pi/3)}\Gamma^1_{11}\Lambda_{n+1}(x, x_1, \dots, x_n)\prod_{i=1}^{n}\frac{1}{D_{11}(\vartheta-\vartheta_j)(x+x_j)}\,.
\end{aligned}\tag{A.18}$$

Considering now the D factors

$$\begin{aligned}
&\frac{D_{11}(\vartheta+i\pi/3-\vartheta_j)D_{11}(\vartheta-i\pi/3-\vartheta_j)}{D_{11}(\vartheta-\vartheta_j)}=\\
&=\frac{\prod_{\sigma_1,\sigma_2=\pm}P_{2/3}(\vartheta+i\pi\sigma_1/3-\vartheta_j)P_{2/5}(\vartheta+i\pi\sigma_2/3-\vartheta_j)}{P_{2/3}(\vartheta-\vartheta_j)P_{2/5}(\vartheta-\vartheta_j)}\times\\
&\qquad\times\frac{\prod_{\sigma_3=\pm}P_{1/15}(\vartheta+i\pi\sigma_3/3-\vartheta_j)}{P_{1/15}(\vartheta-\vartheta_j)}
\end{aligned}\tag{A.19}$$

and using the identity

$$\begin{aligned}
\cos(\pi\gamma)-\cosh(\vartheta)&=2\sin((i\vartheta-\pi\gamma)/2)\sin((i\vartheta+\pi\gamma)/2)\equiv\\
&\equiv\prod_{\sigma=\pm}2\sin((i\vartheta+\pi\gamma\sigma)/2)\,,
\end{aligned}\tag{A.20}$$

Eq. (A.19) can be simplified as

$$\begin{aligned}
&\frac{D_{11}(\vartheta+i\pi/3-\vartheta_j)D_{11}(\vartheta-i\pi/3-\vartheta_j)}{D_{11}(\vartheta-\vartheta_j)}=\\
&=\prod_{\sigma_1,\sigma_2=\pm}\sin\left(\frac{i}{2}(\vartheta-\vartheta_j)+\pi\sigma_1/2\right)\sin\left(\frac{i}{2}(\vartheta-\vartheta_j)+\pi\sigma_2/6\right)\times\\
&\times\frac{\prod_{\sigma_3,\sigma_4=\pm}\sin\left(\frac{i}{2}(\vartheta-\vartheta_j)+2\pi\sigma_3/15\right)\sin\left(\frac{i}{2}(\vartheta-\vartheta_j)+11\pi\sigma_4/30\right)}{\prod_{\sigma=\pm}\cos^2(\pi/3)\cos^2(\pi/5)\cos^2(\pi/30)\sin\left(\frac{i}{2}(\vartheta-\vartheta_j)+\pi\sigma/3\right)}\,.
\end{aligned}\tag{A.21}$$

Using

$$P_{2/5}(2\pi i/3)P_{1/15}(2\pi i/3)=\frac{\sin\frac{8\pi}{15}\sin\frac{2\pi}{15}\sin\frac{3\pi}{10}\sin\frac{11\pi}{30}}{\cos^2(\pi/5)\cos^2(\pi/30)}\tag{A.22}$$

and the identity

$$\prod_{\sigma=\pm}\sin\left(\frac{i}{2}(\vartheta-\vartheta_j)+\sigma\pi\gamma/2\right)=-\frac{1}{4xx_j}(x-e^{-i\pi\gamma}x_j)(x-e^{i\pi\gamma}x_j)\,,\tag{A.23}$$

the final form of the recurrence relation is:

$$\begin{aligned}\frac{\Lambda_{n+2}(xe^{i\pi/3}, xe^{-i\pi/3}, x_1, \dots, x_n)}{x^4 \prod_{i=1}^n (x - e^{-11i\pi/15}x_j)(x - e^{11i\pi/15}x_j)(x + x_j)} &= \\ &= (-1)^n \Lambda_{n+1}(x, x_1, \dots, x_n)\end{aligned} \tag{A.24}$$

provided the H_n are chosen to satisfy

$$\begin{aligned}\frac{H_{n+2}}{H_{n+1}} = \frac{\Gamma^1_{11} \sin\left(\frac{2\pi}{15}\right) \sin\left(\frac{11\pi}{30}\right) \sin\left(\frac{8\pi}{15}\right) \sin\left(\frac{3\pi}{10}\right)}{2\cos^2(\pi/3)\cos^2(\pi/5)\cos^2(\pi/30) G_{11}(2\pi i/3)} \times \\ \times \left[\frac{\sin^2(11\pi/30)\gamma}{4\cos^2(\pi/3)\cos^2(\pi/5)\cos^2(\pi/30)}\right]^n .\end{aligned} \tag{A.25}$$

A.3 Form factors involving higher species from bound state equations

Form factors involving species other than A_1 can be obtained using the bound state singularity equation (3.14). Consider a particle A_c that is the bound state of two A_1 particles, then the relevant singularity takes the form

$$\begin{aligned}-i \lim_{\vartheta_{ab} \to iu^c_{11}} (\vartheta_{ab} - iu^c_{11}) F^{\mathcal{O}}_{n+2}(\vartheta_a, \vartheta_b, \vartheta_1, \vartheta_2, \dots \vartheta_n) &= \\ &= \Gamma^c_{11} F^{\mathcal{O}}_{c,n}(\vartheta_c, \vartheta_1, \vartheta_2, \dots \vartheta_n) ,\end{aligned} \tag{A.26}$$

where the index n is a short-hand for n particles of type A_1.

For form factors containing particles of different species, the Ansatz (A.7) must be generalised to the form

$$\begin{aligned}&F^{\mathcal{O}}_{a_1,a_2,\dots a_n}(\vartheta_1, \vartheta_2, \dots \vartheta_n) = \\ &= Q^{\mathcal{O}}_{a_1,a_2,\dots a_n}(x_1, \dots, x_n) \prod_{i<j}^n \frac{F^{\text{min}}_{a_i,a_j}(\vartheta_i - \vartheta_j)}{D_{a_i,a_j}(\vartheta_i - \vartheta_j)(x_i + x_j)^{\delta_{a_i,a_j}}} ,\end{aligned} \tag{A.27}$$

where the D_{ab} factors ensure the correct position of the bound state poles, the functions F^{min}_{ab} are minimal form factors that have no poles in the strip $\text{Im}\,\vartheta \in [0, \pi]$ and satisfy

$$F^{\text{min}}_{ab}(i\pi - \vartheta) = F^{\text{min}}_{ab}(i\pi + \vartheta) \qquad F^{\text{min}}_{ab}(\vartheta) = S_{11}(\vartheta) F^{\text{min}}_{ab}(-\vartheta) \tag{A.28}$$

$\delta_{a,b}$ is the Kronecker delta, and

$$Q_{a_1,\dots,a_n}(x_1, \dots, x_n) = \sum_{\alpha_1=\alpha'_1}^{\alpha''_1} \cdots \sum_{\alpha_n=\alpha'_n}^{\alpha''_n} d^{\alpha_1,\dots,\alpha_n}_{a_1,\dots a_n} x_1^{\alpha_1} \dots x_n^{\alpha_n} \tag{A.29}$$

is a polynomial symmetric under exchange of particles of the same species and its degree is constrained by the asymptotic behaviour of the form factors [42]. Using this Ansatz Eq. (A.26) can be written as

$$\begin{aligned}
&-i \lim_{\vartheta_{ab}\to iu_{11}^{c}} (\vartheta_{ab} - iu_{11}^{c}) Q^{\mathcal{O}}_{n+2}(x_a, x_b, x_1, \ldots, x_n)\times \\
&\times \prod_{i=1}^{n} \left[\frac{F^{\min}_{11}(\vartheta_a - \vartheta_j) F^{\min}_{11}(\vartheta_b - \vartheta_j)}{D_{11}(\vartheta_a - \vartheta_j) D_{11}(\vartheta_b - \vartheta_j)(x_a + x_j)(x_b + x_j)} \times \right. \\
&\left. \times \frac{F^{\min}_{11}(\vartheta_a - \vartheta_b)}{D_{11}(\vartheta_a - \vartheta_b)(x_a + x_b)} \right] = \\
&= \Gamma^{c}_{11} Q^{\mathcal{O}}_{c,n}(x_c, x_1, \ldots, x_n) \prod_{i=1}^{n} \frac{F^{\min}_{c1}(\vartheta_c - \vartheta_j)}{D_{c1}(\vartheta_c - \vartheta_j)} \,.
\end{aligned} \tag{A.30}$$

For definiteness let us choose the pole at $2i\pi/5$ which corresponds to the particle A_2 (the other pole at $i\pi/15$ corresponding to A_3 can be handled similarly). The residue can be computed using

$$-i \lim_{\vartheta_{ab}\to 2i\pi/5} (\vartheta_{ab} - 2i\pi/5) P_{2/5}(\vartheta_{ab}) = \frac{2\cos^2(\pi/5)}{\sin(2\pi/5)} \,, \tag{A.31}$$

which leads to

$$\begin{aligned}
&Q^{\mathcal{O}}_{n+2}(xe^{i\pi/5}, xe^{-i\pi/5}, x_1, \ldots, x_n) \frac{\sin(\pi/5) G_{11}(2i\pi/5)\cos(\pi/5)}{P_{2/3}(2i\pi/5) P_{1/15}(2i\pi/5) x \sin(2\pi/5)} \times \\
&\times \prod_{i=1}^{n} \frac{\prod_{\sigma=\pm} F^{\min}_{11}(\vartheta - \vartheta_j + i\pi\sigma/5) D_{12}(\vartheta - \vartheta_j)}{\prod_{\sigma'=\pm} F^{\min}_{12}(\vartheta - \vartheta_j) D_{11}(\vartheta - \vartheta_j + i\pi\sigma'/5)(xe^{i\pi/5} + x_j)(xe^{-i\pi/5} + x_j)} \\
&= \Gamma^{2}_{11} Q^{\mathcal{O}}_{2,n}(x, x_1, \ldots, x_n) \,.
\end{aligned} \tag{A.32}$$

Using the identities (A.6) the form factor product simplifies once again, leading to an analogous calculation to that detailed above. The final result reads

$$\begin{aligned}
&\frac{Q^{\mathcal{O}}_{n+2}(xe^{i\pi/5}, xe^{-i\pi/5}, x_1, \ldots, x_n) \prod_{i=1}^{n} \prod_{\sigma=\pm} (x - e^{4i\pi\sigma/5} x_j)}{x \prod_{i=1}^{n} \prod_{\sigma_1,\sigma_2=\pm} (x - e^{13i\pi\sigma_1/15} x_j)(x + x_j e^{i\pi\sigma_2/5})} = \\
&\quad = -(C_2)^{-n} \frac{\sin(2\pi/5) \sin\frac{8\pi}{15} \sin\frac{7\pi}{30} \sin\frac{\pi}{6} \sin\frac{2\pi}{15}}{\sin(\pi/5)\cos^2(\pi/3)\cos(\pi/5)\cos^2(\pi/30) G_{11}(2i\pi/5)} \times \\
&\qquad \times \Gamma^{2}_{11} Q^{\mathcal{O}}_{2,n}(x, x_1, \ldots, x_n)
\end{aligned} \tag{A.33}$$

with

$$C_2 = \frac{(\cos^4(\pi/3)\cos^4(\pi/5)\cos^4(\pi/30))\gamma_2}{\cos^2(2\pi/15)\cos^2(7\pi/30)\cos^2(3\pi/10)\cos^2(2\pi/5)\sin^2(13\pi/30)} \tag{A.34}$$

and

$$\gamma_2 = \frac{\prod_{\sigma_1,\sigma_2,\sigma_3=\pm} G_{1/15}(\sigma_1 i\pi/5) G_{2/5}(\sigma_2 i\pi/5) G_{2/3}(\sigma_3 i\pi/5)}{G_{13/15}(0) G_{7/15}(0) G_{3/5}(0) G_{1/5}(0) G_{-2/15}(0) G_{4/15}(0)} \,. \tag{A.35}$$

Appendix B

Perturbative calculations of overlaps

B.1 Rayleigh–Schrödinger expansion

Taking a Hamiltonian $H = H_0 + \lambda V$, its spectrum and the eigenstates can be found using Rayleigh–Schrödinger perturbation theory based on the Hamiltonian H_0 with eigenstates $|n^{(0)}\rangle$,

$$H_0 \, |n^{(0)}\rangle = E_n^{(0)} \, |n^{(0)}\rangle \ , \tag{B.1}$$

expressed as a power series in λ:

$$\begin{aligned} E_n =& E_n^{(0)} + \lambda E_n^{(1)} + \lambda^2 E_n^{(2)} + \dots \ , & \text{(B.2)} \\ |n\rangle =& |n^{(0)}\rangle + \lambda \, |n^{(1)}\rangle + \lambda^2 \, |n^{(2)}\rangle + \dots \ , & \text{(B.3)} \end{aligned}$$

where the ellipses denote higher order contributions in λ. Here we only need the expansion for the eigenstates up to second order, i.e. the terms

$$|n^{(1)}\rangle = \sum_{k\neq n} \frac{\langle k^{(0)}| \, V \, |n^{(0)}\rangle}{E_n^{(0)} - E_k^{(0)}} \, |k^{(0)}\rangle \tag{B.4}$$

$$\begin{aligned} |n^{(2)}\rangle = \Bigg[& \sum_{k\neq n} \sum_{l\neq n} \frac{\langle l^{(0)}| \, V \, |k^{(0)}\rangle \ \langle k^{(0)}| \, V \, |n^{(0)}\rangle}{(E_n^{(0)} - E_k^{(0)})(E_n^{(0)} - E_l^{(0)})} \, |l^{(0)}\rangle - \\ & - \sum_{k\neq n} \frac{\langle n^{(0)}| \, V \, |n^{(0)}\rangle \ \langle k^{(0)}| \, V \, |n^{(0)}\rangle}{(E_n^{(0)} - E_k^{(0)})^2} \, |k^{(0)}\rangle \Bigg] . \end{aligned} \tag{B.5}$$

Note that the resulting expression for the states is not normalised. Quantities expressed on this basis must be normalised by dividing with the norm of the ground state, which is $\mathcal{N} = 1 + \mathcal{O}(\lambda^2)$. However, for our calculations up to $\mathcal{O}(\lambda^2)$ this is irrelevant since the leading order of the overlaps is always $\mathcal{O}(\lambda)$.

B.2 Two-particle overlaps with multiple species

B.2.1 The case $K_{aa}(\vartheta)$

The additional complication in the calculation of $K_{aa}(\vartheta)$ with respect to $K(\vartheta)$ is due to the different possible disconnected pieces in a theory with multiple particle species. Disconnected contributions appear in the second order of perturbation theory, the relevant contributions can be extracted from Eq. (5.31). Restoring particle labels the relevant contribution to $K_{aa}(\vartheta,-\vartheta)$ is given as

$$\begin{aligned} D_{ab}(\vartheta,-\vartheta) \equiv & \frac{\tilde{\rho}_a(\vartheta)}{\sqrt{\rho_{aa}(\vartheta,-\vartheta)}}\lambda^2 L^2 \times \\ & \times \sum_{\vartheta'} \frac{{}_{ab}\langle\{\vartheta',\vartheta'_{ab}\}|\phi|0\rangle_L \; {}_{aa}\langle\{\vartheta,-\vartheta\}|\phi|\{\vartheta',\vartheta'_{ab}\}\rangle_{ab,L}}{2m_a\cosh\vartheta(m_a\cosh\vartheta' + m_b\cosh\vartheta'_{ab})} \end{aligned} \tag{B.6}$$

which must be summed over the intermediate species label b, and where ϑ'_{ab} is defined similarly to (5.28):

$$\vartheta'_{ab} = -\mathrm{arcsinh}\left(\frac{m_a\sinh\vartheta'}{m_b}\right)\,, \tag{B.7}$$

and the summation over ϑ' runs over the solutions of the following Bethe–Yang equation:

$$\tilde{Q}(\vartheta') = m_a\sinh\vartheta' + \delta^{\mathrm{ps}}_{ab}(\vartheta'-\vartheta'_{ab}) = 2\pi I\,, \tag{B.8}$$

indexed by the quantum number $I\in\mathbb{Z}$. Expressing the finite volume matrix elements with the form factors yields

$$\begin{aligned} D_{ab}(\vartheta,-\vartheta) = & \frac{\lambda^2}{2m_a^2\cosh^2(\vartheta)}\times \\ & \times\sum_{\vartheta'}\frac{F^{\phi*}_{ab}(\vartheta',\vartheta'_{ab})F^{\phi}_{aaab}(i\pi+\vartheta,i\pi-\vartheta,\vartheta',\vartheta'_{ab})}{(m_a\cosh\vartheta'+m_b\cosh\vartheta'_{ab})m_a\cosh\vartheta'\tilde{\rho}_a(\vartheta')}\,, \end{aligned} \tag{B.9}$$

where $\tilde{\rho}_a(\vartheta')$ is obtained by differentiating the function $\tilde{Q}$ defined in Eq. (B.8). Since the four-particle form factor has poles for $\vartheta'=\pm\vartheta$ it is not possible to replace the sum with a simple integral. This problem can avoided by using contour integrals to express the sum. Denoting

$$d_{ab} \equiv \sum_{\vartheta'}\frac{f(\vartheta')}{\tilde{\rho}_a(\vartheta')} \equiv \sum_{\vartheta'}\frac{F^{\phi*}_{ab}(\vartheta',\vartheta'_{ab})F^{\phi}_{aaab}(i\pi+\vartheta,i\pi-\vartheta,\vartheta',\vartheta'_{ab})}{(m_a\cosh\vartheta'+m_b\cosh\vartheta'_{ab})m_a\cosh\vartheta'\tilde{\rho}_a(\vartheta')}\,. \tag{B.10}$$

one can write

$$d_{ab} = -\sum_{\vartheta'}\oint_{\vartheta'}\frac{\mathrm{d}\theta}{2\pi}\frac{f(\theta)}{1-e^{i\tilde{Q}(\theta)}}\,, \tag{B.11}$$

where the contours go around each root ϑ' anticlockwise. The contours can be deformed to give

$$d_{ab} = \left(\int_{-\infty+i\epsilon}^{\infty+i\epsilon} - \int_{-\infty-i\epsilon}^{\infty-i\epsilon} + \oint_{\vartheta} + \oint_{-\vartheta} \right) \frac{\mathrm{d}\theta}{2\pi} \frac{f(\theta)}{1-e^{i\tilde{Q}(\theta)}} \,, \tag{B.12}$$

where ϵ is a small shift. The second integral vanishes in the infinite volume limit due to

$$\begin{aligned} \lim_{L\to\infty} \frac{1}{1-e^{i\tilde{Q}(\theta+i\epsilon)}} = \lim_{L\to\infty} \frac{1}{1-e^{im_a L(\sinh\theta\cos\epsilon + i\cosh\theta\sin\epsilon)+O(L^0)}} = \\ = \begin{cases} 1\,, & \epsilon > 0 \\ 0\,, & \epsilon < 0 \end{cases} \end{aligned} \tag{B.13}$$

and in the first one only the numerator remains. Moreover, the integral contour can be pulled back to the real axis using

$$\int_{-\infty}^{\infty} \mathrm{d}\vartheta' \coth(\vartheta' \pm \vartheta) = 0\,, \tag{B.14}$$

which can be proved by shifting the integration contour to $\operatorname{Im}\vartheta' = \pi/2$:

$$\begin{aligned} \int_{-\infty+i\epsilon}^{\infty+i\epsilon} \frac{\mathrm{d}\theta}{2\pi} f(\theta) = \int_{-\infty}^{\infty} \frac{\mathrm{d}\vartheta'}{2\pi} \Big[f(\vartheta') - R_1(\vartheta)\coth(\vartheta'-\vartheta) - \\ - R_2(-\vartheta)\coth(\vartheta'+\vartheta) \Big]\,, \end{aligned} \tag{B.15}$$

where R_1 and R_2 are the residues of $f(\vartheta')$ at $\vartheta' = \vartheta$ and $\vartheta' = -\vartheta$, respectively, which also appear in the contributions of the two isolated poles:

$$\begin{aligned} \oint_{\vartheta} \frac{\mathrm{d}\theta}{2\pi} \frac{f(\theta)}{1-e^{i\tilde{Q}(\theta)}} &= i\frac{R_1(\vartheta)}{1-e^{i\tilde{Q}(\vartheta)}}\,, \\ \oint_{-\vartheta} \frac{\mathrm{d}\theta}{2\pi} \frac{f(\theta)}{1-e^{i\tilde{Q}(\theta)}} &= i\frac{R_2(-\vartheta)}{1-e^{i\tilde{Q}(-\vartheta)}}\,. \end{aligned} \tag{B.16}$$

The residues can be calculated using the kinematical poles of the form factors (3.13) and the S-matrix:

$$\begin{aligned} R_1(\vartheta) &= \frac{-iF^{\phi}_{ab}(i\pi-\vartheta,\vartheta_{ab})F^{\phi*}_{ab}(\vartheta,\vartheta_{ab})S_{aa}(2\vartheta)(1-S^*_{aa}(2\vartheta)S_{ab}(\vartheta-\vartheta_{ab}))}{(m_a\cosh\vartheta + m_b\cosh\vartheta_{ab})m_a\cosh\vartheta} \\ R_2(-\vartheta) &= \frac{R_1(-\vartheta)}{S_{aa}(-2\vartheta)}\,. \end{aligned} \tag{B.17}$$

The denominators in (B.16) can be simplified using that $\pm\vartheta$ are solutions to another Bethe–Yang equation:

$$\tilde{Q}'(\vartheta) = m_a L\sinh\vartheta + \delta^{\mathrm{ps}}_{aa}(2\vartheta) = 2\pi J \qquad J \in \mathbb{Z} + \frac{1}{2}\,, \tag{B.18}$$

with

$$S_{aa}(\vartheta) = -e^{i\delta^{\mathrm{ps}}_{aa}(\vartheta)}\,. \tag{B.19}$$

Comparing with Eq. (B.8) yields

$$1 - e^{i\tilde{Q}(\vartheta)} = 1 - S^*_{aa}(2\vartheta)S_{ab}(\vartheta - \vartheta_{ab}) \equiv \eta^{-1}(\vartheta)\,. \tag{B.20}$$

Putting everything together one obtains

$$\begin{aligned} D_{ab}(\vartheta, -\vartheta) = &\frac{\lambda^2}{2m_a^2\cosh^2(\vartheta)}\times \\ &\times\left[\int_{-\infty}^{\infty}\frac{\mathrm{d}\vartheta'}{2\pi}\bigg(f(\vartheta') - R_1(\vartheta)\coth(\vartheta'-\vartheta) - R_2(-\vartheta)\coth(\vartheta'+\vartheta)\bigg)+\right. \\ &\left. + iR_1(\vartheta)\eta(\vartheta) + iR_2(-\vartheta)\eta(-\vartheta)\vphantom{\int_{-\infty}^{\infty}}\right], \end{aligned} \tag{B.21}$$

with

$$f(\vartheta') = \frac{F^{\phi *}_{ab}(\vartheta', \vartheta'_{ab})F^{\phi}_{aaab}(i\pi+\vartheta, i\pi-\vartheta, \vartheta', \vartheta'_{ab})}{(m_a\cosh\vartheta' + m_b\cosh\vartheta'_{ab})m_a\cosh\vartheta'}\,. \tag{B.22}$$

Using the above results, one can easily write down the generalisation of Eq. (5.37) to multiple particle species. The final result is

$$\begin{aligned} K_{aa}(-\vartheta, \vartheta) = &-\lambda\frac{F^{\phi *}_{aa}(-\vartheta,\vartheta)}{2m_a^2\cosh^2\vartheta} + \lambda^2\left(\sum_{b=1}^{N_{\mathrm{spec}}}\frac{F^{\phi}_{b}F^{\phi *}_{baa}(i\pi, -\vartheta, \vartheta)}{2m_a^2\cosh^2\vartheta m_b^2}\right. \\ &+\frac{F^{\phi *}_{aa}(-\vartheta,\vartheta)F^{\phi}_{aa}(i\pi,0)}{2m_a^4\cosh^4\vartheta} + \sum_{b=1}^{N_{\mathrm{spec}}} D_{ab}(\vartheta,-\vartheta)+ \\ +\sum_{(c,d)\neq(a,b)}\frac{1}{(2\delta_{cd})!}&\int_{-\infty}^{\infty}\frac{\mathrm{d}\vartheta'}{2\pi}\frac{F^{\phi,s}_{aacd}(i\pi+\vartheta, i\pi-\vartheta, \vartheta', \vartheta'_{cd})F^{\phi *}_{cd}(\vartheta',\vartheta'_{cd})}{2m_a^2\cosh^2\vartheta(m_c\cosh\vartheta' + m_d\cosh\vartheta'_{cd})m_d\cosh\vartheta'_{cd}}+ \\ &\left.+\,\text{contributions from higher form factors}\vphantom{\sum_{b=1}^{N}}\right) + O\left(\lambda^3\right)\,, \end{aligned} \tag{B.23}$$

where $(c,d) \neq (a,b)$ means that the sum excludes those pairs in which exactly one particle is of species a.

B.2.2 The case $K_{ab}(\vartheta)$

The above results can be extended to a pair with different particles. The overlap function is then $K_{ab}(\vartheta, \vartheta_{ab})$, with ϑ_{ab} as in Eq. (B.7). The terms involving no rapidity integrals are given by

$$\begin{aligned} K_{ab}(\vartheta,\vartheta_{ab}) =& -\lambda\frac{F^{\phi *}_{ab}(\vartheta,\vartheta_{ab})}{(m_a\cosh\vartheta+m_b\cosh\vartheta_{ab})m_b\cosh\vartheta_{ab}}+ \\ &+\lambda^2\left(\sum_{c=1}^{N_{\text{spec}}}\frac{F^{\phi}_{c}F^{\phi *}_{cab}(i\pi,\vartheta,\vartheta_{ab})}{m_c^2(m_a\cosh\vartheta+m_b\cosh\vartheta_{ab})m_b\cosh\vartheta_{ab}}+\right. \\ &+\frac{F^{\phi *}_{ab}(\vartheta,\vartheta_{ab})}{(m_a\cosh\vartheta+m_b\cosh\vartheta_{ab})^2m_b\cosh\vartheta_{ab}}\times \\ &\left.\times\left(\frac{F^{\phi}_{aa}(i\pi,0)}{m_b\cosh\vartheta_{ab}}+\frac{F^{\phi}_{bb}(i\pi,0)}{m_a\cosh\vartheta}\right)+\ldots\right)+O\left(\lambda^3\right)\,. \end{aligned} \tag{B.24}$$

Terms containing integrals are similar to the D_{ab} contribution of Eq. (B.6), and the ones with disconnected contributions have the form

$$\begin{aligned} G^{c}_{ab}(\vartheta,\vartheta_{ab}) \equiv& \frac{\tilde{\rho}_a(\vartheta)}{\sqrt{\rho_{ab}(\vartheta,\vartheta_{ab})}}\lambda^2L^2\times \\ &\times\sum_{\vartheta'}\frac{{}_{cc}\langle\{\vartheta',-\vartheta'\}|\phi|0\rangle_{L\,ab}\langle\{\vartheta,\vartheta_{ab}\}|\phi|\{-\vartheta',\vartheta'\}\rangle_{cc,L}}{2m_c\cosh\vartheta'(m_a\cosh\vartheta+m_b\cosh\vartheta_{ab})}\,, \end{aligned} \tag{B.25}$$

with $c=a$ or b. The computation required here is similar to the one above, so we only present the results. The $c=a$ term can be expressed as

$$\begin{aligned} G^{a}_{ab}(\vartheta,\vartheta_{ab}) =& \frac{\lambda^2}{(m_a\cosh\vartheta+m_b\cosh\vartheta_{ab})m_b\cosh\vartheta_{ab}}\times \\ &\times\left[\int_{-\infty}^{\infty}\frac{\mathrm{d}\vartheta'}{2\pi}\left(g(\vartheta')-R_3(\vartheta)\coth(\vartheta'-\vartheta)-R_4(-\vartheta)\coth(\vartheta'+\vartheta)\right)\right. \\ &\left.+iR_3(\vartheta)\eta_2(\vartheta)+iR_4(-\vartheta)\eta_2(-\vartheta)\right]\,, \end{aligned} \tag{B.26}$$

with

$$g(\vartheta')=\frac{F^{\phi *}_{aa}(-\vartheta',\vartheta')F^{\phi}_{abaa}(i\pi+\vartheta,i\pi+\vartheta_{ab},-\vartheta',\vartheta')}{2m_a^2\cosh^2(\vartheta')}\,, \tag{B.27}$$

and

$$\begin{aligned} R_3(\vartheta) =& \frac{-iF^{\phi}_{ba}(i\pi+\vartheta_{ab},-\vartheta)F^{\phi *}_{aa}(-\vartheta,\vartheta)S^{*}_{aa}(2\vartheta)S_{ab}(\vartheta-\vartheta_{ab})}{2m_a^2\cosh^2(\vartheta)}\times \\ &\times\left(1-S_{aa}(2\vartheta)S_{ab}(\vartheta_{ab}-\vartheta)\right)\,, \\ R_4(-\vartheta) =& R_3(\vartheta)\,, \\ \eta_2(\vartheta) =& \frac{1}{1-S_{aa}(2\vartheta)S^{*}_{ab}(\vartheta-\vartheta_{ab})}\,, \end{aligned} \tag{B.28}$$

while G^b_{ab} is slightly different:

$$\begin{aligned} G^a_{ab}(\vartheta,\vartheta_{ab}) = {} & \frac{\lambda^2}{(m_a\cosh\vartheta + m_b\cosh\vartheta_{ab})m_b\cosh\vartheta_{ab}} \times \\ & \Big[\int_{-\infty}^{\infty}\frac{\mathrm{d}\vartheta'}{2\pi}\left(h(\vartheta') - R_5(\vartheta)\coth(\vartheta'-\vartheta) - R_6(\vartheta)\coth(\vartheta'+\vartheta)\right) + \\ & iR_5(\vartheta)\eta_3(\vartheta) + iR_6(\vartheta)\eta_3(-\vartheta)\Big] \end{aligned} \tag{B.29}$$

with

$$h(\vartheta') = \frac{F^{\phi *}_{bb}(-\vartheta',\vartheta')F^{\phi}_{abbb}(i\pi+\vartheta, i\pi+\vartheta_{ab}, -\vartheta',\vartheta')}{2m_b^2\cosh^2(\vartheta')} \tag{B.30}$$

and

$$\begin{aligned} R_5(\vartheta) = {} & \frac{-iF^{\phi}_{ab}(i\pi+\vartheta,-\vartheta_{ab})F^{\phi *}_{bb}(-\vartheta_{ab},\vartheta_{ab})}{2m_b^2\cosh^2(\vartheta_{ab})} \times \\ & \times S^*_{bb}(2\vartheta_{ab})(1 - S_{ab}(\vartheta-\vartheta_{ab})S_{bb}(2\vartheta_{ab}))\,, \\ R_6(\vartheta) = {} & R_5(\vartheta)S_{ab}(\vartheta-\vartheta_{ab})S_{ab}(-\vartheta-\vartheta_{ab})\,, \\ \eta_2(\vartheta) = {} & \frac{1}{1 - S_{aa}(2\vartheta)S^*_{ab}(\vartheta-\vartheta_{ab})}\,. \end{aligned} \tag{B.31}$$

There are additional terms corresponding to inserting a state with only one a or b particle; however, terms including such multi-particle form factors are expected to give very small contributions so we neglect them.

The final result for the K_{ab} function is

$$\begin{aligned} K_{ab}(\vartheta,\vartheta_{ab}) = {} & -\lambda\frac{F^{\phi *}_{ab}(\vartheta,\vartheta_{ab})}{C_{ab}(\vartheta,\vartheta_{ab})} + \lambda^2\Bigg[\sum_{c=1}^{N_{\text{spec}}}\frac{F^{\phi}_{c}F^{\phi *}_{cab}(i\pi,\vartheta,\vartheta_{ab})}{m_c^2 C_{ab}(\vartheta,\vartheta_{ab})} + \\ & + \frac{F^{\phi *}_{ab}(\vartheta,\vartheta_{ab})}{C_{ab}(\vartheta,\vartheta_{ab})(m_a\cosh\vartheta + m_b\cosh\vartheta_{ab})}\left(\frac{F^{\phi}_{aa}(i\pi,0)}{m_b\cosh\vartheta_{ab}} + \frac{F^{\phi}_{bb}(i\pi,0)}{m_a\cosh\vartheta}\right) + \\ & + G^a_{ab}(\vartheta,\vartheta_{ab}) + G^b_{ab}(\vartheta,\vartheta_{ab}) + \\ & + \sum_{\substack{c\neq a,b\\ d\neq a,b}}\frac{1}{(2\delta_{cd})!}\int_{-\infty}^{\infty}\frac{\mathrm{d}\vartheta'}{2\pi}\frac{F^{\phi,s}_{abcd}(i\pi+\vartheta, i\pi+\vartheta_{ab},\vartheta',\vartheta'_{cd})F^{\phi *}_{cd}(\vartheta',\vartheta'_{cd})}{C_{ab}(\vartheta,\vartheta_{ab})(m_c\cosh\vartheta' + m_d\cosh\vartheta'_{cd})m_d\cosh\vartheta'_{cd}} + \\ & + \text{contributions from higher form factors}\Bigg] + O\left(\lambda^3\right)\,, \end{aligned} \tag{B.32}$$

with

$$C_{ab}(\vartheta,\vartheta_{ab}) = (m_a\cosh\vartheta + m_b\cosh\vartheta_{ab})m_b\cosh\vartheta_{ab}\,. \tag{B.33}$$

B.3 Results for the pre-quench expansion

Working in the pre-quench basis one obtains the following results for overlaps with a pair of two particles of the same species:

$$\begin{aligned}
K_{aa}^{(0)}(-\vartheta,\vartheta) = & -\lambda\frac{F_{aa}^{\phi}(-\vartheta,\vartheta)}{2m_a^2\cosh^2\vartheta}+\lambda^2\Bigg(\sum_{b=1}^{N_{\mathrm{spec}}}\frac{F_b^{\phi}F_{baa}^{\phi}(i\pi,-\vartheta,\vartheta)}{2m_a^2\cosh^2\vartheta m_b(2m_a\cosh\vartheta-m_b)}+\\
&+\frac{F_{aa}^{\phi}(-\vartheta,\vartheta)F_{aa}^{\phi}(i\pi,0)}{2m_a^4\cosh^4\vartheta}+\sum_{b=1}^{N_{\mathrm{spec}}}D_{ab}^{(0)}(\vartheta,-\vartheta)+\\
&+\sum_{(c,d)\neq(a,b)}\frac{1}{(2\delta_{cd})!}\int_{-\infty}^{\infty}\frac{\mathrm{d}\vartheta'}{2\pi}\frac{F_{aacd}^{\phi,s*}(i\pi+\vartheta,i\pi-\vartheta,\vartheta',\vartheta'_{cd})F_{cd}^{\phi}(\vartheta',\vartheta'_{cd})}{2m_a^2\cosh^2\vartheta(2m_a\cosh\vartheta-E_{cd}^{(0)}(\vartheta'))m_d\cosh\vartheta'_{cd}}\\
&+\text{contributions from higher form factors}\Bigg)+O\left(\lambda^3\right)\,,
\end{aligned}\tag{B.34}$$

while for a pair composed of particles of different species the result is

$$\begin{aligned}
K_{ab}^{(0)}(\vartheta,\vartheta_{ab}) = & -\lambda\frac{F_{ab}^{\phi}(\vartheta,\vartheta_{ab})}{C_{ab}^{(0)}(\vartheta,\vartheta_{ab})}+\lambda^2\Bigg[\sum_{c=1}^{N_{\mathrm{spec}}}\frac{F_c^{\phi}F_{cab}^{\phi}(i\pi,\vartheta,\vartheta_{ab})}{m_c(E_{ab}^{(0)}(\vartheta)-m_c)C_{ab}^{(0)}(\vartheta,\vartheta_{ab})}-\\
&-\frac{F_{ab}^{\phi}(\vartheta,\vartheta_{ab})}{C_{ab}^{(0)}(\vartheta,\vartheta_{ab})E_{ab}^{(0)}(\vartheta)}\left(\frac{F_{aa}^{\phi}(i\pi,0)}{m_b\cosh\vartheta_{ab}}+\frac{F_{bb}^{\phi}(i\pi,0)}{m_a\cosh\vartheta}\right)+\\
&+G_{ab}^{b(0)}(\vartheta,\vartheta_{ab})+G_{ab}^{a(0)}(\vartheta,\vartheta_{ab})+\sum_{\substack{c\neq a,b\\ d\neq a,b}}\Bigg(\frac{1}{(2\delta_{cd})!}\times\\
&\times\int_{-\infty}^{\infty}\frac{\mathrm{d}\vartheta'}{2\pi}\frac{F_{abcd}^{\phi,s*}(i\pi+\vartheta,i\pi+\vartheta_{ab},\vartheta',\vartheta'_{cd})F_{cd}^{\phi}(\vartheta',\vartheta'_{cd})}{C_{ab}^{(0)}(\vartheta,\vartheta_{ab})(E_{ab}^{(0)}(\vartheta)-E_{cd}^{(0)}(\vartheta'))m_d\cosh\vartheta'_{cd}}\Bigg)+\dots\Bigg]+O\left(\lambda^3\right)\,,
\end{aligned}\tag{B.35}$$

where $E_{ab}^{(0)}(\vartheta)=m_a\cosh\vartheta+m_b\cosh\vartheta_{ab}$ is the (pre-quench) energy of an A_a-A_b particle pair with zero overall momentum. The C, D, and G functions can be simply transformed to the pre-quench basis by replacing the corresponding quantities in the definitions of the previous section.

B.4 Numerical evaluation of the perturbative expressions

Although the end results involving multiple species (5.27), (B.23) and (B.32) look quite complicated, their numerical evaluation reveals that not all contributions are equally important. Here we examine the second order contributions

g_1	A_1	A_2	A_1-A_1	A_3	A_4	A_1-A_2	A_1-A_3	A_5
	5.84879	-0.94431	-0.38934	0.28140	0.03816	0.02552	0.01286	-0.01184

g_2	A_1	A_2	A_1-A_1	A_3	A_4	A_6	A_1-A_2	A_5
	1.78700	-1.18054	0.25376	0.14533	-0.05807	-0.00571	-0.00539	0.00449

g_3	A_1	A_3	A_2	A_4	A_1-A_1	A_1-A_2	A_5	$\mathrm{A}_2 - \mathrm{A}_2$
	0.96636	0.43049	-0.26373	-0.09194	-0.06197	0.01725	-0.00891	-0.00161

Table B.1: Contributions to g_a at order λ^2 sorted by magnitude, with the particle content of the inserted state shown in the top rows.

K_{11}	A_1	$\mathrm{A}_1 - \mathrm{A}_1^{\mathrm{disc}}$	A_2	A_3	$\mathrm{A}_1 - \mathrm{A}_1^{\mathrm{conn}}$	A_5	A_4
	-0.2931 +2.3520i	0.2232 -1.7915i	-0.1541 +1.2366i	-0.0154 +0.1235i	-0.0106 +0.0850i	-0.0079 +0.0636i	-0.0072 +0.0575i

K_{12}	A_1	A_2	$\mathrm{A}_1 - \mathrm{A}_1$	$\mathrm{A}_1 - \mathrm{A}_2^{\mathrm{disc}}$	$\mathrm{A}_1 - \mathrm{A}_2^{\mathrm{conn}}$	A_3	A_5
	-0.2135 +0.0161i	0.0968 -0.1739i	-0.1366 -0.0705i	-0.1396 +0.0105i	0.0130 +0.0523i	-0.0365 -0.0085i	0.0041 -0.0116i

K_{22}	A_1	$\mathrm{A}_2 - \mathrm{A}_2^{\mathrm{disc}}$	A_2	$\mathrm{A}_1 - \mathrm{A}_1$	A_3
	0.3187 -0.0497i	-0.2242 +0.0350i	0.1211 -0.0189i	-0.0380 -0.0897i	0.0200 -0.0031i

Table B.2: Most sizeable contributions in second order to $K_{ab}(\vartheta)$ at $\vartheta = 0.45$. Upper row for each particle indicates the inserted state. The text superscript, where present, indicates whether it is the disconnected or the connected part of the diagonal form factor.

to the post-quench expansion. Table B.1. contains the eight largest coefficients multiplying λ^2 for the one-particle overlap (5.27). Note that there are orders of magnitude difference between the first and last columns, which reflects the fast convergence of the form factor expansions.

For the pair overlap functions, the second order contributions are collected in Table B.2. Again, it is the lowest-lying states that contribute the most, but the coefficients decrease less drastically with the energy of the state, which is the reason why it was important to construct form factors beyond the ones available previously.

Appendix C

Analytical calculations for Kibble–Zurek ramps

C.1 Application of the adiabatic perturbation theory to the E_8 model

To use the framework of adiabatic perturbation theory in the E_8 model we assume that the time-evolved state can be expressed as

$$|\Psi(t)\rangle = \sum_n \alpha_n(t) \exp\{-i\Theta_n(t)\} |n(t)\rangle \ , \tag{C.1}$$

with the dynamical phase factor $\Theta_n(t) = \int_{t_\mathrm{i}}^{t} E_n(t')\,\mathrm{d}t'$. We also assume that there is no Berry phase and thus to leading order in the small parameter $\dot{\lambda}$ the α_n coefficients take the form

$$\alpha_n(\lambda) \approx \int_{\lambda_\mathrm{i}}^{\lambda} \mathrm{d}\lambda' \, \langle n(\lambda')| \, \partial_{\lambda'} \, |0(\lambda')\rangle \exp\{i(\Theta_n(\lambda') - \Theta_0(\lambda'))\} \, . \tag{C.2}$$

Higher derivatives as well as higher order terms in $\dot{\lambda}$ are neglected from now on.

The α_n coefficients can be used to formally express quantities that have known matrix elements in the instantaneous basis of the Hamiltonian:

$$\langle \mathcal{O}(t) \rangle = \sum_{m,n} \alpha_m^*(\lambda(t)) \alpha_n(\lambda(t)) \mathcal{O}_{mn} \, . \tag{C.3}$$

In what follows, we present the evaluation of this sum - approximately, under conditions of low energy density discussed in the main text - for the case of $\mathcal{O}(t) = H(t) - E_0(t)$ in the E_8 model. To generalise this calculation to the defect density or to higher moments of the statistics of work function is straightforward. The work density (or excess heat density) after the ramp reads

$$w(\lambda_\mathrm{f}) = \frac{1}{L} \sum_n \left(E_n(\lambda_\mathrm{f}) - E_0(\lambda_\mathrm{f})\right) |\alpha_n(\lambda_\mathrm{f})|^2 \, . \tag{C.4}$$

The spectrum of the model consists of 8 particle species $A_a, a = 1, \dots, 8$ with masses m_a. The energy and momentum eigenstates are the asymptotic states of the model labelled by a set of relativistic rapidities $\{\vartheta_1, \vartheta_2, \dots \vartheta_N\}$ and particle species indices $\{a_1, a_2, \dots a_N\}$:

$$|n\rangle = |\vartheta_1, \vartheta_2, \dots \vartheta_N\rangle_{a_1,a_2,\dots a_N} \,, \tag{C.5}$$

with energy $E_n = \sum_{i=1}^{N} m_{a_i} \cosh(\vartheta_i)$ and momentum $p_n = \sum_{i=1}^{N} m_{a_i} \sinh(\vartheta_i)$. The summation in Eq. (C.4) in principle goes over the infinite set of asymptotic states. As discussed in the main text, for low enough density we can approximate the sum in Eq. (C.4) with the contribution of one- and two-particle states, analogously to the calculation of Ref. [192] in the sine–Gordon model.

C.1.1 One-particle states

As discussed in the main text the one-particle states do not add to the energy density in the thermodynamic limit. Nevertheless, in a finite volume L they give a finite contribution, which can be expressed as

$$w_{1\text{p}} = \frac{1}{L} \sum_{a=1}^{8} m_a |\alpha_a(\lambda_\text{f})|^2 \,, \tag{C.6}$$

where m_a is the mass of the particle species a and the summation runs over the eight species. We can write the coefficient α_a as

$$\alpha_a(\lambda_\text{f}) = \int_{\lambda_\text{i}}^{\lambda_\text{f}} \text{d}\lambda \, \langle\{0\}_a(\lambda)| \, \partial_\lambda \, |0(\lambda)\rangle \exp\left\{ i\tau_\text{Q} \int_{\lambda_\text{i}}^{\lambda} \text{d}\lambda' m_a(\lambda') \right\} , \tag{C.7}$$

where $\langle\{0\}_a(\lambda)|$ denotes the asymptotic state with a single zero-momentum particle. The matrix elements and masses depend on λ through the Hamiltonian that defines the spectrum. The matrix element can be evaluated as

$$\langle\{0\}_a(\lambda)| \, \partial_\lambda \, |0(\lambda)\rangle = -\frac{\langle\{0\}_a(\lambda)| \, V \, |0(\lambda)\rangle}{m_a(\lambda)} \,. \tag{C.8}$$

For the momentum-conserving E_8 ramps considered in the main text, V is the integral of the local magnetisation operator $\sigma(x)$: $V = \int_0^L \sigma(x)\text{d}x$. Utilising this we further expand

$$\langle\{0\}_a(\lambda)| \, \partial_\lambda \, |0(\lambda)\rangle = -\frac{L F_a^{\sigma *}(\lambda)}{m_a(\lambda)\sqrt{m_a(\lambda) L}} \,, \tag{C.9}$$

where the square root in the denominator emerges from the finite volume matrix element [93] and F_a^σ is the (infinite volume) one-particle form factor of the magnetisation operator. It only depends on the coupling λ through its proportionality to the vacuum expectation value of σ. The particle masses scale as the gap: $m_a(\lambda) = C_a|\lambda|^{z\nu}$, where C_a are some constants. This allows us to write

$$|\alpha_a(\lambda_\mathrm{f})|^2 = L\left|\int_{\lambda_\mathrm{i}}^{\lambda_\mathrm{f}} \mathrm{d}\lambda\, \frac{\tilde{F}_a^{\sigma*}\lambda^{2\nu-1}}{C_a^{3/2}|\lambda|^{3/2z\nu}} \exp\left\{i\tau_\mathrm{Q}\int_{\lambda_\mathrm{i}}^{\lambda} \mathrm{d}\lambda' C_a|\lambda'|^{z\nu}\right\}\right|^2 . \tag{C.10}$$

We can perform the integral in the exponent that leads to a $\tau_\mathrm{Q}|\lambda|^{1+z\nu}$ dependence there. To get rid of the large τ_Q factor in the denominator, we introduce the rescaled coupling ζ with

$$\zeta = \lambda\tau_\mathrm{Q}^{\frac{1}{1+z\nu}} . \tag{C.11}$$

The change of variables yields

$$|\alpha_a(\lambda_\mathrm{f})|^2 = L\tau_\mathrm{Q}^{-\frac{\nu(4-3z)}{1+z\nu}}\left|\int_{\zeta_\mathrm{i}}^{\zeta_\mathrm{f}} \tilde{C}_a \mathrm{sgn}(\zeta)|\zeta|^{2\nu-1-3/2z\nu} \exp\left\{iC_a'|\zeta|^{1+z\nu}\right\}\right|^2 , \tag{C.12}$$

where $\tilde{C}_a$ and C_a' are constants that depend on C_a, the one-particle form factors and the critical exponents. We note the integral is convergent for large ζ due to the strongly oscillating phase factor and also for $\zeta \to 0$ since $2\nu - 1 - 3/2z\nu = -11/15$ in the E_8 model. Substituting $z = 1$ in the exponent of τ_Q leads to the correct KZ exponent of a relativistic model, $\nu/(1+\nu)$.

The result is quite peculiar in the sense that it is proportional to L, giving a volume-independent contribution to the energy density. Taking the thermodynamic limit of Eq. (C.12) naively would result in a finite energy density of 8 states, which is a reductio ad absurdum. Mathematically, the source of this paradox is that we approximated the normalisation of the perturbed state as 1, which is a leading order estimate, and breaks down if L is too large compared to $1/\tau_\mathrm{Q}$. We can intuitively argue that this paradox is eventually resolved by the increasing weight of multi-particle states as L is increased: in a sense, they take on the role of one-particle states in larger volume to create the KZ scaling. From a reversed point of view (i.e., keeping L fixed, and increasing τ_Q), (C.12) serves as an extension of Kibble–Zurek physics by one-particle states, working against the ultimately inevitable adiabatic behaviour brought about by finite volume, a missed shortcut to adiabaticity. This further explains why the KZ scaling window is much more extended towards larger τ_Q in the E_8 model compared to the free fermion line.

Nevertheless, for low-density settings, the multi-particle states mentioned above still effectively factorise to two-particle pairs, which are able to carry a finite density, as infinitely many of them are allowed as $L \to \infty$. Let us now turn to the contribution of pair states.

C.1.2 Two-particle states

The contribution of a two-particle state with species a and b is going to be denoted w_{ab} and reads

$$w_{ab}(\lambda_\mathrm{f}) = \frac{1}{L}\sum_{\vartheta}(m_a\cosh\vartheta + m_b\cosh\vartheta_{ab})|\alpha_\vartheta(\lambda_\mathrm{f})|^2\,, \tag{C.13}$$

where ϑ_{ab} is a function of ϑ determined by the constraint that the state has zero overall momentum. The summation goes over the rapidities that are quantised in finite volume L by the Bethe–Yang equations:

$$Q_i = m_{a_i}L\sinh\vartheta_i + \sum_{j\neq i}^{N}\delta_{a_ia_j}(\vartheta_i-\vartheta_j) = 2\pi I_i\,, \tag{C.14}$$

where I_i are integers numbers and

$$\delta_{ab} = -i\log S_{ab} \tag{C.15}$$

is the scattering phase shift of particles of type a and b. For a two-particle state Eq. (C.14) amounts to two equations of which only one is independent due to the zero-momentum constraint. It reads

$$\tilde{Q}(\vartheta) = m_aL\sinh\vartheta + \delta_{ab}(\vartheta-\vartheta_{ab}) = 2\pi I\,, \qquad I\in\mathbb{Z}\,. \tag{C.16}$$

In the thermodynamic limit $L\to\infty$ the summation is converted to an integral with the integral measure $\frac{\mathrm{d}\vartheta}{2\pi}\tilde{\rho}(\vartheta)$, where $\tilde{\rho}(\vartheta)$ is the density of zero-momentum states defined by

$$\tilde{\rho}(\vartheta) = \frac{\partial\tilde{Q}(\vartheta)}{\partial\vartheta} = m_aL\cosh\vartheta + \left(1+\frac{m_a\cosh\vartheta}{m_b\cosh\vartheta_{ab}}\right)\Phi_{ab}(\vartheta-\vartheta_{ab})\,, \tag{C.17}$$

where $\Phi(\vartheta)$ is the derivative of the phase shift function. The resulting integral is

$$\frac{1}{L}\int_{-\infty}^{\infty}\frac{\mathrm{d}\vartheta}{2\pi}\tilde{\rho}(\vartheta)|\alpha_\vartheta(\lambda_\mathrm{f})|^2\,. \tag{C.18}$$

The $\alpha_\vartheta(\lambda_\mathrm{f})$ term can be expressed as (cf. Eq. (C.2)

$$\begin{aligned}\alpha_\vartheta(\lambda_\mathrm{f}) = &\int_{\lambda_\mathrm{i}}^{\lambda_\mathrm{f}}\mathrm{d}\lambda\,\langle\{\vartheta,\vartheta_{ab}\}_{ab}(\lambda)|\,\partial_\lambda\,|0(\lambda)\rangle\times\\ &\times\exp\left\{i\tau_\mathrm{Q}\int_{\lambda_\mathrm{i}}^{\lambda}\mathrm{d}\lambda'\,[m_a(\lambda')\cosh\vartheta + m_b(\lambda')\cosh\vartheta_{ab}]\right\}.\end{aligned} \tag{C.19}$$

Analogously to the one-particle case we can evaluate the matrix element in the E_8 field theory as

$$-\frac{L\,\langle\{\vartheta,\vartheta_{ab}\}_{ab}(\lambda)|\,\sigma(0)\,|0(\lambda)\rangle_L}{E_n(\lambda)-E_0(\lambda)} = -\frac{LF^{\sigma *}_{ab}(\vartheta,\vartheta_{ab})}{(E_n(\lambda)-E_0(\lambda))\sqrt{\rho_{ab}(\vartheta,\vartheta_{ab})}}\,, \tag{C.20}$$

where $F^{\sigma}_{ab}(\vartheta_1,\vartheta_2)$ is the two-particle form factor of operator σ in the E_8 field theory and the density factor is the Jacobian of the two-particle Bethe–Yang equations (C.14) arising from the normalisation of the finite-volume matrix element [93]. It can be expressed as

$$\begin{aligned}\rho_{ab}(\vartheta_1,\vartheta_2) =& m_a L\cosh\vartheta_1 m_b L\cosh\vartheta_2 + \\ &+(m_a L\cosh\vartheta_1 + m_b L\cosh\vartheta_2)\Phi_{ab}(\vartheta_1-\vartheta_2)\,.\end{aligned} \tag{C.21}$$

Observing Eqs. (C.17) and (C.21) one finds that the details of the interaction enter via the derivative of the phase shift function but crucially, they are of order $1/L$ compared to the free field theory part. So leading order in L we find that

$$\begin{aligned}w_{ab}(\lambda_\mathrm{f}) =& \int_{-\infty}^{\infty}\frac{\mathrm{d}\vartheta}{2\pi}\,(m_a(\lambda_\mathrm{f})\cosh\vartheta + m_b(\lambda_\mathrm{f})\cosh\vartheta_{ab})\,m_a(\lambda_\mathrm{f})\cosh\vartheta\times \\ &\times\Bigg|\int_{\lambda_\mathrm{i}}^{\lambda_\mathrm{f}}\mathrm{d}\lambda\frac{F^{\sigma *}_{ab}(\vartheta,\vartheta_{ab})}{(m_a(\lambda)\cosh\vartheta + m_b(\lambda)\cosh\vartheta_{ab})}\times \\ &\times\frac{\exp\Big(i\tau_\mathrm{Q}\int_{\lambda_\mathrm{i}}^{\lambda}\mathrm{d}\lambda'\,(m_a(\lambda')\cosh\vartheta + m_b(\lambda')\cosh\vartheta_{ab})\Big)}{\sqrt{m_a(\lambda)m_b(\lambda)\cosh\vartheta\cosh\vartheta_{ab}}}\Bigg|^2 + \mathcal{O}(1/L)\,.\end{aligned} \tag{C.22}$$

By a change of variables in the outer integral to the one-particle momentum $p = m_a\sinh\vartheta$ we obtain

$$w_{ab} = \int_{-\infty}^{\infty}\frac{\mathrm{d}p}{2\pi}E_p(\lambda_\mathrm{f})\left|\int\mathrm{d}\lambda G(\vartheta)\exp\left(i\tau_\mathrm{Q}\int\mathrm{d}\lambda' E_\vartheta(\lambda')\right)\right|^2\,. \tag{C.23}$$

Now we can introduce the momentum p in the inner integral as well by noting that the energy can be expressed as a function of momentum via the relativistic dispersion and that the relativistic rapidity also $\vartheta = \operatorname{arcsinh}(p/m)$. Since $m\propto|\lambda|^{z\nu}$ with $z=1$ any expression that is a function of ϑ can be expressed as a function of $p/|\lambda|^\nu$. Having this in mind, the result is analogous to the free case so all the machinery developed there can be used. The key assumptions from this point regard the scaling properties of the energy gap and the matrix element $G(\vartheta)$ in this brief notation:

$$\begin{aligned}E_p(\lambda) &= |\lambda|^{z\nu}F(p/|\lambda|^\nu) \\ G(\vartheta) &= \lambda^{-1}G(p/|\lambda|^\nu)\,.\end{aligned} \tag{C.24}$$

These equations are trivially satisfied with the proper asymptotics for $F(x)\propto x^z$. To obtain the asymptotics og $G(x)$ in the E_8 model we use

$$\begin{aligned}\lim_{L\to\infty}\langle\{\vartheta,\vartheta_{ab}\}(\lambda)|\,\partial_\lambda\,|0(\lambda)\rangle_L =& \frac{\langle\sigma\rangle\,F^{\sigma *}_{ab}(\vartheta,\vartheta_{ab})}{\sqrt{m_a\cosh\vartheta m_b\cosh\vartheta_{ab}}(m_a\cosh\vartheta + m_b\cosh\vartheta_{ab})} \\ =& \lambda^{1/15-8/15-8/15}G(\vartheta) = \lambda^{-1}G(\vartheta)\,,\end{aligned} \tag{C.25}$$

where we neglected the $\mathcal{O}(1/L)$ term from the finite volume normalisation and used $\langle\sigma\rangle \propto \lambda^{1/15}$, $m \propto \lambda^{8/15}$. $F_{ab}(\vartheta, \vartheta_{ab})$ is the two-particle form factor of the E_8 theory that does not depend on the coupling. They satisfy the asymptotic bound [89]:

$$\lim_{|\vartheta_i|\to\infty} F^{\sigma}(\vartheta_1, \vartheta_2 \ldots, \vartheta_n) \leq \exp(\Delta_\sigma |\vartheta_i|/2)\,. \tag{C.26}$$

Since the matrix elements considered here are of zero-momentum states, $\vartheta \to \infty$ means $\vartheta_{ab} \to -\infty$ and $F^{\sigma}_{ab}(\vartheta, \vartheta_{ab}) \leq \exp(\Delta_\sigma \vartheta)$ as the form factors depend on the rapidity difference. Dividing by the factor $\exp(2\vartheta)$ in the denominator yields the correct asymptotics $G(x) \propto x^{\Delta-2} = x^{-1/\nu}$ as an upper bound due to Eq. (C.26). We remark that the scaling forms (C.24) hold true for any value of the coupling λ in the field theory, in contrast to the lattice where they are valid only in the vicinity of the critical point. From this perspective Eq. (C.24) follows from the definition of the field theory as a low-energy effective description of the lattice model near its critical point.

As a consequence, one can introduce new variables in place of λ and p such that the explicit τ_{Q} dependence disappears from the integrand. This is achieved by the following rescaling:

$$\eta = p\tau_{\mathrm{Q}}^{\frac{\nu}{1+z\nu}}\,, \qquad \zeta = \lambda\tau_{\mathrm{Q}}^{\frac{1}{1+z\nu}}\,. \tag{C.27}$$

The result for the energy density is

$$w_{ab} = \tau_{\mathrm{Q}}^{-\frac{\nu}{1+z\nu}} \int_{-\infty}^{\infty} \frac{\mathrm{d}\eta}{2\pi} E_{p=\eta\tau_{\mathrm{Q}}^{-\frac{\nu}{1+z\nu}}}(\lambda_{\mathrm{f}})\, |\alpha(\eta)|^2\,. \tag{C.28}$$

In terms of scaling there are two options: first, let $|\lambda_{\mathrm{f}}| \neq 0$ hence $\zeta_{\mathrm{f}} \to \infty$ in the KZ scaling limit $\tau_{\mathrm{Q}} \to \infty$. Then the energy gap at $p \to 0$ is a constant and $E_{p=0}(\lambda_{\mathrm{f}})$ can be brought in front of the integral. If it converges, Eq. (C.28) completely accounts for the KZ scaling. Second, if $|\lambda_{\mathrm{f}}| = 0$, the energy gap is $E_p \propto p^z$ and an additional factor of $\tau_{\mathrm{Q}}^{-\frac{\nu}{1+z\nu}}$ appears in front of the integral. Note that this is the scaling of κ_1 in Fig. 7.11. The high-energy tail of the integrand is modified due to the extra term of η^z from the energy gap. This leads to a convergence criterion such that once again the crossover to quadratic scaling happens when the exponent of τ_{Q} in front of the integral is less then -2. It is easy to generalise this argument to the nth moment of the statistics of work, which amounts to substituting E_p^n instead of E_p to Eq. (C.28). As argued in the main text, this is the leading term in the nth cumulant of the distribution as well, which concludes the perturbative reasoning behind the results of Sec. 7.4.

C.2 Ramp dynamics in the free fermion field theory

The non-equilibrium dynamics of the transverse field Ising chain is thoroughly studied in the literature. Due to the factorisation of the dynamics to independent fermionic modes solving the time evolution amounts to the treatment of a two-level problem parametrised by the momentum k. This two-level problem can be mapped to the famous Landau–Zener transition with momentum-dependent crossing time. Its exact solution is known and yields a particularly simple expression for the excitation probability of low-momentum modes p_k (or $|\alpha(k)|^2$ with the notation of adiabatic perturbation theory, cf. Sec. 7.1.3) in the limit $\tau_{\mathrm{Q}} \to \infty$. Then the KZ scaling of various quantities follows [189, 215], and extends to the full counting statistics of defects [217] and excess heat [194]. For a finite Landau–Zener problem one can express the solution in terms of Weber functions [182, 186], while for a generic nonlinear ramp profile as the solution of a differential equation [201, 219].

To generalise the analytical solution on the chain to the free field theory we performed the scaling limit on the expressions of Ref. [201]. We remark that in the works cited above there are several parallel formulations of this problem on the chain each with a slightly different focus. Our choice to use this specific one in the continuum limit is arbitrary but the result is the same for all frameworks. We use the following notation: $c_k^{(\dagger)}$ denotes the Fourier transformed fermionic (creation)-annihilation operators obtained by the Jordan–Wigner transformation. In each mode k, $\eta_k^{(\dagger)}$ are the quasiparticle ladder operators and we use $\eta_{k,\mathrm{i}}^{(\dagger)}$ to refer to the operators that diagonalise the Hamiltonian initially before the ramp procedure. The operators c and η are related via the Bogoliubov transformation

$$\eta_k = U_k c_k - i V_k c_{-k}^{\dagger}\,, \tag{C.29}$$

where the coefficients are $U_k = \cos\theta_k/2$ and $V_k = \sin\theta_k/2$ with

$$\exp(i\theta_k) = \frac{g - \exp(ik)}{\sqrt{1 + g^2 - 2g\cos k}}\,. \tag{C.30}$$

From a dynamical perspective, U and V relate the adiabatic (instantaneous) free fermions and quasiparticles, hence we are going to refer to them as adiabatic coefficients. The dynamics can be solved in the Heisenberg picture using the Ansatz

$$c_k(t) = u_k(t)\eta_{k,\mathrm{i}} + i v_{-k}^{*}(t)\eta_{k,\mathrm{i}}^{\dagger}\,. \tag{C.31}$$

The Heisenberg equation of motion yields a coupled first order differential equation system for the time-dependent Bogoliubov coefficients that can be decoupled as [201]:

$$\frac{\partial^2}{\partial t^2} y_k(t) + \left(A_k(t)^2 + B_k^2 \pm i \frac{\partial}{\partial t} A_k(t) \right) y_k(t) = 0\,, \tag{C.32}$$

where the upper and lower signs correspond to $y_k(t) = u_k(t)$ and $y_k(t) = v_{-k}^{*}(t)$ respectively, and $A_k(t) = 2J(g(t) - \cos k)$ and $B_k = 2J\sin k$. To connect with the expression for the time-evolved k mode in the main text,

$$|\Psi(t)\rangle_k = a_k(t)\,|0\rangle_{k,t} + b_k(t)\,|1\rangle_{k,t}\,, \tag{C.33}$$

we have to express $a_k(t)$ and $b_k(t)$ with the time-dependent Bogoliubov coefficients. To do so, first one has to perform a Bogoliubov transformation that relates the quasiparticle operators $\eta_{k,\mathrm{i}}$ defined by the initial value of coupling g_{i} to the instantaneous operators $\eta_{k,t}$ that are given by $g(t)$, then substitute Eq. (C.31) to account for the dynamics. The result is concisely expressed by the following scalar products:

$$a_k(t) = \begin{pmatrix} U_k & -V_k \end{pmatrix} \begin{pmatrix} u_k(t) \\ v^*_{-k}(t) \end{pmatrix} , \qquad b_k(t) = \begin{pmatrix} V_k & U_k \end{pmatrix} \begin{pmatrix} u_k(t) \\ v^*_{-k}(t) \end{pmatrix} \tag{C.34}$$

where U_k and V_k are defined by Eq. (C.30) using the ramped coupling $g(t)$. The population of the mode k is given by $n_k(t) = |b_k(t)|^2$. Notice that the slight difference between Eq. (C.34) and the notation of Refs. [182, 186] is due to a different convention of the Bogoliubov transformation.

To take the continuum limit, one has to apply the prescriptions detailed in Sec. 2.2.1 to Eq. (C.32). Denoting the momentum of field theory modes with p we get

$$A_p(t) = M(t) \,, \qquad B_p = p \,, \tag{C.35}$$

where $M(t)$ is the time-dependent coupling of the field theory. The initial conditions read

$$u_p(t=0) = U_p \,, \qquad \left.\frac{\partial}{\partial t} u_p(t)\right|_{t=0} = -iM_{\mathrm{i}} U_p - ipV_{-p} \tag{C.36}$$

$$v^*_{-p}(t=0) = V_{-p} \,, \qquad \left.\frac{\partial}{\partial t} v^*_{-p}(t)\right|_{t=0} = -ipU_p + iM_{\mathrm{i}} V_{-p} \,, \tag{C.37}$$

where the adiabatic coefficients U and V are defined by the initial coupling M_{i} via the expressions

$$U_p = +\sqrt{\frac{1}{2} + \frac{M}{2\sqrt{p^2 + M^2}}} \tag{C.38}$$

and

$$V_p = \begin{cases} +\sqrt{\frac{1}{2} - \frac{M}{2\sqrt{p^2+M^2}}} & \text{for} \quad p \leq 0 \,, \\ -\sqrt{\frac{1}{2} - \frac{M}{2\sqrt{p^2+M^2}}} & \text{for} \quad p > 0 \,. \end{cases} \tag{C.39}$$

We remark that for a linear ramp profile one can express the solution exactly using the parabolic Weber functions [201]. However, for practical purposes we opted for the numerical integration of Eq. (C.32). The results of Sec. 7.2 are obtained by solving the differential equations substituting the quantised momenta for p. As the excitation probability of a mode p is suppressed as $n_p \propto \exp(-\pi \tau_{\mathrm{Q}} p^2/m)$, we calculated the solution up to a momentum cut-off $p_{\max}/m = 2\pi$. At volume $L = 50$ this amounts to 100 modes in the two sectors together.

For the intensive quantities considered in Secs. 7.3 and 7.4 we worked in the thermodynamic limit $L \to \infty$ where the sum over momentum modes is converted to an integral. Calculating the excitation probabilities of several modes up to a cutoff $p_{\mathrm{max}}/m = 30$ we used interpolation to obtain a continuous n_p function. This was used in the momentum integrals that yield the energy density and its higher cumulants. The need for the higher cutoff stems from the fact that n_p decreases less drastically for ECP ramps.

Appendix D

Numerical details of the TCSA data

D.1 Conventions and applying truncation

The truncated conformal space approach was developed originally by Yurov and Zamolodchikov [55, 56]. It constructs the matrix elements of the Hamiltonian of a perturbed CFT in finite volume R on the conformal basis. The Ising field theory is defined as the near-critical perturbation of the $c = 1/2$ minimal CFT by adding the primary fields σ and ϵ. We recall the form of the dimensionless Hamiltonian:

$$H/\Delta = \frac{2\pi}{r}\left(L_0 + \bar{L}_0 - c/12 + \tilde{\kappa}_1 \frac{r^{2-\Delta_\epsilon}}{(2\pi)^{1-\Delta_\epsilon}} M_\epsilon + \tilde{\kappa}_2 \frac{r^{2-\Delta_\sigma}}{(2\pi)^{1-\Delta_\sigma}} M_\sigma\right) , \tag{D.1}$$

where Δ is the mass gap opened by the perturbation, $r = \Delta R$ the dimensionless volume parameter and Δ_ϕ is the sum of left and right conformal weights of the primary field ϕ. All quantities are measured in units of the mass gap Δ, which is m, the mass of the elementary excitation on the free fermion line; and m_1, the mass of the lightest particle in the E_8 model. Where non-integrable settings are considered, the mass unit is chosen to correspond to the closest axis.

N_{cut}	matrix size	N_{cut}	matrix size	N_{cut}	matrix size
19	338	31	4476	43	40353
21	551	33	6654	45	56867
23	840	35	9615	47	78951
25	1330	37	14045	49	110053
27	1994	39	20011	51	151270
29	3023	41	28624	53	207809

Table D.1: Matrix size vs. cutoff. The more efficient storing of matrix elements in the CFTCSA version allows for the practical usage of the rightmost column.

Quantum quenches				
Observable	Type I		Type II	
	Leading	Subleading	Leading	Subleading
$\langle\epsilon\rangle$	-1	-2	-1^*	-2
$\langle\sigma\rangle$	-7/4	-11/4	-1	-7/4
Overlaps	-11/4	-15/4	$-11/4^\dagger$	-15/4

Kibble–Zurek ramps				
Observable	Free fermion model		E_8 model	
	Leading	Subleading	Leading	Subleading
κ_n	-1	-2	-11/4	-15/4
$\langle\sigma\rangle$	-1	-2	-7/4	-11/4

Table D.2: Extrapolation exponents for the various quantities. * : the $\langle\epsilon\rangle$ one-point function is logarithmically divergent (corresponding to a zero leading exponent), but the divergence is a constant shift in the time-dependent function, and it can be subtracted. The oscillations are then fitted by the exponents written here. † : the non-integrable perturbation in principle modifies the exponents with respect to Type I quenches, but the fitting procedure reveals that the corresponding coefficient is negligible, and the most precise fits are given by the above setting.

The matrix elements of H are calculated using the eigenstates of the conformal Hamiltonian H_0 as basis vectors:

$$H_0 \left|n\right\rangle = \frac{2\pi}{R}\left(L_0 + \bar{L}_0 - \frac{c}{12}\right)\left|n\right\rangle = E_n \left|n\right\rangle \ , \tag{D.2}$$

where $c = 1/2$ is the central charge. The truncation is imposed by the constraint that only vectors with $E_n < E_{\text{cut}}$ are kept, where E_{cut} is the cutoff energy. It is convenient to characterise the cutoff with the $L_0 + \bar{L}_0$ eigenvalue N instead of the energy as it is related to the conformal descendent level. Table D.1 contains the number of states with

$$N - \frac{c}{12} < N_{\text{cut}} \equiv \frac{R}{2\pi}E_{\text{cut}} \tag{D.3}$$

for the range of cutoffs that were used in this work.

D.2 Extrapolation details

As discussed in the main text, the truncation errors can be minimised by applying an extrapolation procedure to approximate the infinite-cutoff value of observables by fitting data obtained using a range of cutoff parameters. The general

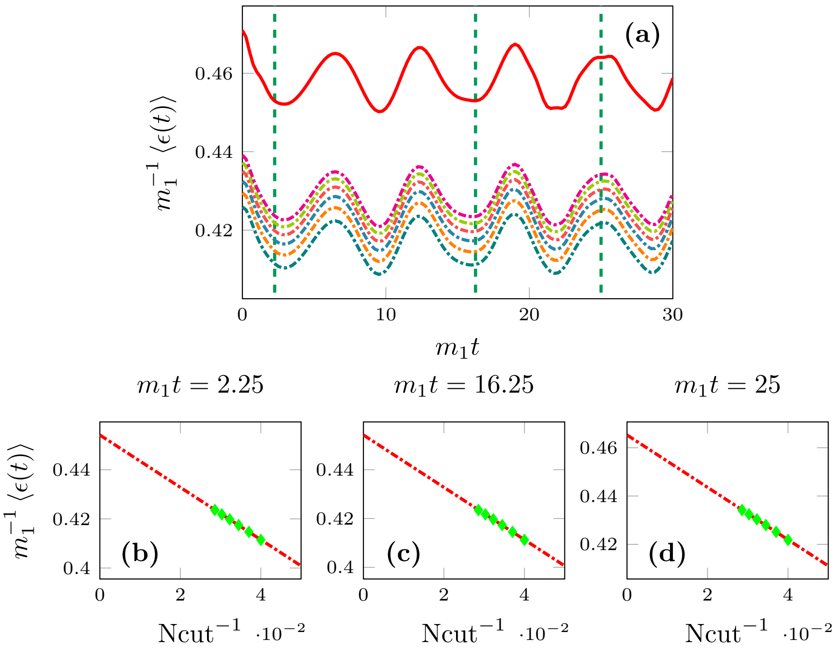

Figure D.1: Extrapolation of the post-quench time evolution of $\langle\epsilon(t)\rangle$ following a Type I quench in the E_8 model, with $\xi = 0.05$ and $m_1 R = 40$. Panel (a) shows the raw data from a range of cutoffs $N_{\text{cut}} = 25 \ldots 35$ with dashdotted lines, while solid lines denote the extrapolated value. Sections of this panel at three time instances denoted by dashed gridlines are presented in panels (b)-(d). Here green diamonds denote the raw data with respect to N_{cut}, the leading exponent, and the fitted function is in dashdotted red lines. Note that the fitted function appears linear: this reflects the fact that only the leading exponent was used for this quantity.

form of the relation between TCSA data at a given cutoff and the truncation-free value reads: [59, 64]

$$\langle\mathcal{O}\rangle = \langle\mathcal{O}\rangle_{\text{TCSA}} + AN_{\text{cut}}^{-\alpha_{\mathcal{O}}} + BN_{\text{cut}}^{-\beta_{\mathcal{O}}} + \ldots . \tag{D.4}$$

The exponents $\alpha_{\mathcal{O}}, \beta_{\mathcal{O}}$ depend on the operator $\mathcal{O}$, and on the primary fields that perturb the CFT. For completeness, we gather all the exponents used for the extrapolation of the various quantities in Tab. D.2.

We applied Eq. (D.4) to obtain what is called throughout the main text as 'extrapolated TCSA data'. Strictly speaking, the relation is established for the vacuum expectation value of a local operator $\mathcal{O}$ in the model, but we utilised under more relaxed conditions: for dynamical quantities, performing extrapolation at each time instant; for post-quench overlaps, where we calculated the $\alpha_{\mathcal{O}}, \beta_{\mathcal{O}}$ exponents using $\mathcal{O} = \mathbb{I}$ the identity operator; and for the cumulants of the statistics of work function. In certain cases the fit with two exponents proved to be numerically unstable reflected by large residual error of the estimated fit coefficients. In these cases, only the leading exponent was used.

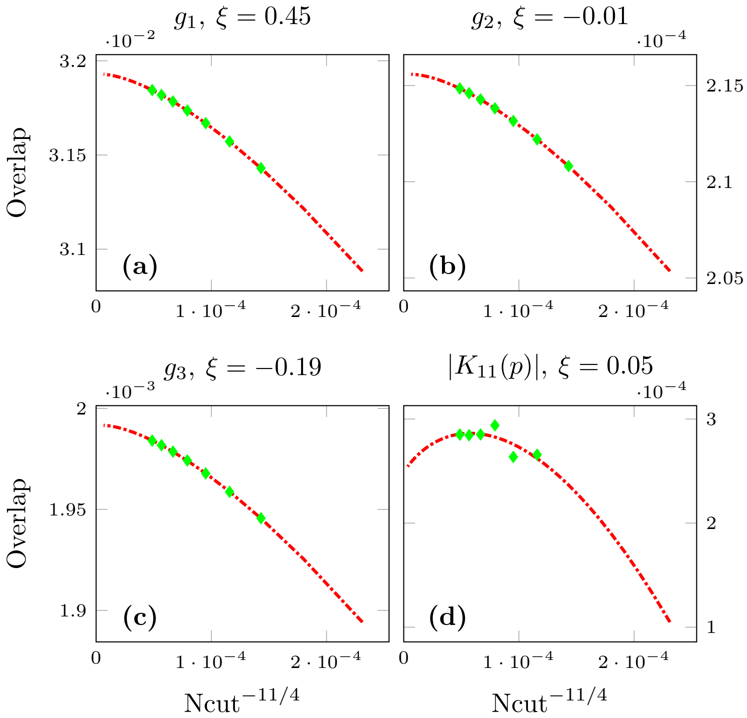

Figure D.2: Extrapolation of the post-quench overlaps for Type I quenches in the E_8 model. The conventions are the same as in Fig. D.1 (b)-(d). The behaviour of one-particle overlaps in panels (a)-(c) is correctly estimated by Eq. (D.4). The same does not hold for the pair overlap depicted in panel (d), where the cutoff-dependence is not monotonous and apparently erratic. Consequently, the numerical two-particle overlaps in the main text are not extrapolated, but rather taken from a highest cutoff considered in this figure, $N_{\text{cut}} = 37$.

In each case, we sampled the extrapolation fits to see whether the power-law dependence on N_{cut} is correct in the regime of cutoff-parameters we used. In the overwhelming majority of the cases, we found a significant improvement by the extrapolation, with the sole exception of pair-state overlaps following a quantum quench. Representative examples are included in Figs. D.1-D.4 as an illustration of the extrapolation for post-quench time evolution, post-quench overlaps, dynamical one-point function along a ramp, and post-ramp cumulant functions, respectively.

As the use of TCSA to directly calculate the cumulant functions is unprecedented, let us elaborate on this part in a bit more detail. Based on the above discussion, we expect that the same expression accounts for the cutoff dependence as in the case of local observables. This is what we find inspecting Fig. D.4. The depicted data is a small subset of all the extrapolations whose results are presented in the main text but they convey the general message that cumulants can be obtained accurately using TCSA. The relative error in the extrapolated value

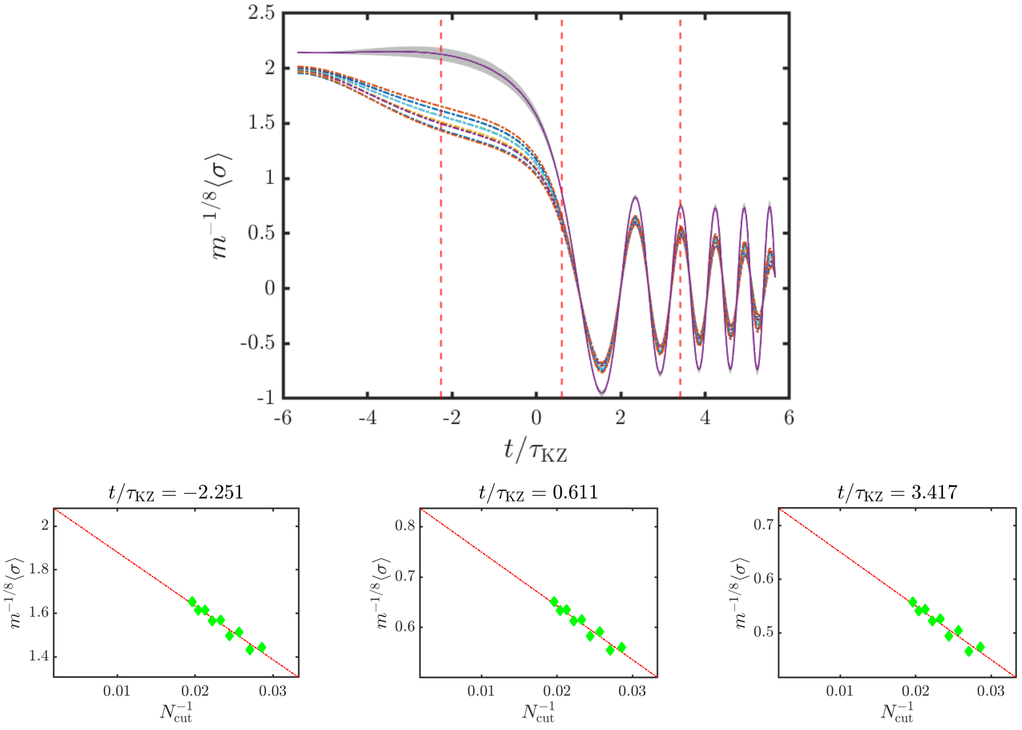

Figure D.3: Details of the extrapolation for the dynamical one-point function of the order parameter for a ferromagnetic-paramagnetic ramp along the free fermion line with $mR = 50$ and $m\tau_{\mathrm{Q}} = 128$. The cutoff parameter is in the range $N_{\mathrm{cut}} = 35 \ldots 51$. The conventions are the same as in Fig. D.1, with the addition that the residual fitting error is denoted by a grey shading.

is typically in the order of $1 - 3\%$ for cumulants in the free fermion model (with an increase towards higher cumulants) and around $0.1 - 0.7\%$ in the E_8 model.

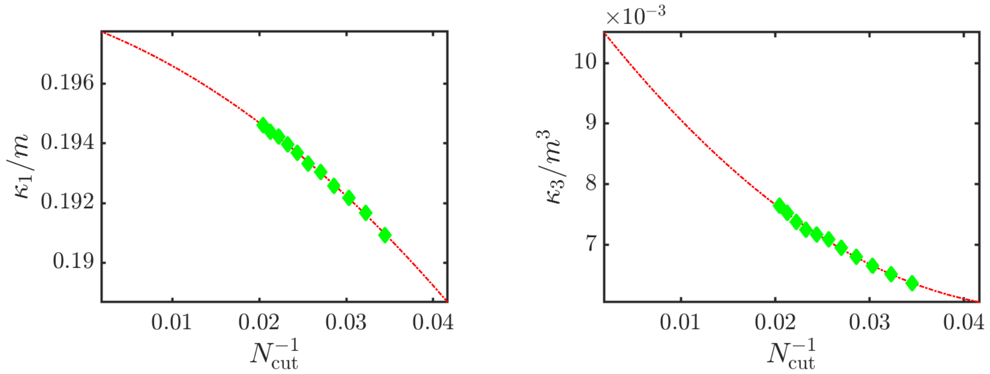

(a) FF ECP ramp, κ_1, $mR = 40$ (b) FF ECP ramp, κ_3, $mR = 70$

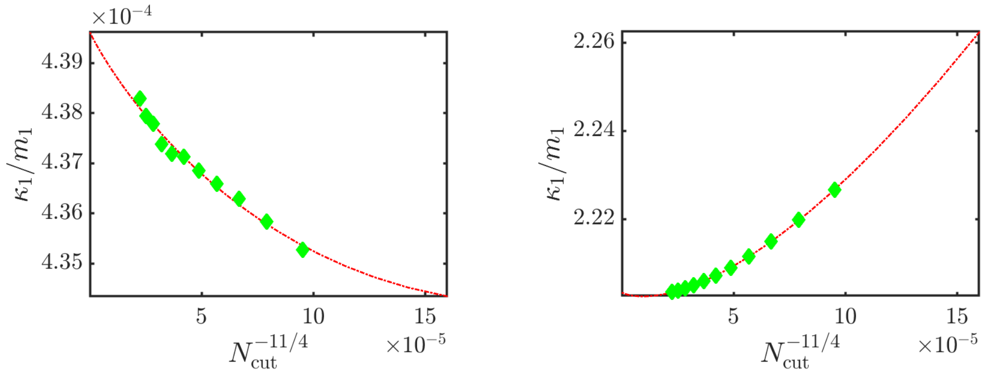

(c) E_8 ECP ramp, κ_2, $m_1R = 65$ (d) E_8 TCP ramp, κ_1, $m_1R = 55$

Figure D.4: Extrapolation of various work cumulants for various protocols. The plots are typical of the overall picture of extrapolating overlaps obtained using TCSA.